Heat Transfer and Flow Regimes During Condensation in Horizontal Tubes

M. K. Dobson, J. C. Chato, J. P. Wattelet, J. A. Gaibel, M. Ponchner,
P. J. Kenney, R. L. Shimon, T. C. Villaneuva, N. L. Rhines, K. A. Sweeney,
D. G. Allen, and T. T. Hershberger

ACRC TR-57 May 1994

For additional information:

Air Conditioning and Refrigeration Center
University of Illinois
Mechanical & Industrial Engineering Dept.
1206 West Green Street
1206 West Green Street
Urbana, IL 61801

(217) 333-3115

Prepared as part of ACRC Project 37
Effect of Geometric Variables and R-22 Alternatives on
Refrigerant-Side Evaporation and Condensation
J. C. Chato, Principal Investigator

The Air Conditioning and Refrigeration Center was founded in 1988 with a grant from the estate of Richard W. Kritzer, the founder of Peerless of America Inc. A State of Illinois Technology Challenge Grant helped build the laboratory facilities. The ACRC receives continuing support from the Richard W. Kritzer Endowment and the National Science Foundation. The following organizations have also become sponsors of the Center.

Acustar Division of Chrysler
Allied-Signal, Inc.
Amana Refrigeration, Inc.
Brazeway, Inc.
Carrier Corporation
Caterpillar, Inc.
E. I. du Pont de Nemours & Co.
Electric Power Research Institute
Ford Motor Company
Frigidaire Company
General Electric Company
Harrison Division of GM
ICI Americas, Inc.
Modine Manufacturing Co.
Peerless of America, Inc.
Environmental Protection Agency
U. S. Army CERL
Whirlpool Corporation

For additional information:

Air Conditioning & Refrigeration Center
Mechanical & Industrial Engineering Dept.
University of Illinois
1206 West Green Street
Urbana IL 61801

217 333 3115

HEAT TRANSFER AND FLOW REGIMES
DURING CONDENSATION IN HORIZONTAL TUBES

Monte Keith Dobson, Ph.D.
Department of Mechanical and Industrial Engineering
University of Illinois at Urbana-Champaign, 1994
John C. Chato, Advisor

ABSTRACT

An experimental study of heat transfer and flow regimes during condensation of refrigerants in horizontal tubes was conducted. Measurements were made in smooth, round tubes with diameters ranging from 3.14 mm to 7.04 mm. Four refrigerants were tested: R-12, R-22, R-134a, and azeotropic blends of R-32/R-125 in 50%/50% and 60%/40% compositions.

Flow regimes were observed visually at the inlet and outlet of the test-condenser as the heat transfer data were collected. Stratified, wavy, wavy-annular, annular, annular-mist, and slug flows were observed. True mist flow without a stable wall film was not observed during condensation tests. For the purpose of condensing heat transfer behavior, the various flow regimes were divided into two broad categories of gravity-dominated and shear-dominated flow.

The heat transfer behavior was strongly related to the flow regime. In the gravity-dominated flow regime, the dominant heat transfer mode was laminar film condensation. This regime was characterized by heat transfer coefficients that depended on the wall to refrigerant temperature difference but were nearly independent of mass flux. In the shear-dominated flow regime, forced convective condensation was the dominant heat transfer mechanism. This regime was characterized by heat transfer coefficients that were independent of temperature difference but very dependent on mass flux and quality. Separate heat transfer correlations that were developed for each of these flow regimes successfully predicted data from the present study and several external sources.

The heat transfer correlations were combined with existing pressure drop correlations to develop a simple condenser model. This model was used to explore the existence of an optimum diameter. Simulations showed that the required condensing length increased slowly as the diameter was decreased over a wide range. As the diameter became sufficiently small, the condensing length began to increase dramatically because much of the driving temperature difference was destroyed by pressure drop. An optimum diameter existed where the condensing surface area was a minimum. An analytical solution showed that this optimum diameter corresponded to a decrease in the inlet temperature difference of between 23% and 37%. The predictions of this analytical solution agreed very well with the simulation model.

Executive Summary

This report on condensation, together with ACRC TR-55 on evaporation, represents the culmination of work done in Project 01 at the ACRC of the University of Illinois on the heat transfer and pressure drop characteristics of pure substances, azeotropes, and near azeotropes; primarily the potentially new refrigerants to be used in refrigeration and air conditioning systems. Some of the work, however, such as the writing of this report, has been performed in Project 37.

The purpose of this work was to obtain experimental, local heat transfer and flow data and to develop from these data appropriate correlations and methods to be used in the design of horizontal-tube condensers. The emphasis on local values was essential because the condensation process goes through several different flow patterns as more and more liquid is formed and the refrigerant decelerates. Thus, the identification of the flow pattern was just as important as the thermal or pressure drop data. We have found that for the range of parameters investigated, which cover primarily refrigerator and air conditioner applications, the two major forces controlling the flow patterns are gravity and vapor shear. At low vapor velocities (low mass flux or quality, or both) gravity dominates and the liquid phase tends to stay at the bottom of the tube; whereas at high vapor velocities (high mass flux or quality, or both) the vapor shear dominates and the liquid phase tends to be uniformly distributed around the entire periphery of the tube with, possibly, some mist also occurring in the central vapor filled space.

In the gravity-dominated flow regime, the dominant heat transfer mode was laminar film condensation in the top of the tube. This regime was characterized by heat transfer coefficients that depended on the wall to refrigerant temperature difference but were nearly independent of mass flux. In the shear-dominated flow regime, forced convective condensation was the dominant heat transfer mechanism. This regime was characterized by heat transfer coefficients that were independent of temperature difference but were very dependent on mass flux and quality. Heat transfer correlations that were developed for each of these flow regimes successfully predicted data from the present study and from several external sources.

Most of the pressure drop data could be estimated by our previously developed correlation based on evaporation data, except for the very low and very high quality ranges. In the very low range the predictions were generally high, whereas in the very high range the predictions were low. These effects need further investigation.

The final analysis performed was the development of a method for properly utilizing our correlations for heat transfer and pressure drop in the design of a complete condenser. The computer model was based on the use of a spreadsheet which considerably simplified the work required. It included the pressure drops created by return bends (reported previously). The results show that the design may be optimized with respect to the minimum surface area required to perform a prescribed refrigeration task.

The details of the work are described in the following order. After the introduction a thorough review of the literature and of the existing theories is presented. Then the experimental apparatus and procedures are explained. The results are presented first for the flow patterns, then for the heat transfer, including the development of the correlations. Next, a spreadsheet-based computer model is given for the simulation and design of a complete condenser. Finally, conclusions and recommendations for future work are described. An extensive reference list and the appendices containing miscellaneous data and calculations close the report.

TABLE OF CONTENTS

Page

LIST OF TABLES

LIST OF FIGURES

NOMENCLATURE

SYMBOLS		DEFINITION
a	constant	
A_c	cross-sectional area	$\pi D^2/4$
A_l	cross-sectional area occupied by liquid	
$\tilde{A}_l$	dimensionless cross-sectional area occupied by liquid	A_l/D^2
A_g	cross-sectional area occupied by gas	
$\tilde{A}_g$	dimensionless cross-sectional area occupied by gas	A_g/D^2
A_v	cross-sectional area occupied by vapor	
A_s	Surface area	πDL
Ar	Archimedes number	$\dfrac{\rho_l^2\sigma^{3/2}}{\mu_l^2 g^{1/2}(\rho_l-\rho_v)^{3/2}}$
Bd	Bond number	$g(\rho_l-\rho_v)D^2/\sigma$
Bi_i	Biot number of inner fluid	h_iL/k_t
Bo	Boiling number	$\dot{Q}''/Gi_{lv}$
C	constant	
c_p	specific heat at constant pressure	
$c_{p,l}$	specific heat at constant pressure for liquid refrigerant	
$c_{p,v}$	specific heat at constant pressure for vapor refrigerant	
$c_{p,w}$	specific heat at constant pressure for water	
$\left(\dfrac{-dP}{dz}\right)_f$	acceleration pressure gradient	$\dfrac{1}{A_c}\dfrac{d}{dz}[\dot{m}_lV_l+\dot{m}_vV_v]$
$\left(\dfrac{-dP}{dz}\right)_f$	frictional pressure gradient	$4\tau_w/D$

D, D_i	tube inner diameter	
D_l	hydraulic diameter of the liquid phase	
D_o	tube outer diameter	
D^+	diameter/turbulent length scale	$D\sqrt{\tau_w/\rho_l}/\nu_l$
D^*	diameter/heat exchanger length scale	$D\Delta T_i/\dot{Q}R'_a$
E	entrained mass fraction	$\dot{m}_e/\dot{m}_l$
f	friction factor	$(-dP/dz)\rho D \Big/ 2G^2$
F	two-phase heat transfer multiplier	Nu/Nu_l
F_2	dimensionless heat transfer resistance of Traviss	Eq. (2.90)
F_{td}	modified Froude number of Taitel and Dukler	$\sqrt{\frac{\rho_g}{\rho_l-\rho_g}}\frac{j_g}{\sqrt{Dg\cos\alpha}}$
Fr_l	liquid-only Froude number	$(G/\rho_l)^2/gD$
Fr_{so}	Soliman's modified Froude number	Eq. (2.31)
g	acceleration due to gravity	
G	mass flux	
G_{cond}	mass flux of condensate into the interface	
Ga	Galileo number	$\rho_l(\rho_l-\rho_v)D^3/\mu_l^2$
h	heat transfer coefficient	
h_l	height of the liquid level	
$\tilde{h}_l$	dimensionless liquid level height	h_l/D
$i_{h,i}$	enthalpy at heater inlet	
i_l	saturated liquid enthalpy	
i_{lv}	enthalpy of vaporization	
i'_{lv}	Rohsenow's [1956] modified enthalpy of vaporization	$i_{lv}+0.68\,c_{pl}(T_{sat}-T_s)$

i_{lv}^{SL}	Sadivisan and Lienhard's [1987] modified i_{lv}	$i_{lv}\left(1+\left(0.683-\frac{0.228}{Pr_l}\right)Ja_l\right)$
$i_{r,i}$	refrigerant enthalpy at test-section inlet	
$i_{r,o}$	refrigerant enthalpy at test-section outlet	
$i_{ts,i}$	enthalpy at test section inlet	
j_l	superficial liquid velocity	$G(1-x)/\rho_l$
j_l^{corr}	corrected superficial liquid velocity	$\sqrt{\rho_l/\rho_w}\,j_l$
j_v	superficial vapor velocity	Gx/ρ_v
j_v^{corr}	corrected superficial vapor velocity	$\sqrt{\rho_v/\rho_a}\,j_v$
Ja_l	liquid Jakob number	$\frac{c_{p,l}(T_{sat}-T_s)}{i_{lv}}$
Ja_v	vapor Jakob number	$\frac{c_{p,v}(T_{sat}-T_s)}{i_{lv}}$
k_l	liquid thermal conductivity	
k_v	vapor thermal conductivity	
k_t	thermal conductivity of inner tube wall	
K_{td}	stratified to wavy parameter of Taitel-Dukler	$F_{td}\sqrt{Re_l}$
L	test-section length	
L_f	length scale for filmwise condensation	$\left[\frac{\mu_l^2}{\rho_l(\rho_l-\rho_v)g}\right]^{1/3}$
$\tilde{L}$	dimensionless heat exchanger length	Eq. (7.9)
L^*	dimensionless heat exchanger length	Eq. (7.19)
m	constant	
$\dot{m}$	mass flow rate	
$\dot{m}_e$	liquid mass flow entrained in the vapor core	

$\dot{m}_l$	liquid mass flow rate	$\dot{m}(1-x)$
$\dot{m}_r$	refrigerant mass flow rate	
$\dot{m}_v$	vapor mass flow rate	$\dot{m}\,x$
$\dot{m}_w$	water mass flow rate	
$\dot{m}'$	mass flow rate/unit width	
$\dot{m}'_g$	mass flow rate/unit width due to gravity	
$\dot{m}'_s$	mass flow rate/unit width due to interfacial shear	
n	constant	
Nu	Nusselt number	hD/k_l
Nu_{bot}	Nusselt number in the bottom of the tube during filmwise condensation	
Nu_{film}	filmwise Nusselt number during wavy flow	
Nu_{forced}	forced convective Nusselt number during wavy flow	
Nu_{top}	Nusselt number in the top of the tube during filmwise condensation	
P	pressure	
P_{crit}	critical pressure	
P_{red}	reduced pressure	P/P_{crit}
Pr, Pr_l	liquid Prandtl number	$\mu_l c_{p,l}/k_l$
Pr_v	vapor Prandtl number	$\mu_v c_{p,v}/k_v$
Pr_t	turbulent Prandtl number	
$\dot{Q}$	heat transfer rate	
$\dot{Q}_{cond,i}$	axial conduction into test-section through inner tube	
$\dot{Q}_{cond,o}$	axial conduction into test-section through outer tube (annulus)	
$\dot{Q}_h$	heat input in the heater	
$\dot{Q}_{l,h}$	heat loss in the heater	

$\dot{Q}_{l,ts}$	heat loss in the test-section	
$\dot{Q}_r$	refrigerant side heat transfer rate in the test-section	
$\dot{Q}_w$	water side heat transfer rate in the test-section	
$\dot{Q}'$	heat transfer rate/unit length	
$\dot{Q}''$	heat flux	
R'_a	air-side thermal resistance per unit length	
R'_i	thermal resistance per unit length of inner fluid	
R'_{ref}	thermal resistance per unit length of refrigerant	
R'_o	thermal resistance per unit length of outer fluid	
R'_t	total thermal resistance per unit length	$R'_i + R'_o$
Re_{eq}	equivalent Reynolds number of Cavallini Zecchin	$Re_l + (Re_{lo} - Re_l)\sqrt{\rho_l/\rho_v}$
Re_f	film Reynolds number for filmwise condensation	$4\dot{m}'/\mu_l$
Re_l	superficial liquid Reynolds number	$GD(1-x)/\mu_l$
$Re_{l,act}$	liquid Reynolds number based on D_l and actual velocity	$\dfrac{Re_l}{(1-\phi_l/\pi)}$
Re_{lo}	liquid only Reynolds number	GD/μ_l
Re_m	Soliman's mixture Reynolds number	Eq. (2.98)
Re_v	superficial vapor Reynolds number	GDx/μ_v
Re_{vo}	vapor only Reynolds number	GD/μ_v
S	circumference	πD
S_i	interfacial area/unit length in stratified flow	
$\tilde{S}_i$	dimensionless interfacial area/unit length in stratified flow	S_i/D
S_l	circumference covered by liquid	

S_g	circumference covered by gas	
St_t	Stanton number based on the turbulent friction velocity	$h\big/\left(\rho_l c_{p,l}\sqrt{\tau_w/\rho_l}\right)$
Su_v	Suratman number	$\rho_v D\sigma/\mu_v^2$
t	tube thickness	
T	temperature	
T_a	air temperature	
T_{sat}	saturation temperature	
T_s	surface temperature of tube wall	
$T_{ts,i}$	refrigerant temperature at test-section inlet	
$T_{ts,o}$	refrigerant temperature at test-section outlet	
T_{td}	intermittent to dispersed bubble parameter of Taitel-Dukler	$\dfrac{\left(-dP/dz\right)_l}{(\rho_l-\rho_v)g\cos\alpha}$
$T_{w,i}$	water temperature at test-section inlet	
$T_{w,o}$	water temperature at test-section outlet	
$\tilde{T}$	dimensionless temperature drop	Eq. (7.10)
T^*	dimensionless temperature drop	Eq. (7.21)
u^+	velocity/friction velocity	$u / \sqrt{\tau_w/\rho_l}$
$\tilde{u}_l$	liquid velocity/superficial liquid velocity	
$\tilde{u}_v$	vapor velocity/superficial vapor velocity	
U_{eg}	velocity at the edge of the vapor boundary layer	
$UA_{l,ts}$	overall conductance for test-section heat loss	
V	cross-sectionally averaged velocity	
V_l	liquid cross-sectionally averaged velocity	
V_v	liquid cross-sectionally averaged velocity	
We	Weber number	$G^2D/\rho_v\sigma$

We_{so}	Soliman's modified Weber number	Eq. (2.32)
x	vapor quality	
$x_{ts,i}$	refrigerant quality at test-section inlet	
$x_{ts,o}$	refrigerant quality at test-section outlet	
X	Lockhart Martinelli parameter	$(dP/dz)_l/(dP/dz)_v$
X_{TT}	turbulent turbulent Lockhart Martinelli parameter	$\left(\frac{\rho_v}{\rho_l}\right)^{0.5}\left(\frac{\mu_l}{\mu_v}\right)^{0.1}\left(\frac{1-x}{x}\right)^{0.9}$
α	void fraction	A_v/A_c
α	angle of inclination in Taitel-Dukler criteria	
α_i	inlet void fraction	
α_o	outlet void fraction	
β	fraction of the circumference where filmwise condensation prevails	
δ	liquid film thickness, uncertainty in a component	
ΔP_{acc}	acceleration pressure drop	Eq. (2.20)
ΔP_f	frictional pressure drop	$\frac{4\tau_w}{D}$
ΔP_{rb}	return bend pressure drop	
ΔP_t	turning pressure drop	
ε	dimensionless resistance for return bend pressure drop	Eq. (7.16)
ϕ_l^2	two-phase pressure drop multiplier	$\frac{(dP/dz)}{(dP/dz)_l}$
ϕ_{lo}^2	two-phase pressure drop multiplier	$\frac{(dP/dz)}{(dP/dz)_{lo}}$
ϕ_v^2	two-phase pressure drop multiplier	$\frac{(dP/dz)}{(dP/dz)_v}$

ϕ^2_{vo}	two-phase pressure drop multiplier	$\frac{(dP/dz)}{(dP/dz)_{vo}}$
μ_l	dynamic viscosity of liquid refrigerant	
μ_v	dynamic viscosity of vapor refrigerant	
μ_w	dynamic viscosity of water	
ν	kinematic viscosity	μ/ρ
ρ_a	density of air	
ρ_l	density of liquid refrigerant	
ρ_l	density of vapor refrigerant	
ρ_w	density of water	
σ	surface tension of refrigerant	
σ_w	surface tension of water	
τ_{acc}	shear stress due to acceleration	
τ_i	shear stress at liquid vapor interface	
τ_w	shear stress at the wall	
τ_{wg}	shear stress at the wall for the portion of the tube occupied by gas	
τ_{wl}	shear stress at the wall for the portion of the tube occupied by liquid	

CHAPTER 1

INTRODUCTION

Concern over the depletion of the stratospheric ozone layer by chemical compounds began with the publication of a technical paper in 1974 by Rowland and Molina [Rowland and Molina, 1974]. In this paper, the authors described a complicated chemical reaction that could result in man-made chlorofluorocarbons (CFCs) depleting the ozone layer for decades. The concerns generated by this paper grew over a period of years, ultimately leading to the Montreal Protocol in 1987. This agreement called for a 50% reduction in CFC use by 1998 but no phase-out of hydrofluorocarbons (HCFCs). These phase-out timetables were shortened internationally by the 1990 London Convention, and domestically by the 1990 Clean Air Act. This act called for 100% elimination of CFC use by 1996 and 100% elimination of HCFC use by 2015. The impact of this decision on the refrigeration industry was profound, since CFCs or HCFCs were used as the working fluid in refrigerators, mobile and stationary air conditioners, and chillers.

At the same time that these manufacturers faced the daunting task of changing working fluids, concerns over energy efficiency were also gaining attention. The National Appliance Energy Conservation Act (NAECA) of 1987 promulgated a wide range of increases in minimum energy efficiency standards for refrigerators, freezers, air conditioners, and heat pumps. While the standards set by this act were not identical for all products, the 25% increase in energy efficiency that was mandated for domestic refrigerators was typical.

The simultaneous impact of these two regulatory decisions has had, and continues to have, a profound impact on the heating, ventilating and air conditioning (HVAC) industry. Various issues that have been addressed for years with "rules of thumb" are being examined more rigorously. As a part of this process, the Air Conditioning and Refrigeration Center (ACRC) at the University of Illinois was initiated in 1989 to help manufacturers of refrigeration equipment successfully make the transition to alternative refrigerants. The purpose of the first project initiated in the ACRC was to focus on the heat and momentum transfer characteristics of alternative refrigerants during condensation and evaporation. Two sets of experimental equipment were constructed as part of this project, one for condensation and one for evaporation. Data collected with the condensation apparatus form the experimental basis of the present study.

Studies of condensation are numerous in the technical literature. These studies include analytical efforts to model the physics of condensation processes, experimental efforts to measure the heat transfer behavior of certain fluids, and various combinations of the two. Most investigators have collected data for a limited number of fluids under a range of operating conditions that was suitable for the application that they were studying. Efforts to match their data with existing correlations or to develop correlations to fit their own data have met with some success. Many correlations that are available come with no explicit range of parameters over which they can be expected to give accurate results. The result for a design engineer who is searching the technical literature for a suitable heat transfer correlation is a series of seemingly contradictory reports about what correlation is "best". The differences between the lowest and highest predicted heat transfer coefficients, in certain cases, can be as high as a factor of two or three [Hinde et al., 1992].

Although a cohesive theory for in-tube condensation does not presently exist, there is agreement in the literature that the mechanisms of heat transfer and pressure drop are intimately linked with the prevailing two-phase flow regime. This has led to many studies aimed at predicting what dimensionless parameters govern specific flow regime transitions, and at what values of these dimensionless parameters certain transitions are expected to occur. Although debates still exist in the literature concerning differences in the flow regime predictions of various researchers, a basic understanding has been established of what the various flow regimes are and, in most cases, what parameters are suitable for determing the transition from one flow regime to the next.

The work described herein represents an extensive effort to combine the topics of heat transfer and flow regimes. In Chapter 2, the existing literature relating to condensation heat transfer, pressure drop, and two-phase flow regime prediction is reviewed. In Chapter 3, details of the experimental apparatus are explained. Chapter 4 describes the experimental methods used to collect and verify the data from this study. The observed flow regimes are reviewed and compared to various predictive techniques in Chapter 5. In Chapter 6, the experimental heat transfer data from the project are presented. The trends from the data are first discussed, particularly their relation to the flow regime. Then, physically based heat transfer correlations are developed and compared to the experimental data. Chapter 7 applies the insights developed from the heat transfer data to design issues, focusing considerable attention on optimal tube sizing. Chapter 8 summarizes the results of the study and recommends areas for future research.

CHAPTER 2

THEORY AND LITERATURE REVIEW

This chapter discusses the literature relating to the present study and establishes the theoretical aspects necessary for understanding the results. Background information for the study is presented in Section 2.1. This includes a description of the dimensionless groups that are used throughout the remainder of the manuscript, their ranges during the experiments described herein, and a condensed discussion of two-phase pressure drop models. Section 2.2 describes the flow regimes that occur during two-phase condensation, while Section 2.3 discusses several approaches for predicting the conditions under which each flow regime will occur. Section 2.4 reviews the extensive body of literature relating to condensation in the gravity-dominated flow regimes. This is followed by a discussion of condensation in the annular flow regime in Section 2.5. Section 2.6 discusses the limited range of literature describing condensation in the mist flow regime.

2.1 Background Information

Before the review of the relevant literature begins, a modest amount of background information is discussed. First, some of the dimensionless groups that are frequently used throughout the present study are reviewed. Second, the one-dimensional model of two-phase separated flow is presented. This model is used to define the frictional and acceleration components of pressure drop. It also serves as a useful way to introduce the frictional pressure drop correlation of Lockhart and Martinelli [1947], and the Lockhart-Martinelli parameter.

2.1.1 Dimensionless groups

Some of the dimensionless groups that are frequently used throughout the remainder of the study are defined in Table 2.1. Those groups that are used exclusively with properties of either the liquid or vapor phase are defined in that manner in the table. Some of the dimensionless groups are used in the present study with properties of both the liquid and vapor phases. In the definitions of these groups, the properties are left unsubscripted to indicate that they can refer to either the liquid or vapor phase. Listed along with each of the dimensionless groups is the approximate range of values that were utilized in the present study.

Table 2.1 Dimensionless groups utilized in the present study

Group	Interpretation	Definition	Range
Reynolds number, Re	Ratio of inertial to viscous forces	GD/μ	Listed Below
Superficial Reynolds number	Assumes that actual phase flow rate occupies entire tube	$Re_l = \frac{G(1-x)D}{\mu_l}$ (liquid) $Re_v = \frac{GxD}{\mu_v}$ (vapor)	50 to 26,000 600 to 351,000
Liquid or vapor only Reynolds number	Assumes all flow consists of the phase of interest and occupies the entire tube	$Re_{lo} = \frac{GD}{\mu_l}$ (liquid-only) $Re_{vo} = \frac{GD}{\mu_v}$ (vapor-only)	900 to 27,000 12,000 to 370,000
Nusselt number, Nu	Dimensionless heat transfer coefficient	$Nu = hD/k_l$	50 to 1000
Prandtl number, Pr	Ratio of momentum diffusivity to heat diffusivity	$Pr = \frac{\mu c_p}{k}$	2.1 to 3.8 liquid 0.8 to 1.5 vapor
Galileo number, Ga	A ratio of gravitational to viscous forces	$Ga = \frac{\rho_l(\rho_l - \rho_v)gD^3}{\mu_l^2}$	1.05×10^{-7} to 1.76×10^{-8}
Jakob number, Ja	Ratio of sensible to latent energy transfer	$Ja_l = \frac{c_{p,l}(T_{sat} - T_w)}{i_{lv}}$	0.01-0.06
Froude number, Fr	Ratio of inertial to gravitational forces	$Fr = \frac{V_l}{\sqrt{gD}} = \frac{G/\rho_l}{\sqrt{gD}}$ $Fr = \frac{V_l^2}{gD} = \frac{(G/\rho_l)^2}{gD}$	0.08 to 4.56 0.007 to 20.8
Weber number, We	Ratio of inertial to surface tension forces	$We = \frac{G^2 D}{\rho_v \sigma}$	6 to 10,000
Bond number, Bd	Ratio of gravitational to surface tension forces	$Bd = \frac{g(\rho_l - \rho_v)D^2}{\sigma}$	19 to 76
Boiling number, Bo	Dimensionless heat flux	$Bo = \dot{Q}''/(G i_{lv})$	4×10^{-4} to 5×10^{-3}
Lockhart-Martinelli parameter, X_{tt}	Dimensionless liquid inventory	$X_{tt} = \left(\frac{\rho_v}{\rho_l}\right)^{0.5}\left(\frac{\mu_l}{\mu_v}\right)^{0.1}\left(\frac{1-x}{x}\right)^{0.9}$	0.018 to 6.0

Several items from Table 2.1 warrant brief discussion. The wide range of mass fluxes used in the study resulted in significant variations in both superficial and single-phase Reynolds numbers. Data were obtained in both laminar and highly turbulent flows. The liquid Froude numbers ranged from much less than unity, reflecting strong gravity dominance, to higher values indicative of strong inertial dominance. The Jakob numbers were much less than unity and the liquid Prandtl numbers were greater than unity, which will later be shown to indicate the validity of Nusselt's assumptions in the wavy flow regime. The fact that the Bond number, an indicator of the relative magnitude of gravity to surface tension forces, was always above 19 for the present study was initially surprising since tubes as small as .123" in diameter were used. These values of Bond number are indicative of gravity dominance over surface tension, primarily because of low surface tension values for refrigerants.

2.1.2 Two-phase pressure drop

While the fluid dynamics of two-phase flow is a very complicated subject, useful results for two-phase pressure drop can be obtained from a one-dimensional treatment using the separated flow model. This model assumes that there are two distinct phases flowing in the tube, and utilizes cross-sectionally averaged values of velocity for each phase. The pressure and all thermophysical properties are assumed to be constant at a given cross-section. A schematic of the separated flow that is analyzed is presented in Fig. 2.1.

Applying the continuity equation across a differential element results in:

$$\dot{m}_l\big|_z - \dot{m}_l\big|_{z+dz} + \dot{m}_v\big|_z - \dot{m}_v\big|_{z+dz} = 0 \tag{2.1}$$

Expressing the phase mass flow rates as a Taylor series truncated at the first term gives:

$$d\dot{m}_l = -d\dot{m}_v \tag{2.2}$$

For the horizontal flow case, there are no body forces in the z-direction. The z-momentum equation then reflects a balance between the net momentum flux entering the element and the surface forces acting on it. If this equation is written for the entire element, it gives:

$$\left(P\big|_z - P\big|_{z+dz}\right)A_c - \tau_w S\Delta z = \left(\dot{m}_l V_l\big|_{z+dz} - \dot{m}_l V_l\big|_z\right) + \left(\dot{m}_v V_v\big|_{z+dz} - \dot{m}_v V_v\big|_z\right) \tag{2.3}$$

Expressing these terms in a Taylor Series and rearranging gives:

$$\frac{-dP}{dz} = \underbrace{\frac{4\tau_w}{D}}_{(-dP/dz)_f} + \underbrace{\frac{1}{A_c}\frac{d}{dz}\left[\dot{m}_l V_l + \dot{m}_v V_v\right]}_{(-dP/dz)_{acc}} \tag{2.4}$$

Equation (2.4) divides the pressure gradient into components due to friction and change of phase. The term due to phase-change is often called acceleration pressure drop because it produces this effect in evaporation. In condensation, however, the phase-change process decelerates the flow and results in a pressure increase.

Lockhart and Martinelli [1947] proposed a method which has formed the basis for many later attempts at correlating the two-phase frictional pressure drop. They began by defining two-phase multipliers that related the actual two-phase frictional pressure gradient to single-phase pressure gradients. The two-phase multipliers can take on several forms:

$$\phi_l^2 \equiv \frac{(dP/dz)}{(dP/dz)_l} \tag{2.5}$$

$$\phi_{lo}^2 \equiv \frac{(dP/dz)}{(dP/dz)_{lo}} \tag{2.6}$$

$$\phi_v^2 \equiv \frac{(dP/dz)}{(dP/dz)_v} \tag{2.7}$$

$$\phi_{vo}^2 \equiv \frac{(dP/dz)}{(dP/dz)_{vo}} \tag{2.8}$$

The numerator of each of the two-phase multipliers is the actual two-phase frictional pressure gradient, with the various forms differing only based on the denominator. The subscript l refers to the two-phase pressure gradient calculated based on the liquid mass flow, while the lo subscript refers to the two-phase pressure gradient calculated assuming that the entire mass flows in liquid form. The subscripts v and vo refer to the vapor phase in an analogous manner.

Once the definitions given by Eq. (2.5) to Eq. (2.8) were made, the work of predicting the two-phase multipliers still remained. Lockhart and Martinelli accomplished this by again referring to the behavior of the pressure drop in single-phase flows. For a single-phase pipe flow, the pressure drop is given by:

$$\frac{-dP}{dz} = \frac{2\,f\,G^2}{\rho D} \tag{2.9}$$

For either laminar or turbulent flow, the friction factor for a smooth tube can be predicted based on the Reynolds number, Re. The following form arises analytically for laminar flow and is frequently used as a correlating form for turbulent flow:

$$f = \frac{a}{\mathrm{Re}^n} \tag{2.10}$$

Appropriate values of a and n for laminar and turbulent flow are given in Table 2.2. Turbulent flow is typically assumed for Re>2300.

Table 2.2 Pressure drop parameters for laminar and turbulent pipe flow

Flow Regime	a	n
Laminar	16	1
Turbulent	0.046	0.2

Lockhart and Martinelli [1947] proposed that the two-phase multipliers should depend on the ratio of the pressure gradients of the liquid and vapor phases. The resulting quantity, now known as the Lockhart-Martinelli parameter, is given by:

$$X^2 = \frac{\left(dP/dz\right)_l}{\left(dP/dz\right)_v} = \frac{\dfrac{2a_l}{\mathrm{Re}_l^{n,l}} \dfrac{G^2(1-x)^2}{\rho_l D}}{\dfrac{2a_v}{\mathrm{Re}_v^{n,v}} \dfrac{G^2 x^2}{\rho_v D}} = \frac{a_l}{a_v} \frac{\mu_l^{n,l}}{\mu_v^{n,v}} \frac{\rho_v}{\rho_l} \frac{(1-x)^{2-n,l}}{x^{2-n,v}} \tag{2.11}$$

The definition of X differs depending on whether the flow in each of the phases is laminar or turbulent. The most frequently used form arises when both phases are flowing turbulently, resulting in the turbulent-turbulent Lockhart-Martinelli parameter, X_{tt}:

$$X_{tt} = \left(\frac{\rho_v}{\rho_l}\right)^{0.5} \left(\frac{\mu_l}{\mu_v}\right)^{0.1} \left(\frac{1-x}{x}\right)^{0.9} \tag{2.12}$$

For the sake of completeness, the less frequently encountered cases of laminar liquid and turbulent vapor (lt), turbulent liquid and laminar vapor (tl), and laminar liquid and vapor (ll), are also defined below:

$$X_{lt} = 18.65 \left(\frac{\rho_v}{\rho_l}\right)^{0.5} \left(\frac{1-x}{x}\right) \frac{\mathrm{Re}_v^{0.1}}{\mathrm{Re}_l^{0.5}} \tag{2.13}$$

$$X_{tl} = \frac{1}{18.65}\left(\frac{\rho_v}{\rho_l}\right)^{0.5}\left(\frac{1-x}{x}\right)\frac{Re_v^{0.5}}{Re_l^{0.1}} \tag{2.14}$$

$$X_{ll} = \left(\frac{\rho_v}{\rho_l}\right)^{0.5}\left(\frac{\mu_l}{\mu_v}\right)^{0.5}\left(\frac{1-x}{x}\right)^{0.5} \tag{2.15}$$

Lockhart and Martinelli were indeed able to correlate their adiabatic pressure drop data for air-water and oil-water mixtures based on X. The results that they presented in graphical form were later curve fitted by Chisholm [1968]:

$$\phi_l^2 = 1 + \frac{C}{X} + \frac{1}{X^2} \tag{2.16}$$

$$\phi_v^2 = 1 + CX + X^2 \tag{2.17}$$

The values of C for the turbulent turbulent, laminar turbulent, turbulent laminar, and laminar laminar cases are given in Table 2.3.

Table 2.3 Values of the constant C in Eq. (2.16) and Eq. (2.17) given by Chisholm [1968]

Liquid Phase	Vapor Phase	C
turbulent	turbulent	20
laminar	turbulent	12
turbulent	laminar	10
laminar	laminar	5

Lockhart and Martinelli also used the parameter X to correlate their void fraction data. Their results were later curve fitted by Butterworth [1975] as:

$$\alpha = \frac{1}{1 + 0.28X^{0.71}} \tag{2.18}$$

While later investigators have noted that the two-phase multiplier also varies systematically with mass flux, the basic approach of Lockhart and Martinelli remains widely used. The number of times that their parameter appears in various contexts in the study of two-phase flow is a strong testament to its worth.

The Lockhart-Martinelli data were obtained for adiabatic conditions where no acceleration pressure drop existed. Martinelli and Nelson [1948] studied diabatic pressure drop during flow boiling of water. Their most fundamental assumption was that the frictional component of pressure drop remained identical to the adiabatic case. Thus, the only complicating factor was calculating the acceleration pressure drop. For a phase-change process with inlet conditions subscripted by i and outlet conditions subscripted by o, the acceleration pressure drop can be evaluated from Eq. (2.4):

$$-\Delta P_{acc} = \int_{z_i}^{z_o} \frac{1}{A_c} \frac{d}{dz}\left[\dot{m}_l V_l + \dot{m}_v V_v\right] dz \qquad (2.19)$$

Writing the result in terms of mass flux, quality, and void fraction gives:

$$-\Delta P_{acc} = G^2 \left\{ \left[\frac{x_o^2}{\rho_v \alpha_o} + \frac{(1-x_o)^2}{\rho_l (1-\alpha_o)} \right] - \left[\frac{x_i^2}{\rho_v \alpha_i} + \frac{(1-x_i)^2}{\rho_l (1-\alpha_i)} \right] \right\} \qquad (2.20)$$

Once a void fraction model is assumed, calculation of the acceleration pressure drop from Eq. (2.20) is straightforward.

2.2 Flow Regimes in Horizontal Two-Phase Flow

One of the most important characteristics of a two-phase flow is the way in which the liquid and vapor phases orient themselves. This is referred to as the flow regime or the flow pattern. A variety of flow patterns can occur, depending primarily on the flow rates and physical properties of the two phases, and the geometry of the tube.

Figure 2.2 is a compilation of some of the most typical two-phase flow regimes that are observed in condensation processes. These differ slightly from observations during adiabatic or evaporating conditions because the condensation process tends to wet the top of the tube wall in all flow regimes. The flow regimes in Fig. 2.2 are divided into two groups: (1) those that occur at high void fractions ($\alpha>0.5$), and (2) those that occur only at low void fractions ($\alpha<0.5$).

The first category includes five flow regimes: stratified flow, wavy flow, wavy-annular flow, annular flow, and annular-mist flow. The second category includes slug, plug, and bubbly flow. The five flow regimes in the first category are arranged such that each successive flow regime corresponds to an increase in the vapor velocity. The three flow regimes in the second category are arranged such that the transition from one flow regime to the next corresponds to an increase in the liquid inventory (or a decrease in α).

At very low vapor velocities, the stratified flow regime is observed. During stratified flow, condensate forms in the upper portion of the tube and is driven downward by gravity. The condensate collects in a liquid pool at the bottom of the tube, where it is driven out of the tube either by the vapor flow passing over it or by a gravitational head. The velocity in the top of the tube is primarily downward, while the velocity in the pool at the bottom of the tube is primarily in the mean flow direction. Because the vapor velocity is low, the liquid vapor interface remains smooth.

As the vapor velocity is increased, the liquid vapor interface becomes Helmholtz unstable giving rise to surface waves [Carey, 1992]. This is referred to as wavy flow. The condensation process in the top of the tube is similar to that in stratified flow, with a gradually thickening liquid layer forming and feeding into the pool of liquid at the bottom of the tube. The condensation process on the portion of the tube wall near the interface between the liquid pool and the vapor is affected by the waves, though, since it is alternately exposed to a thin condensate film flowing downward and the crest of a wave moving in the mean flow direction.

As the vapor velocity is increased further, the wavy flow becomes unstable and can result in two different transitions. At high liquid fractions, the slug flow case that is described subsequently occurs. At lower liquid fractions, the waves begin to wash up and around the tube wall leading to an annular flow. Before the annular flow pattern is reached, however, a transitional flow pattern called wavy-annular flow is observed. In the wavy-annular flow regime, some liquid from the waves begins to wash up and around the circumference of the tube, but not enough to create a symmetric annular film. This liquid moves primarily in the mean flow direction rather than downward, pointing out the primary difference from the wavy flow regime.

With still further increases in the vapor velocity, the liquid migration from the pool at the bottom of the tube to the top of the tube continues until the film thickness becomes nearly uniform. The visual appearance of this type of flow is one of an annular film of liquid on the wall and a high-speed vapor core in the center, hence the name annular flow. The liquid vapor interface in annular flow is nearly always characterized by surface waves due to the high speed vapor flowing over it.

At yet higher vapor velocities, the crests of the waves on the liquid film are sheared off by the vapor flow and entrained in the core in the form of liquid droplets. This is referred to as the annular-mist flow regime because of the appearance of an annular film with a mixture of vapor and mist in the core flow. In an equilibrium situation, the liquid which is removed from the liquid film by the shearing of the waves is replenished by liquid droplets from the core flow which collide with and are redeposited into the liquid film.

The second category of flow regimes shown in Fig. 2.2 includes the slug, plug, and bubbly flow regimes. Slug flow is formed when interfacial waves grow sufficiently in amplitude to block the entire cross-section at some axial locations, leading to the visual appearance of slugs of liquid flowing down the tube. These slugs have been shown by Hubbard and Dukler [1966] and Lin and Hanratty [1989] to create large pressure spikes due to rapid deceleration of the vapor flow. In other cases, a flow that would visually be identified as slug flow does not create these large pressure spikes. This regime has been designated by Lin and Hanratty [1989] as pseudo-slug flow. They proposed that, unlike true slugs, pseudo-slugs either did not entirely block the tube or did so only momentarily. A regime with a similar qualitative description to pseudo-slug flow was designated as proto-slug flow by Nicholson, Aziz, and Gregory [1978], and wavy-annular flow by Barnea et al. [1980]. This illustrates the considerable subjectivity in certain flow regime classifications.

As condensation continues, the slugs coalesce into bubbles within a predominantly liquid flow. This is referred to as the plug flow regime. Turbulent fluctuations within the liquid eventually break these plugs into smaller vapor bubbles that become dispersed throughout the liquid. This is called the bubbly flow regime. The slug, plug, and bubbly flow regimes occur at the end of the condensation process when the liquid inventory is large (or α is small). In combination, they occupy only 10% to 20% of the total quality range. The plug and bubbly flow regimes are confined to the bottom 1% to 2% of the quality range, and will not be discussed in detail during the remainder of this report.

2.3 Flow Regime Mapping Efforts

Since the flow patterns strongly influence the heat and momentum transfer processes, it is important for designers to predict what flow pattern is expected based on the flow rate, quality, fluid properties, and tube diameter. In recognition of this fact, many flow regime maps or flow regime prediction techniques have evolved over the years. Several of the more widely known flow regime maps are discussed below. Following the discussion of the flow regime maps, relevant experimental and analytical results from some more recent flow regime studies are reviewed.

2.3.1 Baker map

One of the earliest attempts at a flow regime map was by Baker [1954]. The Baker map was based on observations of adiabatic, gas-liquid flows in tubes ranging from 1.0 to 4.0" in diameter. The data used to develop the Baker map included both air-water and oil-water flows, providing a fairly wide range of fluid properties. The horizontal and vertical coordinates on the Baker map are the superficial liquid and vapor mass fluxes times scaling factors that account for fluid property variations. These two coordinates are given by:

$$G(1-x)\left(\frac{\sigma_w}{\sigma}\right)\left(\frac{\mu_l}{\mu_w}\right)^{1/3}\left(\frac{\rho_w}{\rho_l}\right)^{2/3} \tag{2.21}$$

$$G\,x\left[\left(\frac{\rho_v}{\rho_a}\right)\left(\frac{\rho_l}{\rho_w}\right)\right]^{1/2} \qquad (2.22)$$

The subscripts w and a in Eq. (2.21) and (2.22) refer to properties for air and water at room temperature and atmospheric pressure, respectively. Although subsequent flow regime maps have achieved improved accuracy, Baker's work retains historical significance as the first widely recognized flow regime map.

2.3.2 Mandhane map

Mandhane et al. [1974] developed a flow regime map similar to Baker's [1954] using a larger database of 5935 observations. The abscissa and ordinate of the Mandhane map are the superficial gas velocity and superficial liquid velocity, which makes it rather simple to use. The Mandhane map correctly predicted the flow regime for 68 percent of the observations in their database, as opposed to 42 percent for the original Baker map. The boundaries of the Mandhane map were constructed primarily for air-water data in tubes larger than those used in the present study. Comparisons with recent data for refrigerants revealed systematic problems with the Mandhane map [Wattelet, 1994]. These problems were likely because the vapor density of the refrigerants in Wattelet's study were much higher than the air density from the Mandhane data. This problem would be worse for the data from the present study, since the vapor density is considerably higher at condensation temperatures than evaporation temperatures. The Mandhane map is shown in Fig. 2.3.

2.3.3 Taitel-Dukler map

Perhaps the most theoretically-based flow regime map is that of Taitel and Dukler [1976]. They reasoned that each flow regime transition was based on a different set of competing forces, and that a single parameter or set of coordinates should not be expected to predict all flow regime transitions. The Taitel-Dukler map includes five flow regimes: stratified smooth, stratified-wavy, annular, intermittent (plug and slug), and dispersed bubble. The map was developed for adiabatic flows, but has been used with success by other investigators for diabatic flows [Barnhart, 1992; Wattelet, 1994].

Taitel and Dukler developed a mechanistic approach for predicting when a smooth, stratified flow would undergo a transition to another flow regime based on the appropriate physical mechanisms. Their method relied first on a description of the forces in a smooth-stratified flow. A schematic of such a horizontal, stratified flow is shown in Fig. 2.4 with the appropriate forces. The momentum equations for the liquid phase and vapor phases are, respectively:

$$-A_l\left(\frac{dP}{dz}\right)-\tau_{wl}S_l+\tau_i S_i=0 \qquad (2.23)$$

$$-A_g\left(\frac{dP}{dz}\right)-\tau_{wg}S_g-\tau_i S_i=0 \qquad (2.24)$$

Setting Eq. (2.23) equal to Eq. (2.24), assuming uniform pressure at each z location, and assuming that the three shear stresses could be evaluated with the typically used friction factors, Taitel and Dukler showed that a dimensionless equation arose which predicted the Lockhart-Martinelli parameter, X, as a function of several dimensionless variables that were all exclusively a function of the dimensionless liquid level, $\tilde{h}_l$[1]. The dimensionless liquid level is defined as:

$$\tilde{h}_l=\frac{h_l}{D} \qquad (2.25)$$

The Lockhart-Martinelli parameter is always given by the flow rate, quality, and fluid properties, and the relationship between $\tilde{h}_l$ and X is monotonic. Thus, $\tilde{h}_l$ can be determined for any value of X by inverting the function or looking it up on a graph. This step is important since knowledge of $\tilde{h}_l$ is necessary for predicting some of the flow regime transitions. The flow regime transitions that are described by Taitel and Dukler are discussed briefly below.

For the stratified to wavy flow transition, Taitel and Dukler hypothesized that waves would be formed when the pressure and shear forces acting on a wave were sufficient to overcome viscous dissipation in the wave. Their ideas were based on the work of Jeffreys [1925, 1926], and in dimensional form they deduced that waves would be expected to form when a critical vapor velocity was exceeded. In dimensionless form, the inequality can be expressed as:

$$K_{td}=F_{td}\sqrt{Re_l}\geq\frac{20}{\tilde{u}_g\sqrt{\tilde{u}_l}} \qquad (2.26)$$

The right hand side of Eq. (2.26) follows the nomenclature set forth by Taitel and Dukler, where all quantities with tildes are dimensionless variables. In this scheme, actual phase velocities are scaled by superficial phase velocities and lengths are scaled by the tube diameter.

The first term in K_{td} was referred to by Taitel and Dukler as a modified Froude number. The term is defined as follows:

---

[1] Actually, a third parameter Y arises for non-zero angles of inclination.

$$F_{td} = \sqrt{\frac{\rho_g}{\rho_l - \rho_g}} \frac{Gx/\rho_g}{\sqrt{Dg\cos\alpha}} \tag{2.27}$$

The second term in Eq. (2.27) is a superficial vapor Froude number (ratio of inertial to gravity forces in the vapor), while the first is a modifier which is dependent on the density ratio.

The transition from a stratified-wavy flow to an intermittent or annular flow was observed experimentally by several investigators [Butterworth, 1972; Dukler and Hubbard, 1975]. They described wave growth on a stratified-wavy flow which led to one of two effects. At low liquid fractions, the wave washed liquid around the circumference of the tube leading to an annular flow. At high liquid fractions, the wave bridged the tube cross-section and led to an intermittent (slug or plug) flow.

Taitel and Dukler predicted this transition based on a modification of the Kelvin-Helmholtz stability analysis [Milne-Thompson, 1960]. The Kelvin-Helmholtz theory is for an infinitesimal wave between two horizontal plates. Taitel and Dukler extended this theory to predict the stability of finite waves inside a tube. In dimensionless form, their result can be expressed as follows:

$$F_{td}^2\left[\frac{1}{\left(1-\tilde{h}_l\right)^2}\frac{\tilde{u}_g^2\sqrt{1-\left(2\tilde{h}_l-1\right)^2}}{\tilde{A}_g}\right] \geq 1 \tag{2.28}$$

All terms in the bracketed portion of Eq. (2.28) are exclusively functions of the Martinelli parameter, so the boundary is a function of only F_{td} and X.

Whether a growing wave leads to intermittent or annular flow is based on the liquid level, as discussed previously. At low liquid levels, there is insufficient liquid to completely block the tube. Thus, a stable slug flow can not be formed. This implies that the liquid fraction, or alternately $\tilde{h}_l$, solely determines whether intermittent or annular flow will result after the transition from a stratified-wavy flow occurs. Since the crest of the wave must be supplied with liquid from an adjacent trough, Taitel and Dukler [1976] argued that if the tube was less than half full, the trough would reach the bottom of the tube before the crest reached the top of the tube. Thus, annular flow should be expected for $\tilde{h}_l<0.5$ and intermittent flow should be expected for $\tilde{h}_l>0.5$. Since $\tilde{h}_l$ is a function of X, this transition criterion can also be posed in terms of X. This results in a prediction of intermittent flow for X>1.6, and annular flow for X<1.6.

The intermittent flow regime discussed by Taitel and Dukler [1976] includes slug and plug flows, while the dispersed bubble flow regime is the same as the bubbly flow regime discussed previously. The transition from intermittent to bubble flow occurs when the large coalesced vapor bubbles which are characteristic of slug and plug flows are broken up into smaller bubbles that are dispersed throughout the liquid. They proposed that the transition was governed by a balance between buoyancy forces which would tend to keep the vapor bubble together and near the top of the pipe, and turbulent fluctuations which would tend to mix the vapor and liquid. In dimensionless form, the transition criterion is:

$$T_{td}^2 \geq \left[\frac{8\tilde{A}_g\left(\tilde{u}_l\tilde{D}_l\right)^n}{\tilde{S}_i\tilde{u}_l^2}\right] \tag{2.29a}$$

where:

$$T_{td} = \left[\frac{-(dP/dz)_l}{(\rho_l - \rho_v)g\cos\alpha}\right] = \left[\frac{2a}{Re_l^n}\frac{j_l^2}{gD\cos\alpha}\frac{1}{(1-\rho_v/\rho_l)}\right] \tag{2.29b}$$

All terms in the bracket of Eq. (2.29a) can be determined solely based on X, so the transition can be expressed on a two-dimensional plot of T_{td} versus X. The parameter T_{td}, as written in Eq. (2.29b), is the product of the superficial liquid friction factor, the superficial liquid Froude number, and a function of the density ratio that will typically be near unity. It should be noted that this transition can only occur at $X_{tt}>1.6$, since the liquid inventory must be sufficient for intermittent flow for either of these flow regimes to exist.

Since each of the transitions described by Taitel and Dukler [1976] can be expressed in terms of a single dimensionless parameter and X, the transition criteria can be shown on a two-dimensional flow pattern map with X on the abscissa and a different coordinate for each transition on the ordinate. A flow pattern map of this type is depicted in Figure 2.5 for the case of horizontal flow.

2.3.4 Soliman's flow regime transitions

Another approach to predicting flow regime transitions, this one specifically for condensation, has been developed by Soliman [1982, 1983]. Soliman distinguished between three flow regimes that he deemed to be important for condensing flows: wavy flow, annular flow, and mist flow. He developed two flow regime transition criteria, one for the wavy to annular transition and one for the annular to mist transition. It is important to note that the wavy flow regime of Soliman includes the regimes commonly called stratified, slug, and wavy flow. While these regimes have important differences from the standpoint of flow regime classification, particularly concerning the stability of the wavy interface, Soliman apparently concluded that these differences were less important than the significant stratification that they all had in common.

Soliman [1982] postulated that the wavy to annular transition was based on a balance between inertial and gravitational forces on the liquid film. The Froude number represents a balance between these forces:

$$Fr = \frac{V^2}{gL} \tag{2.30}$$

Soliman proposed that the appropriate velocity in Eq. (2.30) was the actual liquid velocity, and the appropriate length scale was the film thickness, δ. These parameters were not known based solely on G, x, and the fluid properties. Soliman obtained expressions for them based on relations for two-phase pressure drop in annular flow. Thus, his transition criteria is opposite to that of Taitel and Dukler in that it assumes that an annular flow exists and seeks to determine when gravitational forces will cause a transition to wavy flow. The resulting expression for the Froude number is given by:

$$Fr_{so} = 0.025 Re_l^{1.59} \left(\frac{1 + 1.09 X_{tt}^{0.039}}{X_{tt}} \right)^{1.5} \frac{1}{Ga^{0.5}} \text{ for } Re_l \leq 1250 \tag{2.31a}$$

$$Fr_{so} = 1.26 Re_l^{1.04} \left(\frac{1 + 1.09 X_{tt}^{0.039}}{X_{tt}} \right)^{1.5} \frac{1}{Ga^{0.5}} \text{ for } Re_l > 1250 \tag{2.31b}$$

Based on comparisons with data in tubes of 4.8 mm to 25 mm in diameter, and with fluids including water, refrigerants, and acetone, Soliman [1982] concluded that wavy flow was observed for $Fr_{so}<7$, and annular flow was observed for $Fr_{so}>7$. Dobson et al. [1994] reported that $Fr_{so}=7$ served as a good indicator of the transition from wavy to wavy-annular flow, although a symmetric annular flow was not observed until around $Fr_{so}=18$.

Soliman [1983, 1986] also developed a parameter for predicting the transition from annular to mist flow. He postulated that the primary forces tending to prevent entrainment were liquid viscous forces and surface tension forces, and that the primary force which promoted mist formation was vapor inertia. He formulated a modified Weber number that represented a balance between these forces:

$$We_{so} = 2.45 \frac{Re_v^{0.64}}{Su_v^{0.3} (1 + 1.09 X_{tt}^{0.039})^{0.4}} \text{ for } Re_l \leq 1250 \tag{2.32a}$$

$$\mathrm{We}_{so} = 0.85\left[\left(\frac{\mu_v}{\mu_l}\right)^2\left(\frac{\rho_l}{\rho_v}\right)\right]^{0.084} \frac{\mathrm{Re}_v^{0.79} X_{tt}^{0.157}}{\mathrm{Su}_v^{0.3}(1+1.09X_{tt}^{0.039})^{0.4}} \text{ for } \mathrm{Re}_l > 1250 \quad (2.32b)$$

Based on visual observations from various studies, Soliman [1986] concluded that annular flow was always observed for $\mathrm{We}_{so}<20$, and pure mist flow with no stable liquid film on the wall was always observed for $\mathrm{We}_{so}>30$. The region of We_{so} between 20 and 30 was reported to be a mix of annular and mist flow, called annular-mist flow.

2.3.5 Evaluation and improvement of flow regime maps

Since the flow regime maps were developed, many experimental and analytical studies have attempted to verify their findings or to include additional effects. A few of these studies that relate to the research conducted herein are described below.

Barnea et al. [1980] experimentally studied the effect of pipe inclination on flow regimes to validate the predictions of the Taitel-Dukler map. They studied upward and downward inclinations from 0 to 10°, with very interesting findings. They found that upward inclinations of as little as 0.25° significantly increased the region occupied by slug flow at the expense of stratified flow, while downward inclinations had the opposite effect. These effects were adequately predicted by the Taitel-Dukler criteria. The reason for this phenomena is that upward inclination thickens the liquid layer, supplying the liquid necessary to bridge the tube cross-section and initiate slug flow earlier than for a horizontal flow. This suggests that the effect of the increasing liquid layer depth due to condensation might also result in more slug flow and less wavy flow than predicted by the Taitel-Dukler maps. This was in fact substantiated by Rahman et al. [1985], who found that slug flow was initiated in their condensing steam experiments earlier than predicted by the maps of either Mandhane [1974] or Taitel and Dukler [1976]. The transition from wavy to annular flow, which will be shown to be the most important transition in this study, was not significantly altered by either the upward inclination experiments of Barnea or the condensing experiments of Rahman.

In a later study, Barnea et al. [1983] compared the predictions of the Taitel-Dukler [1976] map with flow regime data gathered in "small" tubes ranging from .157" to .472" in diameter. The agreement between their experimental observations and the predictions of the wavy to annular and annular to intermittent transitions was good. Surface tension forces were found to promote more elongated bubble flow and less stratified flow as the tube diameter was reduced. A model was included to account for this effect, but this transition occurs at such low qualities that it is of little interest in the present study.

Damianides and Westwater [1988] extended the range of diameters of Barnea et al., studying air-water flow in round tubes from .039" to .197" Experimentally determined flow regime maps were drawn on superficial velocity coordinates for each of the tubes, and comparisons were made with the Taitel-Dukler [1976] predictions for the .039" and .197" tubes. The predictions matched the observations very poorly for the .039" tube, where the authors observed completely different transition mechanisms than those described for large tubes. In the .197" tube, the Taitel-Dukler predictions agreed reasonably well in trend with the experimentally observed flow regimes. For the range of superficial velocities used in the present study, Damianides and Westwater found that the intermittent to annular transition occurred at higher vapor velocities than predicted by the Taitel-Dukler theory. They also found that the wavy flow regime persisted to superficial liquid velocities twice those predicted by the Taitel-Dukler theory. Although the range of diameters used by Damianides matched those used in the present study, comparing the Bond numbers is more appropriate for assessing the significance of surface tension effects. The highest Bond number from the Damianides study was over 4 times greater than the lowest Bond number from the present study, indicating significantly more surface tension effects in their data. This was primarily because the surface tension of their air-water system was around 10 times higher than the values for the refrigerants in this study.

Galbiatti and Andreini [1992] pointed out that in the air-water data of Barnea et al. [1983], the transition from wavy to annular flow was delayed to higher gas velocities as the tube diameter was reduced. They proposed that this discrepancy was due to a stabilizing effect of surface tension that became increasingly important in small diameter tubes. They added the effect of surface tension to the analysis of Taitel and Dukler, giving a new transition criteria. In dimensionless form, their correction can be made by replacing F_{td} on the Taitel-Dukler map with the following quantity:

$$\frac{F_{td}}{\sqrt{1+\frac{1.306\sigma}{g(\rho_l-\rho_v)D^2}}}=\frac{F_{td}}{\sqrt{1+\frac{1.306}{Bd}}} \qquad (2.33)$$

If surface tension forces are large compared to gravity forces (low Bd), this quantity is decreased and the wavy flow remains stable for larger gas velocities. For large Bond numbers, the surface tension effects are irrelevant. Galbiatti and Andreinni compared the resulting predictions to the .157" data of Barnea et al. [1983], and the agreement was much better than for the unmodified case. An important assumption in their analysis was that the most unstable wave had a wavelength of 5.5D, a value they obtained from potential flow theory. The calculated effect of surface tension is very sensitive to this value, increasing substantially as the most unstable wavelength is decreased. If the most unstable wave was assumed to have a wavelength of D, for example, the 1.306 in Eq. (2.33) would be replaced by 39.5. Such a change would result in important surface tension effects persisting to higher values of the Bond number.

2.4 Gravity-Driven Condensation

The gravity-driven flow regimes as discussed in this report include the stratified, wavy, and slug flow regions. These regimes are lumped together primarily because the dominant heat transfer mechanism in each regime is conduction across the film at the top of the tube. This type of condensation is commonly referred to as film condensation, and was the first mode of condensation to be modeled and studied [Nusselt, 1916]. The original analysis of film condensation on a flat plate by Nusselt will be discussed first, and its evolution into the realm of internal condensation will be traced. The more complex subject of slug flow condensation will be addressed at the end of the section.

2.4.1 External condensation

Analytical studies of condensation began with Nusselt's pioneering analysis [1916] of gravity-driven condensation of a pure component on a vertical plate. He simultaneously solved the continuity, momentum, and energy equations under the following set of simplifying assumptions:

1. Laminar flow of the liquid with constant properties.
2. Negligible inertial forces in the momentum equation.
3. Negligible subcooling of the liquid in the energy equation.
4. Stationary vapor which imposes negligible drag on the liquid.
5. Constant wall temperature.
6. No interfacial waves.

A schematic of the physical situation modeled by Nusselt is shown in Figure 2.6. Subject to the assumptions above, the x-momentum equation reduces to:

$$0 = -\frac{\partial P}{\partial x} + \rho_l g + \mu_l \frac{\partial^2 u}{\partial y^2} \tag{2.34a}$$

$$\text{with: } u(y=0) = 0 \tag{2.34b}$$

$$\frac{\partial u}{\partial y}(y = \delta) = 0 \tag{2.34c}$$

Subject to the boundary-layer assumptions, the y-momentum equation reduces to $\partial P/\partial y=0$ which implies that the pressure field is imposed from the stagnant vapor. With this realization, integration of Eq. (2.34a) twice yields the following:

$$u=\frac{g(\rho_l-\rho_v)\delta^2}{\mu_l}\left[\frac{y}{\delta}-\frac{1}{2}\left(\frac{y}{\delta}\right)^2\right] \tag{2.35}$$

Eq. (2.35) can be integrated across the film to give the mass flow rate in the x-direction per unit width in the z-direction, $\dot{m}'$. The result is:

$$\dot{m}'=\rho_l\int_0^\delta u\,dy=\frac{g(\rho_l-\rho_v)\delta^3}{3\nu_l} \tag{2.36}$$

With the convective terms neglected, the assumption of constant thermophysical properties, and steady state assumed, the energy equation reduces to the one-dimensional heat conduction equation:

$$\frac{d^2T}{dy^2}=0 \tag{2.37a}$$

$$\text{with: } T(y=0)=T_s \tag{2.37b}$$

$$T(y=\delta)=T_{sat} \tag{2.37c}$$

The solution to Eq. (2.37) is given by:

$$T=T_s+\left(T_{sat}-T_s\right)\left(\frac{y}{\delta}\right) \tag{2.38}$$

With the temperature field known, the heat transfer coefficient is given by:

$$h=\frac{k_l}{\delta} \tag{2.39}$$

The heat transfer rate per unit width in the z-direction can be expressed in terms of the heat transfer coefficient as:

$$\dot{Q}'=\int_{x_1}^{x_2}h(x)(T_{sat}-T_s)dx \tag{2.40}$$

Conservation of mass and energy on the differential element shown in Fig. 2.6 results in the following two equations:

$$\dot{m}'_{cond}=\dot{m}'(x_2)-\dot{m}'(x_1) \tag{2.41}$$

$$\dot{Q}' = \dot{m}'_{cond} i_{lv} \tag{2.42}$$

Equating Eq. (2.40) and Eq. (2.42) and substituting Eq. (2.41) results in:

$$\int_{x_1}^{x_2} \frac{k_l}{\delta(x)}(T_{sat} - T_s)dx = \left(\dot{m}'(x_2) - \dot{m}'(x_1)\right)i_{lv} \tag{2.43}$$

Provided that $d\dot{m}'/d\delta$ is continuous from x_1 to x_2, the term in parentheses in Eq. (2.43) can be expressed in integral form using the fundamental theorem of calculus. Since the area of integration is arbitrary, the integrands must be equal. This leads to the following equation:

$$\frac{d\delta}{dx} = \frac{k_l(T_{sat} - T_s)}{\delta(x) i_{lv} \frac{d\dot{m}'}{d\delta}} = \frac{k_l \nu_l (T_{sat} - T_s)}{g(\rho_l - \rho_v) i_{lv} \delta^3(x)} \tag{2.44a}$$

$$\text{with: } \delta(x=0)=0 \tag{2.44b}$$

The solution to Eq. (2.44) is given by:

$$\delta = \left[\frac{4 k_l \nu_l \Delta T x}{g(\rho_l - \rho_v) i_{lv}}\right]^{1/4} \tag{2.45}$$

Once $\delta(x)$ is known, the heat transfer coefficient at any location can be computed by Eq. (2.39). The heat transfer coefficient decreases as x increases since h is inversely proportional to the film thickness. The local Nusselt number is given by:

$$Nu_x = \frac{hx}{k_l} = \left[\frac{g(\rho_l - \rho_v) i_{lv} x^3}{4 k_l \nu_l (T_{sat} - T_s)}\right]^{1/4} \tag{2.46}$$

The mean Nusselt number at x=L is then given by:

$$\overline{Nu_l} = \frac{\bar{h} L}{k_l} = \left[\frac{1}{L}\int_0^L h(x)dx\right]\frac{L}{k_l} = 0.943\left[\frac{(\rho_l - \rho_v) g\, i_{lv} L^3}{k_l \nu_l (T_{sat} - T_s)}\right]^{1/4} \tag{2.47}$$

The bracketed term in Eq. (2.47) can be expressed in dimensionless form as:

$$\overline{Nu_l} = 0.943\left[\frac{Ga * Pr_l}{Ja}\right]^{1/4} \tag{2.48}$$

Dhir and Lienhard [1971] devised a simple way to extend the analysis for the vertical wall to arbitrary axisymmetric bodies. They showed that the local Nusselt number can be predicted by replacing "g" in Eq. (2.46) with an effective acceleration of gravity:

$$g_{\text{eff}} = \frac{x(gR)^{4/3}}{\int_0^x g^{1/3} R^{4/3} dx} \tag{2.49}$$

In Eq. (2.49), R(x) is the local radius of curvature and g(x) is the local gravity component in the x-direction. For the horizontal cylinder, the effective gravity can be evaluated numerically and averaged over the circumference of the tube to show:

$$\mathrm{Nu} = 0.729\left[\frac{\mathrm{Ga_D\,Pr}}{\mathrm{Ja}}\right]^{1/4} \tag{2.50}$$

The Galileo number in Eq. (2.50) is subscripted with a D to indicate that the diameter is the length scale.

The analysis presented above for the vertical wall is very similar to the original analysis presented by Nusselt [1916]. Since Nusselt's analysis, the theory has been refined by many investigators. The validity of many of the assumptions have been explored in a systematic way. It should be recalled at this point that Nusselt's analysis and the refinements to it are all strictly valid for external condensation only. For this reason, the review of literature refining Nusselt's analysis will not be exhaustive since the ultimate goal of the present work is to understand the limitations of the theory as applied to the problem of internal condensation.

Based on integral analyses, Bromley [1952] and Rohsenow [1956] corrected for the assumption of a linear temperature profile. This is equivalent to including the convective terms which were originally neglected in the energy equation. Once Bromley [1952] included cross-flow terms which were neglected in his original analysis, he and Rohsenow [1956] agreed that this effect could be corrected for by replacing the latent heat in Eq. (2.40) by a modified latent heat given by:

$$i_{lv}' = i_{lv}(1 + 0.68\mathrm{Ja}_l) \tag{2.51}$$

This correction shows that the assumption of a linear temperature profile in the original analysis is quite acceptable for Ja much less than unity.

Sparrow and Gregg [1959] presented a similarity solution to the full boundary-layer equations governing falling film condensation with the assumption of zero vapor drag. Their solution included both the inertial terms in the momentum equation and the convective terms in the energy equation. Their similarity solution showed that the inertial terms vanished for an infinite Prandtl number. Numerically, their results were identical to Rohsenow's [1956] integral analysis for $\mathrm{Pr}_l > 100$ at any value of Ja. For a Prandtl number of unity, their deviation from Rohsenow's [1956] heat transfer results were negligible for

Ja<0.2 and less than 5% for Ja=1. This confirmed the validity of the basic Nusselt analysis for Prandtl numbers greater than unity and Jakob numbers less than unity. Sadasivan and Lienhard [1987] showed that the Prandtl number correction from Sparrow and Gregg's [1959] analysis could also be accounted for by modifying the latent heat. Their result was:

$$i_{lv}^{SL} = i_{lv}\left[1+\left(0.683-\frac{0.228}{Pr_l}\right)Ja_l\right] \tag{2.52}$$

This expression clearly approaches Eq. (2.51) as Pr_l increases, and increases in importance as Ja increases. Sadisivan and Lienhard [1987] warned that this correction would be inappropriate for cases with significant shear at the liquid-vapor interface.

Another idealization in the original Nusselt analysis that has been analyzed subsequently is the assumption of zero shear at the interface. In reality, the downward motion of the liquid induces downward motion in the vapor which vanishes in the freestream. The actual and idealized physical situations are shown in Fig. 2.7. Including this effect, in general, requires a solution to the coupled partial differential equations for the liquid and vapor. Koh, Sparrow, and Hartnett [1961] presented a boundary-layer solution to this problem which was an extension of the one presented by Sparrow and Gregg [1959]. The inclusion of interfacial drag added an additional dimensionless group to the heat transfer results, $\sqrt{\rho_l\mu_l/\rho_v\mu_v}$. As the value of this parameter decreases, vapor shear should become increasingly important. This analysis showed that the effects of vapor shear decreased as Pr increased. For Pr=10, the addition of shear decreased the Nusselt number by less than 1.4% for a wide range of Jakob numbers, and was insensitive to $\sqrt{\rho_l\mu_l/\rho_v\mu_v}$. For a Prandtl number of unity, interfacial shear reduced the local Nusselt number by less than 5% for Ja<0.35 and less than 8% for Ja<0.75. Again, the deviation was insensitive to $\sqrt{\rho_l\mu_l/\rho_v\mu_v}$. Inclusion of vapor drag had a serious deleterious effect only for very low Prandtl number fluids such as liquid metals.

The problem of condensation from a flowing vapor onto an isothermal surface is similar to that of including vapor drag since coupled equations for the vapor and liquid must be solved simultaneously. This has been accomplished numerically in several studies [Denny and Mills, 1969a; Denny et al., 1971; Gaddis, 1979]. An important simplification was achieved by Denny and Mills [1969b], who used the asymptotic shear method [Shekriladze and Gomelauri, 1966] to decouple the conservation equations for the liquid and vapor. Denny and Mills [1969b] found that, for the circular cylinder, their explicit solution using the asymptotic shear method agreed with their numerical results to within 1% to 2%. The asymptotic shear method was recently used by Jacobi [1992] to develop a solution for filmwise condensation in the more general axisymmetric case. His solution predicted Nusselt numbers around 15% lower than measured results for a spherical geometry, probably as a result of increased heat transfer due to interfacial waviness [Hu and Jacobi, 1992].

The asymptotic shear method of Shekriladze and Gomelauri [1966] decouples the liquid and vapor conservation equations by invoking a solution for the vapor flow under strong-suction. Under these conditions, the liquid shear at the interface is equal to the momentum lost by the condensing vapor:

$$\tau(y=\delta)=G_{cond}U_{eg} \tag{2.53}$$

If the interaction between the freestream vapor flow and the liquid are neglected [Denny and Mills, 1969b; Jacobi, 1992], the velocity at the edge of the boundary-layer, U_{eg}, can be predicted using potential flow solutions.

One deviation from Nusselt's assumptions that does not easily yield to analytical treatment is the effect of interfacial waviness. A first attempt at assessing this effect can be obtained by calculating the film Reynolds number. The film Reynolds number is defined as:

$$\mathrm{Re}_f=\frac{4\dot{m}'}{\mu_l} \tag{2.54}$$

The highest film Reynolds number on a cylinder is obtained at the bottom, and can be expressed as [Carey, 1992]:

$$\mathrm{Re}_f=4.576\left[\frac{\mathrm{Ja}^3\mathrm{Ga}_D}{\mathrm{Pr}^3}\right] \tag{2.55}$$

As a first approximation, interfacial waves can be expected for film Reynolds numbers greater than 33 [Kapitsa, 1948]. Brauer [1960] presented a slightly more refined criterion for the onset of interfacial waviness that inlcuded both a film Reynolds number and an additional dimensionless variable that included fluid properties, the Archimedes number:

$$\mathrm{Re}_f>2.3\mathrm{Ar}^{1/5} \tag{2.56}$$

$$\mathrm{Ar}=\frac{\rho_l^2\sigma^{3/2}}{\mu_l^2 g^{1/2}\left(\rho_l-\rho_v\right)^{3/2}} \tag{2.57}$$

For the lowest Archimedes number in the present study, Eq. (2.56) predicts a critical film Reynolds number of around 27. Since the highest film Reynolds number from the present study was less than 15, both of the above criteria indicate negligible impact of interfacial waves due to instability of the falling film.

2.4.2 Internal condensation

At low vapor velocities, gravitational forces which tend to pull condensate down the tube wall are much stronger than vapor shear forces which tend to pull the condensate in the direction of the mean flow. Thus, a condensate film forms on the top of the tube and grows in thickness as it flows around the circumference. The bottom portion of the tube is filled with a liquid pool which transports the condensed liquid through the tube in the direction of the mean flow. This heat transfer mechanism, shown schematically in Fig. 2.8, is very similar to that in external falling-film condensation. For this reason, heat transfer analyses for gravity-driven internal condensation rely heavily on the extensive theory developed for external condensation.

Chato [1962] completed one of the earliest studies of internal condensation, concentrating on stratified flows with low vapor velocities. He developed a similarity solution for the condensate film in this problem which was patterned after Chen's [1962] analysis of falling film condensation on a horizontal cylinder. He applied this solution to the portion of the tube where falling-film condensation prevailed (i.e., up to the flow angle where the liquid pool began). To predict the depth of the liquid pool, he developed a separate model for the flow in the liquid pool based on open channel hydraulics. Both his analytical model and experimental results for R-113 showed that the depth of the liquid level was relatively constant. This allowed his heat transfer data to be approximated reasonably well by the following Nusselt type correlation:

$$\mathrm{Nu} = \frac{\bar{h}\,D}{k_l} = 0.555\left[\frac{\rho_l(\rho_l - \rho_v)g\, i_{lv}^{'} D^3}{k_l \mu_l (T_{sat} - T_w)}\right]^{1/4} \tag{2.58}$$

The prefactor of 0.555 is 76% of the value of 0.728 which is accepted for external condensation on a cylinder. This decrease in heat transfer is because the portion of the tube perimeter that is covered by the liquid pool is not available for falling film condensation. Chato [1962] showed that, based on conduction only, the heat transfer in the liquid pool was negligible compared to that in the remainder of the tube because of the greater liquid depth.

Rufer and Kezios [1966] pointed out some differences between the situation modeled by Chato [1962] and what they thought would be observed in a typical condenser. The liquid flow model developed by Chato assumed that the flow was driven by a hydrostatic gradient in the liquid, not an imposed pressure gradient. Such a model predicts a condensate depth that decreases along the length of the tube, even though more condensate is being added. This type of model also assumes that the tube does not completely fill with liquid when the quality is zero. Chato pointed out that his model was very sensitive to the liquid depth that was assumed at the outlet of the tube.

Rufer and Kezios [1966] developed a model of stratified flow where the liquid was driven by an imposed pressure gradient rather than a hydraulic gradient. Their model differed from Chato's in several fundamental aspects. First, their model predicted that the liquid depth increased with increases in the axial coordinate due to the continuous conversion of vapor to liquid. Second, it predicted that the tube would fill with liquid when the quality approached zero. The outlet depth of the condensate was independent of conditions upstream of it, unlike Chato's model. In a discussion at the end of the paper, Rufer and Kezios left open the possibility that the conditions assumed in the Chato [1962] analysis could prevail at very low flow rates where the pressure gradient might become dominated by the hydrostatic gradient. Rufer and Kezios did not develop a heat transfer model, only a model for the liquid depth that would allow heat transfer coefficients to be solved for based on Nusselt theory. As noted by Jaster and Kosky [1976], the model of Rufer and Kezios is too cumbersome for practical use.

Jaster and Kosky [1976] proposed a correlation similar to Chato's for stratified flow condensation. To account for the variation of the liquid pool depth in a manner consistent with pressure-driven flow, they replaced the constant in the Chato correlation with a function of the void fraction. This resulted in:

$$\mathrm{Nu} = \frac{\bar{h}\,D}{k_l} = 0.728\,\alpha^{3/4}\left[\frac{\rho_l(\rho_l-\rho_v)g\,i'_{lv}D^3}{k_l\mu_l(T_{sat}-T_w)}\right]^{1/4} \tag{2.59}$$

They recommend using Zivi's correlation for the void fraction:

$$\alpha = \left[1+\frac{1-x}{x}\left(\frac{\rho_v}{\rho_l}\right)^{2/3}\right]^{-1} \tag{2.60}$$

Figure 2.9 compares the prediction of Jaster and Kosky's correlation to Chato's for R-134a at a saturation temperature of 95 °F. For this case, Jaster and Kosky's correlation overpredicts the Chato correlation for all qualities greater than about 0.2. It had a mean deviation of 37% with their own data, which it appeared to consistently overpredict [Jaster and Kosky, 1976].

The correlations of Chato [1962] and Jaster and Kosky [1976] both neglect the heat transfer that occurs in the liquid pool at the bottom of the tube. Chato showed that this heat transfer was normally negligible compared to that through the upper part of the tube based on conduction only. This assumption was reasonable for his low speed, stratified flows, but might not be for higher mass flux, low quality situations where wavy or stratified flow could prevail in the presence of substantial convective heat transfer in the bottom of the tube. Other investigators have considered this possibility.

Rosson and Myers [1965] collected experimental data in what they called the intermittent flow regime, which in their terminology included stratified flow, wavy flow, and slug flow. They measured the variation of heat transfer coefficient with angle around the tube, unlike most researchers who measure only a circumferentially averaged value of h. They found that the heat transfer coefficient continuously decreased from the top to the bottom of the tube. Their data suggested that filmwise condensation occurred in the top of the tube with superimposed effects of vapor shear. They proposed accounting for the vapor shear by replacing the constant in the Nusselt's solution with an empirically determined function of vapor Reynolds number:

$$Nu_{top} = 0.31\ Re_v^{0.12}\left[\frac{\rho_l(\rho_l - \rho_v)g\, i'_{lv} D^3}{k_l \mu_l (T_{sat} - T_w)}\right]^{1/4} \tag{2.61}$$

In the bottom of the tube, they postulated forced convective heat transfer. Using a heat and momentum transfer analogy, they recommended the following correlation for the heat transfer there:

$$Nu_{bot} = \frac{\phi_{l,lt}\sqrt{8 Re_l}}{5\left[1 + \dfrac{\ln(1+5\ Pr_l)}{Pr_l}\right]} \tag{2.62}$$

$$\text{where:}\quad \phi_{l,lt} = \sqrt{1 + \frac{1}{X_{lt}} + \frac{12}{X_{lt}^2}} \tag{2.63}$$

The remaining part of their correlation was dedicated to predicting the fraction of the tube in which each heat transfer mechanism prevailed. They characterized this by a parameter, β, which represented the fraction of the tube perimeter over which filmwise condensation occurred. They recommended predicting the value of β as follows:

$$\beta = Re_v^{0.1} \quad \text{if} \quad \frac{Re_v^{0.6} Re_l^{0.5}}{Ga} < 6.4 \times 10^{-5} \tag{2.64}$$

$$\beta = \frac{1.74 \times 10^{-5}\ Ga}{\sqrt{Re_v Re_l}} \quad \text{if} \quad \frac{Re_v^{0.6} Re_l^{0.5}}{Ga} > 6.4 \times 10^{-5} \tag{2.65}$$

Then, the circumferentially averaged Nusselt number was given by:

$$Nu = \beta\, Nu_{top} + (1-\beta)\, Nu_{bot} \qquad (2.66)$$

Rosson and Myers compared their predicted values to their own experimental data for acetone and methanol, and the agreement was reasonable. A large amount of scatter was inherent due to inaccuracies in their experimental technique, so it is difficult to discern whether the deviations were due to theoretical deficiencies or experimental scatter.

Tien et al. [1988] presented an analysis for gravity-driven condensation that they proposed to be valid for stratified, wavy, and slug flow. Their analysis was similar to that of Rosson and Myers, although more deeply rooted in conservation equations than empirically determined expressions. The correlation will be discussed conceptually herein, rather than listing all of the equations, since the procedure is rather involved. They assumed that a flow existed that was composed of an orderly procession of slug units. This is shown in Fig. 2.10. The ratio of the length of the vapor portion of the slug to the total slug length was characterized by a parameter β, which was essentially a flow regime predictor. An equation was developed which predicted the variation of β with the flow parameters. Within the slug unit, they hypothesized three types of heat transfer:

1. Filmwise heat transfer at the top of the two-phase region.
2. Forced convective condensation at the bottom of the two-phase region.
3. Single-phase forced convection in the single-phase region.

The mean heat transfer coefficient was then determined by appropriate integration of the local values over the slug unit. The heat transfer in the top of the tube was predicted by Nusselt's analysis with no modification, the forced convective condensation in the bottom of the two-phase region was predicted with a heat to momentum transfer analogy, and the single-phase forced convection was predicted by the familiar Dittus-Boelter correlation [Incropera and DeWitt, 1992]. The Tien analysis approaches the correct values in the asymptotic limits. That is, for a quality of zero it predicts a single phase liquid Nusselt number and for situations where stratified flow exists rather than slug flow it reduces to the form of Rosson and Myers. To use the Tien model, six simultaneous, nonlinear equations must be solved. Although novel and well structured, the technique is probably too involved for a practical design correlation.

2.5 Annular Flow Condensation

The gravity-driven condensation regime just discussed occurs when the interfacial shear stresses that tend to pull the liquid film in the mean flow direction are dominated by gravitational forces that tend to pull the liquid film toward the bottom of the tube. The annular flow regime represents the other limit, that is the situation where the interfacial shear stresses dominate the gravitational forces and result in a nearly symmetric annular film with a high speed vapor core. As might be expected, the heat transfer characteristics in the annular flow regime differ significantly from those in the gravity-driven regime.

A variety of approaches for predicting heat transfer during annular flow condensation have been developed. While these approaches can be divided into many different categories, they will be reduced to three for the purposes of this review: (1) two-phase multiplier approaches, (2) shear-based approaches, and (3) boundary-layer approaches. These three categories of correlations will be discussed separately.

2.5.1 Two-phase multiplier correlations

The simplest method of heat transfer prediction in the annular flow regime is the two-phase multiplier approach. This approach was pioneered for predicting convective evaporation data by Dengler and Addoms [1956], and was adapted for condensation by Shah [1979]. The theoretical hypothesis is that the heat transfer process in annular two-phase flow is similar to that in single-phase flow of the liquid (through which all of the heat is transferred), and thus their ratio may be characterized by a two-phase multiplier. This reasoning is in fact very similar to that of Lockhart and Martinelli [1947], who pioneered the two-phase multiplier approach for predicting two-phase pressure drop. The single-phase heat transfer coefficients are typically predicted by modifications of the Dittus and Boelter [Incropera and Dewitt, 1992] correlation, which results in the following form:

$$Nu = 0.023 Re_l^{0.8} Pr_l^m F\left(x, \frac{\rho_l}{\rho_v}, \frac{\mu_l}{\mu_v}, Fr_l\right) \qquad (2.67)$$

where: m = a constant between 0.3 and 0.4

F = the two-phase multiplier

While the two-phase multiplier can depend on more dimensionless groups than those indicated in Eq. (2.67), the groups shown are the most prevalent. The type of single-phase correlation shown is valid for turbulent flow, and is based primarily on an analogy between heat and momentum transfer. It then follows that the same assumptions which are made in its development are implicitly included in the form given by Eq. (2.67).

The most widely cited correlation of the two-phase multiplier type is the Shah [1979] correlation. Shah's correlation first resulted from his observation that the mechanisms of condensation and evaporation were very similar in the absence of nucleate boiling. With this idea, he set out to modify the convective component of his flow boiling correlation for use during condensation. The form of his correlation is:

$$\mathrm{Nu} = 0.023\,\mathrm{Re}_l^{0.8}\,\mathrm{Pr}_l^{0.4}\left[1+\frac{3.8}{\mathrm{P}_{\mathrm{red}}^{0.38}}\left(\frac{x}{1-x}\right)^{0.76}\right] \tag{2.68}$$

The bracketed term is the two-phase multiplier. It properly approaches unity as x approaches 0, indicating that it predicts the single-phase liquid heat transfer coefficient when all liquid is present. As the reduced pressure is increased, the properties of the liquid and vapor become more alike and the two-phase multiplier decreases. Thus, the qualitative behavior is as expected. Shah compared his correlation with data from the open literature for refrigerants, water, methanol, benzene, toluene, trichloroethylene, and ethanol. The mean deviation between his correlation and the experimental data (474 points) was 17%. Although he classified his correlation as a "generalized" correlation which was independent of flow regime, it is categorized herein as an annular flow correlation since it will later be shown to be appropriate only for this flow regime.

Cavallini and Zecchin [1974] used the results of a theoretical annular flow analysis to deduce the dimensionless groups that should be present in an annular flow correlation. They then used regression analysis to justify neglecting many of the groups that did not appear in their empirically developed correlation. The form that they wrote their correlation in is:

$$\mathrm{Nu} = 0.05\,\mathrm{Re}_{\mathrm{eq}}^{0.8}\,\mathrm{Pr}_l^{0.33} \tag{2.69}$$

$$\text{where: } \mathrm{Re}_{\mathrm{eq}} = \mathrm{Re}_l + \mathrm{Re}_v\,\frac{\mu_v}{\mu_l}\left(\frac{\rho_l}{\rho_v}\right)^{0.5} \tag{2.70}$$

This correlation can be shown to be of the two-phase multiplier form by rewriting it in the following way:

$$\mathrm{Nu} = 0.023\,\mathrm{Re}_l^{0.8}\,\mathrm{Pr}_l^{0.33}\left\{2.64\left[1+\left(\frac{\rho_l}{\rho_v}\right)^{0.5}\left(\frac{x}{1-x}\right)\right]\right\}^{0.8} \tag{2.71}$$

Again, the bracketed term represents the two-phase multiplier. Cavallini and Zecchin compared their correlation with experimental data from six different studies with R-113, R-12, and R-22. The standard deviation between their correlation and the experimental data sets varied from 8% to 47%. The mean deviation of all the data combined was 30% if each point was given equal weight and 22% if each set was given equal weight.

2.5.2 Shear-based correlations

The use of shear-based correlations for annular flow condensation dates back to the early work of Carpenter and Colburn [1951]. They argued that the resistance to heat transfer in the turbulent liquid flow was entirely inside the laminar sublayer. Based on this argument, they deduced a relationship for the local Nusselt number that can be written in the following way:

$$\mathrm{Nu} = b\frac{\sqrt{\tau_w/\rho_l}\,D}{\nu_l}\mathrm{Pr}_l^m = bD^+\,\mathrm{Pr}_l^m \tag{2.72}$$

The constants b and m in Eq. (2.72) were empirically determined to be equal to 0.043 and 0.5, respectively. They argued that the wall shear stress was composed of additive components due to friction, acceleration, and gravity:

$$\tau_w = \tau_f + \tau_{acc} + \tau_g \tag{2.73}$$

Although it was later pointed out [Soliman et al., 1968] that their equation for the accelerational shear component was incorrect, the framework that they established at a relatively early point in the history of forced convective condensation remains useful.

Soliman et al. [1968] utilized the framework established by Carpenter and Colburn [1951] to develop their own semi-empirical heat transfer correlation for annular flow. They accepted the basic validity of the form presented by Carpenter and Colburn, but refined it in several ways. First, they corrected the equation for predicting the wall shear stress due to phase-change. Their corrected form showed that this component was normally negligible in comparison to the frictional component except at low qualities. Second, they implemented an improved correlation for the frictional pressure drop. Third, they used data from other researchers to determine new values of the constants b and m in Eq. (2.72). Their final form can be written as:

$$\mathrm{Nu} = 0.036\,D^+\,\mathrm{Pr}_l^{0.65} \tag{2.74}$$

Utilizing their corrected form for the phase-change shear stress and neglecting the gravitational term (which is appropriate for horizontal flow), the Soliman correlation can be written as:

$$\mathrm{Nu} = 0.036\,\mathrm{Re}_{lo}\,\mathrm{Pr}_l^{0.65}\left(\frac{\rho_l}{\rho_v}\right)^{0.5}\sqrt{\frac{2(.046)x^2}{\mathrm{Re}_v^{0.2}}\phi_v^2 + \mathrm{Bo}\sum_{n=1}^{5} a_n\left(\frac{\rho_v}{\rho_l}\right)^{n/3}} \tag{2.75a}$$

$$\text{where:}\quad \begin{aligned} a_1 &= x(2-\beta)-1 \\ a_2 &= 2(1-x) \\ a_3 &= 2(\beta-1)(x-1) \\ a_4 &= \frac{1}{x}-3+2x \\ a_5 &= \beta\left[2-\frac{1}{x}-x\right] \end{aligned} \qquad (2.75\text{b-f})$$

$$\beta = \frac{\text{interface velocity}}{\text{mean film velocity}} = 1.25 \text{ for turbulent liquid} \qquad (2.75\text{g})$$

Soliman et al. [1968] compared the predictions of their correlation to data for steam, R-113, R-22, ethanol, methanol, toluene, and trichloroethylene. The agreement was correct in trend, although even on log-log axes the deviations appeared quite large. No statistical information regarding deviations was given.

Chen et al. [1987] developed a generalized correlation for vertical flow condensation which included several effects combined with an asymptotic model. They stated, as did Carey [1992], that their correlation for the shear-dominated regime was also appropriate for horizontal flow. Their correlation used the general form of Soliman [1968] with two modifications. First, the acceleration terms were neglected since they were normally negligible at the relatively high quality conditions at which annular flow was expected to exist. Second, the pressure drop model was replaced by one from Dukler [1960]. The final result was the following:

$$\mathrm{Nu} = 0.018\left(\frac{\rho_l}{\rho_v}\right)^{0.39}\left(\frac{\mu_v}{\mu_l}\right)^{0.078} \mathrm{Re}_l^{0.2}\left[\mathrm{Re}_{lo}-\mathrm{Re}_l\right]^{0.7}\mathrm{Pr}_l^{0.65} \qquad (2.76)$$

Chen et al. [1988] made no comparison with horizontal flow data for the annular flow regime.

2.5.3 Boundary-layer analyses

The most theoretical approach to annular flow condensation is that of the boundary-layer analyses. These analyses represent solutions to simplified forms of the continuity, momentum, and energy equations. Examples of these analyses are the correlations of Dukler [1960], Azer et al. [1972], and Traviss et al. [1973]. The approaches of these researchers are so similar that there is little to be offered by reviewing them all in detail. Since the Traviss correlation is the most widely quoted of this general class, it will be reviewed in detail and differences between it and the other analyses will be discussed subsequently.

The Traviss analysis relies on the following important assumptions:

1. The validity of extrapolating the universal velocity profile from single-phase pipe flow to the liquid film in two-phase flow.
2. An axisymmetric annular film ($\delta \neq \delta(\theta)$).
3. No entrainment of liquid in the core flow.
4. Applicability of cartesian coordinates in the film ($\delta/D \ll 1$).

An idealized schematic of the annular flow that was analyzed by Traviss is shown in Fig. 2.11.

By assuming turbulent flow and that cross-stream diffusion dominates advective terms in the energy equation, one arrives at:

$$\frac{\partial}{\partial y}\underbrace{\left[\rho_l c_{p,l}(\alpha_l + \varepsilon_h)\frac{\partial T}{\partial y}\right]}_{\dot{Q}''} = 0 \tag{2.77}$$

This implies that the heat flux is constant in the y-direction. This equation can be rearranged immediately and solved in quadrature form for the heat transfer coefficient:

$$\int_{T_w}^{T_{sat}} \frac{dT}{\dot{Q}''} = \frac{1}{h} = \int_0^{\delta} \frac{dy}{\rho_l c_{p,l}(\alpha_l + \varepsilon_h)} \tag{2.78}$$

If the integrand is converted to wall coordinates and the turbulent Prandtl number ($\varepsilon_m/\varepsilon_h$) is introduced, this becomes:

$$\frac{\rho_l c_{p,l}\sqrt{\tau_w/\rho_l}}{h} = \frac{1}{St_t} = \int_0^{\delta^+} \frac{dy^+}{1/Pr_l + (1/Pr_t)(\varepsilon_m/\nu_l)} \tag{2.79}$$

Thus, if the dimensionless film thickness δ^+, the turbulent Prandtl number, and the variation of ε_m with y^+ are known, the Stanton number (which can easily be converted to a Nusselt number) is known immediately. In the rest of their analysis, they develop the conservation equations required to solve for these unknown quantities.

Conservation of liquid across the film, assuming no entrainment, results in the following expression in wall coordinates:

$$Re_l = 4\int_0^{\delta^+} u^+ dy^+ \tag{2.80}$$

This expression, combined with the universal velocity profile (or any turbulence model in the more general case), establishes a unique relationship between Re_l, which is known, and δ^+, which is unknown.

The eddy diffusivity is related to the shear stress in a turbulent flow by:

$$\tau = \rho_l(\nu_l + \varepsilon_m)\frac{\partial u}{\partial y} \tag{2.81}$$

In wall coordinates, this expression can be rewritten as:

$$\frac{\varepsilon_m}{\nu_l} + 1 = \frac{(\tau/\tau_w)}{du^+/dy^+} \tag{2.82}$$

To solve for the quantity (τ/τ_w) in terms of known parameters of the flow, several applications of the momentum equation are necessary.

First, applying the momentum equation over a differential element of the entire tube cross-section yields:

$$-\frac{dP}{dz} = \frac{\tau_w S_w}{A_c} + G^2\frac{d}{dz}\left[\frac{x^2}{\rho_v\alpha} + \frac{(1-x)^2}{\rho_l(1-\alpha)}\right] = -\left(\frac{dP}{dz}\right)_f - \left(\frac{dP}{dz}\right)_{acc} \tag{2.83}$$

Eq. (2.83) is a familiar statement in two-phase flow which divides the total pressure drop into additive components due to friction and acceleration, respectively. No gravitational component is included since the analysis presented herein is for horizontal flow. Applying the momentum equation to the entire liquid film results in:

$$-\left(\frac{dP}{dz}\right) + \frac{\tau_i S_i}{A_c(1-\alpha)} - \frac{\tau_w S_w}{A_c(1-\alpha)} = \frac{G^2}{(1-\alpha)}\frac{d}{dz}\left[\frac{(1-x)^2}{\rho_l(1-\alpha)}\right] - \frac{GV_i}{(1-\alpha)}\frac{d}{dz}[1-x] \tag{2.84}$$

The terms in Eq. (2.84) represent, respectively, the pressure gradient which drives the liquid, the interfacial shear which pulls the liquid forward, the wall shear which retards the liquid, the momentum change across the two ends of the liquid layer, and the momentum added by condensate crossing the interface. After making several geometric simplifications, they rewrote Eq. (2.84) as:

$$\tau_w = \tau_i + F_o\delta \tag{2.85}$$

$$\text{where: } F_o = -\left(\frac{dP}{dz}\right) - \frac{G^2}{(1-\alpha)}\frac{d}{dz}\left[\frac{(1-x)^2}{\rho_l(1-\alpha)}\right] + \frac{GV_i}{(1-\alpha)}\frac{d}{dz}[1-x] \tag{2.86}$$

Traviss then wrote a similar momentum equation across a portion of the liquid layer extending from the interface to an arbitrary value of y. They approximated this equation as:

$$\tau = \tau_i + F_o(\delta - y) \tag{2.87}$$

The approximation in Eq. (2.87) is that the entire momentum difference across the two ends of the control volume (the second term in F_0) is assumed to be felt no matter how thin the liquid layer is. This is incorrect, especially at values of y near δ. Equations (2.84) and (2.87) can be combined to eliminate the interfacial shear stress, an unknown quantity. The resulting expression provides the expression for $\tau(y)$ that is needed for closure in Eq. (2.82).

With the eddy diffusivity known, the local Stanton number can be solved for by performing the integration in Eq. (2.79). Expressing the final result as a Nusselt number, their solution can be written as:

$$\mathrm{Nu} = \frac{hD}{k_l} = \frac{D^+ \mathrm{Pr}_l}{F_2(\mathrm{Re}_l, \mathrm{Pr}_l)} \tag{2.88}$$

$$\text{where:} \quad F_2 = \int_0^{\delta^+} \frac{dy^+}{1/\mathrm{Pr}_l + (1/\mathrm{Pr}_t)(\varepsilon_m / \nu_l)} \tag{2.89}$$

Since the universal velocity profile is a piecewise function, the solution for F_2 is also. It is given by:

$$\mathrm{Re}_l<50 \qquad F_2 = 0.707\,\mathrm{Pr}_l\,\mathrm{Re}_l^{0.5} \tag{2.90}$$

$$50<\mathrm{Re}_l<1125 \qquad F_2 = 5\mathrm{Pr}_l + 5\ln\left[1 + \mathrm{Pr}_l\left(0.09636\,\mathrm{Re}_l^{0.585} - 1\right)\right] \tag{2.91}$$

$$\mathrm{Re}_l>1125 \qquad F_2 = 5\left[\mathrm{Pr}_l + \ln(1 + 5\mathrm{Pr}_l)\right] + 2.5\ln(0.00313\,\mathrm{Re}_l^{0.812}) + 2.5\ln\left[\frac{M\left(30 - 2.5/\mathrm{Pr}_l\right) - 0.095\,\mathrm{Re}_l^{0.812}}{M\left(0.095\,\mathrm{Re}_l^{0.812} - 2.5/\mathrm{Pr}_l\right) - 0.095\,\mathrm{Re}_l^{0.812}}\right] \tag{2.92}$$

The quantity M in the fourth term of Eq. (2.92) is given by:

$$M = \frac{F_o \delta^+ \nu_l}{\tau_w u^*} = 1 - \frac{\tau_i}{\tau_w} \tag{2.93}$$

Thus, M represents the decrease in the interfacial shear stress relative to the wall shear stress because of the momentum added to the liquid layer by the condensate. This parameter only arises in the fourth term of Eq. (2.92), so the effect of momentum transfer due to phase-change is isolated to this term. By comparing the fourth term with the preceding three terms, Traviss et al. [1973] showed that this term was negligible for Pr greater than unity except at very low qualities and very high condensation rates. It is unlikely that annular flow models are applicable at these low quality conditions, so the most widely quoted form of the Traviss correlation includes only the first three terms of Eq. (2.92). Under conditions where the fourth term is important, a void fraction model must be assumed and the heat flux must be known to evaluate M. This results in a complicated iterative procedure for calculating the heat transfer coefficient. Traviss et al. [1973] recommended using the void fraction model of Zivi [1964] when M is important.

The analysis of Traviss is by no means the only such analysis of annular flow. Abis [1969] developed a similar analysis in his dissertation, which was utilized and refined subsequently by Azer et al. [1972], Said [1982], and Said et al. [1982]. Their analysis was similar to that of Traviss et al. [1973] in its use of the universal velocity profile and its handling of the momentum pressure drop. However, it differed because geometric complications related to the cylindrical geometry were retained. Perhaps because of these complications, their solution could only be accomplished numerically. This lack of an explicit expression for the Nusselt number probably explains the fact that subsequent investigators have not utilized their work. Kosty and Staub [1971] neglected the effects of momentum transfer due to phase-change and arrived at a result which was identical to the Traviss [1973] correlation with M=0.

Dukler [1960] used a similar concept to solve the problem of annular flow condensation. The primary difference between his analysis and those discussed above is that he extrapolated expressions for eddy diffusivity from single-phase pipe flows rather than expressions for the turbulent velocity profile. This changes the solution procedure slightly, but does not result in significant differences in the final results. His solution was accomplished numerically and is available only in tabular or graphical form.

For any of the solutions discussed above, the final result relates the Nusselt number to D^+, which contains an unknown wall shear stress. This means that a pressure drop model must be assumed to close the problem. If the pressure drop model utilizes the two-phase multiplier approach of Lockhart and Martinelli, the final solution can be written in either of two forms:

$$\mathrm{Nu} = \frac{\sqrt{0.023}\,\mathrm{Re}_l^{0.9}\,\mathrm{Pr}_l\,\phi_l(X_{tt})}{F_2(\mathrm{Re}_l, X_{tt})} \tag{2.94}$$

$$\mathrm{Nu} = \frac{\sqrt{0.023}\,\mathrm{Re}_v^{0.9}\,\mathrm{Pr}_l\left(\frac{\mu_v}{\mu_l}\right)\left(\frac{\rho_l}{\rho_v}\right)^{0.5}\phi_v(X_{tt})}{F_2(\mathrm{Re}_l, X_{tt})} \tag{2.95}$$

Since two-phase pressure drop models contain relatively high uncertainties, this step can introduce significant error in the final result. Traviss utilized a two-phase multiplier correlation that was developed by Soliman [1968] as a fit to the data of Lockhart and Martinelli [1947]. The resulting expression for the Nusselt number is given by:

$$\mathrm{Nu} = \frac{\mathrm{Re}_l^{0.9}\,\mathrm{Pr}_l}{F_2}\left[0.15\left(\frac{1}{X_{tt}} + \frac{2.85}{X_{tt}^{0.476}}\right)\right] \tag{2.96}$$

The expression given by Eq. (2.96) agreed well with experimental data for low qualities or high values of X_{tt}, but significantly underpredicted the data at high qualities or low values of X_{tt}. Traviss et al. [1973] recommended using Eq. (2.96) for $X_{tt}>0.155$. To match their data at high qualities, they recommended raising the bracketed term in Eq. (2.96) to the 1.15 power for $X_{tt}<0.155$. The discrepancy at high qualities was attributed to entrainment, although the proposed correction was purely empirical.

2.6 Annular-Mist Flow Condensation

At sufficiently high vapor velocities, crests of waves on the liquid film are ripped from the liquid and entrained in the core flow in the form of small liquid droplets. Although this removal of liquid from the film can potentially have a significant effect on the heat transfer process, this effect has received little attention in the published literature. The limited literature that is available regarding this subject will be discussed herein.

Several researchers have pointed out that the effect of entrainment could be important [Traviss et al., 1973; Shah, 1981; Soliman, 1986]. Both Shah and Traviss hypothesized that significant entrainment would increase the heat transfer coefficient above theoretical predictions due to a decrease in the film thickness. Their logic was based on simple conduction arguments which suggest that the resistance to heat transfer is directly proportional to thickness.

Some debate exists in the literature concerning the most fundamental aspects of condensation in the annular-mist flow regime. Carey [1992] proposed the idea of a liquid annulus on the wall with liquid droplets entrained in the core flow. Based on this view, the heat transfer mechanism would be similar to that for pure annular flow, forced convection through a turbulent liquid layer. If this view of annular-mist flow is correct, heat transfer could be analyzed by modifying the annular flow theories discussed previously. The primary obstacle would be predicting the entrainment rate as a function of the operating conditions. Knowledge of the fraction of the liquid that was entrained in the core flow would then allow the conservation of liquid statement across the film to accurately predict the film thickness.

A second view of annular-mist flow was proposed by Soliman [1986]. Soliman described a regime which occurs at high qualities and high mass fluxes where nearly all of the liquid flows as entrained droplets in the core flow and no stable liquid film exists on the wall. He developed a parameter to predict the transition from annular flow to pure mist flow, We_{so}, which was introduced in Section 2.3.4. He then computed We_{so} for data from several investigators which had a substantial amount of mist flow. Using correlations developed for annular flow [Akers et al., 1958; Traviss et al., 1973] he predicted the heat transfer coefficients for all the data. He then examined how the ratio h_{exp}/h_{pred} varied with We_{so}. He stated that the annular flow correlations that he selected became increasingly inappropriate as We_{so} was increased. He concluded based on these data that annular flow correlations were applicable only for $We_{so}<30$.

Soliman then developed a correlation that modeled the heat transfer behavior in what he described as the mist flow region in which no stable liquid film existed. He postulated that the flow was composed of a homogeneous mixture of liquid and vapor in thermodynamic equilibrium, with all heat being transferred through the wall. Further, he proposed that when condensate formed it was blown off the wall by shear forces and that heat transfer occurred mostly in the dry spots. Since the pattern of dry spots and intermittent film in this type of flow should depend on the wall shear, Soliman originally attempted to use a heat to momentum transfer analogy that gave a simple power law type expression including a mixture Reynolds number and a vapor Prandtl number. In testing this type of correlation, however, Soliman noted deviations from his prediction that seemed to depend on the driving temperature difference. He included a Jakob number in his correlation to account for this. The final correlation that resulted was:

$$Nu = \frac{hD}{k_l} = 0.00345\, Re_m^{0.9}\, Pr_v^{0.33}\, Ja_v^{-0.33} \tag{2.97}$$

$$Re_m = \frac{GD}{\mu_m} \tag{2.98}$$

$$1/\mu_m = x/\mu_v + (1-x)/\mu_l \tag{2.99}$$

This correlation agreed with the data in his database better than the annular flow correlations of Traviss et al. [1973] and Akers et al. [1958].

Several questions can be raised with Soliman's work. First, the idea of a dry wall during condensation is counterintuitive. In fact, the flow regime studies that he cited as validation for this idea were all made in adiabatic sections. It is questionable to infer that a wall which appears dry in an adiabatic section remains so during condensation. Also, several conclusions that he drew from the experimental data used to develop his correlation are open to argument. Figure 2.12 is a plot from his paper that shows how the predictions of the Traviss correlation differed from the experimental data. Soliman inferred from this plot that the Traviss correlation was inappropriate for $We_{so}>30$. Careful examination of the plot points to another possible explanation. For R-113, the Traviss correlation remained a good predictor of the experimental data for values of We_{so} up to 70 and the deviations from the correlation were insensitive to We_{so}. The Traviss correlation was a reasonable predictor of the R-12 data, actually matching the data best for values of $We_{so}>30$. The large deviations for the R-12 data at low Weber numbers could be due to the data being in the wavy flow regime. For the two sets of steam data, the Traviss correlation was a poor predictor for any value of We_{so}. Thus, the basic premise that deviations from annular flow correlations are dependent on Weber number (or mist flow) is questionable.

The way that Soliman obtained agreement with the various sets of data was by introducing a dependence on temperature difference (or Jakob number). Figures 2.13 and 2.14 are the plots from Soliman's paper that were used to justify including this dependence. These plots show that for any one set of data, little dependence on temperature difference was noted. The primary differences on the plots appeared to be between various sets of data. At least two plausible explanations for this behavior can be presented other than a dependence on temperature difference. First, systematic errors in the data from different researchers could be present due to experimental artifacts. Second, the proposed correlating form could work well for some of the fluids and poorly for the others. Close examination of the plots, in fact, shows that the only fluid that could not have been correlated equally well with a constant rather than a Ja_v term was steam. A similar trend was observed for the Traviss correlation, which was a reasonable predictor of the refrigerant data and a poor predictor of the steam data. Based on these arguments, it appears that further examination of Soliman's conclusions is warranted.

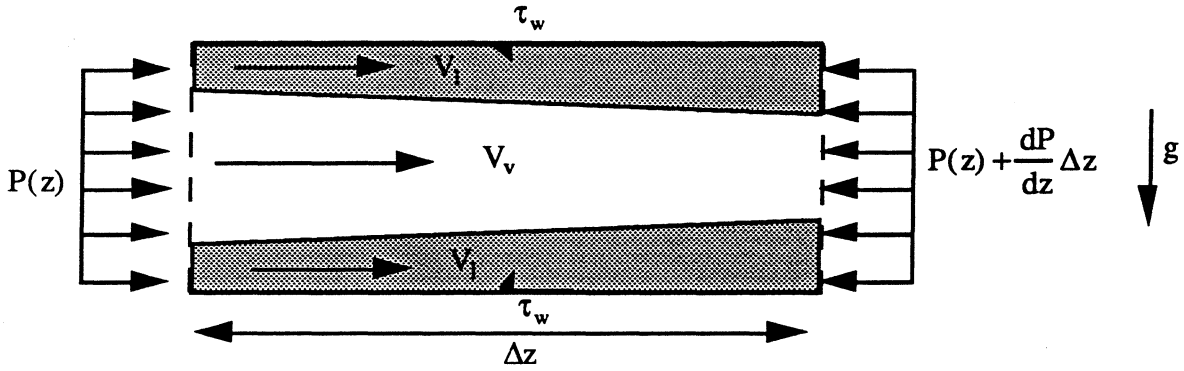

Figure 2.1 Schematic of horizontal, separated two-phase flow.

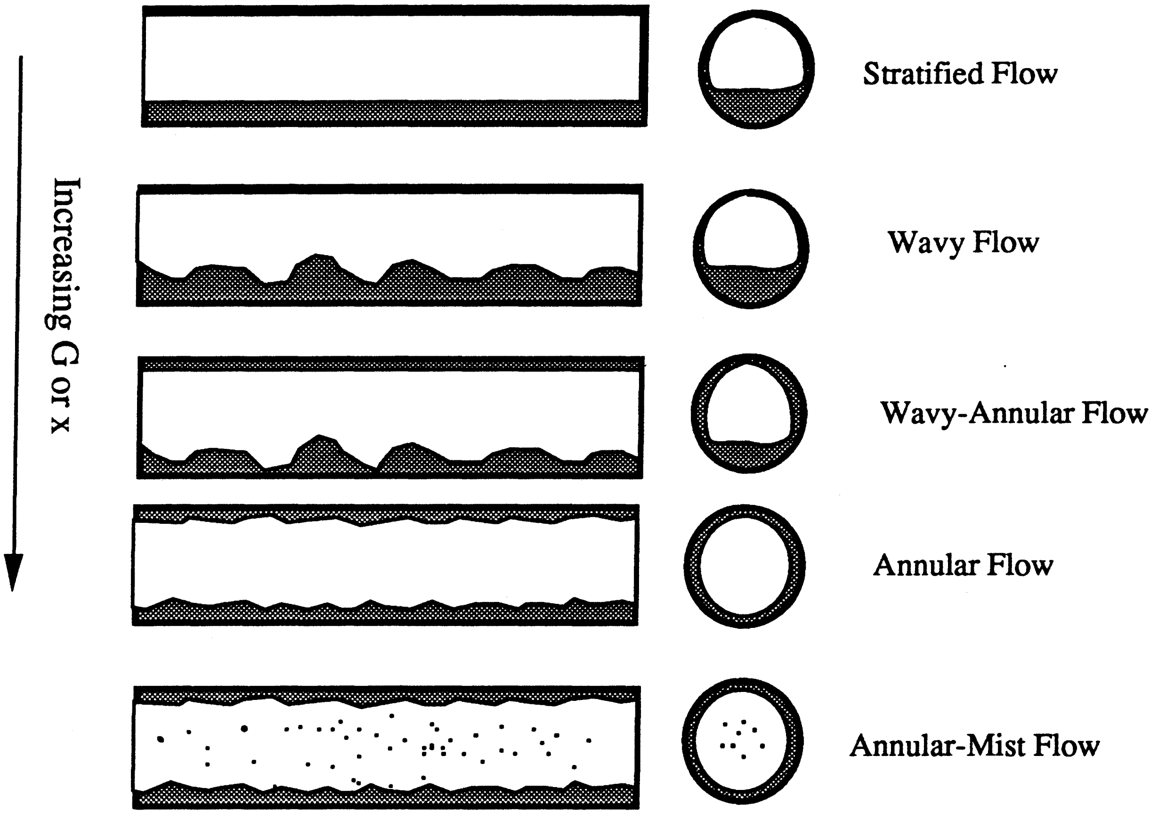

Flow regimes encountered at high void fractions

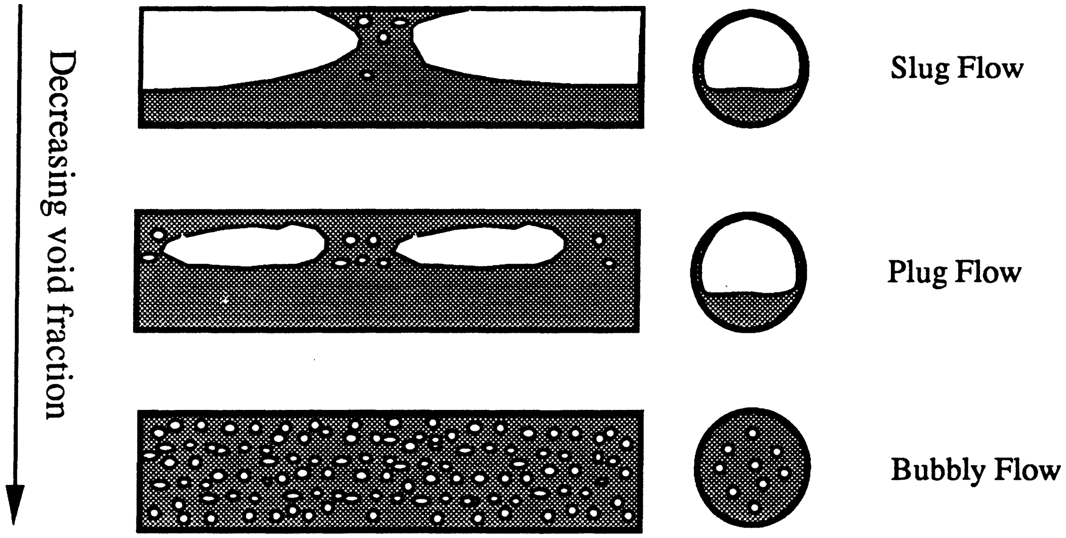

Flow regimes encountered at low void fractions only

Figure 2.2 Flow regimes typically encountered in condensation processes.

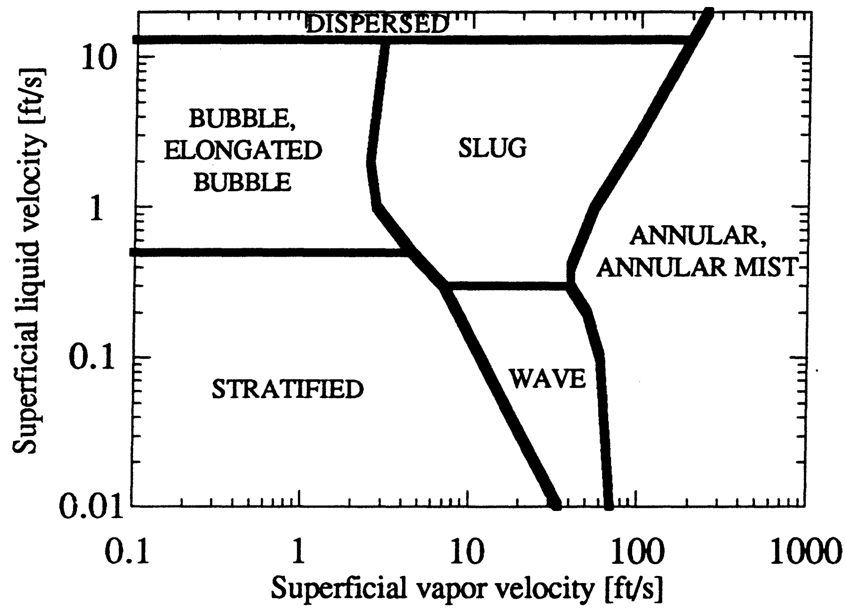

Figure 2.3 The flow regime map of Mandhane et al. [1974].

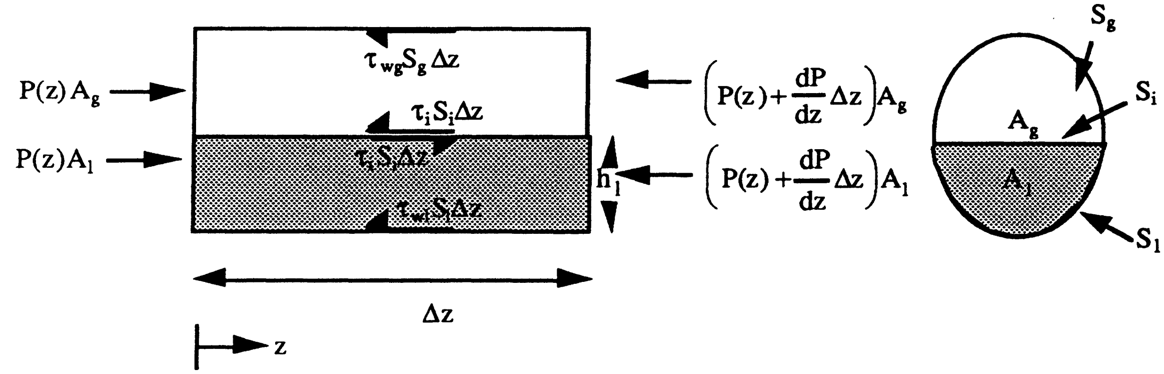

Figure 2.4 Stratified flow schematic from Taitel and Dukler [1976] analysis.

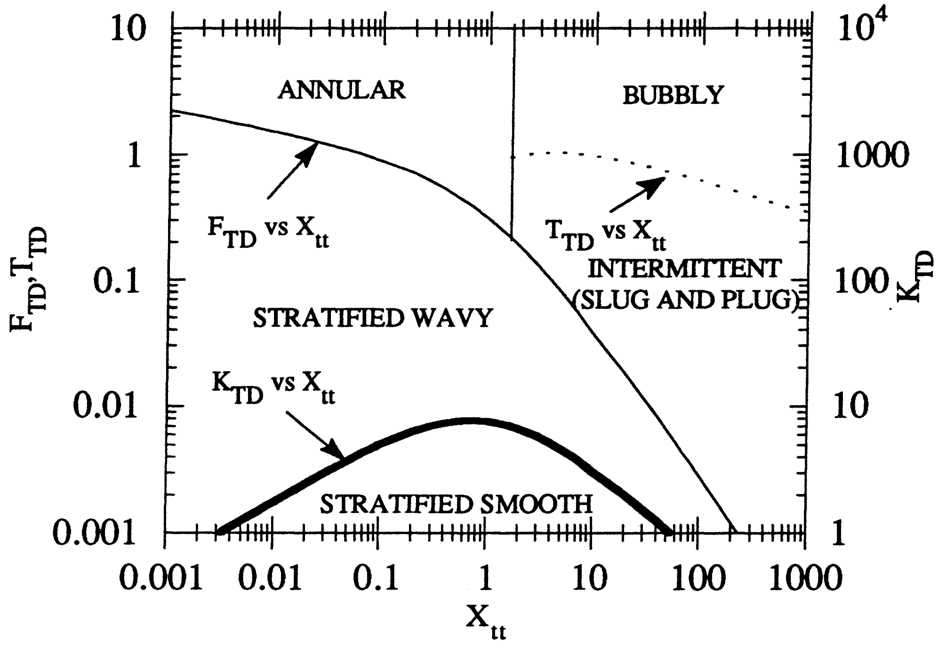

Figure 2.5 Flow regime map proposed by Taitel-Dukler for horizontal flow with both phases flowing turbulently.

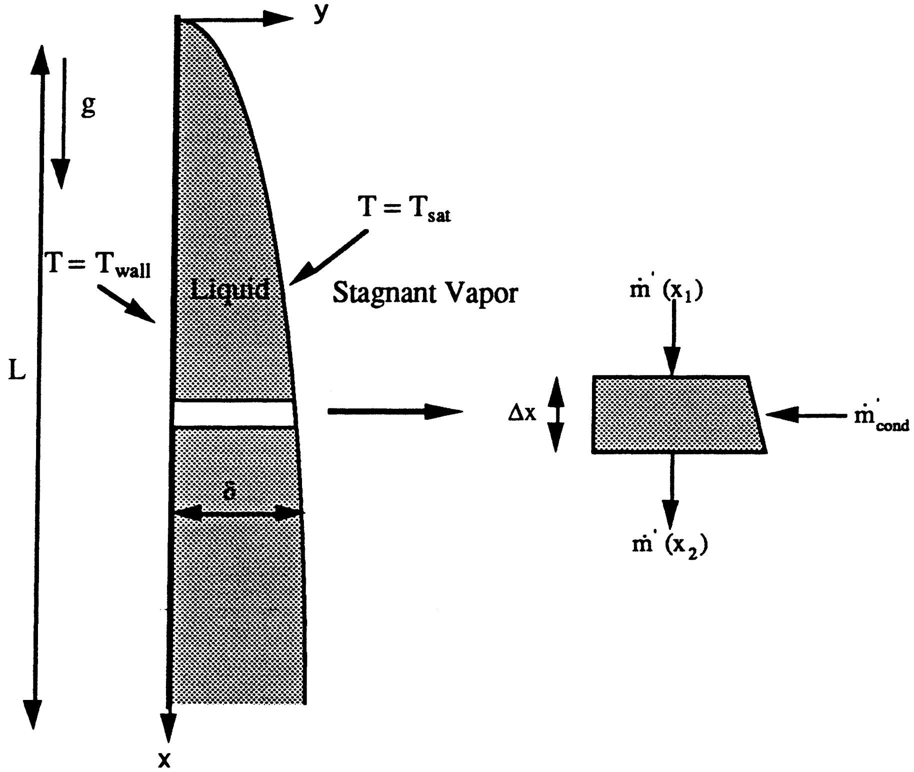

Figure 2.6 Idealized schematic of falling-film condensation.

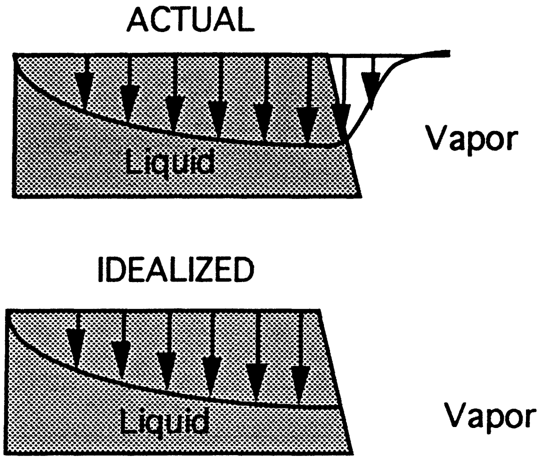

Figure 2.7 Actual and idealized velocity profile for falling film condensation.

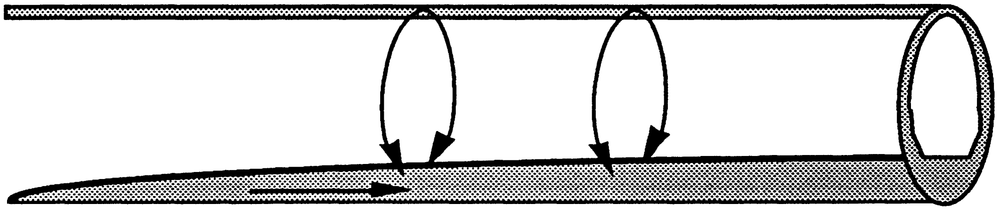

Figure 2.8 Idealized condensation process during stratified flow.

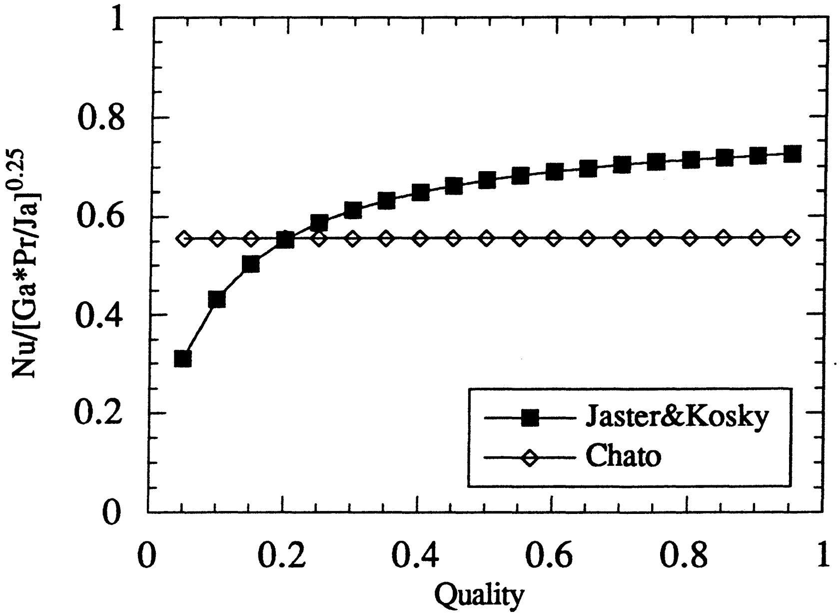

Figure 2.9 Predictions of Jaster and Kosky [1976] and Chato [1962].

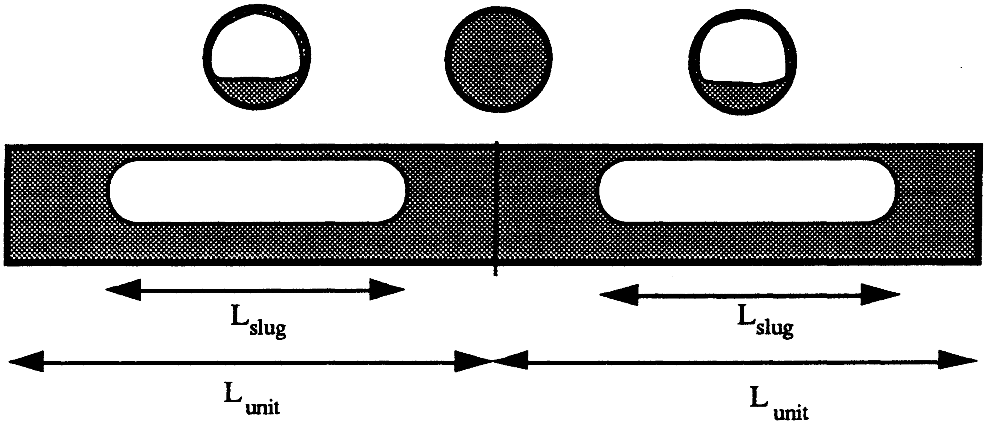

Figure 2.10 Slug flow schematic as hypothesized by Tien et al. [1988].

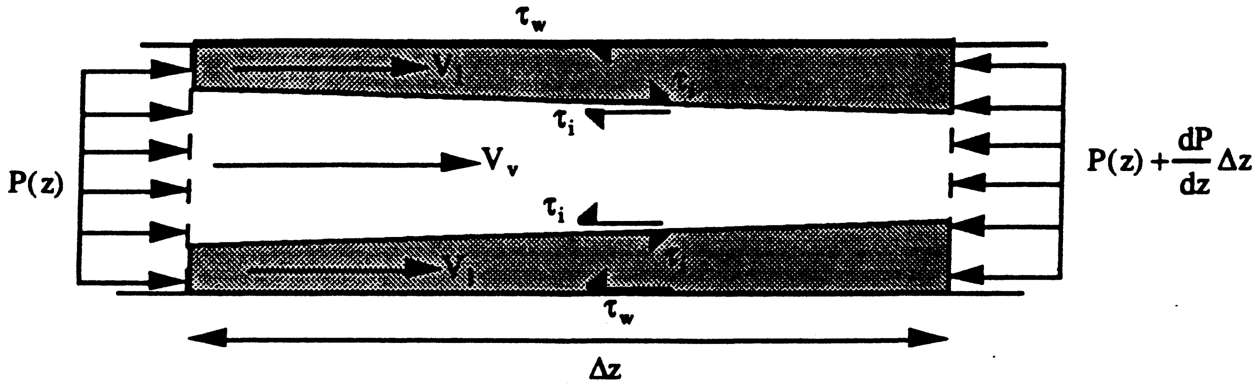

Figure 2.11 Annular flow schematic of Traviss [1973].

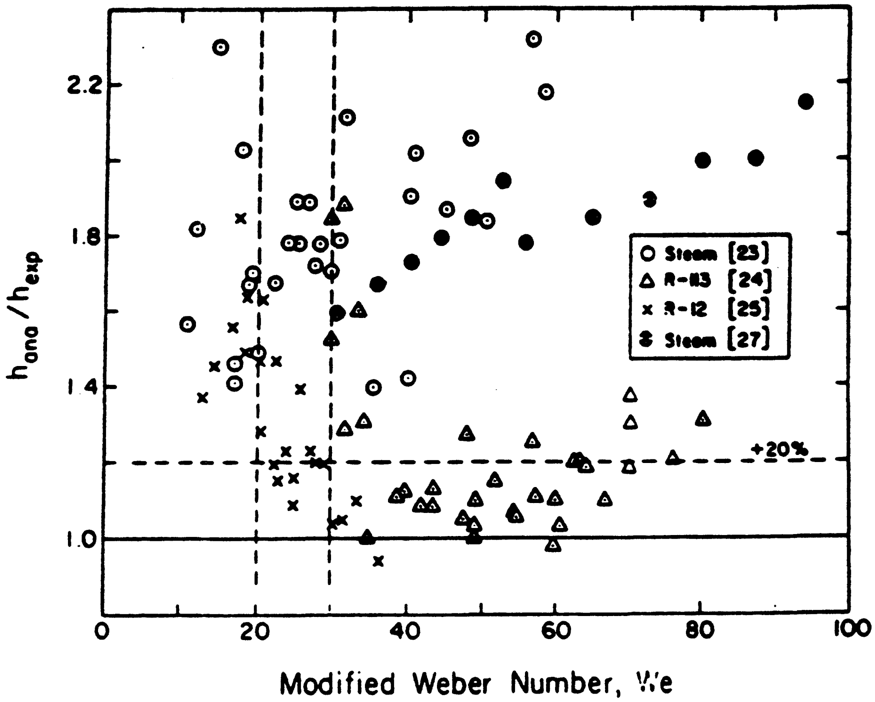

Figure 2.12 Comparison of the Traviss [1973] correlation with experimental data used by Soliman [1986].

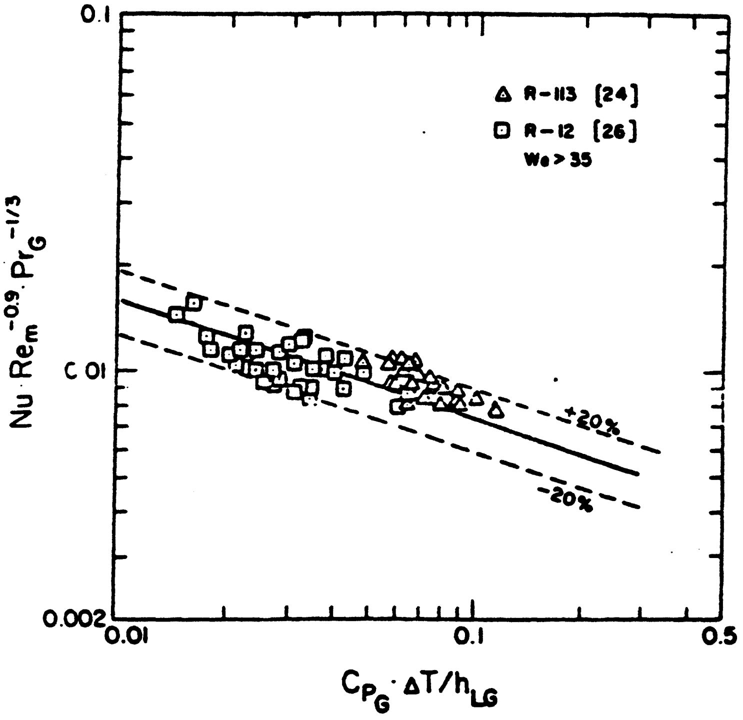

Figure 2.13 Effect of Ja_v on the Nusselt number for R-113 and R-12 as presented by Soliman [1986].

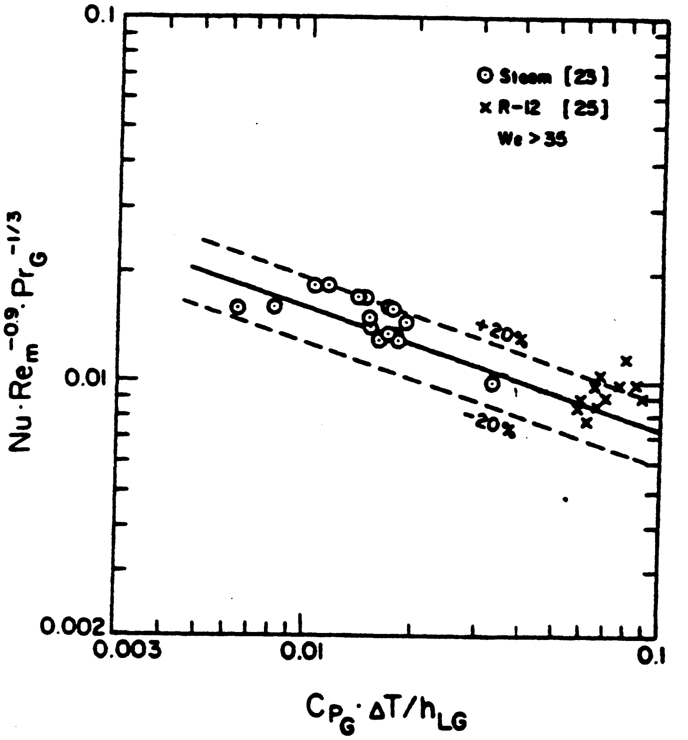

Figure 2.14 Effect of Ja_v on the Nusselt number for steam and R-12 as presented by Soliman [1986].

CHAPTER 3

EXPERIMENTAL FACILITY

An apparatus has been designed in the ACRC at the University of Illinois that allows in-tube condensation data to be collected over a wide range of operating conditions. Earlier versions of this apparatus have been described in the theses of Bonhomme [1991] and Hinde [1992]. An updated discussion of the experimental apparatus in this chapter describes the general features of the experimental facility, including recent improvements.

The purpose of the condensation test facility is to supply a working fluid to the inlet of a test-condenser at a variety of thermodynamic states ranging from subcooled liquid to superheated vapor. In the test-condenser, in-tube heat transfer coefficients and pressure drops of the working fluid are measured. A schematic of the apparatus is provided in Figure 3.1. The discussion of the apparatus provided in this chapter is divided into five sections: (1) the refrigerant loop, (2) the water loop, (3) the test-condensers, (4) the instrumentation, and (5) the data acquisition system.

3.1 Refrigerant Loop

The refrigerant loop of the test facility is depicted in Figure 3.1. The flow in the loop is driven by a variable speed gear pump. This pump is powered by a three-phase motor that is digitally controlled using an AC inverter. Unlike a compressor, the gear pump requires no lubrication so the loop can be operated in an oil-free environment. The flow rate through the refrigerant loop can be controlled in three ways. The most sensitive method of adjustment is provided by digital controls on the AC inverter. A second, coarser method of controlling the flow is to divert some of the fluid circulating through the pump in a bypass line around the pump. This recirculating flow is controlled by a needle valve in the bypass line, and allows the flow through the loop to be less than that through the pump. A third method of controlling the flow rate is provided by a needle valve downstream of the pump exit. Closing this valve provides additional pressure drop that is necessary to achieve the lowest flow rates.

Following the pump, the refrigerant flow rate is measured by one of two flow meters. A Micro Motion D6 mass flow meter is used for all flows which fall inside of its 2.0 lb/min range. A Max machinery positive displacement flow meter with a 0-0.13 ft^3/min range is used at flow rates above the range of the Micro Motion meter. The two flow meters and a bypass line are connected in parallel and are valved such that the flow can be sent through any combination of the lines. In practice, two of the circuits are normally closed. The bypass line is sometimes necessary during transient situations since two-phase flow can damage the positive displacement flow meter.

A serpentine heater is used to heat the subcooled liquid refrigerant to the desired state at the inlet of the test-condenser. Figure 3.2 is a schematic of the refrigerant heater. The heater consists of five passes of .315" i.d. tubing, each of 5.91 feet length. Each pass of the heater is wrapped with four 180 Ω resistance heaters of 1.25 ft. length, providing 21,840 Btu/hr of total power. The heaters are wrapped tightly onto the tube surface with shrink tape, and insulated with three layers of armaflex insulation to an outer diameter of 4.13". The first nine heaters are turned on at all times and are powered by a 0 to 240 V variable voltage transformer (variac). These nine heaters provide 9827 Btu/hr of heat. The next nine heaters are controlled by a separate variac, and are used when the total heat requirements are greater than the capacity of the first heater. The last two heaters are controlled in an on/off manner only, and are rarely used.

The refrigerant next flows through the test-condenser where the experimental heat transfer data are collected. In this section, heat is exchanged from the two-phase refrigerant to water in a counterflow heat exchanger. The flow regime is observed visually at the inlet and outlet of the test-condenser in sight glasses of an inner diameter that matches the test-condenser. These glasses are each approximately 5" long, and made of thick walled tubing that is annealed to remove stress concentrations. The glasses are held securely at each end by compression fittings using teflon ferrules. These compression fittings are mounted in a unistrut frame that prevents them from being blown off the ends of the glass. These glasses have sustained operating pressures of up to 450 psi for prolonged periods with no incidents of failure.

After exiting the test-condenser, the refrigerant is returned to a subcooled liquid state by extracting heat in a water cooled aftercondenser. The aftercondenser is a nominal 23,890 Btu/hr counterflow heat exchanger manufactured by Refrigeration Research. This unit has a refrigerant-side volume of .039 ft^3, holding approximately 3.0 lbs. of R-134a at 68 °F .

For most of the experiments described herein, the operating pressure in the loop was controlled by a bladder accumulator connected to a nitrogen bottle and a pressure regulator. This device controlled the pressure by maintaining mechanical equilibrium between the bladder and the refrigerant. As refrigerant was vaporized, the increased system volume occupied by the vapor was matched by a decreased volume in the bladder. This allowed the loop to operate in a nearly isobaric sense (the decreased volume in the bladder increased its pressure unless nitrogen was extracted) as long as the vapor volume in the loop was less than the unused volume in the nitrogen side of the bladder. This requirement was always met since the bladder volume (.67 ft^3) was over six times greater than the volume of the entire refrigerant loop (0.10 ft^3).

Throughout the course of the experiments, two bladders failed due to material incompatibility problems. The first failure was caused by incompatibility between the Buna-N bladder and R-22. A replacement bladder made of viton was ordered to alleviate this problem, but through a vendor error the replacement bladder that was shipped was also made of Buna-N. This bladder failed during testing of R-22 in the .278" i.d. tube. The last set of data presented in this study were collected with R-32/R-125 in the .278" i.d. tube. Since supplies of this fluid were scarce, an alternate method of pressure control was used. This consisted of placing a refrigerant bottle in a temperature controlled bath, and connecting this bottle to a charging valve on the loop. Two-phase refrigerant was maintained in the bottle, thereby allowing its temperature to set the working pressure for the loop in a manner similar to the bladder accumulator. This method provided excellent pressure control, and a modified version of it is now in place on the refrigerant loop. Since this new configuration was not used for any of the data described herein, its description is left to the thesis of Gaibel [1994].

3.2 Water Loop

The refrigerant in the test-condenser and aftercondenser is cooled with water from the building supply. The purpose of the water loop is to supply water for these processes at appropriate temperatures and flow rates to transfer the required amount of heat. The water loop is shown schematically in Fig. 3.3.

To cool the refrigerant in the test-condenser, water flows as indicated schematically in Fig. 3.3. After entering from the building supply, its flow rate is measured approximately by a 0-1 gal/min rotameter. It is then heated in a single-pass heat exchanger by a 5120 Btu/hr variac controlled heating element. After exiting the test-condenser, the water is discharged into a holding tank through a plastic tube. This holding tank is periodically emptied into the building waste line by a centrifugal pump controlled by a float actuated switch. When heat transfer data are collected, the flow rate of the water is determined by collecting a timed sample using a graduated cylinder and stopwatch. The mass flow rate is currently measured by weighing the cylinder before and after the sample is collected on a precision scale. During earlier experiments, the volumetric flow rate was measured and converted to a mass flow rate by multiplying by the density of water. Although measuring the mass flow rate directly yields lower values of experimental uncertainty, comparisons made between the two methods differed by less than 0.7%.

Two needle valves in the water line are available to control the flow rate and pressure. The valve directly before the water exit is adjusted at the beginning of testing to set the pressure in the annulus of the test-condenser to the desired level. Once the pressure is set, a needle valve at the inlet of the rotameter is used to control the water flow rate.

The operating pressure in the annulus of the test-condenser is an important parameter in some cases. Increasing this pressure increases the solubility of dissolved air in the water, keeping it from coming out of solution in the test-condenser where it can potentially form air pockets over thermocouple locations. Unfortunately, it also increases the tendency for water leaks. In the .123" i.d. test-section, observations of water flow before the annulus was insulated indicated that a pressure of at least 10 psig was necessary to keep the air from coming out of solution. The operating pressure was accordingly maintained between 10 and 20 psig while using this test-section. Similar observations in the .278" i.d. test-section revealed little tendency for air pockets to form in the annulus regardless of the pressure, probably because of decreased pressure drop through the mixers. This allowed the operating pressure in this test-section to be maintained between 5 and 10 psi, resulting in fewer leaks.

The purpose of the aftercondenser is to transfer sufficient heat to bring the refrigerant back to a subcooled liquid state. Since the amount of heat transfer necessary to accomplish this is irrelevant in the data reduction procedures, the water flow rate through this component is not recorded. This allows the water in the aftercondenser to be run in a closed loop from the building supply line to the building waste line, without requiring a holding tank and waste pump.

3.3 Test-Condensers

The heat transfer data reported herein were collected in three separate test-sections of .123", .180" and .278" inner diameters. Characteristics that are common to all of these test-sections are discussed first, followed by geometric data that are specific to each test-section.

The test-condensers in this study simulated a single horizontal tube in a condenser, providing heat transfer and pressure drop data under a range of conditions that included those experienced by condensers in a variety of refrigeration applications. They were cooled by water flowing countercurrently through a concentric annular tube. At various axial and circumferential locations along the tube wall, thermocouples were soldered into machined grooves and mounted so that they did not protrude into the water flow. This arrangement provided an accurate measurement of the outer tube wall temperature, with minimal fin effects since the thermocouple did not extend into the thermal boundary layer of the water.

The technique for soldering the wall thermocouples became progressively better with each test-section. First, the thermocouple grooves were cleaned with a solvent and a cotton swab. A small amount of solder was melted in the groove before installing the thermocouples to guarantee good metallic contact. All thermocouples at each axial location were then placed in the grooves and secured with tightly wound wire strips. A small quantity of flux was applied near each of the thermocouple beads, and solder shavings were placed in the flux. The tube was heated uniformly a few inches from the thermocouple beads until the solder melted. Using a magnifying glass to enhance the visibility, the solder was sanded until it was flush with the rest of the tube. A small amount of thermally conductive epoxy was applied with toothpicks to cover any bare thermocouple wire. This epoxy also proved helpful in reducing the tendency of water to wick through the thermocouple insulation.

To provide an indication of the saturation temperature, additional grooves were machined into the tube about 6" before and after the test-condenser. Since these sections were adiabatic and the tube was well insulated, the temperature reading at these locations provided a non-intrusive method of measuring the saturation temperature. Validation of this technique is provided in Chapter 4.

Static pressure taps were installed at two to three locations along the length of each condenser. These taps were constructed by drilling a 1/8" hole into a copper union and brazing a 1/8" o.d. piece of copper tubing inside the hole. The center rim inside the union was filed so that the fitting could be positioned at the desired location on the tube. It was then soldered to the test-section with a low temperature solder. Finally, a 1/32" o.d. drill bit was used to drill through the tap and the test-section. The metal burr inside the test-section was carefully removed with a file to minimize flow disturbances around the pressure measurement location. A drawing of a pressure tap used for the .278" i.d. tube is provided in Fig. 3.4.

The annuli for all of the test-sections were made of transparent plastic to aid in the construction process. At various locations along the length of the tube, plastic disks with holes drilled in them were inserted between the test-condenser and the inner wall of the annulus and bonded to the tube wall with a thin layer of epoxy. These disks mixed the water flow, preventing temperature stratification and enhancing water side heat transfer. The wires from the thermocouples that measured the test-condenser wall temperatures were removed from the annulus through tees. Sealing these tees from water leaks was difficult. First, the leg of the tees through which the wires passed was filled with epoxy. Next, a straight section of clear plastic tubing around 4" in length was inserted into the open leg of the tee and slit down its axis so that the thermocouple wires could be inserted in it. It was then filled with epoxy using a syringe. This extra length of mating surface between the wires and the epoxy helped inhibit leaks. In some cases, reducing couplings were added to the end of the plastic tubing to provide extra sealing ability.

The first test-condenser in which data for this study were collected was a .180" i.d. tube described by Hinde et al. [1992]. Figure 3.5 is a schematic of this test-section. Several features of this test-section are noteworthy. First, it had two separate water circuits and could be used to determine two heat transfer coefficients per experiment. At all wall thermocouple stations except the inlet and outlet, the temperature was measured at the top and bottom of the tube only. At the inlet and outlet wall thermocouple stations, temperatures were measured at angles of 0°, 60°, 120°, and 180° from the top of the tube. Differential pressure was measured across the entire test-condenser, not across each individual test-section. Since there was no separation between the two test-sections, saturation temperature measurements were available only at the inlet of the first test-section and the outlet of the second test-section.

Several problems were encountered with this first test-section, primarily due to problems with the wall thermocouple installation technique. First, several of the thermocouple wires were broken. At some axial locations, significant deviations in the circumferential wall temperature field were also observed. The direction of these deviations was indicative of some wall thermocouples protruding into the water flow. Later analysis of the heat transfer data from this tube gave heat transfer coefficients that were consistently 20% lower than expected based on either single-phase or two-phase heat transfer correlations. These data were not used to develop the heat transfer correlations presented in this study, although the trends were similar to later observations.

The second test-condenser in which data for this study were collected was a .123" i.d. tube shown in Figure 3.6. Again, several features of this test-condenser are worthy of discussion. It had two water circuits, like the .180" i.d. test-section, but these circuits were separated by about 6" Surface thermocouples and a pressure tap were installed in this length, providing differential pressure measurements across each test-section and an intermediate saturation temperature measurement. An error in construction resulted in solder blocking the tube at the first pressure tap, which had to be drilled out. This roughened the tube and disturbed the flow in the vicinity of this pressure tap, resulting in enhanced pressure drop and heat transfer in the first test-section. For this reason, the first test-section was not used for either heat transfer or pressure drop measurements. The wall temperature measurements along its length provided redundant verification of the inlet saturation temperature to the second test-section, since the first test-section served as a long adiabatic section. Since the tube diameter was so small, surface temperature measurements were only made at the top and bottom of the tube. The wall temperature field measured in this tube was significantly improved over that in the .180" i.d. tube.

The third and final test-section for which data are reported herein was a .278" i.d. smooth copper tube which is depicted in Fig. 3.7. It included several improvements over previous designs. To simplify construction, only one cooling water circuit was used. The region that would have previously been used for a first test-section was used to collect adiabatic pressure drop data, providing additional data from which to verify or refine pressure drop correlations. Two sets of grooved wall thermocouple stations were included in this length, providing an indication of the inlet saturation temperature. The wall thermocouple measurement stations in the test-condenser were spaced closer than in previous designs, and at each station the wall temperature was measured at four circumferential locations (0°, 60°, 180°, and 240°). An additional set of water temperature measurements was included at the inlet and outlet of the test-section, providing a redundant check of the water side heat transfer rate.

3.4 Instrumentation

The measurement devices used in this study included thermocouples, absolute pressure transducers, differential pressure transducers, watt-hour transducers, and flow meters. These devices are discussed separately.

3.4.1 Temperature measurements

All temperature measurements in this study were made with type-T, copper-constantan, thermocouples. In general, a separate spool of wire was used for each new test-condenser. Differential thermocouples referenced to an ice-bath were made with several samples from each spool of wire, and were calibrated over a range of 32-176 °F in an isothermal bath using NIST-traceable thermometers with an uncertainty of 0.09 °F. Separate calibration curves were developed for each spool of wire. These curves were able to predict the measured temperature within ±0.2 °F.

The measurement methods for the various refrigerant temperatures are summarized in Table 3.1. Two different methods were used. Most measurements were made by installing the thermocouples inside .126" o.d. stainless steel protection tubes from Omega. These tubes projected a minimum of 4" into the refrigerant flow, and were filled with either oil or thermal grease to aid in their transient response. On the test-condenser, the refrigerant temperature was measured by soldering thermocouples into grooves on the surface. These thermocouples were mounted in adiabatic sections and extensively insulated. They had two primary advantages over thermocouples mounted in wells. First, they did not require an elbow to be installed and were therefore easier to mount. Second, since they were non-intrusive they did not accelerate or decelerate the two-phase flow (thereby changing the temperature) like a probe.

The measurement techniques for the water temperatures are summarized in Table 3.2. The most critical water temperature measurements were those at the inlet and outlet of the test-section, since they determined the heat transfer rate for the two-phase experiments. These measurements were made with type-T thermocouple probes that directly exposed the thermocouple bead to the water. These probes were made by crimping the ends of 1/8" o.d. brass tubing tightly around a pre-welded thermocouple wire and sealing the end of the tube from water leaks with low temperature solder. Once constructed, the accuracy of these probes was verified by checking their readings against the NIST-traceable precision thermometers in the isothermal bath at several temperatures. In all cases, their readings deviated from those of the thermometer by less than 0.2 °F. In both the .123" i.d. and .278" i.d. tubes, two sets of thermocouples were used at the test-section inlet and outlet to provide a redundant check of the temperature difference. The two sets of temperature differences were always within 0.09 °F and were within 0.05 °F over 72% of the time for a sample of 100 randomly selected points. The water temperatures were measured at the inlet and outlet of the aftercondenser with type-T thermocouple probes mounted in oil-filled wells. These readings were not used in the data reduction procedures, although they were archived.

3.4.2 Absolute pressure measurements

Absolute pressure was measured throughout the refrigerant loop with strain-gage type pressure transducers. The range and type of each pressure transducer is summarized in Table 3.3. The most critical pressure measurements were those at the inlet of the test-condenser. There, both a 300 psi and a 500 psi transducer were installed. These transducers were both manufactured by BEC, and were calibrated together on a dead weight tester over their range of applicability. Linear calibration curves that were fit to the data matched the measured values to within ±0.3 psi. Day to day shifts were observed once these transducers were installed in the refrigerant loop, though, and caused the uncertainty estimate to be increased to ±1 psi. The primary purpose of these two pressure transducers was to verify agreement between the saturation temperature based on pressure and the measured temperature. During single-phase testing, they were also used to compute the refrigerant enthalpy from equations of state.

Absolute pressure was also measured at the heater inlet, test-section outlet, and aftercondenser outlet with 0-1000 psi transducers from Setra. Of these measurements, only the pressure at the heater inlet was used in the data reduction procedures. The other transducers were used primarily for detecting leaks while the loop was charged with nitrogen. The fact that these were not critical measurements was fortunate since the zero reading of these transducers was found to shift significantly from day to day. Although the slope of the transducers was very constant, their uncertainty was estimated at ±5 psi.

Table 3.1 Refrigerant temperature measurement summary

Location	Installation Method	Use	Uncertainty
Heater inlet	Oil-filled thermocouple well	Calculate heater inlet enthalpy	±0.5 °F
Adiabatic section inlet	Oil-filled thermocouple well	Calculate test-section inlet enthalpy for 1-phase tests	±0.4 °F
Adiabatic section inlet (6"past sight glass)	Soldered into grooves on wall and insulated	Redundant check of surrounding measurements	±0.4 °F
Adiabatic section outlet (6" before test-section)	Soldered into grooves on wall and insulated	Measure T_{sat} at the test-section inlet	±0.4 °F
Test section outlet (6" after outlet, before sight glass)	Soldered into grooves on wall and insulated	1).Redundant check of T_{sat} at test-section outlet 2). Redundant check of surrounding measurements	±0.4 °F
Test section outlet (after sight glass)	Oil-filled thermocouple well	1). Estimate enthalpy during 1-phase tests 2). Redundant check of T_{sat} at test-section outlet	±0.4 °F
Aftercondenser outlet	Soldered onto the wall and insulated	Assess effectiveness of the aftercondenser (no quantitative use)	±1.8 °F

Table 3.2 Water temperature measurement summary

Location	Installation Method	Use	Uncertainty
Test-section inlet	Thermocouple well with direct bead exposure	Compute water side heat transfer rate	±0.2 °F
Test-section outlet	Thermocouple well with direct bead exposure	Compute water side heat transfer rate	±0.2 °F
Aftercondenser inlet	Oil-filled thermocouple well	Archived, but not used for calculations	±0.5 °F
Aftercondenser outlet	Oil-filled thermocouple well	Archived, but not used for calculations	±0.5 °F

Table 3.3 Absolute pressure transducer readings summary

Location	Range	Output	Use	Uncertainty
Heater Inlet	0-1000 psi	0-5 VDC	Calculate heater inlet enthalpy	±5 psi
Test Section Inlet	0-300 psi	2-10 VDC from 4-20 mA	Calculate test-section inlet enthalpy, check T_{sat}	±1 psi
Test Section Inlet	0-500 psi	0-5 VDC	Calculate test-section inlet enthalpy, check T_{sat}	±1 psi
Test Section Outlet	0-1000 psi	0-5 VDC	Check for leaks	±5 psi
Aftercondenser Outlet	0-1000 psi	0-5 VDC	Check for leaks	±5 psi

3.4.3 Differential pressure measurements

The pressure drop across each of the test-condensers was measured with strain-gage type differential pressure transducers. Different combinations of transducers were used for experiments in the different tubes.

Pressure drop in the .180" i.d. test-condenser was originally measured with a 0-15 psi transducer from Sensotec which had a 0-20 mV output. The uncertainty of this transducer was estimated as 0.2 psi. This was the only differential pressure transducer used for the experiments with R-134a and R-12 in the .180" i.d. tube. For the experiments using R-22 and R-32/R-125 in this tube, a 0-5 psi transducer from Sensotec was installed in parallel with the 0-15 psi transducer. This transducer also had a 0-20 mV output, but was calibrated with an in-line amplifier from Sensotec that amplified its signal to a 0-5 V range. This transducer was used to measure the pressure drop for all experiments within its range, while the higher range transducer was used for readings above 5 psi.

Pressure drop in both the .123" i.d. and .278" i.d. tubes was measured with two 0-5 psi transducers from Sensotec. One transducer was used across the adiabatic section, and one transducer was used across the diabatic section. Both transducers had a 0-5 V output and an estimated uncertainty of ±0.07 psi. In the .278" i.d. tube, a 0-1 psi transducer from Setra was added in parallel with the other transducer in the adiabatic section for added resolution at low values of pressure drop. The uncertainty of this transducer was estimated as ±0.03 psi.

Table 3.4 Differential pressure measurement summary

Range	Tubes Used In	Output	Uncertainty
0-15 psi	.180"	0-20 mV	±.15 psi
0-5 psi	All	0-5 V	±0.07 psi
0-5 psi	.123" and .278"	0-20 mV	±0.07 psi
0-1 psi	.278"	2-10 V from 4-20 mA	±0.03 psi

3.4.4 Power measurements

The power input into the refrigerant heater was measured using two watt-hour transducers from Ohio Semitronics. One transducer measured the power input into the nine heaters that were controlled by the variac, while the other transducer measured the power input into the remaining eleven heaters. These transducers both produced a pulse output for each 9.5×10^{-5} Btu of energy input. These pulses were counted over the monitored period and divided by the elapsed time to yield a power measurement. The uncertainty of these devices was factory estimated at 0.2% of the reading. They were indirectly verified by energy balance checks across the refrigerant heater.

3.4.5 Flow rate measurements

Two flow meters were used to monitor the refrigerant flow rate. For flow rates below 0.033 lb/s, a Micro Motion D6 mass flow meter was used. This flow meter provided a 0-10 V output and an uncertainty of ±0.1% of the reading.

For higher flow rates, a positive displacement flow meter from Max Machinery was used to measure the volumetric flow rate. This flow meter also had a 0-10 V output, and an uncertainty of 0.31% of its full scale reading. The range of this flow meter was 0-0.13

ft^3/min, which corresponds to a mass flow range of approximately 0-0.15 lb/s with R-134a at 95 °F. The lowest flow rate at which this flow meter was used corresponded with the upper limit of the Micro Motion flow meter, which was over 20% of its full scale range. This was fortunate, since operation was avoided in the bottom 10% of the range of the flow meter where unmeasured slip could be important.

Early energy balance tests that were performed with the positive displacement flow meter indicated that its output might be slightly lower than the actual flow rate. This hypothesis was checked by calibrating the flow meter over its full range of operation against a Micro Motion D12 mass flow meter. This calibration revealed that the indicated flow rate was consistently lower than the flow rate measured by the Micro Motion meter by approximately 3%. This was accounted for by increasing the K-factor of the positive displacement meter by 3%. After this adjustment, the readings of the two meters differed by less than 0.5% across the full range of the calibration. When re-installed in the loop, the energy balance problems that had led to the original suspicions were resolved.

3.5 Data Acquisition

All data were logged into a Macintosh IIci computer using data acquisition hardware from National Instruments and Campbell Scientific. The data acquisition program was written using National Instruments LabView software. Figure 3.8 presents a schematic of the data acquisition system.

A National Instruments NB-MIO-16L data acquisition board that was installed in the Macintosh computer could measure up to eight analog input channels at sampling rates up to 40 kHz. This board was used to monitor the refrigerant flow rates and differential pressures, since these readings had relatively fast time response. These measurements were input into a CB-50 terminal block that was connected to the computer by a shielded 50 pin cable.

The serial port of the computer was connected to a Campbell Scientific 21X datalogger, allowing it to be polled every 10 seconds. This datalogger was connected to two Campbell Scientific AM64 multiplexers, providing the ability to read up to 64 analog signals in differential mode. The Campbell Scientific equipment was used to read all the thermocouples, since it provided excellent noise rejection with the low level signals. It was also used to read absolute pressure transducers, since these signals were normally very steady and required few points to obtain a good average.

The data acquisition program displayed all measured quantities on a graphical display in real time. In addition, secondary quantities such as refrigerant quality, heat transfer coefficient, and various dimensionless groups were output to the screen. This allowed the user to closely monitor system parameters until they reached target values.

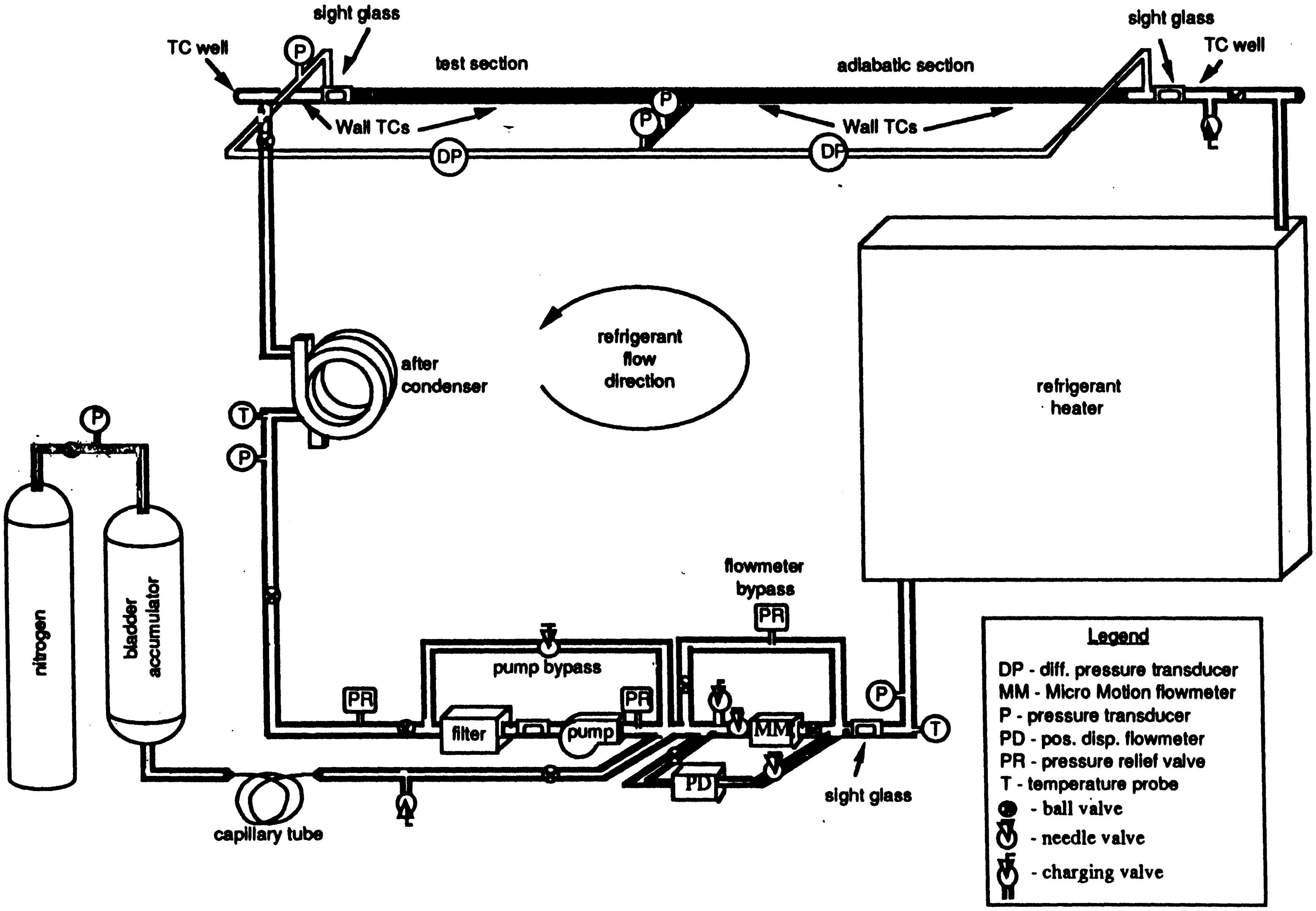

Figure 3.1 Schematic of the condensation test apparatus.

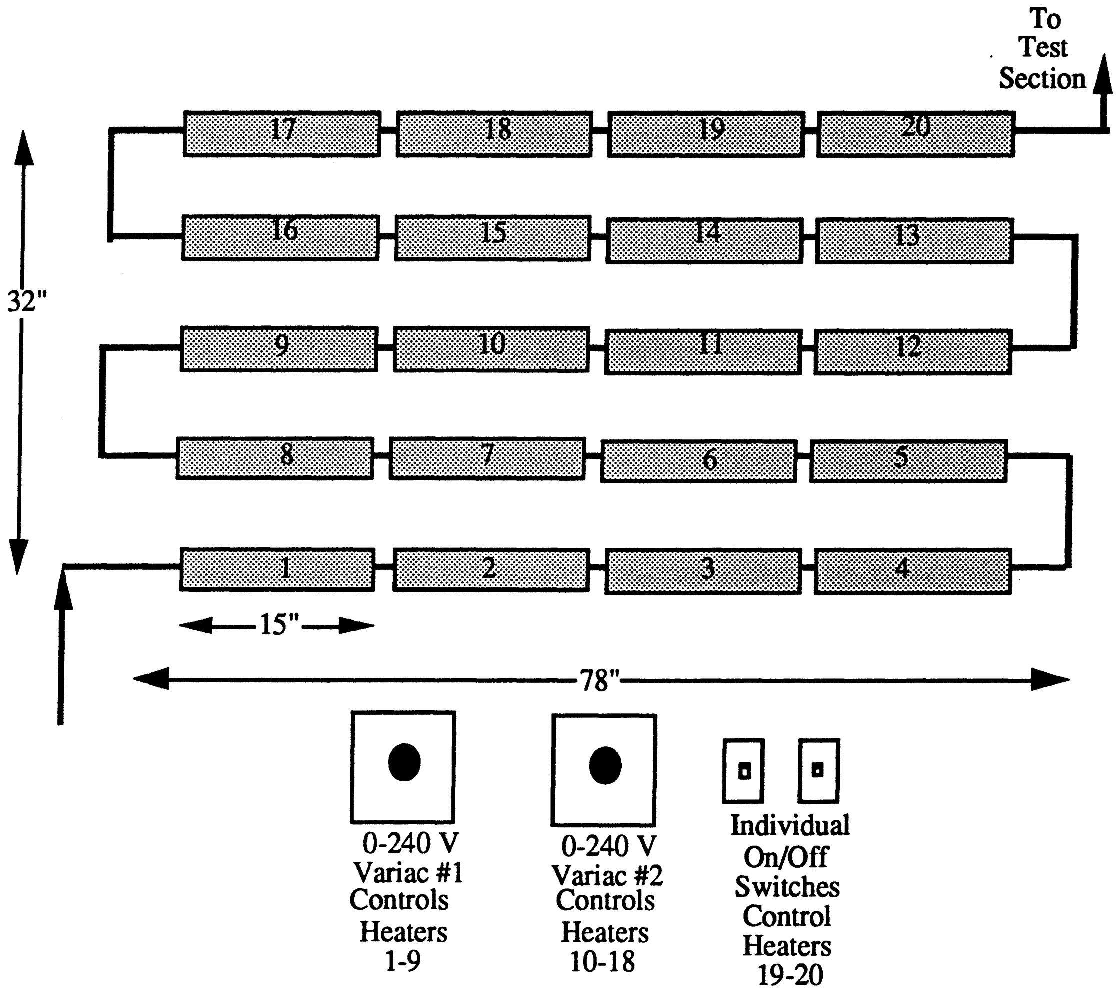

Figure 3.2 Schematic of the refrigerant heater.

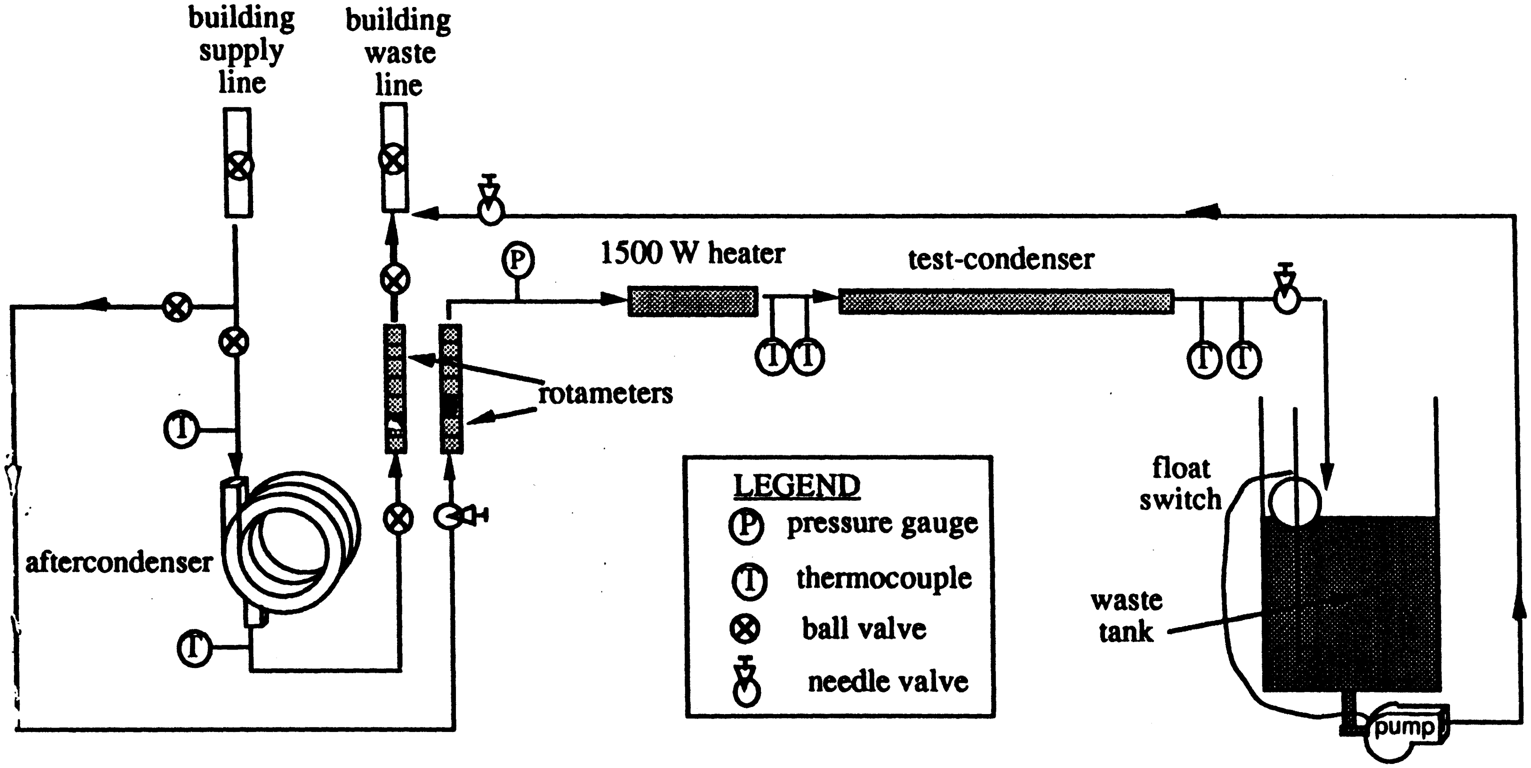

Figure 3.3 Schematic of the cooling water loop.

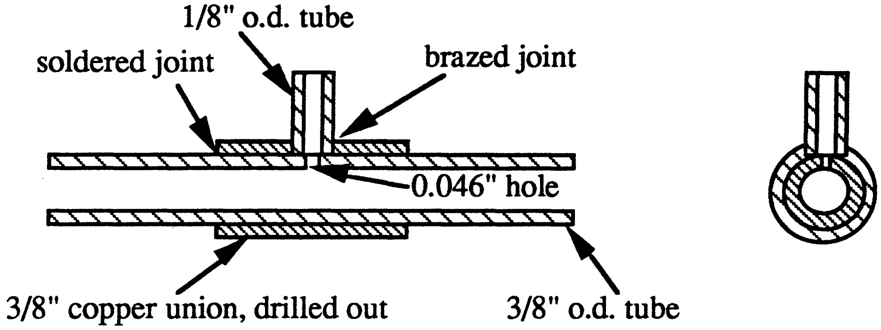

Figure 3.4 Schematic of pressure tap design for .278" i.d. tube.

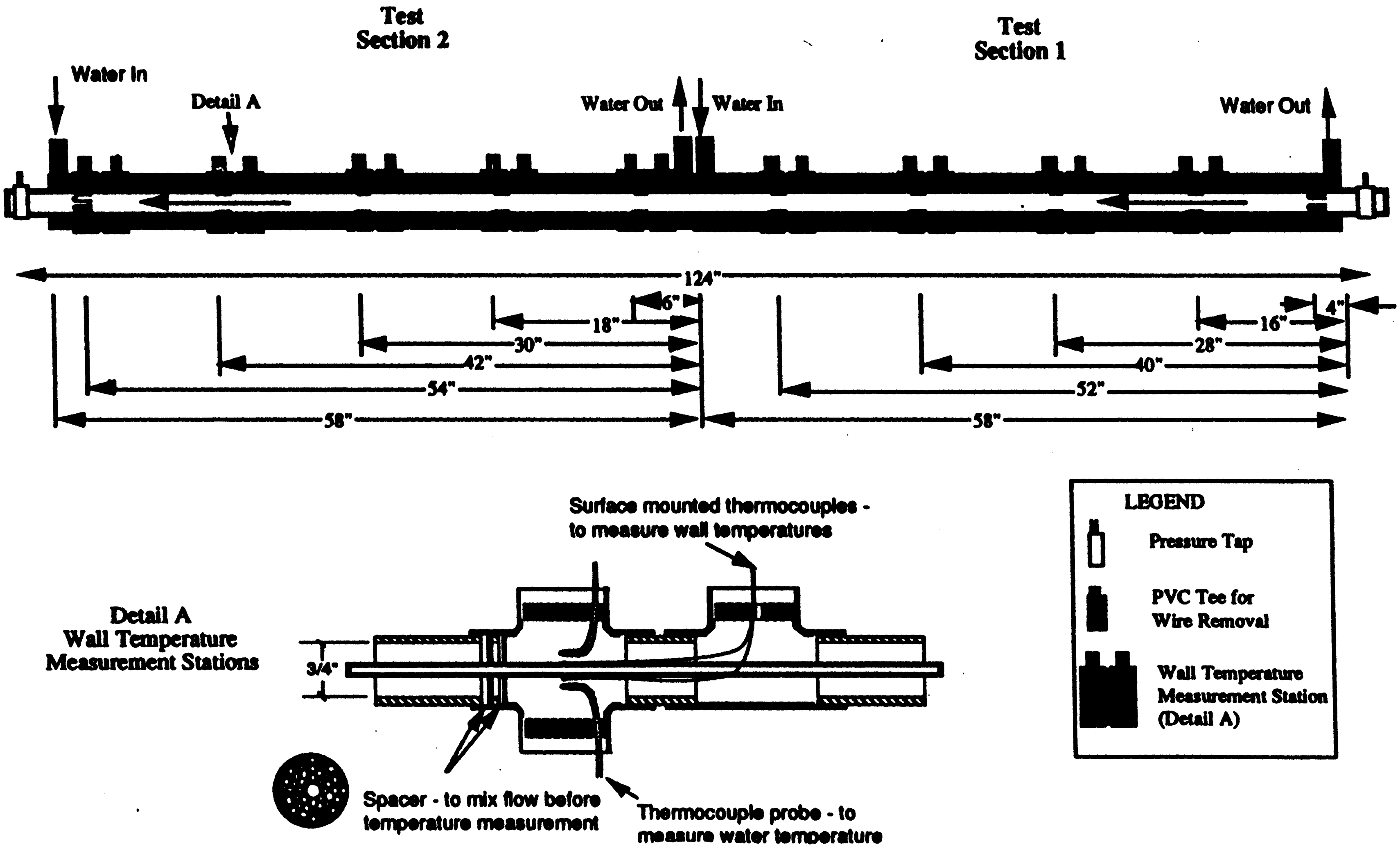

Figure 3.5 Schematic of the .180" i.d. test-section.

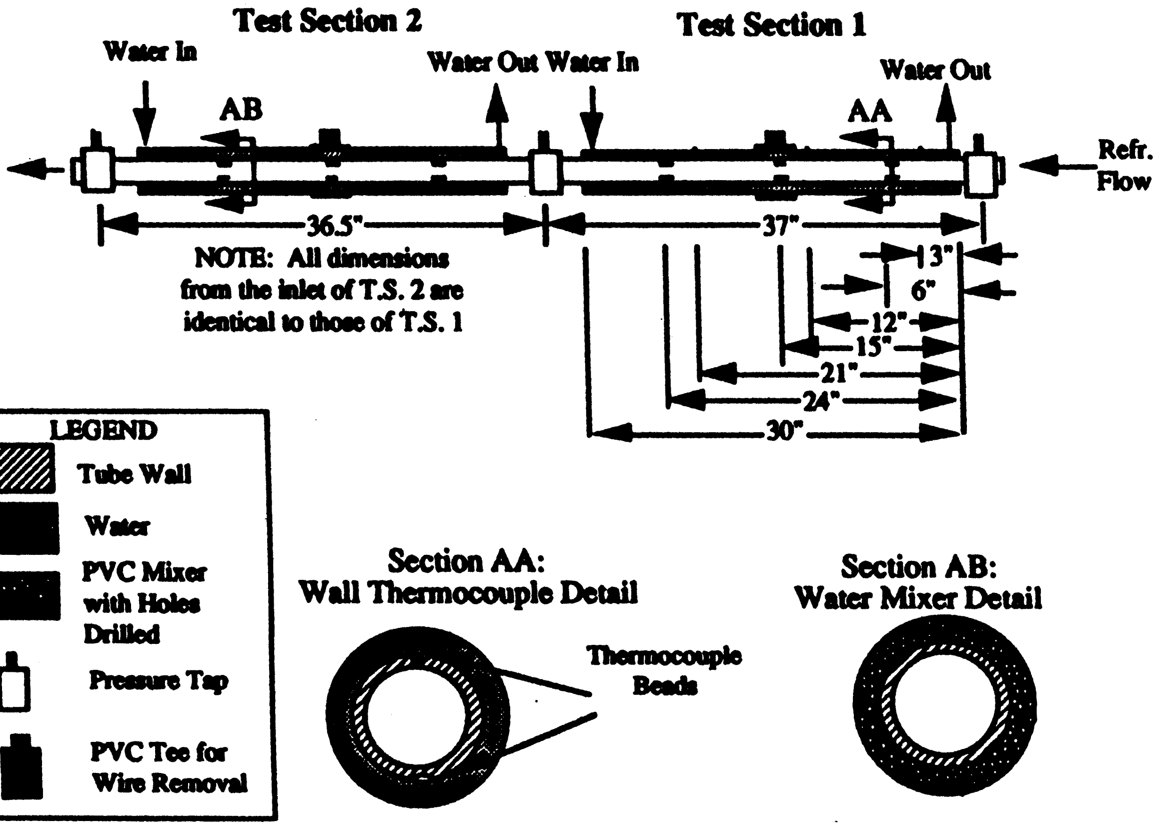

Figure 3.6 Schematic of the .123" i.d. test-section.

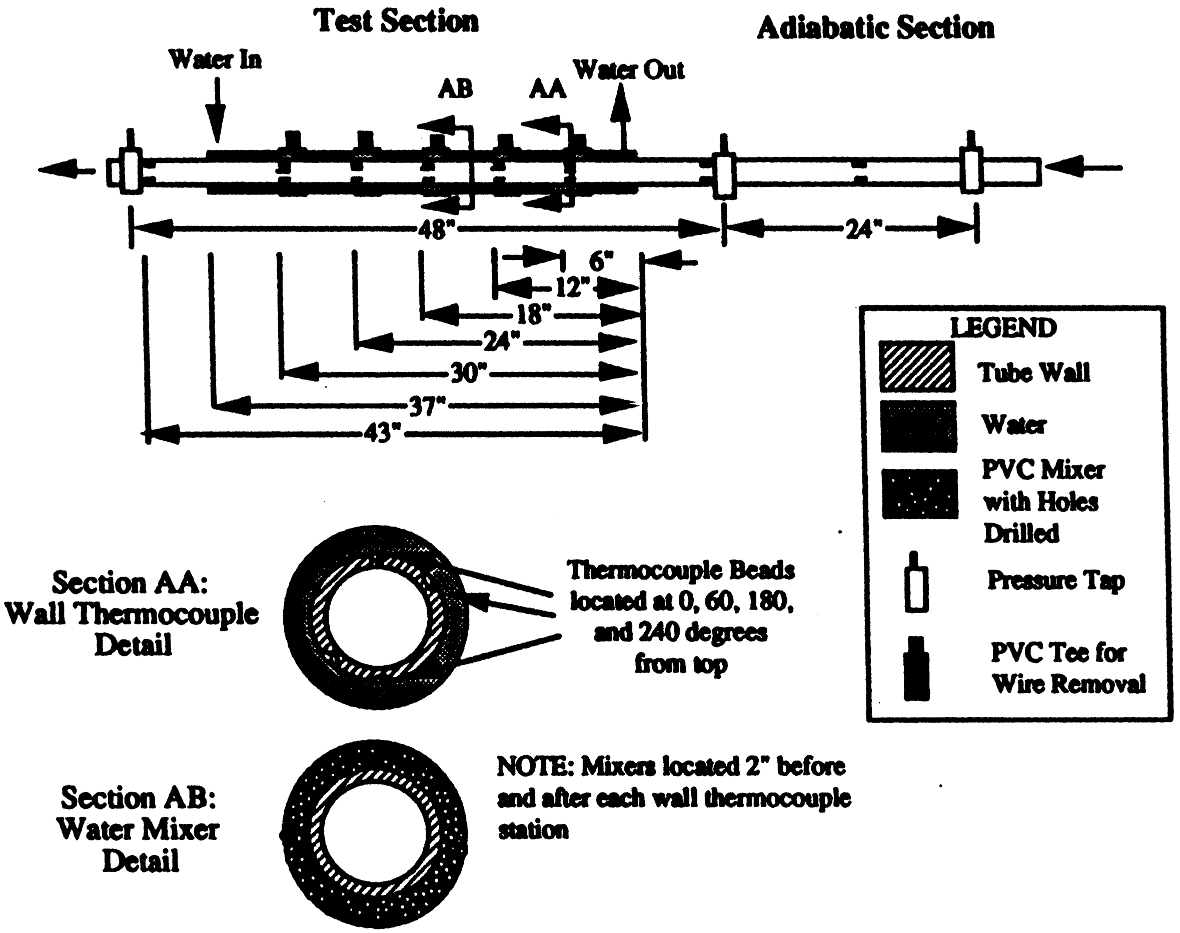

Figure 3.7 Schematic of the .278" i.d. test-section.

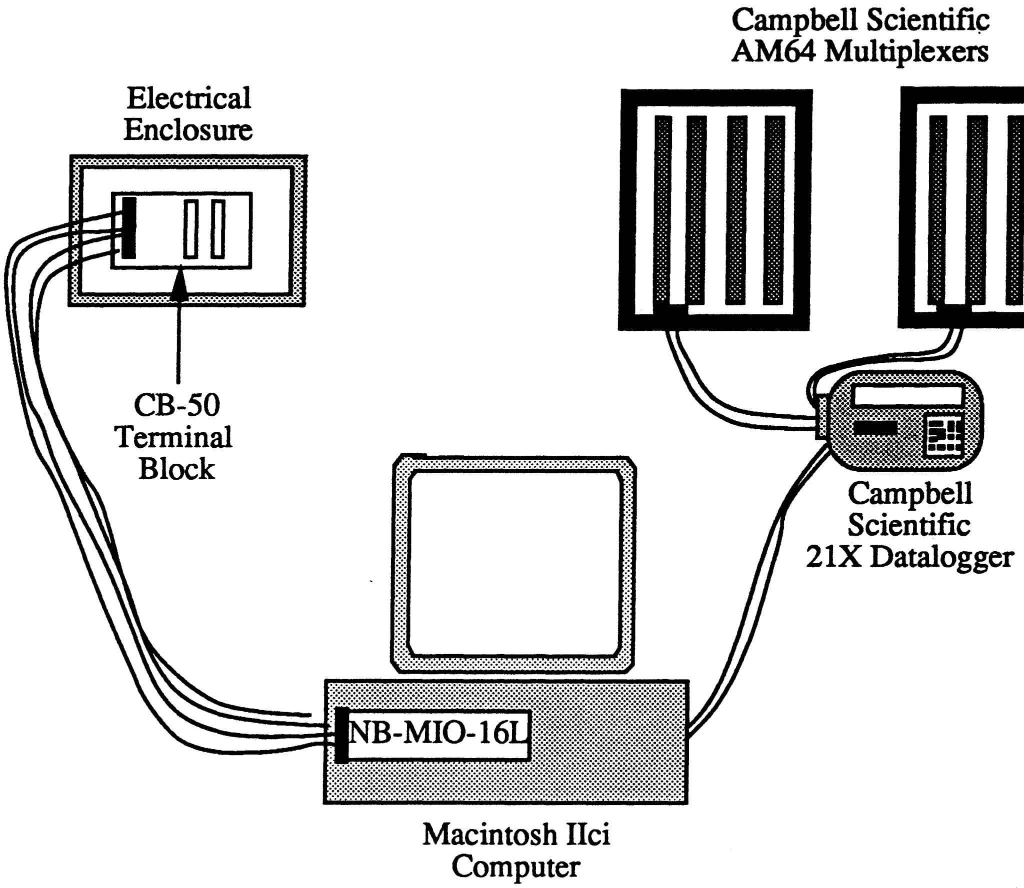

Figure 3.8 Schematic of the data acquisition system.

CHAPTER 4

EXPERIMENTAL PROCEDURES

This chapter describes the procedures used to collect and analyze the experimental data, and the range over which these data were collected. Section 4.1 discusses operation of the experimental facility, including preparation of the facility for testing and procedures used for data collection. Section 4.2 describes the methods used to calculate single and two-phase heat transfer coefficients from the raw data, selected analyses to correct for experimental errors, and calculation of experimental uncertainties. Validation procedures used to ensure that the system and instrumentation were operating properly prior to two-phase testing are discussed in Section 4.3. The range of experimental conditions over which data were collected is described in Section 4.4.

4.1 System Operation

Operation of the experimental system was preceded by a series of rigorous procedures to ensure the integrity of the experimental data. These procedures, including system evacuation, leak testing, and charging, are discussed in Section 4.1.1. This is followed by a discussion of the procedures used to collect single-phase and two-phase experimental data in Section 4.1.2.

4.1.1 System preparation

After a new test-condenser was installed or after testing was completed with a particular refrigerant, it was necessary to evacuate the loop and verify that no leaks were present in the system. First, the refrigerant loop was filled with compressed nitrogen to a pressure around 400 psi. Next, ball valves throughout the loop were shut so that the loop was divided into three sections in which the pressure could be monitored. If the pressure in any of these sections decreased more than would be expected based on temperature variations, that section was searched for leaks using a soapy water solution. Leaks were most commonly found either at threaded fittings or at compression fittings. When detected, leaks at threaded fittings were repaired by re-applying teflon tape and leaks at compression fittings were repaired by tightening and/or replacing the ferrules. Leaks at soldered connections were rare.

Once the system was deemed leak-free based on the high pressure nitrogen tests, a vacuum pump was used to evacuate the system for a minimum of four hours. The vacuum pump was normally shut off at the end of the day and the system was left evacuated overnight. The system pressure the following morning was compared to that of the previous night, providing another opportunity to check for leaks. Although the pressure difference across the loop in an evacuated state was substantially less than that during the high-pressure nitrogen tests, there were occasions when leaks were found in an evacuated state that were not detected in the high-pressure tests. If the system pressure had risen more than 0.3 psi overnight, the refrigerant loop was once again divided into compartments using ball valves so that the location of the leak could be narrowed. The leaks were then searched for again, using either the high-pressure nitrogen tests described above or a refrigerant leak detector and a small amount of refrigerant vapor.

Once the system had been evacuated and deemed leak-free, it was charged with the desired refrigerant. Several precautions were taken prior to this charging. First, a check was made to ensure that all the valves in the system were open. This prevented any unwanted air or refrigerant from being trapped in a compartment of the refrigerant loop that might later be opened and contaminate the charge. Second, the hose that was used for charging was filled with vapor prior to connecting it to the loop to guarantee that no unwanted air entered the apparatus. Once the hose was filled, the refrigerant bottle was inverted so that the loop was charged with liquid rather than vapor. A sufficient pressure difference for driving the refrigerant from the bottle into the loop was generated by simultaneously heating the bottle with a heat gun and cooling the loop with cold water in the aftercondenser and test-condenser. After 10 to 30 minutes, the loop was normally filled with the 7.5 to 9 lb_m of refrigerant that was required. At this point, the bladder was still fully extended and no refrigerant was in the accumulator. The nitrogen pressure in the accumulator was then decreased slightly below the pressure of the loop so that it began to fill with a small quantity of refrigerant. Proper execution of this step was verified by increasing the pressure in the accumulator above that in the loop. When a sufficient quantity of refrigerant was present, the pressure in the loop increased along with that in the accumulator. The charging process was continued until the accumulator functioned properly.

4.1.2 Data collection procedures

Before operating the experimental facility, several procedures were undertaken to guarantee that the various components were functioning properly. After the data acquisition program was turned on, temperature and pressure readings throughout the loop were checked for consistency. The ice-bath that was used for indirectly referencing the thermocouple readings was emptied, then filled with crushed ice and a small amount of water. The refrigerant pump was turned on, the data acquisition program set to work with the flow meter that was appropriate for the desired flow rate, and then observed to make sure that the pump was operating properly. Once the supply and waste water lines were opened, water flow was started through the aftercondenser and test-condenser. Finally, the pressure in the accumulator was set to a level that was appropriate for the desired saturation temperature.

The parameters that were controlled during experiments differed slightly for single-phase and two-phase tests. For single-phase tests, the primary items that were controlled were the refrigerant mass flux and inlet temperature. For two-phase tests, the parameters that were controlled were the saturation temperature, mass flux, inlet quality, and wall to refrigerant temperature difference.

Before the first data point was collected, the system was observed closely to guarantee that steady-state conditions had been reached. This normally occurred after 30 to 60 minutes. During this transient period, several quantities tended to stabilize in a particular order. First, the temperature of the water entering the aftercondenser and test-condenser slowly stabilized as the large lines in the building were emptied of water that had occupied them overnight. Once these temperatures stabilized, the subcooled refrigerant temperature exiting the pump and entering the heater began to stabilize as the tubing and insulation reached their steady-state temperatures. The last item to stabilize was usually the refrigerant temperature at the inlet of the test-condenser, which slowly increased as the extensive insulation covering the heater increased in temperature. After this initial transient period was completed, system conditions could be altered fairly rapidly. The typical delay between collecting subsequent data points ranged from 10 to 25 minutes.

Before data were collected, the mass flux had to be within ±5% of its target value and the saturation temperature had to be within ±0.9 °F of its target value. When the wall to refrigerant temperature difference was controlled, it was maintained within a range of ±0.36 °F. When the system parameters remained within their target ranges for 2 to 3 minutes, data collection began. Data were logged to a tab-delimited output file for 3 to 5 minutes. During this time, the water flow rate was measured at least twice and the inlet and outlet flow regimes were recorded based on visual observations. If the operating parameters deviated outside the target range during this process, the system was allowed to re-stabilize and the data collection process was repeated. The procedures used to reduce the experimental data during post-processing are described in Section 4.2

4.2 Data Analysis

This section describes the procedures used to analyze the experimental data. The software procedures and data reduction equations that were used to reduce the raw experimental data to useful form are discussed in Section 4.2.1. The results of an analysis that assesses the impact of a sharp transition in the wall temperature near the test-section inlet and outlet is described in Section 4.2.2. The equations used to determine the uncertainty of the experimental heat transfer data are presented in Section 4.2.3.

4.2.1 Energy balance and heat transfer calculations

Once the experimental data were collected, they were reduced to a useful format using spreadsheet macros written in Microsoft Excel. Two spreadsheet files were written. The first file contained command macros that averaged the columns of data, calculated the quantities of interest from these average values, and formatted them into a readable format. A sample output sheet from the 0.278" i.d. test-section is included in Fig. 4.1. The second file contained function macros that computed thermophysical properties, flow regime predictors, and other items of interest. By writing the programs in this way, little time was needed to effect the required changes when a new test-section or a new refrigerant was installed. The sources of thermophysical properties used in the spreadsheets are discussed in Appendix A.

The refrigerant always entered the heater in a subcooled liquid state. Based on available temperature and pressure readings there, the inlet enthalpy was calculated as:

$$i_{h,i} = i_l(T_{h,i}) + \upsilon_l(T_{h,i})\big(P_{h,i} - P_{sat}(T_{h,i})\big) \tag{4.1}$$

A first law statement written across the refrigerant heater yields the following:

$$\dot{Q}_h - \dot{Q}_{l,h} = \dot{m}_r(i_{ts,i} - i_{h,i}) \tag{4.2}$$

For single-phase tests, all quantities in Eq. (4.2) were known except the heat loss, $\dot{Q}_{l,h}$. For two-phase tests, empirical expressions for the heat loss that were developed based on the single-phase tests were used so that the enthalpy at the inlet of the test-section, $i_{ts,i}$, could be calculated. The quality at the test-section inlet was then computed by:

$$x_{ts,i} = \frac{i_{ts,i} - i_l(T_{ts,i})}{i_{lv}(T_{ts,i})} \tag{4.3}$$

Figure 4.2 is a schematic showing the primary sources of energy transfer across the boundaries of the test-section. Three sources are included in addition to the usual sources of energy advection due to the refrigerant and water flow: (1) axial conduction through the copper refrigerant tube, (2) axial conduction through the plastic water annulus, and (3) spurious heat loss from the water to the environment. Treating both axial conduction terms as sources and the ambient heat exchange as a loss, the first law yields:

$$\dot{m}_w c_{p,w}(T_{w,i} - T_{w,o}) + \dot{m}_r(i_{r,i} - i_{r,o}) + \dot{Q}_{cond,i} + \dot{Q}_{cond,o} - \dot{Q}_{l,ts} = 0 \quad (4.4)$$

The impact of the two axial conduction terms will be discussed in Section 4.2.2. For the remainder of this section, these terms will be ignored as is customary in other similar studies [Traviss et al., 1973; Eckels and Pate, 1991]. If these terms are ignored, Eq. (4.4) can be rearranged to yield:

$$\underbrace{\dot{m}_r\left(i_{r,i} - i_{r,o}\right)}_{\dot{Q}_r} = \underbrace{\dot{m}_w c_{p,w}(T_{w,o} - T_{w,i})}_{\dot{Q}_w} + \dot{Q}_{l,ts} \quad (4.5)$$

During single-phase testing, both the energy loss of the refrigerant and the energy gain of the water could be directly calculated. This allowed the heat loss to the environment to be calculated, and based on a series of such tests empirical models for the heat loss were developed. During two-phase testing, the empirically developed heat loss expressions and the measured heat gain of the water were used in Eq. (4.5) to allow the refrigerant enthalpy at the outlet of the test-section to be calculated. The outlet quality, $x_{ts,o}$, was then computed in a way analogous to Eq. (4.3).

For two-phase experiments, the heat transfer coefficients were calculated by Newton's law of cooling:

$$h = \frac{\dot{Q}_r}{A_s(\overline{T}_{sat} - \overline{T}_s)} = \frac{\dot{m}_w c_{p,w}(T_{w,o} - T_{w,i}) + \dot{Q}_{l,ts}}{A_s(\overline{T}_{sat} - \overline{T}_s)} \quad (4.6)$$

The average wall temperature in Eq. (4.6) should be that of the inner wall, but the outer wall temperature was measured in this study. Although these temperatures were nearly identical because of the high conductivity of the copper wall, one-dimensional heat conduction calculations were used to correct for the small discrepancy. The resulting formula for the two-phase case gives:

$$h = \left[\frac{A_s(\overline{T}_{sat} - \overline{T}_s)}{\dot{m}_w c_{p,w}(T_{w,o} - T_{w,i}) + \dot{Q}_{l,ts}} - \frac{D_i}{2k_t}\ln\left(D_o/D_i\right)\right]^{-1} \quad (4.7)$$

The difference between the results of Eq. (4.6) and Eq. (4.7) was never greater than 2%.

The average saturation temperature across the test-section, $\overline{T}_{sat}$, was computed as follows:

$$\overline{T}_{sat} = T_{ts,i} - \left(\frac{dT}{dP}\right)_{sat}\frac{\Delta P}{2} \quad (4.8)$$

The inlet temperature used in Eq. (4.8) was the average of two thermocouples that were soldered into an adiabatic section of the tube wall about 6.0" before the test-section inlet. The readings of these thermocouples were within 0.09 °F of one another, and within 0.36 °F of the saturation temperature based on pressure. The outlet saturation temperature was inferred based on the pressure drop rather than using measured values because the temperature there was measured only 20 diameters downstream of the test-section outlet. It seemed unlikely that the liquid refrigerant that was subcooled in the test-section would reach thermodynamic equilibrium in such a short distance, particularly when the liquid fraction was high. In practice, though, the measured temperature at the test-section outlet agreed well with the value computed based on pressure drop except at very low qualities (<10%). The wall temperature in Eq. (4.7) was averaged both circumferentially and length-wise, with each thermocouple reading weighted based on the fraction of the surface area that it represented.

Computing the single-phase heat transfer coefficients was complicated by the fact that the refrigerant temperature neither remained constant nor varied in a linear fashion. This made it difficult to calculate the average refrigerant temperature, since the inlet and outlet values that were measured were not sufficient to construct the profile. This problem was remedied by dividing the test-section into elements for which the average wall temperature was measured and solving the resulting set of algebraic equations. A schematic of the situation that was modeled is shown in Fig. 4.3. For simplicity, the equations are derived for the case of the 0.123 " i.d. tube, where the wall temperature was measured at three locations only and each of these measurements represented one-third of the surface area. Conservation of energy statements for each of the three elements yield the following three equations:

$$\begin{aligned}
\dot{m}_r c_{p,r}\left(T_{r,in} - T_{r,1}\right) &= \frac{hA}{3}\left(\frac{T_{r,in} + T_{r,1}}{2} - T_{w,1}\right) \\
\dot{m}_r c_{p,r}\left(T_{r,1} - T_{r,2}\right) &= \frac{hA}{3}\left(\frac{T_{r,1} + T_{r,2}}{2} - T_{w,2}\right) \qquad \text{(4.9a-c)} \\
\dot{m}_r c_{p,r}\left(T_{r,2} - T_{r,out}\right) &= \frac{hA}{3}\left(\frac{T_{r,2} + T_{r,out}}{2} - T_{w,3}\right)
\end{aligned}$$

Equations (4.9a-c) are three nonlinear equations with three unknowns, one of which is the heat transfer coefficient. Equations can be constructed in an analogous manner for a situation with an arbitrary number and spacing of known wall temperatures. This procedure was carried out for single-phase tests in each test-section, and the resulting equations were solved with the *Engineering Equation Solver* (*EES*).

4.2.2 Axial conduction effects

As indicated in Eq. (4.3), axial conduction from the copper test-section and plastic annulus represent sources of energy transfer in addition to the desired sources of advection from the fluid streams. Due to the low conductivity of the plastic annuli used in this study and the fact that they experienced no steep temperature gradients near the inlet or outlet of the test-section, conduction through them was ignored. Making a similar assumption about the copper test-section was not necessarily justified, however. Far away from the test-section, adiabatic conditions prevailed resulting in the tube wall and the refrigerant being at the same temperature. Near the test-section inlet, however, the wall temperature made a transition from the refrigerant temperature to a value between it and the cooling water temperature. A schematic of the physical situation and the resulting temperature profile is presented in Fig. 4.4. Two primary aspects of this transition were of interest: (1) the extent to which the transition region affected the measured wall-temperature profile, and (2) the amount of heat that was conducted through the ends of the test-section.

Both issues mentioned above were addressed quantitatively by solving for the wall temperature profile in the regions before and within the test-section. A detailed analysis for this purpose is presented in Appendix B, while the most pertinent results are summarized here. It is shown in Appendix B that the dimensionless temperature profile depends on two nondimensional parameters. These parameters are:

$$\xi_i^2 = \mathrm{Bi}_i \frac{A_s}{A_t} = \frac{h_i L}{k_t} \frac{L/t}{\left(1 + t/D_i\right)} \tag{4.10}$$

$$\Gamma^2 = \frac{R_o'}{R_t'} = \frac{1/h_o D_o}{1/h_o D_o + 1/h_i D_i} \tag{4.11}$$

The first parameter, ζ_i, is the square root of product of the Biot number based on the half-length of the test-section and the ratio of the surface area to the area of the cross-section of the tube. Increasing either of these parameters decreases the effect of axial conduction relative to convection from the inner fluid. This can be accomplished by: (1) increasing the heat transfer coefficient, length, or inner diameter, or (2) decreasing the thickness or the conductivity of the tube. The second parameter, Γ, is the square root of the ratio of the outer thermal resistance to the total thermal resistance. This parameter governs the fully developed temperature profile, with high values of Γ corresponding to tube wall temperatures close to that of the inner fluid. High values of Γ would also be expected to decrease the axial conduction, since the tube wall would not undergo as steep a gradient at the ends of the test-section.

The full solution to the problem posed above is presented in Appendix B. This analysis was applied to three areas of interest in the present study: (1) whether the first location at which the test-section wall temperature was measured was inside the transition region, (2) the extent to which ignoring the transition region in the wall temperature measurements decreased the measured heat transfer coefficient, and (3) the extent to which undesired axial conduction inflated the measured heat transfer coefficients.

The calculations in Appendix B show that for all two-phase tests and most single-phase tests in this study, the first thermocouple station was outside of the transition region and therefore did not result in underprediction of the average temperature difference. This means that the measured wall temperature profile effectively ignored the short transition region, which in itself would produce measured heat transfer coefficients that were slightly lower than the true value. This effect was small (<5%) for the present study. The effect of axial conduction was to give measured heat transfer rates in the outer fluid that were higher than the convection from the inner fluid, resulting in measured heat transfer coefficients that were higher than the true value. Thus, these two errors tended to counteract one another.

These two effects were solved for analytically, and combined to calculate the ratio of the measured heat transfer coefficient to the true heat transfer coefficient. A plot of this ratio is shown in Fig. 4.6 for values of ζ_i from 10 to 100. At lower values of ζ_i, the error is greater than that shown in Fig. 4.6. However, at values of ζ_i lower than 10 wall temperature measurements themselves are biased and any data should be viewed with caution. For this reason, only heat transfer data that correspond to ζ_i greater than 10 are reported here. With these considerations in mind, it can be seen from Fig. 4.6 that the maximum effect of the two errors discussed above is 7% for $\zeta_i>10$. The lowest value of ζ_i for two-phase testing was slightly greater than 20, resulting in a maximum error of less than 3.5%. The largest errors occurred during single-phase testing, where the values of ζ_i ranged between 10 and 20. Some single-phase data at low mass fluxes were discarded because they had values of $\zeta_i<10$. All the data presented herein were corrected for these effects using the analysis outlined in Appendix B.

Before progressing to the next topic, it is worthwhile to discuss shortly why the test-sections were not designed such that both the axial conduction and wall temperature measurement errors were completely negligible. This could, in theory, be accomplished by using long, thin-walled tubing that would result in higher values of ζ_i. Unfortunately, such changes were contrary to other demands of the study. The use of long test-sections, for instance, would result in larger quality changes at a given cooling rate and therefore make it more difficult to obtain local data. The use of thin-walled tubing was impossible due to the simultaneous requirements of high operating pressures and machined grooves in the tube wall to allow temperature measurement. Given these constraints, correcting the measured data for the phenomena modeled above seemed to be the most prudent course of action.

4.2.3 Experimental uncertainties

Uncertainties in the experimental data were calculated using the familiar methods described by Moffat [1988]. The method estimates the uncertainty in a variable y that depends on N independent variables (x_i's) that can not be determined exactly. The equation for the uncertainty in y, δy:

$$\delta y = \sqrt{\sum_{i=1}^{N} \left(\frac{\partial y}{\partial x_i} \delta x_i \right)^2} \qquad (4.12)$$

The data from the present study were classified as single sample since the succession of readings during each experiment were collected using the same equipment, the same observer, and under identical conditions [ASHRAE Guidelines, 1986]. The uncertainty of each measured quantity consisted of the uncertainty of the measurement device, the uncertainty of the data-acquisition system, interactions between the sensor and the experimental system, and conceptual errors. Two uncertainties were of interest in the present study: (1) the uncertainty of the measured heat transfer coefficient, and (2) the uncertainty of the quality at the inlet and outlet of the test-section.

For the two-phase experiments, the heat transfer coefficient was calculated using Eq. (4.7) and corrected after the fact for the transition effects discussed in Section 4.3.2. All the components that contributed to uncertainty in this calculation, ranked in approximate order of importance, are listed below:

1. Wall temperature measurement
2. Saturation temperature measurement
3. Inlet and outlet water temperatures
4. Heat loss prediction
5. Surface area measurement
6. Water flow rate measurement
7. Prediction of transition region effects from Section 4.3.2
8. Prediction of the thermal resistance of the copper tube wall

In the strictest sense, the uncertainty calculations should include the uncertainty due to all these effects. Practically speaking, though, the root sum square method of combining the uncertainty components minimizes the effect of small uncertainties relative to larger uncertainties so greatly that second-order effects can be neglected with negligible loss of accuracy. With that in mind, the uncertainty in the seventh and eighth components listed above were neglected. The correction of the heat transfer coefficient due to transition region effects was always less than 3% for two-phase tests, so even a 20% uncertainty in this correction would affect the heat transfer coefficient by only 0.6%. The maximum correction as a result of the tube wall resistance was 2%, so modest errors in this correction would also result in a component uncertainty of well under 1%.

By reducing the number of components considered in the uncertainty analysis, it was possible to work with the simpler equation for the heat transfer coefficient given by Eq. (4.6). Using this equation to evaluate the necessary partial derivatives, the following expression was obtained for the fractional uncertainty:

$$\frac{\delta h}{h}=\left[\begin{array}{l}\dfrac{\left(\dot{m}_w c_{p,w}\right)^2\left(\delta T_{w,i}^2+\delta T_{w,o}^2\right)+\left(c_{p,w}\left(T_{w,o}-T_{w,i}\right)\right)^2\delta\dot{m}_w^2+\delta\dot{Q}_l^2}{\left(\dot{m}_w c_{p,w}\left(T_{w,o}-T_{w,i}\right)+\dot{Q}_l\right)^2}+\ldots \\ \dfrac{\delta T_{sat}^2+\delta T_s^2}{\left(T_{sat}-T_s\right)^2}+\left(\dfrac{\delta D_i}{D_i}\right)^2+\left(\dfrac{\delta L}{L}\right)^2\end{array}\right]^{0.5} \qquad (4.13)$$

Equation (4.13) provides considerable insight into the uncertainty of the heat transfer coefficient. The uncertainty in the saturation and wall temperature measurements are divided by temperature difference between them, each yielding a component uncertainty equal to the percentage uncertainty in the temperature difference. The uncertainty in the water side heat transfer rate and the rate of spurious heat loss are both divided by their sums. This indicates that when the heat loss makes up little of the overall heat transfer, even a large percentage uncertainty in its prediction results in little uncertainty in the heat transfer coefficient. This insight was extremely important for testing in the 0.123" i.d. tube, where the water side heat transfer rates were necessarily very small.

The uncertainty in the heat transfer coefficient was predominantly a result of uncertainties in the water, saturation, and surface (wall) temperatures. These temperatures were all measured with thermocouple wire that had been calibrated in a thermostatic bath using NIST traceable precision thermometers with an uncertainty of 0.09 °F. Separate calibration curves were fit to the data for each spool of wire. The predictions of these curves never deviated from the thermometer reading by more than 0.18 °F, and were usually within 0.09 °F. Thus, the uncertainty of the wire and data acquisition system alone was estimated as 0.18 °F. This value, which was the minimum uncertainty, was used as the uncertainty of the inlet and outlet water temperature measurements. This was because these measurements were made at a point with a flat radial temperature profile with probes that directly exposed the thermocouple bead to the water and protruded into the flow at least 300 thermocouple diameters. Thus, these measurements were relatively easy to make and subject to little conceptual error. The estimated uncertainty was validated by the excellent agreement in the water-side temperature differences measured by two sets of redundant probes. These two measured temperature differences were always within 0.09 °F of one another, and were within 0.05 °F of one another more than 72% of the time. The uncertainties in the saturation and wall temperature measurements were estimated at twice this value, or 0.36 °F. The saturation temperature readings were validated in two ways. First, the adiabatic wall temperature that was taken to be T_{sat} agreed with readings from an adjacent thermocouple probe which measured the vapor temperature within 0.18 °F except at very high mass fluxes, where acceleration of the flow by the probe brought its accuracy into question. Second, the agreement between both of these measured temperatures and the saturation temperature based on pressure readings was within 0.36 °F.

The uncertainty in the inferred heat loss is discussed in Section 4.3. For testing at a saturation temperature of 95 °F, the heat loss was only a few percent of the total heat transfer rate and contributed little to the overall uncertainty. Its impact was most important for low mass flux testing at high saturation temperatures, where heat loss sometimes contributed up to 15% of the total heat transfer rate.

The length was measured with a tape measure which had an uncertainty of only around 0.12". The diameter of each test-section was taken to be the value supplied by the commercial vendor. This value was verified using a dial caliper to within 0.002", which was taken as the uncertainty. These uncertainties contributed little to the overall uncertainty except for cases where both temperature differences were very high.

The water flow rate was determined by collecting a sample of water for a fixed amount of time. The time was measured with a stopwatch, and was estimated to have an uncertainty of ±0.2 s due to operator timing errors. For some tests, the volume of the sample was measured using a graduated cylinder with an uncertainty of $\pm 0.3 \text{ in}^3$. For other tests, the mass of the sample was measured with a scale that had an uncertainty of $\pm 2.2 \times 10^{-4} \text{ lb}_m$. The uncertainty was lower when the mass was measured directly, although the uncertainty in either method was never greater than 1.5%. For selected samples where both the mass and volume measurement techniques were used, they differed by less than 0.7%.

Uncertainty in the quality was computed similarly. The enthalpy entering the test-section was computed with a manipulated version of Eq. (4.2). Including the dominant[1] components that contribute to the uncertainty in this quantity yields:

$$\delta i_{TS,i} = \left[\begin{array}{l} \left(\left(\frac{\partial i_l}{\partial T}\right)^2 + \left(\upsilon_l \frac{\partial P_{sat}}{\partial T}\right)^2 \right) \delta T_{h,i}^2 + \left(\upsilon_l \, \delta P_{h,i}\right)^2 + \ldots \\ \frac{\delta \dot{Q}_h^2 + \delta \dot{Q}_{l,h}^2}{\dot{m}_r^2} + \left(\frac{\dot{Q}_h - \dot{Q}_{l,h}}{\dot{m}_r}\right)^2 \left(\frac{\delta \dot{m}_r}{\dot{m}_r}\right)^2 \end{array} \right]^{0.5} \qquad (4.14)$$

The uncertainty in the inlet quality is then given by:

$$\delta x_{ts,i} = \left[\frac{\delta i_{ts,i}^2 + \left(\frac{\partial i_l}{\partial T} \delta T_{ts,i}\right)^2}{i_{lv}^2(T_{ts,i})} + x_{ts,i}^2 \left(\frac{\partial i_{lv}/\partial T \, \delta T_{ts,i}}{i_{lv}(T_{ts,i})} \right)^2 \right]^{0.5} \qquad (4.15)$$

The uncertainty in the outlet enthalpy depends on the uncertainty in the inlet enthalpy, the heat transfer rate across the test-section, and the mass flow rate:

$$\delta i_{ts,o} = \left[\begin{array}{l} \frac{\left(\dot{m}_w c_{p,w}\right)^2 \left(\delta T_{w,o}^2 + \delta T_{w,i}^2\right) + c_{p,w}^2 \left(T_{w,o} - T_{w,i}\right)^2 \delta \dot{m}_w^2 + \delta \dot{Q}_{l,h}^2}{\dot{m}_r^2} + \ldots \\ + \delta i_{ts,i}^2 + \left(i_{ts,o} - i_{ts,i}\right)^2 \left(\frac{\delta \dot{m}_r}{\dot{m}_r}\right)^2 \end{array} \right]^{0.5} \qquad (4.16)$$

The uncertainty in the outlet quality was then computed based on the uncertainty in the inlet enthalpy and the uncertainty in the outlet temperature by the following equation:

$$\delta x_{ts,o} = \left[\frac{\delta i_{ts,o}^2 + \left(\frac{\partial i_l}{\partial T} \delta T_{ts,o}\right)^2}{i_{lv}^2(T_{ts,o})} + x_{ts,o}^2 \left(\frac{\partial i_{lv}/\partial T \, \delta T_{ts,o}}{i_{lv}(T_{ts,o})} \right)^2 \right]^{0.5} \qquad (4.17)$$

The uncertainty in the average quality was calculated based on the uncertainty in the inlet and outlet values:

$$\delta \overline{x}_{ts} = \sqrt{\delta x_{ts,i}^2 + \delta x_{ts,o}^2} \qquad (4.18)$$

---

[1] Uncertainty in the liquid specific volume due to temperature measurement was omitted

Most of the component uncertainties used for calculating the quality have been discussed previously with regard to the heat transfer coefficient uncertainty. The uncertainty in the temperature and pressure readings at the heater inlet was estimated at ±0.54 °F and ±5 psi, respectively. The uncertainty in the refrigerant mass flow rate was estimated at ±0.1% when the Micro Motion flowmeter was used, as recommended by the manufacturer. When the positive displacement flowmeter was used, the uncertainty in the refrigerant flow rate was estimated as ±0.75%. This value was estimated based on calibration against a higher range Micro Motion flowmeter. The uncertainty in the heat losses across the heater and the test-section are discussed and quantified in Section 4.3.

4.3 Single-Phase Data Validation Experiments

Single-phase liquid tests provided a valuable tool for verifying that the experimental equipment and instrumentation were functioning properly. First, single-phase testing allowed the refrigerant side enthalpies to be calculated directly based on temperature and pressure measurements. This allowed energy balances to be checked across the refrigerant heater and test-section. The existence of well verified single-phase heat transfer and pressure drop correlations to compare with the measured data allowed validation of the wall temperature and pressure drop measurements.

4.3.1 Energy balance testing

During single-phase testing, energy balances were checked across both the refrigerant heater and the test-section. Once it was confirmed that any apparent deviations in these energy balances were consistent with small heat losses or gains with the environment, simple empirical expressions were developed to predict the heat losses

The heat loss across the test-section, $\dot{Q}_{l,ts}$, was computed based on the difference between the energy lost from the refrigerant and that gained by the water using Eq. (4.5). When the water was warmer than room temperature, a small amount of the heat that it gained from the refrigerant was lost to the environment. This resulted in its measured heat gain being lower than the heat lost from the refrigerant. The opposite trend was observed when the water was cooler than room temperature. The amount of this heat loss was small, less than 37 Btu/hr for temperature differences of up to 27 °F. Since some of the tests had heat transfer rates of less than 341 Btu/hr, though, correlating the spurious heat exchange based on simple physical principles offered an opportunity to reduce the experimental uncertainty. This was accomplished by solving for an overall heat conductance, $UA_{l,ts}$, of the insulation. The model equation upon which this idea was based is:

$$\dot{Q}_{l,ts} = UA_{l,ts}(\overline{T}_w - T_a) \tag{4.19}$$

The overall conductance in Eq. (4.19) can be thought of in resistance terms as consisting of resistances due to convection from the water, conduction through the plastic annulus, conduction through the insulation, and free convection to the air. The dominant resistance in this network should be that of the insulation. Since this dominant resistance should be constant for a fairly wide range of temperatures, it is reasonable to expect a constant value of the overall conductance also.

The uncertainty in the inferred heat loss is composed of uncertainties in the refrigerant-side and water-side heat transfer rates:

$$\frac{\delta\dot{Q}_{l,ts}}{\dot{Q}_{l,ts}} = \left[\frac{\left(\frac{\delta\dot{Q}_r}{\dot{Q}_r}\right)^2}{\left(1-\frac{\dot{Q}_w}{\dot{Q}_r}\right)^2} + \frac{\left(\frac{\delta\dot{Q}_w}{\dot{Q}_w}\right)^2}{\left(1-\frac{\dot{Q}_r}{\dot{Q}_w}\right)^2} \right]^{0.5} \tag{4.20}$$

Equation (4.20) reveals the fundamental difficulty in determining the heat loss in an accurate manner. Even if the percentage uncertainties in the refrigerant and water side heat losses are small, they are divided by quantities that are much less than unity since the extensive insulation guarantees relatively small heat losses. As the heat loss approaches zero, the uncertainty in its determination becomes infinite. Although it is still useful to develop a heat loss model, Eq. (4.20) reveals *a priori* that only modest accuracy should be expected.

To determine the overall conductance, a series of single-phase heat loss tests were conducted in each tube. Some single-phase tests were conducted with each refrigerant as a validity check of the thermodynamic data, although most of the testing was performed with R-134a. For each refrigerant in each tube, a linear regression model was fit to the $\dot{Q}_{l,ts}$ versus $\left(\overline{T}_w - T_a\right)$ data, and the slope was taken as $UA_{l,ts}$. A zero-intercept was not forced to allow for small fixed errors that might bias either the water or refrigerant side heat transfer rates upward or downward. For each tube, the value of overall conductance used for data reduction purposes was the average of the values obtained with the different refrigerants.

The results of these single-phase heat loss tests are summarized in Table 4.1. For each tube, four quantities are listed. The first is the number of single-phase tests conducted in the tube, this being the sum of those using all the different refrigerants. The second value is the overall conductance that was estimated from these tests. The third column is the maximum heat loss from any of the tests expressed both in Btu/hr and as a percentage of the refrigerant-side heat transfer rate. The fourth column is the maximum difference between the predicted and measured heat loss values. This is the error that would have existed if the heat transfer was inferred based on the measured water-side heat transfer and the model predicted heat loss. This value is relevant because using the predicted heat loss and the measured water-side heat transfer rate is precisely what was done during two-phase testing.

Table 4.1 Summary of liquid heat loss data from test-sections

Tube i.d. [in]	# of Points	$UA_{l,ts}$ [Btu/hr-R]	$\dot{Q}_{l,ts,max}$ [Btu/hr]	Max Error [Btu/hr]
.123	12	1.33	30.7	13.6
.278	15	0.86	40.9	17.1

Heat loss to the environment from the refrigerant heater was also carefully monitored since neglecting this would result in overprediction of the quality throughout the loop. Techniques for predicting this heat loss evolved through the course of the experiments. In the 0.180" i.d. tube, two-phase testing at every mass flux and temperature was preceded by a liquid test and followed by a vapor test. The heat loss from the heater was calculated for each of these tests. The liquid heat loss was taken as the heat loss with a quality of zero, and the vapor heat loss was taken as the heat loss with a quality of one. Heat losses for two-phase tests were estimated based on linear interpolation between these values using the inlet quality to the test-section as the independent variable. In this tube at a saturation temperature of 95 °F, the heat loss was typically 50 Btu/hr for liquid tests and 85 Btu/hr for vapor tests. The small difference between these values could easily have been an artifact due to slight inaccuracies in the latent heat.

Before testing began in the 0.123" i.d. test-section, the refrigerant-heater was changed to reduce the system charge and higher heat flux heaters were installed. Before two-phase testing was begun, liquid tests were run over a wide range of heater outlet temperatures to quantify the heat loss from the refrigerant heater and verify that it was functioning properly. Based on these tests, an overall conductance type heat loss model was fit to the experimental data. The measured heat loss data are compared to predictions of the model in Fig. 4.6. Most of the heat loss data were predicted to within 15%, with the worst error being approximately 17 Btu/hr. Based on this agreement, the uncertainty in the UA value for the heater was estimated at ±20%.

A similar procedure was used to obtain a model for the heat loss from the heater for data collected in the 0.278" i.d. test-section. The measured heat loss data are compared to those predicted by the model in Fig. 4.7. Again, the agreement was reasonable. The worst case residual was 27 Btu/hr, while the average residual was 14 Btu/hr. Based on these data, the uncertainty in the UA value for the heater was estimated at ±20%.

4.3.2 Comparisons with single-phase correlations

For the data in the 0.123" and 0.278" i.d. test-sections, heat transfer and pressure drop data were also collected during single-phase testing. These data were compared with single-phase correlations that have been well verified by many investigators, providing a validity check of the surface thermocouple and differential pressure measurements.

Single-phase heat transfer data for R-134a in the 0.123" and 0.278" i.d. tubes are compared with predictions of the Gnielinski [1976] correlation in Fig. 4.8. The Gnielinski correlation was chosen as the basis for comparison since it was recommended by the Handbook of Single-Phase Convective Heat Transfer [Shah, 1981] as the most accurate correlation available for turbulent flow in round tubes. The data shown in Fig. 4.9 had Reynolds numbers ranging from 6000 to 29,000, all with Prandtl numbers near 3.5. The data were nearly all within 10% of the Gnielinski predictions, with a mean deviation of 5.5% for the 0.123" i.d. tube and 6% for the 0.278" i.d. tube. In general, the data were slightly higher than the predicted values. Over the range of Reynolds and Prandtl numbers tested, the predictions of the Gnielinski [1976] correlation were 10% to 20% higher than the simpler but less accurate Dittus-Boelter [1930] correlation.

Although single-phase pressure drop data were collected in each tube, only the 0.123" i.d. tube had high enough single-phase pressure drops to provide a reasonable check of the differential pressure transducer. A set of seven points with R-134a in the 0.123" i.d. tube had pressure drops of 3% to 12% higher than predicted by the Blasius [1913] correlation. This agreement was satisfactory, especially considering that the pressure drop in these tests was never greater than 8% of the full-scale range of the transducer.

4.4 Test Envelope

The experimental envelope was designed to allow data collection over the range of flow regimes encountered in condensers for mobile air-conditioners, residential air-conditioners, and domestic refrigerators. The data were collected over a two year period in three tubes, although the data used for model development were only those from the final two tubes.

The first tube in which heat transfer data were collected was a .180" i.d. tube. The refrigerants tested in this tube were R-12, R-134a, R-22, and a 60/40 blend of R-32/R-125. The range of conditions over which the data in this tube were collected are summarized in Table 4.2. The flow regimes encountered in these experiments included wavy flow, annular flow, and annular-mist flow. Later analysis of these data revealed that they were consistently around 20% too low, based on comparisons with later two-phase data and single-phase correlations. At this stage in the project, the thermocouple mounting technique was still being perfected and several of the thermocouple readings had to be discarded because they were too low in comparison with other thermocouples at the same axial location. It is possible that the other thermocouples at the same location were also too low, which would occur if they protruded too far into the water flow. This would tend to make the heat transfer coefficients too low, as was observed. Although these data were not used for developing the correlations, they were useful for developing an early understanding of the heat transfer trends and how they depend on flow regime. Furthermore, the comparison of the heat transfer behavior between the refrigerants in this tube yielded identical results to that obtained in later tubes.

The second tube in which heat transfer data were collected was the 0.123" i.d. tube. The thermocouple mounting techniques were refined before installing this tube, resulting in excellent agreement between the thermocouples at each axial location during single-phase testing. Fluids tested in this tube were R-134a, 60/40 R-32/R-125, and R-22. The range of conditions that these data were collected over is summarized in Table 4.3. This testing also included data in the wavy, annular, and annular mist flow regimes.

The final tube in which heat transfer data were collected was a 0.278" i.d. tube. The refrigerants tested in this tube were R-134a, R-22, and a 50/50 blend of R-32/R-125. The lower mass flux limit was decreased from 55 klb_m/ft^2-hr to 18 klb_m/ft^2-hr in this tube, adding new data in the purely stratified flow regime. Also, the temperature difference was controlled at several different levels during this testing to more clearly reveal its effect on the heat transfer behavior. The range of conditions over which data were collected in this tube is described in Table 4.4.

Table 4.2 Condensation test envelope for the .180" i.d. tube

Quantity	Range
Mass flux	55-475 klb_m/ft^2-hr
Average quality	10%-90%
Heat flux	1.6-4.8 $kBtu/hr\text{-}ft^2$
T_{sat} - T_s	3.2-7.2 °F
Saturation temperature	95 - 140 °F
Refrigerant	R-134a, R-12, R-22, R-32/R-125
Reduced pressure	0.21-0.40
Flow regimes	Wavy, annular, annular-mist

Table 4.3 Condensation test envelope for the 0.123" i.d. tube

Quantity	Range
Mass flux	55-585 klb_m/ft^2-hr
Average quality	10%-90%
Heat flux	1.6-4.8 $kBtu/hr\text{-}ft^2$
T_{sat} - T_s	3.2-7.2 °F
Saturation temperature	95 - 113 °F
Refrigerant	R-134a, R-22, R-32/R-125
Reduced pressure	0.21-0.57
Flow regimes	Wavy, annular, annular-mist

Table 4.4 Condensation test envelope for the 0.278" i.d. tube

Quantity	Range
Mass flux	18-585 klb_m/ft^2-hr
Average quality	10%-90%
Heat flux	1.6-4.8 kBtu/hr-ft^2
$T_{sat} - T_s$	3.2-7.2 °F
Saturation temperature	95 - 113 °F
Refrigerant	R-134a, R-22, R-32/R-125
Reduced pressure	0.21-0.57
Flow regimes	Stratified, wavy, annular, annular-mist

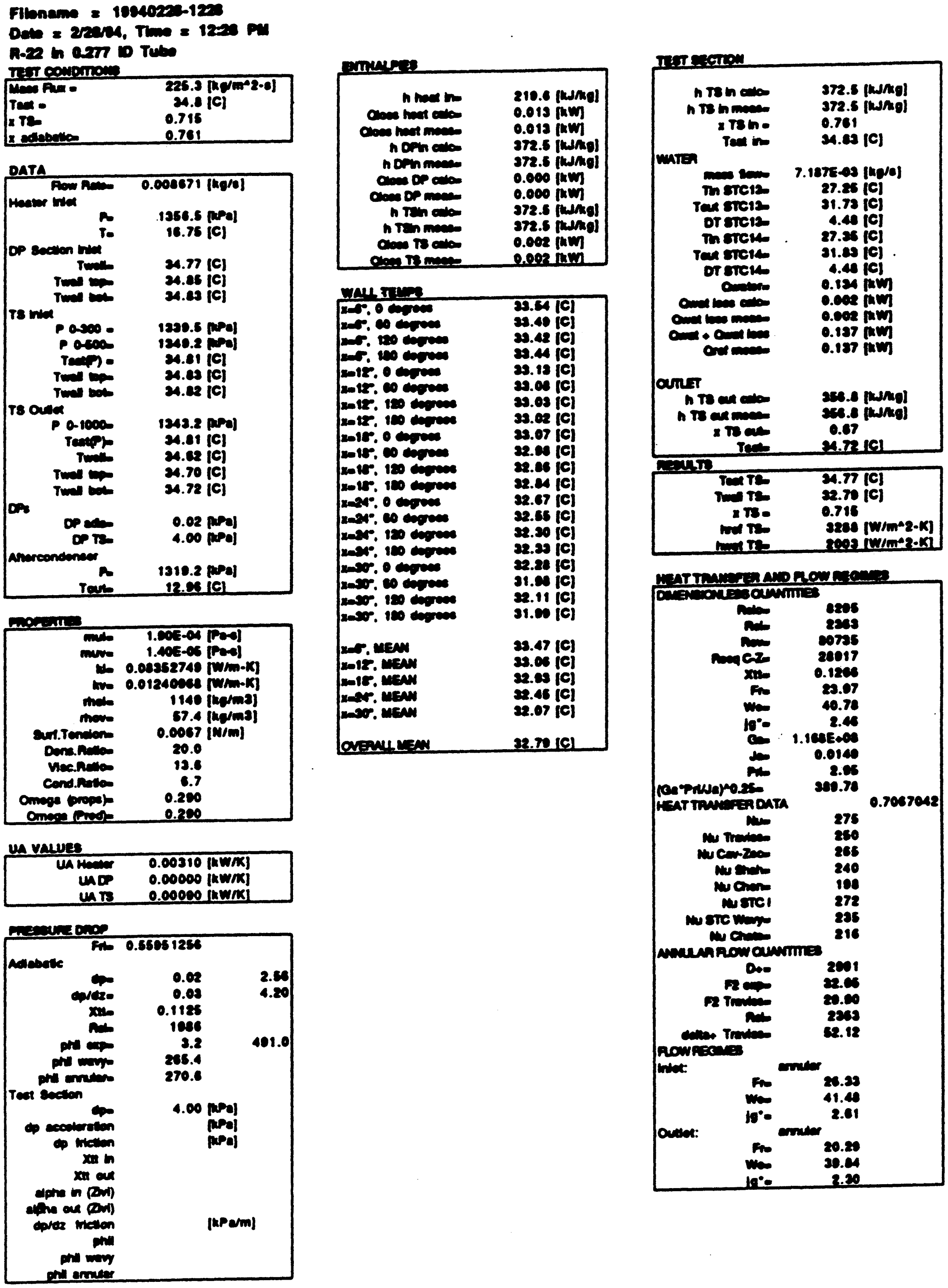

Filename = 19940228-1228
Date = 2/28/94, Time = 12:28 PM
R-22 in 0.277 ID Tube

TEST CONDITIONS

Mass Flux =	225.3 [kg/m^2-s]
Tsat =	34.8 [C]
x TS=	0.715
x adiabatic=	0.761

DATA

Flow Rate=	0.008671 [kg/s]
Heater inlet	
P=	1356.5 [kPa]
T=	16.75 [C]
DP Section inlet	
Twall=	34.77 [C]
Twall top=	34.85 [C]
Twall bot=	34.83 [C]
TS inlet	
P 0-300 =	1339.5 [kPa]
P 0-500=	1349.2 [kPa]
Tsat(P) =	34.81 [C]
Twall top=	34.83 [C]
Twall bot=	34.82 [C]
TS Outlet	
P 0-1000=	1343.2 [kPa]
Tsat(P)=	34.81 [C]
Twall=	34.62 [C]
Twall top=	34.70 [C]
Twall bot=	34.72 [C]
DPs	
DP adia=	0.02 [kPa]
DP TS=	4.00 [kPa]
Aftercondenser	
P=	1319.2 [kPa]
Tout=	12.96 [C]

PROPERTIES

mul=	1.90E-04 [Pa-s]
muv=	1.40E-05 [Pa-s]
kl=	0.08352749 [W/m-K]
kv=	0.01240968 [W/m-K]
rhol=	1149 [kg/m3]
rhov=	57.4 [kg/m3]
Surf.Tension=	0.0067 [N/m]
Dens.Ratio=	20.0
Visc.Ratio=	13.6
Cond.Ratio=	6.7
Omega (props)=	0.290
Omega (Pred)=	0.290

UA VALUES

UA Heater	0.00310 [kW/K]
UA DP	0.00000 [kW/K]
UA TS	0.00090 [kW/K]

PRESSURE DROP

Frl=	0.55951256	
Adiabatic		
dp=	0.02	2.56
dp/dz=	0.03	4.20
Xtt=	0.1125	
Rel=	1986	
phil exp=	3.2	491.0
phil wavy=	265.4	
phil annular=	270.6	
Test Section		
dp=	4.00 [kPa]	
dp acceleration	[kPa]	
dp friction	[kPa]	
Xtt in		
Xtt out		
alpha in (Zivi)		
alpha out (Zivi)		
dp/dz friction	[kPa/m]	
phil		
phil wavy		
phil annular		

ENTHALPIES

h heat in=	219.6 [kJ/kg]
Qloss heat calc=	0.013 [kW]
Qloss heat meas=	0.013 [kW]
h DPin calc=	372.5 [kJ/kg]
h DPin meas=	372.5 [kJ/kg]
Qloss DP calc=	0.000 [kW]
Qloss DP meas=	0.000 [kW]
h TSin calc=	372.5 [kJ/kg]
h TSin meas=	372.5 [kJ/kg]
Qloss TS calc=	0.002 [kW]
Qloss TS meas=	0.002 [kW]

WALL TEMPS

x=6", 0 degrees	33.54 [C]
x=6", 60 degrees	33.49 [C]
x=6", 120 degrees	33.42 [C]
x=6", 180 degrees	33.44 [C]
x=12", 0 degrees	33.13 [C]
x=12", 60 degrees	33.06 [C]
x=12", 120 degrees	33.03 [C]
x=12", 180 degrees	33.02 [C]
x=18", 0 degrees	33.07 [C]
x=18", 60 degrees	32.96 [C]
x=18", 120 degrees	32.86 [C]
x=18", 180 degrees	32.84 [C]
x=24", 0 degrees	32.67 [C]
x=24", 60 degrees	32.55 [C]
x=24", 120 degrees	32.30 [C]
x=24", 180 degrees	32.33 [C]
x=30", 0 degrees	32.28 [C]
x=30", 60 degrees	31.98 [C]
x=30", 120 degrees	32.11 [C]
x=30", 180 degrees	31.90 [C]
x=6", MEAN	33.47 [C]
x=12", MEAN	33.06 [C]
x=18", MEAN	32.93 [C]
x=24", MEAN	32.46 [C]
x=30", MEAN	32.07 [C]
OVERALL MEAN	32.79 [C]

TEST SECTION

h TS in calc=	372.5 [kJ/kg]
h TS in meas=	372.5 [kJ/kg]
x TS in =	0.761
Tsat in=	34.83 [C]
WATER	
mass flow=	7.187E-03 [kg/s]
Tin STC12=	27.25 [C]
Tout STC12=	31.73 [C]
DT STC12=	4.48 [C]
Tin STC14=	27.35 [C]
Tout STC14=	31.83 [C]
DT STC14=	4.48 [C]
Qwater=	0.134 [kW]
Qwat loss calc=	0.002 [kW]
Qwat loss meas=	0.002 [kW]
Qwat + Qwat loss	0.137 [kW]
Qref meas=	0.137 [kW]
OUTLET	
h TS out calc=	356.8 [kJ/kg]
h TS out meas=	356.8 [kJ/kg]
x TS out=	0.67
Tsat=	34.72 [C]

RESULTS

Tsat TS=	34.77 [C]
Twall TS=	32.79 [C]
x TS =	0.715
href TS=	3288 [W/m^2-K]
hwat TS=	2003 [W/m^2-K]

HEAT TRANSFER AND FLOW REGIMES

DIMENSIONLESS QUANTITIES		
Relo=	8295	
Rel=	2363	
Rev=	80735	
Reeq C-Z=	28817	
Xtt=	0.1266	
Fr=	23.97	
We=	40.78	
jg*=	2.46	
Ga=	1.168E+08	
Ja=	0.0149	
Prl=	2.95	
(Ga*Prl/Ja)^0.25=	389.78	
HEAT TRANSFER DATA		0.7067042
Nu=	275	
Nu Traviss=	250	
Nu Cav-Zec=	265	
Nu Shah=	240	
Nu Chen=	198	
Nu STC I	272	
Nu STC Wavy=	235	
Nu Chato=	216	
ANNULAR FLOW QUANTITIES		
D+=	2991	
F2 exp=	32.96	
F2 Traviss=	29.90	
Rel=	2363	
delta+ Traviss=	52.12	
FLOW REGIMES		
Inlet:	annular	
Fr=	26.33	
We=	41.48	
jg*=	2.61	
Outlet:	annular	
Fr=	20.29	
We=	39.84	
jg*=	2.30	

Figure 4.1 Data sheet from the 0.278" i.d. test-section.

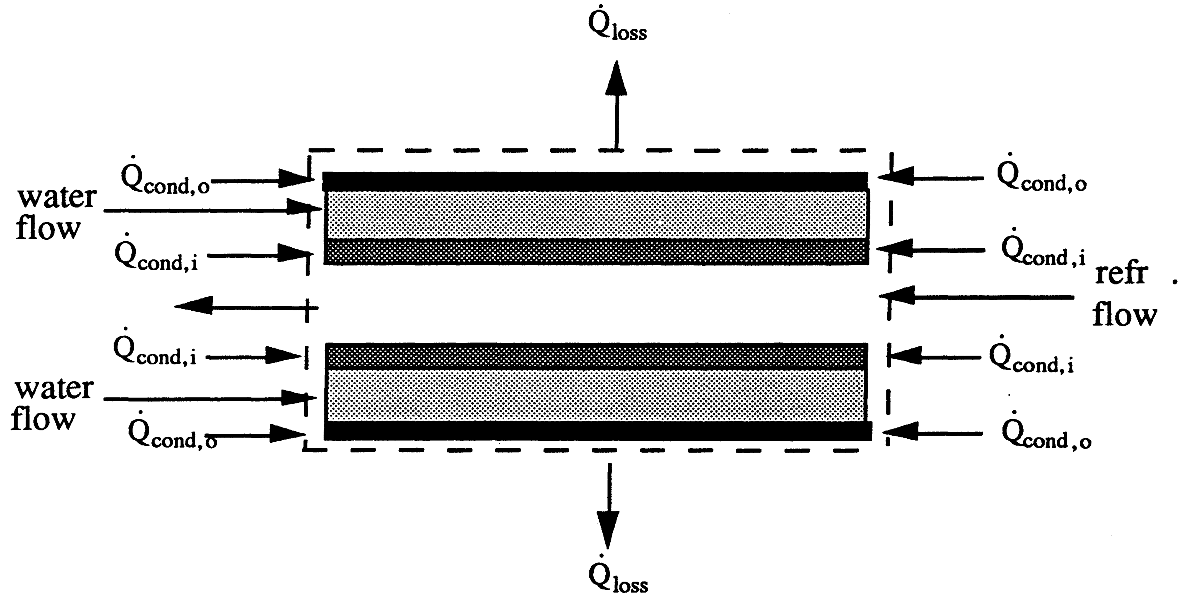

Figure 4.2 Energy transfer modes across the test-section.

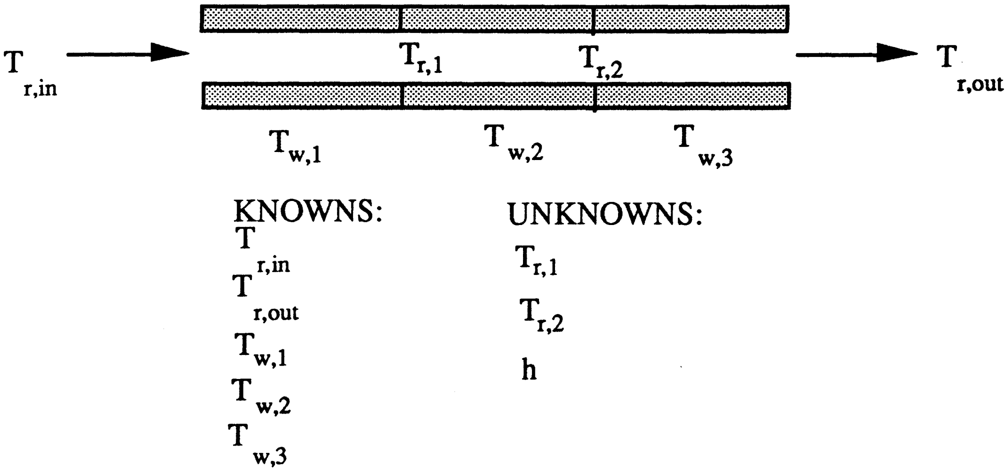

Figure 4.3 Schematic for computing single-phase heat transfer coefficients.

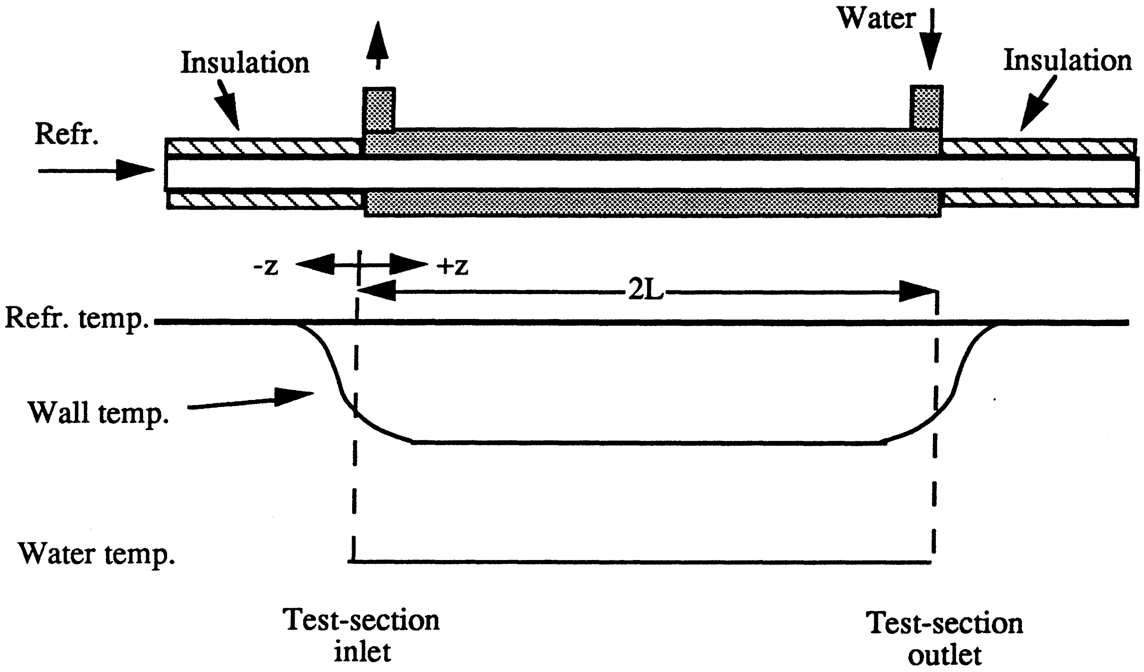

Figure 4.4 Schematic of the physical situation for axial conduction analysis.

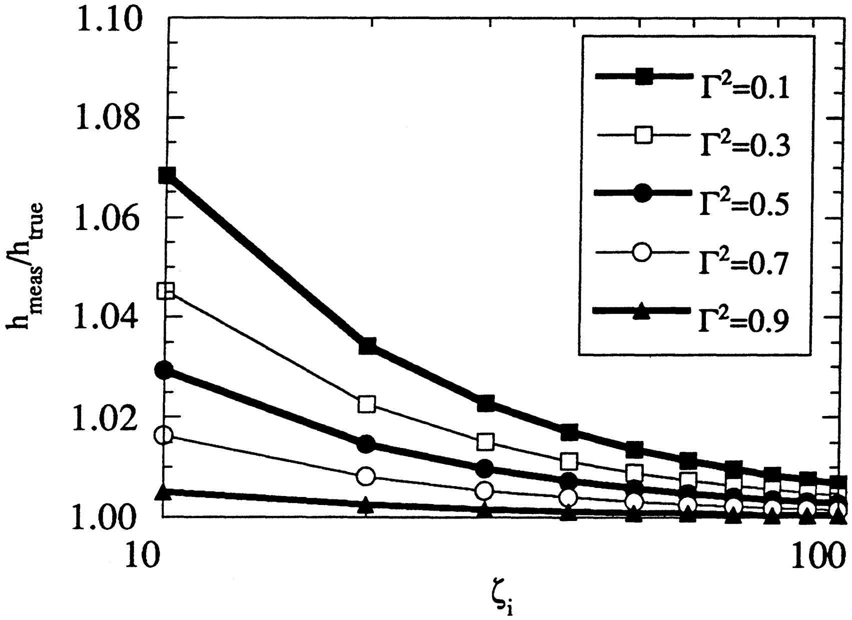

Figure 4.5 Effect of ζ_i and Γ on h_{meas}/h_{true} for ζ_i between 10 and 100.

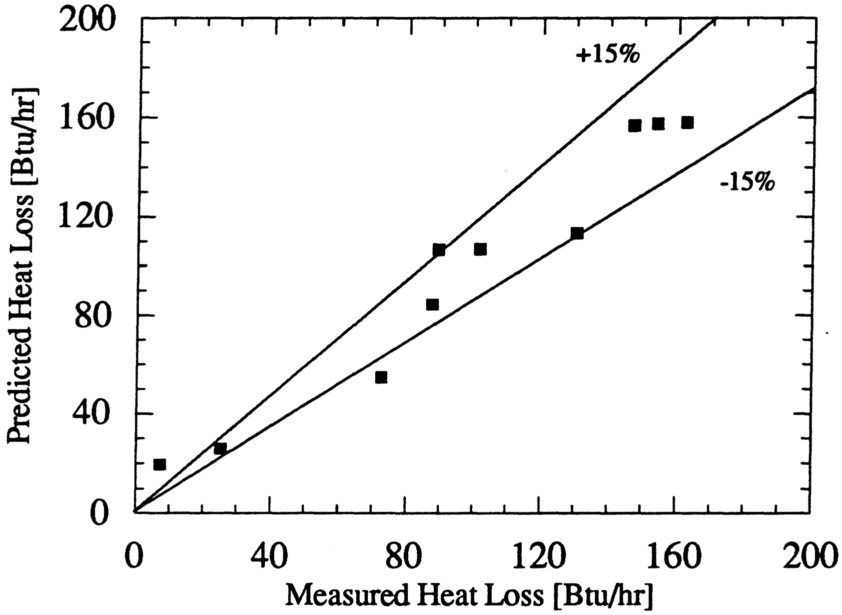

Figure 4.6 Heat loss data from the 0.123" i.d. tube.

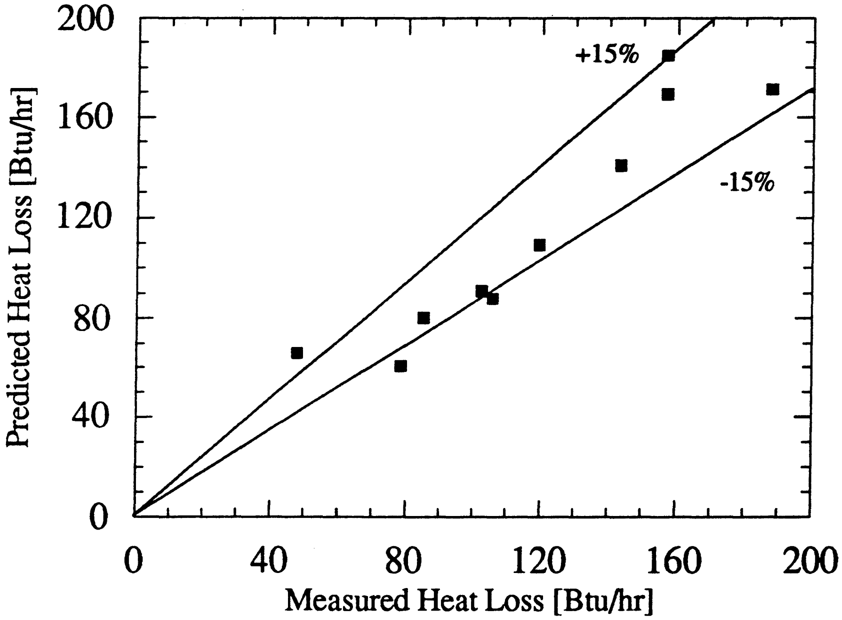

Figure 4.7 Heater heat loss data from the 0.278" i.d. tube.

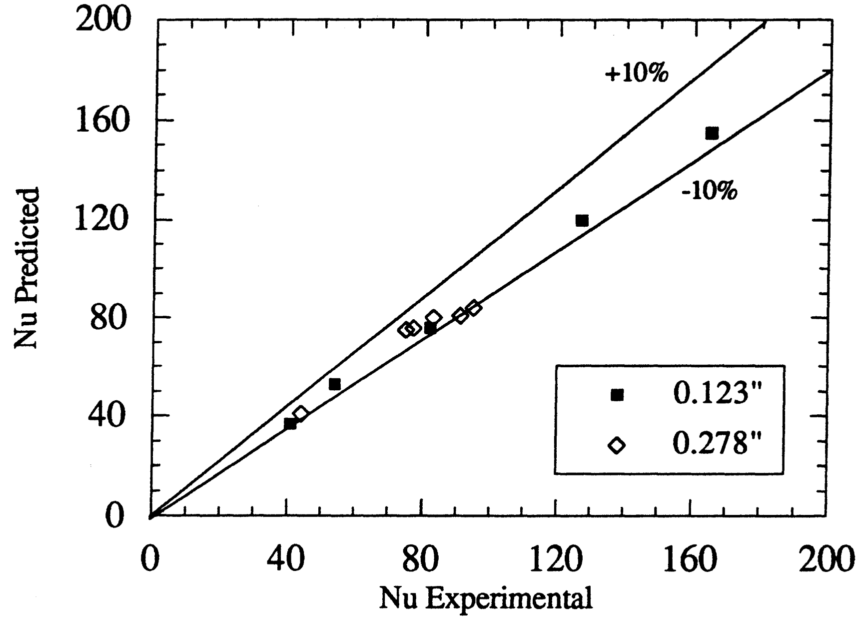

Figure 4.8 Comparison of liquid heat transfer data for R-134a with predictions of the Gnielinski [1976] correlation.

CHAPTER 5

FLOW REGIME OBSERVATIONS

This chapter presents the experimental flow regime observations from this study and compares them to various flow regime predictors from the literature. These observations were gathered in tubes of .123", .180", and .278" inner diameters. The refrigerants used were R-134a, R-22, and 60/40 and 50/50 blends of R-32 and R-125. The properties of the 60/40 and 50/50 blends of R-32 and R-125 were so similar to each other and so different from the other fluids that they will both be referred to only as R-32/R-125 for the remainder of this chapter.

5.1 General Observations

A variety of flow regimes were observed over the course of the study. At low mass fluxes, the smooth-stratified and wavy flow regimes were the dominant flow patterns. At higher mass fluxes, the flow regimes were slug at low quality, followed sequentially by wavy, wavy-annular, and annular flow regimes. Some mist was visible inside the annular core at high mass fluxes, although pure mist flow was never observed at qualities below 90%.

5.1.1 Effect of mass flux and quality

The dominant factors affecting the flow regimes were the mass flux and the quality. Tests were normally conducted at mass fluxes ranging from 18 klb_m/ft^2-hr to 475 klb_m/ft^2-hr . Since sight glasses were present at both the inlet and outlet of the test-section, visual observations were made over a range of quality from less than 5% to around 99%.

At the lowest mass flux in the study, 18 klb_m/ft^2-hr, smooth-stratified flow was observed across the entire range of quality. As the mass flux was increased to 55 klb_m/ft^2-hr, interfacial waves developed and wavy flow was observed for the entire range of quality. For these two mass fluxes, the flow regime was not affected by changes in diameter or refrigerant.

At mass fluxes of 110 klb_m/ft^2-hr and 220 klb_m/ft^2-hr several different flow regimes were observed as the quality was changed. Slug flow was observed at low qualities, followed sequentially by wavy, wavy-annular, and annular flow. At these mass fluxes, the tube diameter and fluid properties influenced the range of quality over which each of the flow regimes occurred. These effects are discussed in Section 5.1.2.

The highest mass fluxes from this study were 365, 475, and 585 klb_m/ft^2-hr . At these mass fluxes, the flow regimes included slug flow at low quality, followed by wavy-annular, annular, and annular-mist flow as the quality was increased. Although the quality range over which each of these regimes occurred depended somewhat on fluid properties and diameter, annular or annular-mist flow normally occurred for 70% to 80% of the condensation path. These were the only mass fluxes where significant entrainment occurred. Detecting any details of the mist was difficult since it normally flowed inside a wall film, but it was clearly visible at high qualities. The amount of mist showed significant temporal variations, with periods of no entrainment being followed by periods with a rather dense mist in the core flow. This is consistent with the findings reported by Barnhart [1992], who found that droplets formed at slug initiation propagated far downstream. Perhaps the most significant observation at these high mass fluxes was that pure mist flow (without a stable wall film) was observed only at qualities over 90% , and even then never at the outlet sight glass. Thus, what was mist flow in the adiabatic section appeared to develop a stable liquid film as soon as condensation began. Over the range of parameters tested in this study, then, Soliman's [1986] idea of pure mist flow as a distinct condensation regime was not verified.

5.1.2 Effects of fluid properties and tube diameter

Although mass flux and quality were the primary factors affecting the flow regimes, the thermophysical properties of the fluids and the tube diameter also played a secondary role. Their influence was most evident at the intermediate mass fluxes of 110 and 220 klb_m/ft^2-hr , where the mass velocities were not so high or low as to clearly mandate dominance of one flow regime over the others.

The primary fluid properties that affect the flow regimes are the vapor and liquid densities and viscosities, the ratios between these quantities, and the surface tension. Values of these properties for the three fluids used in this study are listed in Table 5.1 for saturation temperatures of both 95 °F and 113 °F. Much of the variation in the fluid properties can be explained by the reduced pressure. At high values of reduced pressure, the liquid and vapor phases are more similar. This dictates higher values of vapor density and viscosity and lower values of liquid density and viscosity. The surface tension, which has the interpretation of the work required to increase the interfacial area [Carey, 1992], also decreases as the reduced pressure increases and the phases become more similar. At a given temperature, the reduced pressure is lowest for R-134a, followed by R-22 and R-32/R-125. The values of the other properties follow accordingly.

Table 5.1 Property comparison of R-134a, R-22, and 50/50 R-32/R-125

Property	R-134a 95 °F/113 °F	R-22 95 °F/113 °F	R-32/R-125 95 °F/113 °F
ρ_l (lb$_m$/ft^3)	72.8/70.3	71.7/70.0	63.2/59.3
ρ_v (lb$_m$/ft^3)	2.7/3.5	3.6/4.8	5.4/7.1
ρ_l/ρ_v	27.2/19.9	19.9/13.9	11.8/8.4
μ_l (lb$_m$/ft-h)	0.43/0.39	0.46/0.43	0.33/0.29
μ_v (lb$_m$/ft-h)	0.029/0.031	0.034/0.036	0.034/0.036
μ_l/μ_v	14.4/12.8	13.6/12.2	9.5/7.9
$(\mu_l/\mu_v)^{0.1}(\rho_v/\rho_l)^{0.5}$	0.250/0.289	0.291/0.344	0.365/0.425
σ (mlb$_f$/ft)	0.467/0.383	0.459/0.368	0.406/0.292
P_r	0.218/0.285	0.268/0.343	0.430/0.549

The most noticeable effect of the property differences on the flow regimes was the extent to which annular flow prevailed over wavy or wavy-annular flow. At a given mass flux where wavy, wavy-annular, and annular flows all occurred, the size of the quality range occupied by annular flow was greater at lower reduced pressures. Thus, the most annular flow was observed for R-134a at 95 °F and the least annular flow was observed for R-32/R-125 at 113 °F. The differences in the observed flow regimes for these two cases were significant. At a mass flux of 220 klb$_m$/ft^2-hr, the transition to annular flow that occurred at 25% for the low temperature R-134a case was delayed until 50% quality for the high temperature R-32/R-125 case. Even at the highest mass flux of 475 klb$_m$/ft^2-hr, significant stratification was observed across the entire quality range for the high temperature R-32/R-125 case. For the low temperature R-134a case at the same mass flux, a symmetric annular film was established at 15% quality. Smaller changes in reduced pressure, such as changing the temperature of the same fluid, produced similar but smaller changes.

Another item that is affected by the reduced pressure is the length of the slug flow region. Taitel and Dukler's [1976] criterion for slug flow is that $X_{tt}>1.6$. Combining this with the fact that $(\rho_v/\rho_l)^{0.5}(\mu_l/\mu_v)^{0.1} \cong 0.551P_{red}^{0.492}$ [Wattelet, 1994] yields an algebraic expression for the quality below which slug flow is expected to occur:

$$x_{slug} = \frac{1}{1+3.27P_r^{-0.547}} \tag{5.1}$$

This equation predicts that the most slug flow will occur for R-32/R-125, followed by R-22 and R-134a. For R-32/R-125 at 113 °F, for instance, Eq. (5.1) predicts that slug flow will be observed for all qualities below 19%. For R-134a at 95 °F, it predicts a slug flow region confined to qualities below 11%. This lengthening of the slug flow region with increases in reduced pressure was observed experimentally.

The tube diameter also affected the flow regime transitions. As the tube diameter was reduced at a fixed mass flux, the transition from wavy flow to wavy-annular flow and the transition from wavy-annular flow to annular flow shifted to lower qualities. This trend is summarized in Table 5.2, which shows the estimated quality at which these transitions occurred in each of the tubes for R-134a at 95 °F. The quality where the wavy to wavy-annular transition occurred shifted the most at a mass flux of 110 klb$_m$/ft^2-hr, where it decreased from 37% in the .278" i.d. tube to 23% in the .123" i.d. tube. The quality at which the wavy-annular to annular transition occurred decreased from 65% to 45% at this same mass flux. At higher mass fluxes, most of the quality range was occupied by annular flow even in the .278" i.d. tube. Thus, the diameter effects were less pronounced.

Table 5.2 Effect of tube diameter on R-134a flow regime transitions at 95 °F

Tube i.d. [in]	Wavy to wavy-annular		Wavy-annular to annular	
	x for G=110 klb$_m$/ft^2-hr	x for G=220 klb$_m$/ft^2-hr	x for G=110 klb$_m$/ft^2-hr	x for G=220 klb$_m$/ft^2-hr
.123	0.23	0.15	0.45	0.29
.180	0.35	0.25	0.50	0.38
.278	0.37	0.25	0.65	0.41

Pure stratified flow was observed only in the .278" i.d. tube, primarily because this was the only tube where a mass flux of 18 klb$_m$/ft^2-hr could be stabilized. Thus, no observations on the effect of diameter could be made with respect to this transition. Entrainment was only observed at mass fluxes of 365 klb$_m$/ft^2-hr and above in each of the tubes. Although visually estimating the amount of entrainment was difficult, it appeared that entrainment was less pronounced in the smaller tubes.

5.2 Comparison with Flow Regime Maps

A major goal of this study was to eliminate the need for testing with every refrigerant that might be considered as a candidate in the future. Since the flow regimes clearly affect the heat transfer processes, it was necessary to evaluate the potential of existing flow regime prediction techniques for condensation conditions. Evaluations will be made herein for the maps of Mandhane et al. [1974], Taitel and Dukler [1976], and Soliman [1982, 1983]. The potential role of surface tension will also be briefly explored for the data in the .123" i.d. tube. The baseline case that will be used to evaluate each of these maps will be R-134a in the .278" i.d. tube at 95 °F. The validity of the maps for other diameters, fluids, and temperatures will be addressed by examining how their predictions change with diameter and reduced pressure.

5.2.1 Mandhane map

Figure 5.1 traces the condensation path for mass fluxes ranging from 18 klb_m/ft^2-hr to 475 klb_m/ft^2-hr of R-134a on the Mandhane map. The points on the map cover a range of quality from 5% to 95% in 5% increments. Increasing the quality corresponds to moving left to right on the map. The predictions of the Mandhane map are grossly different from the experimental observations. For the mass flux of 18 klb_m/ft^2-hr, the flow pattern is correctly predicted as stratified across the range of quality. The stratified region is much wider than the experimental observations, however. For instance, the data at mass fluxes of 55 and 110 klb_m/ft^2-hr are predicted to be in the stratified flow regime across the entire range of quality. In practice, the observed flow regimes for these mass fluxes were wavy, wavy-annular, and annular. For the higher mass fluxes of 220, 365, and 475 klb_m/ft^2-hr, the Mandhane map predicts primarily slug and wavy flow. In reality, annular flow was observed for most of the quality range at these mass fluxes. To bring the Mandhane map into closer agreement with the observed behavior, its boundaries should be shifted to the left or the path lines should be shifted to the right. Similar behavior for evaporating refrigerants was noted by Wattelet [1994].

The Mandhane map, as pointed out in Section 2.2, was developed primarily from air-water data. At atmospheric pressure and temperature, the density of air is about .07 lb_m/ft^3. This is between 40 and 100 times lower than the vapor densities from this study. Hanratty [1994] pointed out that the Mandhane map could be brought into better agreement with refrigerant data by accounting for the large differences in vapor density. To effect this change, the superficial vapor velocity of the refrigerant was multiplied by the square root of the ratio of the vapor density to the density of atmospheric air. The resulting quantity is referred to herein as a modified superficial vapor velocity:

$$j_v^{corr} = \sqrt{\rho_v / \rho_a}\, j_v \qquad (5.2)$$

From a physical standpoint, this modified superficial velocity is proportional to the square root of the vapor kinetic energy. This simple change was made in both the vapor and liquid superficial velocities, using 0.07 lb_m/ft^3 as the density of air and 62.5 lb_m/ft^3 as the density of water. The results are plotted on the Mandhane coordinates in Fig. 5.2.

Making this simple correction to the Mandhane map produced much better agreement with the experimental data. The 18 klb_m/ft^2-hr data were still correctly predicted to be in the stratified flow regime. The data at 55 and 110 klb_m/ft^2-hr were moved from the being exclusively in the stratified flow regime to being predominantly wavy flow, consistent with experimental observations. Furthermore, the highest quality data at 110 klb_m/ft^2-hr was correctly predicted to be on the line between wavy and annular flow. The data at the high mass fluxes of 220, 365, and 475 klb_m/ft^2-hr were all correctly shifted rightward, so that they were predominantly in the annular or annular-mist flow regime. The only obvious deficiency was an overprediction in the length of the slug flow region, particularly at 220 klb_m/ft^2-hr. Barnea et al. [1980], however, also noted that their wavy-annular flow data occupied the slug flow region on the Mandhane map. They suggested this was due to different interpretations of what constituted slug flow, and that data observed to be in the wavy-annular flow regime should be classified as slug flow for comparisons with the Mandhane map (or conversely that points lying near the right edge of Mandhane's slug flow region might be expected to correspond to wavy-annular flow). Incorporating this suggestion results in excellent agreement with the Mandhane map.

Having established the basic validity of the corrected Mandhane map for the case of R-134a in the .278" i.d. tube, questions remain about how it incorporates the effects of diameter and reduced pressure. Neither coordinate on the Mandhane map includes a diameter term, and investigators as early as Taitel and Dukler [1976] have noted systematic deviations in the Mandhane map because of this. This means that the increased amount of annular flow from the .123" i.d. tube would not be predicted using the Mandhane map.

The effect of reduced pressure is addressed in Fig. 5.3, which plots the condensation paths for R-32/R-125 at 113 °F on the corrected Mandhane map. This combination of refrigerant and temperature was selected for comparison since it corresponded to the highest reduced pressure tested in this study. The trends predicted by the Mandhane map regarding the change in fluid properties are consistent with the experimental observations. Comparing the predictions of the low reduced pressure case (Fig. 5.2) and the high reduced pressure case (Fig. 5.3), the lines for a given mass flux were shifted left on the Mandhane map. The mass flux of 110 klb_m/ft^2-hr was correctly predicted to lie entirely in the wavy flow regime. The quality at which annular flow was expected to begin for the high mass flux cases was correctly increased over the R-134a case, although a portion of the slug flow region was again occupied by either wavy or wavy-annular flow.

5.2.2 Taitel-Dukler map

Fig. 5.4 traces condensation paths for the baseline R-134a case on the Taitel-Dukler map. The points again range from 5% to 95% quality at 5% increments, with increasing quality corresponding to moving left on the map. Since the Taitel-Dukler map uses different coordinates for different transitions, in general three different lines would be needed for each mass flux. For the range of parameters in this study, though, no dispersed bubble flow was observed or predicted. Thus, the T_{td} parameter was irrelevant. The two parameters that were needed were K_{td} and F_{td}, used respectively for predicting the stratified to wavy and wavy to annular or intermittent transitions. These parameters were reviewed in Section 2.3.3.

Plots of K_{td} versus X_{tt} are shown for the two lowest mass fluxes only, since these were the only mass fluxes at which any stratified flow was predicted. The map predicted stratified flow up to 80% for the 18 klb_m/ft^2-hr flux case, where stratified flow was observed across the entire range of quality. For a mass flux of 55 klb_m/ft^2-hr, the Taitel-Dukler map correctly predicted nearly all wavy flow.

Plots of F_{td} versus X_{tt}, used for predicting the transition from wavy to annular or intermittent flow, are shown for all the mass fluxes in the study. It is interesting to note that the transition boundary is nearly parallel to the condensation path lines. This implies that a particular mass flux, to a close approximation, will be either wavy or annular across the entire range of quality. This causes no problems for the 18 and 55 klb_m/ft^2-hr mass fluxes, where the map correctly predicts that no annular flow will be observed. For mass fluxes slightly above the transition boundary (in the annular regime), the slug flow regime at low qualities was always followed by regions of wavy, wavy-annular, then annular flow. The quality range over which the wavy and wavy-annular flow regimes occurred decreased as mass flux was increased. At a mass flux of 110 klb_m/ft^2-hr, the wavy regime persisted up to 25% quality, followed by wavy-annular flow up to 65% quality and annular flow at higher qualities.

The predictions of the Taitel-Dukler map are translated onto mass flux-quality (G-x) coordinates in Fig. 5.5. At low mass fluxes, stratified flow is predicted across the entire range of quality. At slightly higher mass fluxes, wavy flow is predicted across most of the quality range with a small amount of stratified flow at low quality. At mass fluxes above 110 klb_m/ft^2-hr, slug flow is predicted for qualities below 11.8% and annular flow is predicted for all higher qualities. It is close to this boundary that the observed flow regimes deviated most significantly from the Taitel-Dukler predictions. The length of the slug flow region was underpredicted, and this was consistently followed by some wavy or wavy-annular flow that was not predicted by the Taitel-Dukler map.

The apparent discrepancy between the observed and predicted flow regimes at mass fluxes slightly above the annular boundary of the Taitel-Dukler map is largely due to differences in terminology. In an early experimental verification of the Taitel-Dukler map, Barnea et al. [1980] used the term wavy-annular flow to refer to a hybrid pattern observed at the lowest gas rates where the slug to annular transition occurred. They described this as a regime where most of the liquid flowed at the bottom of the pipe and the upper walls were intermittently wet by large unstable waves that were not sufficient to completely bridge the cross section. A similar regime has been termed "proto-slug" flow by Nicholson, Aziz and Gregory [1978], and "pseudo-slug" flow by Lin and Hanratty [1989]. Since this pattern occurs <u>after</u> the wavy flow has become unstable, it is properly labeled as intermittent or annular flow in Taitel-Dukler terminology. From a heat transfer standpoint, however, the instability of the wavy flow near this boundary is less important than the significant stratification due to gravity. At higher mass fluxes, the range of quality occupied by this hybrid flow pattern becomes so small that proper classification is unimportant.

Of the boundaries from the Taitel-Dukler map that were used in this study, only that between wavy and intermittent or annular flow depends on the diameter. The parameter used for predicting this transition, F_{td}, is proportional to $D^{-0.5}$ at a fixed mass flux and quality. Thus, decreasing the diameter increases the Froude number and decreases the mass flux at which the annular transition is expected to occur. This is consistent with the observed trend of more annular flow in the smaller tubes. While the trend is physically correct, the predictions themselves were incorrect when applied to the data in the .123" i.d. tube. The Taitel-Dukler method predicts annular flow across nearly the entire range of quality at a mass flux of 55 klb_m/ft^2-hr, while wavy flow was observed exclusively at this mass flux.

The predicted trend of the Taitel-Dukler map to an increase in the reduced pressure is shown in Fig. 5.6. This figure plots the predicted boundaries of the Taitel-Dukler map on G-x coordinates for R-32/R-125 in the .278" i.d. tube at 113 °F. The slug flow region is wider, as predicted by Eq. (5.1). This prediction was consistent with the experimental observations.

Physically, one would also expect the stratified to wavy and wavy to annular transitions to be shifted to higher mass fluxes due to the lower vapor velocity at a given mass flux and quality. Although this expected trend did occur, close comparison of the transition lines from Fig. 5.5 and Fig. 5.6 shows that the shift was very modest. At a quality of 50%, for instance, the wavy to annular transition shifted from a mass flux of 55 klb_m/ft^2-hr for the R-134a case to 61 klb_m/ft^2-hr for the R-32/R-125 case. This small shift was due to two opposing trends brought about by the changes in fluid properties. At constant mass flux and quality, the value of F_{td} for the high temperature R-32/R-125 refrigerant was only 71% of that for the low temperature R-134a case, moving it downward relative to the transition boundary on the Taitel-Dukler map. The value of X_{tt} for R-32/R-125 increased 70% relative to the R-134a case at constant quality, however, moving it right on the Taitel-Dukler map and therefore closer to the boundary. At 50% quality, for an example, these two effects result in the low temperature R-134a case being only 11% higher relative to the transition boundary than the high temperature R-32/R-125 case. From a practical standpoint, this predicted shift in the transition boundary is insignificant.

The apparent discrepancy between the predictions and the observations at mass fluxes slightly above the annular flow boundary that was previously discussed for R-134a was also present with R-32/R-125. For a mass flux of 110 klb_m/ft^2-hr, for instance, a region of wavy flow persisted at qualities up to 50%, while the Taitel-Dukler map predicted all annular flow for qualities greater than 20%. A similar pattern was observed with all the refrigerants used in this study.

5.2.3 The Soliman transitions

As discussed in Section 2.2, Soliman [1982,1986] developed criteria for two flow regime transitions for condensation: (1) wavy or slug flow to annular flow, and (2) annular flow to mist flow. His transition criteria are displayed on G-x coordinates in Fig. 5.7. Several interesting observations can be made from comparing the predictions of Soliman to those of Taitel and Dukler. First, at high qualities Soliman's prediction of the wavy to annular transition agrees fairly well with that of Taitel and Dukler. Unlike the Taitel-Dukler map, though, Soliman predicts a wavy region at low qualities over the entire mass flux range of this study. This is partially because Soliman lumps the wavy and slug flow regions together. At high mass fluxes, the region predicted to be wavy flow by Soliman corresponds almost exactly with the slug flow region on the Taitel-Dukler map. At lower mass fluxes, though, the region predicted to be occupied by wavy flow extends to higher qualities than the slug flow boundary on the Taitel-Dukler map. This is consistent with the experimental data in both magnitude and trend if the predicted transition line is considered that of wavy flow to wavy-annular flow. It was shown in Dobson et al. [1994] that the transition from wavy-annular flow to annular flow was well predicted by a value of $Fr_{so}=18$, as opposed to $Fr_{so}=7$ for the wavy to wavy-annular transition.

Soliman's map also includes a distinct mist flow region, unlike the maps of Mandhane and Taitel-Dukler. Before evaluating the validity of Soliman's mist flow predictions, it is necessary to carefully define what is meant by this term. According to

Soliman, mist or spray flow is a regime with all the liquid flowing as entrained droplets in the core flow and no stable film on the wall. Annular mist flow would refer to a regime with a stable liquid film on the wall and significant entrainment in the core flow. According to the observations of this study, most of the region labeled as mist flow by Soliman's map would more properly be called annular-mist flow. Although the amount of entrainment was very significant, a stable liquid film was always observed on the wall at qualities below 90%. Even when the flow entered the first sight glass (after the adiabatic section) as mist flow, the outlet sight glass always had an annular-mist flow. This suggests that the net mass flux toward the wall during condensation always results in a stable liquid film, no matter what the observations might indicate in an adiabatic section. This finding is important for interpreting the annular-mist flow heat transfer data.

If Soliman's mist flow region is interpreted as annular-mist flow, the predictions seem quite reasonable. No mist flow is predicted at mass fluxes below 220 klb_m/ft^2-hr, which is consistent with the observations. At a mass flux of 475 klb_m/ft^2-hr, mist flow is predicted for qualities greater than about 20%. This again seems consistent with the experimental data, although a great amount of subjectivity was present in categorizing a regime as annular or annular-mist.

The diameter effects predicted by Soliman's transition criteria are demonstrated in Fig. 5.8. This figure presents transition lines on G-x coordinates for R-134a at 95 °F in both the .278" and .123" i.d. tubes. The lower mass flux limit at which annular flow was predicted was relatively insensitive to the diameter change, much like the predictions of Taitel and Dukler. At mass fluxes slightly above this, however, the wavy to annular transition line was shifted to lower qualities. This was consistent with the experimental observations in both direction and magnitude. The predicted effect on the mist flow regime was much more dramatic, with a significant stabilizing effect on the liquid film being predicted as the tube diameter was decreased. This was consistent with the trend of the observations, although the transition was very difficult to detect visually.

The effect that increasing the reduced pressure has on the wavy to annular flow regime transition predicted by Soliman is explored in Fig. 5.9. This figure compares the predicted wavy to annular transition lines for R-134a at 95 °F and R-32/R-125 at 113 °F. The predicted trends are consistent with the experimental observations. The mass flux below which no annular flow is predicted was increased by approximately 22 klb_m/ft^2-hr. Since testing was not performed at mass fluxes between 55 and 110 klb_m/ft^2-hr, this prediction could not be verified. At the 110 klb_m/ft^2-hr mass flux, Fig. 5.9 predicts a transition from wavy to wavy-annular flow at 41% quality for R-134a and 57% quality for R-32/R-125. These predictions agree well with the experimentally observed values, which were estimated at 37% and 50%, respectively. At mass fluxes near 730 klb_m/ft^2-hr, the predicted quality range for wavy flow for R-32/R-125 is very near the 19% range for the slug flow regime predicted by Taitel and Dukler.

Since reliable surface tension data are not yet available for this mixture and drawing any conclusions concerning mist flow from the visualization was difficult, only the lines for the wavy to annular transition were included in Fig. 5.9. As another way of assessing the effect of increasing reduced pressure, the magnitude of the Weber number was examined as the temperature was increased for both R-134a and R-22. The Weber number increased as temperature increased due to the reduced liquid viscosity and surface tension, but only slightly (less than 10% as the temperature of both fluids was raised from 95 °F to 131 °F). This small change indicates that the decreased surface tension and liquid viscosity are nearly balanced by corresponding decreases in the density ratio. Based on these trends, one would expect slightly more entrainment to occur for R-32/R-125 than the other refrigerants at identical mass flux and quality.

5.2.4 Potential role of surface tension

In any situation where a free surface exists, the potential role of surface tension should not be overlooked. The analytical approach in the original Taitel-Dukler maps clearly does ignore surface tension forces, however. Investigators have subsequently considered the role of surface tension, as reviewed in Chapter 2. The consensus is that surface tension forces become increasingly important as the diameter is decreased, and may dominate for sufficiently small tube sizes. Of primary interest in this study was the effect on the wavy to annular transition, particularly in the .123" i.d. tube.

Galbiatti and Andreini [1992] started with Taitel and Dukler's analysis of a Kelvin-Helmholtz instability for the wavy to annular flow transition. In the original analysis, as discussed in Chapter 2, the stabilizing effect of gravity is opposed by the effect of an accelerating vapor flowing over a wave. Galbiatti and Andreini included surface tension forces which supplement the stabilizing gravity forces. Their final result for the transition criterion can be obtained by plotting the following parameter on the Taitel-Dukler map in place of F_{td}:

$$\frac{F_{td}}{\sqrt{1+\dfrac{1.305\sigma}{gD^2(\rho_l-\rho_v)}}}=\frac{F_{td}}{\sqrt{1+\dfrac{1.305}{Bd}}} \qquad (5.3)$$

For values of the Bond number (Bd) much greater than unity, surface tension plays no significant stabilizing role. The lowest value of the Bond number for this study, that for R-

134a at 95 °F in the .123" i.d. tube, was about 16. This Bond number results in a value of the denominator of Eq. (5.3) of only 1.04, indicating gravity dominance. This is surprising since Galbiatti and Andreinni stated that the surface tension and gravity forces were of equal magnitude for D=.120", but the value of surface tension for their air water system was significantly larger than that for the high temperature refrigerants in this study. The value of diameter at which surface tension forces become important is quite sensitive to what wavelength is considered most unstable (λ=5.5D was used by Galbiatti and Andreini), so this issue might warrant further attention if tubes in the .120" range are implemented commercially. While the experimental observations from this study did not reveal large differences that could be attributed to surface tension forces, the addition of oil that is present in real condensers could alter this finding.

5.3 Summary of Flow Regime Information for Condensing Refrigerants

Flow regimes were observed visually in three smooth tubes with diameters ranging from .123" to .278" inner diameter. These observations were made over the entire range of quality, and a range of mass flux that bounds that experienced by most refrigeration condensers. Based on these observations, and comparisons of them with three commonly used flow regime predictors, several conclusions can be made.

The primary flow patterns that can be expected in refrigeration condensers are wavy, wavy-annular, annular, and annular-mist. At low qualities, slug or pseudo slug flow will occur. Over the range of conditions from this study, it appears that mist flow without a stable liquid film does not exist during condensation. Stratified flow without any interfacial waves was obtained at the lowest mass flux in this study, but it is unlikely that such a low mass flux will be encountered in typical applications.

Three techniques for flow regime prediction were compared to the experimental observations. While these flow regime predictors could be compared by tabulating the percentage of the observations that they successfully placed, several problems would mitigate the usefulness of such an exercise. First, the subjectivity involved in visually determining the flow regimes is considerable. Determining the difference between slugs, pseudo-slugs, and wavy-annular flow, for instance, is quite difficult. Categorizing a flow as annular, annular-mist, or pure mist is subject to similar problems. Second, the number of categories included in the different maps also presents a problem. While Soliman includes stratified, wavy, and slug flows in one regime, the Mandhane and Taitel-Dukler maps treat these as three separate regimes. Similarly, the Mandhane and Taitel-Dukler maps do not have a separate mist flow regime, while Soliman's map does. The possibility for an incorrect placement clearly increases with the number of distinct flow regimes.

Given these difficulties, a discussion of the merits and drawbacks of each technique seems more suitable.

The unmodified map of Mandhane was an extremely poor predictor of the experimental data from this study. This was because the vapor densities from this study were much higher than those from which the map was developed. A simple correction to the superficial velocities of the vapor and liquid phases overcomes this problem, and gives each axis the physical interpretation of square root of kinetic energy. With this correction applied, the Mandhane map was an excellent predictor of the experimental data and the easiest of the three methods to use. Based on the data from this study and earlier suggestions from the literature, the flow regime described as wavy-annular in this study lies in the right portion of the slug flow region on the Mandhane map. The region labeled as annular flow corresponds closely with the establishment of a nearly symmetric annular film. The absence of a diameter dependence could prove problematic for very small tubes, but was not a significant problem for the range of this study.

The Taitel-Dukler map successfully distinguished the stratified and wavy flow regimes at 18 and 55 klb_m/ft^2-hr for each refrigerant. Also, the increase in the length of the slug flow region as reduced pressure was increased was correctly predicted. The main difference between the predictions of the Taitel-Dukler map and the observed flow regimes was found at mass fluxes slightly above the wavy flow transition line. For this range of mass flux, the Taitel-Dukler map predicts that slug flow at low qualities is followed immediately by annular flow for the remainder of the quality range. The experimental observations in this region indicated that the slug flow regime was consistently followed by wavy, wavy-annular, and annular flows as the quality was increased. Observations of wavy-annular flow in the region predicted to be annular flow are not due to a deficiency in the Taitel-Dukler technique, since wavy-annular flow represents an early stage of annular flow in their terminology. Observations of wavy flow where annular flow was predicted do represent an error, but are possibly due to subjectivity in classification. Perhaps the most important conclusion concerning this map, though, is that significant stratification of the liquid can be expected in the lower part of the range labeled as annular flow on the Taitel-Dukler map. This stratification is most significant at low qualities, or high values of the Lockhart-Martinelli parameter. For pipe diameters smaller than those used in this study, each of the flow regime transitions predicted by the Taitel-Dukler map should be examined for surface tension influences.

The Soliman flow regime predictors, although less theoretically justified than those of Taitel and Dukler, matched the experimental observations very well. As is true for the other flow regime maps, one must make sure that the definitions of the different regimes are clearly understood. The wavy flow region of Soliman includes stratified flow, wavy flow, and slug flow. With this in mind, the annular flow transition predicted by Soliman corresponded very well with the wavy to wavy-annular transition from this study. It has been shown elsewhere [Dobson, 1994] that the transition from wavy-annular to annular flow is well predicted by a value of $Fr_{so}=18$ (as opposed to 7 for the wavy to wavy-annular transition). The region labeled as mist flow by Soliman was found to correspond well with the annular-mist flow regime in this study (despite indications to the contrary in the original paper). Pure mist flow without a stable wall film was confined to qualities greater than 90%, however, and even then appeared to become annular-mist once condensation began. This will be shown to have serious implications for heat transfer analysis.

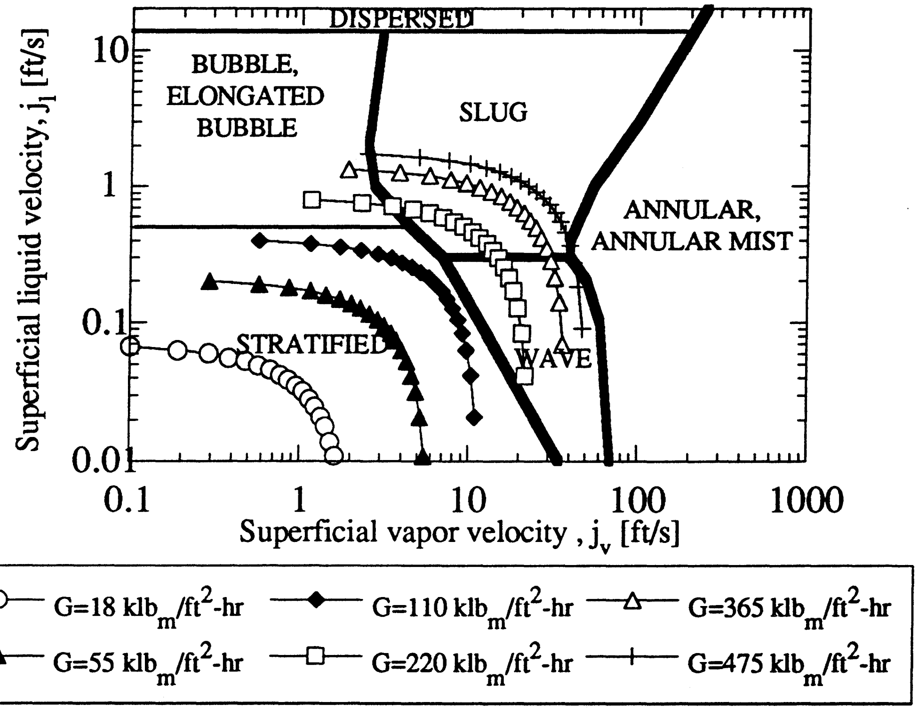

Figure 5.1 Predicted flow patterns for R-134a on the Mandhane [1974] map.

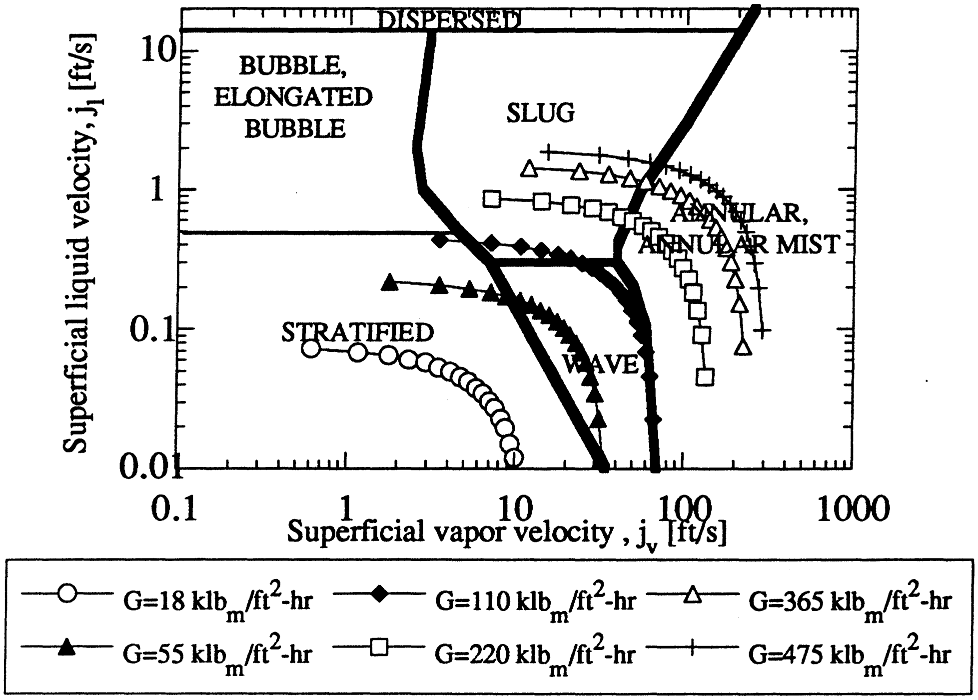

Figure 5.2 Predicted flow patterns for R-134a on the Mandhane [1974] map using corrected superficial velocities.

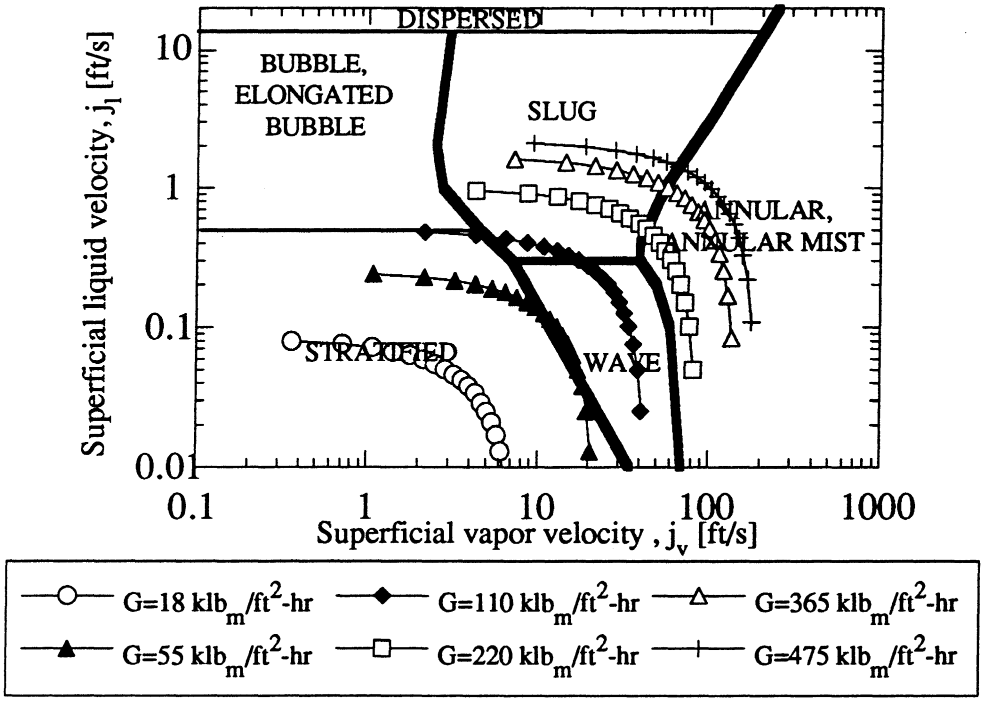

Figure 5.3 Predicted flow patterns for R-32/R-125 at 113°F on the Mandhane [1974] map using corrected superficial velocities.

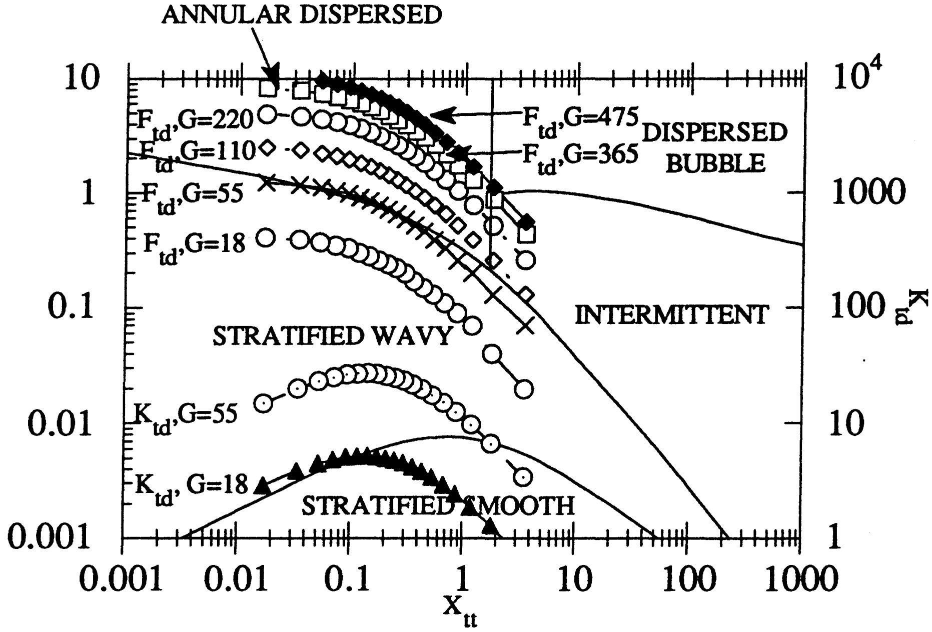

Figure 5.4 Flow regime predictions of the Taitel-Dukler [1976] map for R-134a at 95 °F in the .278" i.d. tube.

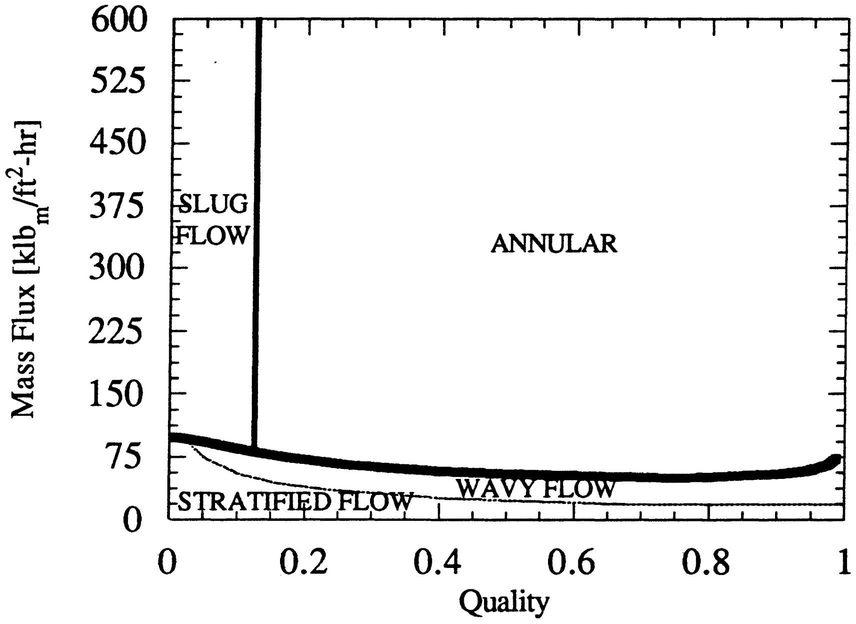

Figure 5.5 Taitel-Dukler [1976] predictions on G-x coordinates for R-134a at 95 °F in a .278" i.d. tube.

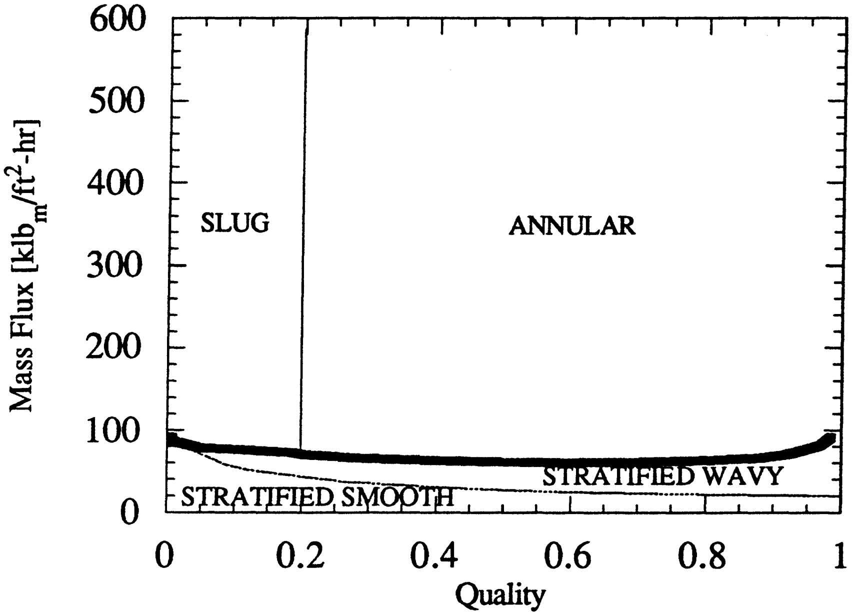

Figure 5.6 Taitel-Dukler [1976] predictions on G-x coordinates for R-32/R-125 at 113 °F in a .278" i.d. tube.

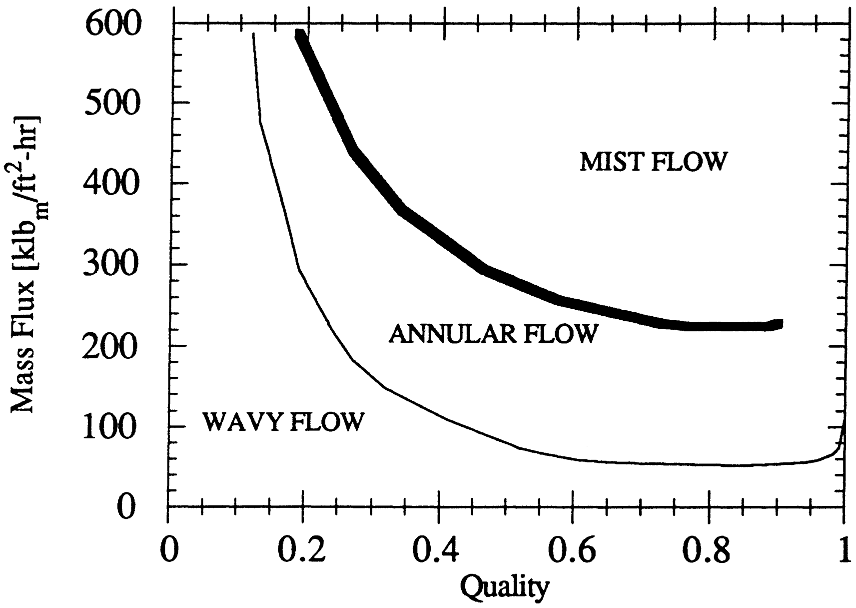

Figure 5.7 Soliman [1982, 1983] predicted flow regimes on G-x coordinates for R-134a at 95 °Fin a .278" i.d. tube.

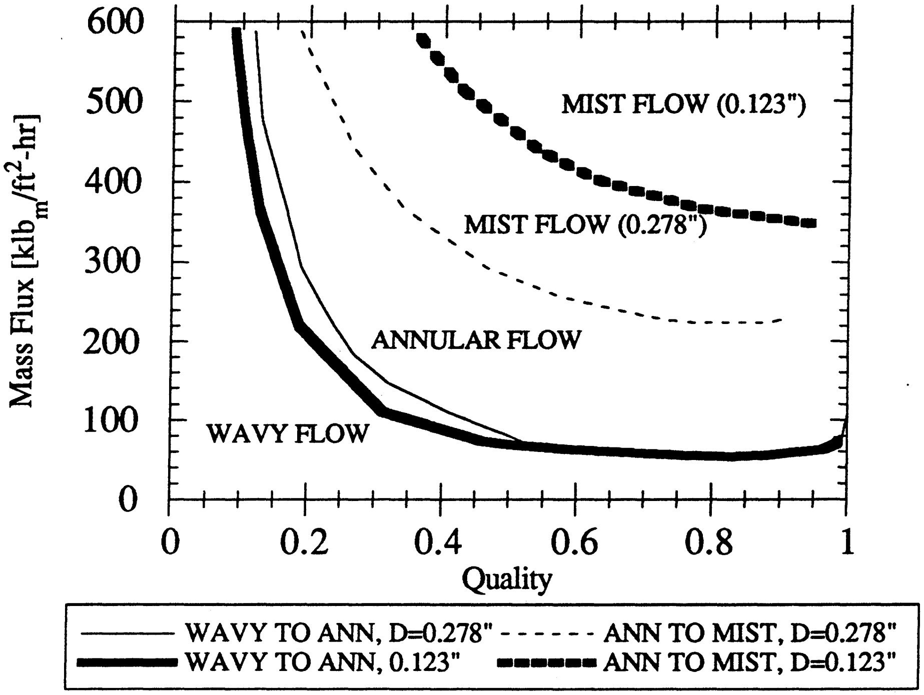

Figure 5.8 Effect of diameter predicted by Soliman's [1982,1983] flow regime criteria.

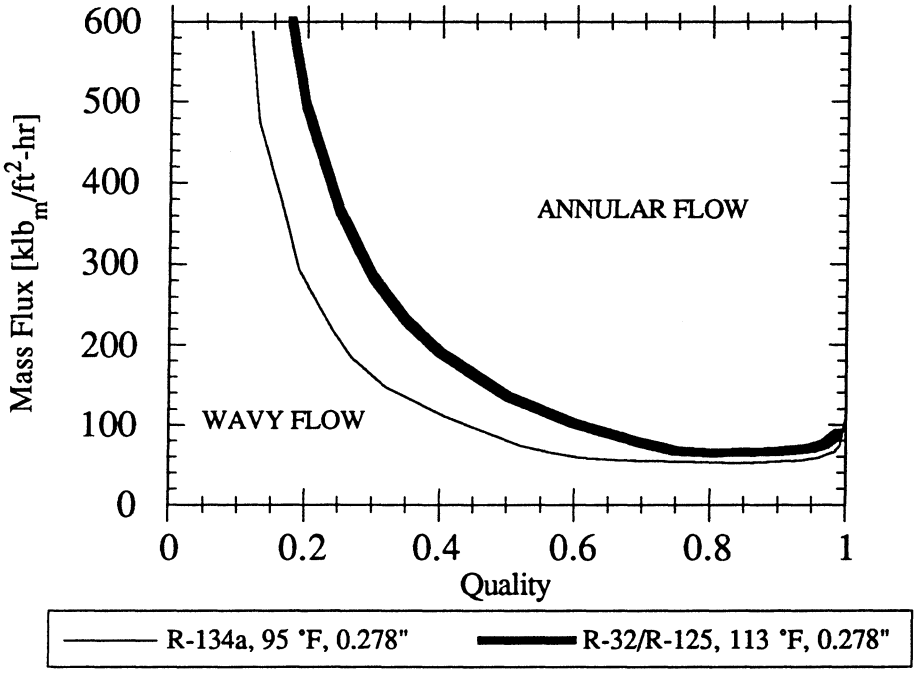

Figure 5.9 Effect of reduced pressure on Soliman's [1982] wavy to annular flow regime transition.

CHAPTER 6

HEAT TRANSFER RESULTS

This chapter presents the heat transfer data from the present study and the correlations that were developed using these data. First, the experimental data are presented to illustrate the effects of mass flux, quality, and temperature difference. The flow regime results are called on frequently within this discussion, since the heat transfer phenomena differed widely based on the flow regime. The experimental heat transfer data are compared with several of the correlations that were discussed in Chapter 2. Deficiencies in these correlations are noted, since these helped guide the development of the final heat transfer correlations.

Next, the development of the heat transfer correlations for the wavy and annular flow regimes is discussed. Development of the annular flow correlation is preceded by a comparison of the three types of annular flow correlations that were discussed in Section 2.5. This comparison shows the strong similarities between the three types of correlations, lending technical merit to the widely used two-phase multiplier correlations. This discussion also demonstrates the robustness of these correlations to the simplifying assumptions used in their development. The annular flow correlation from this study is then described.

Development of the wavy flow correlation is then discussed. This development was guided by relevant results from external condensation in conjunction with trends from the experimental data. An analysis to assess the impact of the vapor velocity on filmwise condensation is summarized. The analysis verified the basic applicability of filmwise condensation results from external condensation for flows inside a tube. The applicability of neglecting the heat transfer in the bottom of the pool during wavy flow condensation is addressed by carefully examining the experimental data.

Data from the wavy-annular flow regime were compared to both correlations to determine whether the heat transfer mechanism in this regime was more similar to annular or wavy flow condensation. At low mass fluxes, the heat transfer behavior in the wavy-annular flow regime was more indicative of wavy flow. At high mass fluxes, the heat transfer behavior was indicative of forced convective condensation across the entire quality range. These observations were used to develop limits of applicability for each of the heat transfer correlations. The correlations are compared to data from the present study and external data sources.

6.1 Experimental Heat Transfer Data

The experimental apparatus was used to collect condensing heat transfer data for four refrigerants in the three tubes described in Chapter 3. These tubes were .123", .180", and .278" in diameter. As discussed previously, only the data from the .123" and .278" i.d. tubes were used to develop the heat transfer coefficient models because of increased accuracy in these tubes. Overall, 261 heat transfer points were collected in the .123" i.d. tube and 387 heat transfer points were collected in the .278" i.d. tube. These points included data in the smooth-stratified, wavy-stratified, wavy-annular, annular, and annular-mist flow regimes. The nominal range of parameters over which these data were collected is described in Tables 4.3 and 4.4. Additional tests to clearly illustrate certain trends are also discussed in this chapter.

6.1.1 Overall trends --effect of mass flux and quality

Figure 6.1 presents heat transfer data for R-32/R-125 in the .123" i.d. tube at a saturation temperature of 95 °F. These data illustrate the general effects of mass flux and quality rather clearly. At the lowest mass flux of 55 klb_m/ft^2-h, the Nusselt number increased very modestly as the quality was increased. A similar quality dependence was exhibited as the mass flux was doubled to 110 klb_m/ft^2-h. Perhaps more interesting, the Nusselt numbers remained nearly identical as the mass flux was doubled. As the mass flux was doubled once again to 220 klb_m/ft^2-h, a different trend began to emerge. At low qualities, the heat transfer coefficients remained nearly identical to the lower mass flux cases. As the quality was increased to around 30%, the Nusselt number began to display a much more pronounced effect of quality. At mass fluxes above 220 klb_m/ft^2-h, the dependence of the Nusselt number on quality remained similar. Even at low qualities, the Nusselt numbers were substantially higher than those for the low mass flux cases.

The same data are presented in an alternate way in Fig. 6.2. Figure 6.2 presents the variation of Nu with mass flux for three different qualities (0.25, 0.50, and 0.75). Since experimental data were not available at exactly these qualities, some of the points in the figure were obtained by interpolation. For each quality, the heat transfer coefficient remained relatively constant at low mass fluxes. At a sufficiently high mass flux, the slope of the heat transfer versus mass flux curve exhibited a distinct change in slope. At mass fluxes beyond this point, this slope remained relatively constant. The mass flux at which this change in slope occurred increased as the quality was decreased. For the 25% quality points, this shift was delayed until a mass flux of 220 klb_m/ft^2-h, .

The change in heat transfer behavior exhibited in Fig. 6.1 and Fig. 6.2 is closely linked to changes in the two-phase flow regime. For the two lowest mass fluxes, 55 and

110 klb_m/ft^2-h, wavy or wavy-annular flow prevailed over much of the quality range. In the wavy flow regime, heat is transferred primarily by conduction across the thin condensate film at the top of the tube. This condensate flows down the tube under the action of gravity, and is then transported out of the tube in the liquid pool at the bottom of the tube as shown in Fig. 6.3. The modest increase in heat transfer coefficient with quality in this flow regime occurs because of the corresponding increase in interfacial area (or increase in ϕ). The primary item affecting the heat transfer coefficient in this flow regime is the film thickness. Since the film thickness is insensitive to mass flux in the wavy flow regime, wavy flow heat transfer coefficients are also relatively insensitive to mass flux.

At the highest mass fluxes of 365, 475, and 585 klb_m/ft^2-h, annular flow prevailed over most of the quality range as pointed out in Chapter 5. In the annular flow regime, correlations such as those of Soliman [1968] and Traviss [1973] clearly illustrate the interdependence between pressure drop and heat transfer $\left(h \propto \sqrt{\Delta P/\Delta z}\right)$. Since the pressure drop increases sharply as the quality is increased, the heat transfer coefficients in the annular flow regime show significant quality dependence.

Perhaps the most interesting heat transfer trends were displayed at a mass flux of 220 klb_m/ft^2-h, At this mass flux, the flat Nu versus x behavior that is characteristic of wavy flow was observed at low qualities while annular flow behavior was observed at higher qualities. The change in slope of the Nusselt number versus quality graph occurred between 30% and 40% quality, which corresponded closely with an observed change from the wavy-annular to the annular flow regime. At this mass flux, it would be inappropriate to use a single heat transfer model over the entire quality range.

6.1.2 Tube diameter effects

The effect of tube diameter on heat transfer coefficients was largely as expected. As will be shown in later sections, the relationships between h and D that were predicted by annular and wavy flow heat transfer correlations agreed well with the experimental data. Although this was expected for the .278" i.d. tube, a commonly used and tested size, some doubt existed about whether the heat transfer behavior in the .123" i.d. tube would correspond with that predicted by "large tube" correlations.

The most noticeable effect of the tube diameter had to do with the point at which the heat transfer mechanism changed from filmwise (wavy) to forced convective (annular). This point is demonstrated by Fig. 6.4, which shows the variation of Nu with quality for R-32/R-125 in the .278" i.d. tube at 95 °F. This is the same refrigerant and saturation temperature for which data are shown in Fig. 6.1, with the only difference being the increased tube diameter. The primary difference in the heat transfer behavior in the two tubes was observed at a mass flux of 220 klb_m/ft^2-h, . In the .123" i.d. tube, the heat transfer behavior showed a change in slope between 30% and 40% quality as the flow regime changed from wavy-annular to annular. In the larger .278" i.d. tube, this transition was only observed for the highest quality point (89%). Again, it corresponded closely with an observed transition to annular flow at around 80% quality. The heat transfer characteristics at the other mass fluxes were similar in both tubes.

6.1.3 Effect of changes in refrigerant

A comparison of wavy flow heat transfer for R-134a, R-22, and 50/50 R-32/R-125 is made in Fig. 6.5. This figure shows the heat transfer coefficients at a mass flux of 55 klb_m/ft^2-h, and a saturation temperature of 95 °F in the .278" i.d. tube. Since the wavy flow heat transfer coefficients are dependent on the refrigerant to wall temperature difference, this difference was maintained near 5.4 °F (5.17 °F to 5.60 °F) for all the tests. Perhaps the primary conclusion from these data is that little difference exists in the wavy flow heat transfer coefficients of the three fluids, with a maximum difference of around 10%. It appeared that the highest heat transfer coefficients were obtained for R-22, followed by R-134a and R-32/R-125. Based on the wavy flow property index from the Chato [1962] correlation, $\left[\rho_l(\rho_l-\rho_v)k_l^3 i_{lv}/\mu_l\right]^{0.25}$, R-32/R-125 would be expected to have the highest wavy flow heat transfer coefficients (4.7% above R-134a), followed by R-22 (3.5% above R-134a) and R-134a. These predicted differences are very small in light of the considerable uncertainty in transport properties. The index itself also neglects the effect of void fraction variations between the fluids, which would tend to reverse the predicted differences.

Figure 6.6 compares the annular flow heat transfer coefficients of R-134a, R-22, and 50/50 R-32/R-125. These data were collected at a mass flux of 475 klb_m/ft^2-h, and a saturation temperature of 95 °F in the .278" i.d. tube. The best fluid for annular flow heat transfer was R-134a, while the heat transfer coefficients of R-22 and R-32/R-125 were nearly identical. The single-phase liquid heat transfer index, $k_l^{0.6}c_{pl}^{0.4}/\mu_l^{0.4}$, was highest for R-32/R-125, followed by nearly identical values for R-134a and R-22. This resulted in R-32/R-125 having slightly better annular flow heat transfer than the other fluids at low qualities, where the heat transfer coefficient was close to the single-phase liquid value. As the quality was increased, the two-phase multiplier increased in value and became increasingly important. The two-phase multiplier was highest for R-134a, the lowest reduced pressure fluid. This resulted in R-134a having higher heat transfer coefficients than the other fluids at high qualities.

Figures 6.5 and 6.6 compared the heat transfer coefficients of the fluids at mass fluxes where one flow regime prevailed over the entire quality range. At intermediate mass fluxes, a transition quality was reached where the flow regime and heat transfer characteristics changed from wavy flow to annular flow. This point was also affected by the fluid, as discussed in Chapter 5. Based on the flow regime results, one would expect annular flow to occur at lower qualities for R-134a than for R-32/R-125. This is demonstrated in Fig. 6.7, which compares the heat transfer coefficients of R-134a, R-22, and R-32/R-125 at a mass flux of 220 klb$_m$/ft^2-h, . At this mass flux, the quality where the wavy-annular to annular transition occurred was 40% for R-134a, 50% for R-22, and 72% for R-32/R-125. The heat transfer points were connected with lines in this figure to make changes in slope clearer. The data showed that, as expected, the change in slope occurred slightly earlier for R-134a than for the other fluids. At the highest qualities, where annular flow was observed for all fluids, R-134a had the highest heat transfer coefficients of the three fluids. Across the full range of quality, the heat transfer coefficients of the three fluids were within 10%.

6.1.4 Effect of temperature difference

As indicated in the literature review, the refrigerant to wall temperature difference has an impact on the heat transfer coefficients in the wavy flow regime. This dependence occurs because, for a falling film, a larger driving temperature difference results in a thicker film at a given location (hence lower heat transfer coefficients). In the annular flow regime, a significant amount of experimental and analytical evidence suggests a negligible impact of temperature difference or heat flux. Studying the impact of temperature difference on the heat transfer coefficients then provides a non-visual method of assessing the extent of filmwise and/or forced convective condensation.

Unlike evaporation experiments where the heat flux can be controlled with a variac, precisely controlling the temperature difference during internal condensation experiments is very difficult. For this reason, few internal condensation data are available for which the temperature difference was deliberately controlled. This was also the case for much of the data collected in this study. To gain an added understanding of ΔT effects, though, the temperature difference was controlled at two different levels for all mass fluxes during testing with R-22 and R-32/R-125 in the .278" i.d. tube.

Figure 6.8 shows the variation of Nusselt number with quality for R-32/R-125 at a saturation temperature of 95 °F and a mass flux of 55 klb$_m$/ft^2-h. The two different sets of points correspond to temperature differences of approximately 3.6 °F (3.38 °F to 3.82 °F) and 5.4 °F (5.17 °F to 5.60 °F). As predicted by Nusselt theory, the Nusselt numbers were lower for the higher temperature difference data across the full range of quality. These same data were corrected for varying temperature differences by computing the quantity $Nu/[Ga*Pr/Ja]^{0.25}$. If all of the heat transfer occurred by filmwise condensation and none occurred in the bottom of the tube, this correction should collapse the two different sets of data onto a single line. Figure 6.9 shows that, to a large extent, making this correction does just that. As the quality approaches unity and the liquid pool vanishes, moreover, the value of $Nu/[Ga*Pr/Ja]^{0.25}$ appears to properly approach the accepted value of 0.728 for condensation on a horizontal cylinder.

Figures 6.10 through 6.12 present similar plots for R-32/R-125 in the .278" tube as the mass flux was increased to 220 klb_m/ft^2-h, and 475 klb_m/ft^2-h. The trends are very interesting. At 220 klb_m/ft^2-h, the unmodified Nusselt numbers increased with decreasing temperature difference up to a quality of 75%. At that point, they appeared to converge as would be expected for annular flow. In Fig. 6.11, the quantity $Nu/[Ga*Pr/Ja]^{0.25}$ is plotted for the same set of data. The trends on this plot are "flipped" in comparison to the data of Fig. 6.10, with the highest values of $Nu/[Ga*Pr/Ja]^{0.25}$ occurring for the highest values of ΔT. This indicates that at this mass flux, additional heat transfer by forced convective condensation resulted in a dependence on ΔT less than the -0.25 power dependence from Nusselt theory. Stated another way, the heat transfer in the bottom of the liquid pool was no longer negligible. Figure 6.12 shows that at a mass flux of 475 klb_m/ft^2-h, the unmodified Nusselt numbers exhibited no dependence on temperature difference, as expected for annular flow.

6.2 Comparison With Existing Heat Transfer Correlations

Several correlations from the literature were selected for comparison with the experimental data. For the wavy flow data, the correlations of Chato [1962], Jaster and Kosky [1976], and Rosson and Myers [1965] were selected. The correlations of Shah [1979], Cavallini and Zecchin [1974], Traviss et al. [1973], and Chen [1987] were selected for comparison with the annular flow data.

6.2.1 Gravity-dominated correlations

Figure 6.13 compares the experimental data with the Chato [1962] correlation. Chato's correlation was developed for stratified flow, and was recommended for use at vapor Reynolds numbers of less than 35,000. It was compared with 210 experimental data points that met this criteria, and had a mean deviation of 12.8%. The primary deficiency in the Chato correlation was that it predicted no variation of the Nusselt number with quality. Comparisons with the wavy flow data presented earlier show that such variations did exist.

Figure 6.14 compares the experimental data with the correlation of Jaster and Kosky [1976]. The range of applicability for their correlation is specified by an upper limit of a dimensionless wall shear, $F_{jk}=5$. The data presented in Fig. 6.14 represent the 213 experimental points which met this criterion. The mean deviation between the experimental data and the predicted values was 14.5%, slightly higher than the simpler Chato correlation. Although the deviations between their correlation and the present data were sometimes large, the mean deviation of 14.5% was substantially better than the 37% standard deviation with their own data.

Figure 6.15 compares the experimental data with the correlation of Rosson and Myers [1965]. Since no guidelines were given for when to use this correlation, it was compared against the full database of points that were later used to develop the wavy flow correlation for this study. Although Rosson and Myers attempted to account for forced convective condensation in the liquid pool at the bottom of the tube, unlike Chato and Jaster and Kosky, Fig. 6.15 shows that their correlation was actually a worse predictor of the experimental data. The correlation had a mean deviation of 21.3% with the experimental data, almost 10% worse than the simpler Chato and Jaster and Kosky correlations. The most problematic part of the correlation seemed to be prediction of the parameter β, which represents the fraction of the tube circumference occupied by filmwise condensation. At low mass fluxes, this parameter should clearly be related to the void fraction and approach unity as the quality approaches unity. The empirical expressions developed by Rosson and Myers do not behave in this manner, however. Figure 6.16 shows the predicted variation of β with quality for R-134a in a .278" i.d. tube at mass fluxes of 18, 36, 55, and 110 $\mathrm{klb_m/ft^2}$-h. The trends were very erratic, particularly for mass fluxes over 18 $\mathrm{klb_m/ft^2}$-h, where the relationship was not even monotonic. The success of each of the gravity-dominated correlations in predicting the experimental heat transfer data is summarized in Table 6.1

Table 6.1 Comparison of wavy flow heat transfer data with correlations

Correlation	Mean Deviation	Maximum Deviation	% of Points within ±10%	% of Points within ±25%
Chato	12.8%	67%	52%	79%
Jaster & Kosky	14.5%	51%	39%	71%
Rosson & Myers	21.3%	68%	26%	60%

6.2.2 Annular flow correlations

The annular flow correlations that were selected for comparison with the experimental data were those of Shah [1979], Cavallini and Zecchin [1974], Traviss et al. [1973], and Chen et al. [1987]. These correlations encompass at least one member of each of the three broad classes discussed in Section 2.5 -- two-phase multiplier correlations (Shah, Cavallini and Zecchin), shear-based correlations (Chen), and boundary layer analyses (Traviss).

Of the four correlations, only Shah's [1979] came with specific guidelines for a lower limit of applicability. Shah stated that his correlation should not be used at mass fluxes where the vapor velocity with x=1 was less than 9.8 ft/s. For R-134a at 95 °F, this corresponds to a lower mass flux limit of 95 $\mathrm{klb_m/ft^2}$-h. This value is higher for the other refrigerants, which have higher vapor densities. In all cases, this represents a vapor velocity well above the wavy to annular transition line on the Taitel-Dukler map. This criterion was selected for each of the correlations so that they would be compared on an equal basis.

The predictions of the Shah correlation are compared to the selected data in Fig. 6.17. The predictions agree fairly well with the data, with a mean deviation of 9.1%. Nearly all of the data were predicted within ±25%. The most significant deviations occurred for some low Nusselt number data that were in the wavy-annular flow regime, and some very high mass flux, high quality data. In general, the Shah correlation seemed to underpredict the experimental data.

The predictions of the Cavallini and Zecchin correlation are compared with the experimental data in Fig. 6.18. The mean deviation of this correlation with the experimental data was 11.6%, slightly higher than the Shah correlation. Despite the slightly higher mean deviation, though, the predictions of the Cavallini-Zecchin correlation were more correct in trend than those of the Shah correlation. When the

Cavallini-Zecchin correlation was in error, it tended to overpredict the experimental data. The largest errors occurred at low qualities. This is because the Cavallini-Zecchin approaches a value of 2.18 times the single-phase Nusselt number at a quality of zero.

The predictions of the Traviss are plotted versus the measured Nusselt numbers in Fig. 6.19. The mean deviation of the Traviss correlation was 11.8%, slightly higher than the Cavallini-Zecchin correlation. The Traviss correlation tended to overpredict the experimental data. This overprediction was most pronounced at high qualities, where their empirical correction was used. If this correction was omitted, their correlation would have underpredicted the high quality data.

The Chen correlation is compared to the experimental data in Fig. 6.20. This correlation was the worst predictor of the annular flow data, with a mean deviation of 23.3%. This correlation significantly underpredicted nearly all of the data. The correlation of Soliman [1968], discussed in Section 2.5, generally predicts lower Nusselt numbers than the Chen correlation. Thus, it would have performed even worse against the present data. Relevant statistics comparing the four annular flow correlations are presented in Table 6.2.

Table 6.2 Comparison of annular flow heat transfer data with correlations

Correlation	Mean Deviation	Maximum Deviation	% of Points within ±10%	% of Points within ±25%
Shah	8.8%	46.1%	68%	94%
Cavallini & Zecchin	11.6%	85.7%	59%	90%
Traviss et al.	11.8%	39.2%	47%	93%
Chen et al.	23.3%	71.0%	13%	61%

6.2.3 Discussion of heat transfer correlations

The correlations of Chato [1962] and Jaster and Kosky [1976] were both able to predict most of the experimental data for the wavy flow regime within a range of ±25%. Neither predicted the variation with quality successfully, and neither accounted for heat transfer in the bottom of the liquid pool. For very low mass fluxes, this assumption is reasonable. The flow regime and heat transfer data showed, though, that some contribution from filmwise condensation persisted to mass fluxes where this assumption is no longer valid. Accounting for this was the purpose of the Rosson and Myers [1965] correlation. This correlation, though, was the worst predictor of the experimental data. The poor predictive ability of this correlation was likely due to a flawed method of weighting the filmwise and forced convective heat transfer components.

The annular flow correlations, with the exception of the Chen correlation, were slightly better predictors of much of the heat transfer data. The lowest mean deviation was obtained for the Shah correlation, although it underpredicted much of the data. The Cavallini-Zecchin correlation was very successful at predicting the Nusselt numbers at high quality, but did not approach a single-phase Nusselt number at zero quality.

One problem with the annular flow correlations that is not apparent in a plot of experimental versus predicted Nusselt numbers concerns their range of applicability. Figure 6.21 compares experimental and predicted Nusselt numbers versus quality for R-22 in the .278" i.d. tube at a mass flux of 165 klb_m/ft^2-h and a saturation temperature of 95 °F. According to the Taitel-Dukler maps, this mass flux should be annular at all qualities above 12%. The velocity with vapor only would be 12.8 ft/s, 30% above the lower limit of applicability specified by Shah. Thus, the best information available in the literature would suggest that annular flow correlations should be applicable over nearly the entire quality range. Still, Fig. 6.21, shows that the Nusselt numbers were well above the annular flow predictions at low qualities. As the quality reached about 70% and the flow pattern became fully annular, the predictions of the Cavallini and Zecchin correlation agreed very well with the experimental data. These data suggest that the need for further development of heat transfer models in the wavy or wavy-annular regions at higher mass fluxes.

6.3 Development of the Heat Transfer Correlations

In this section, the development of the annular flow correlation for forced convective condensation is first described. This discussion establishes the strong similarities between the most theoretical approach for annular flow condensation, the boundary layer analyses, and the simpler two-phase multiplier approaches. Then, an annular flow correlation is developed using the two-phase multiplier approach. Next, the wavy flow data from this study are used to develop a wavy flow correlation. This correlation uses a similar approach to that unsuccessfully tried by Rosson and Myers [1965], but with more attention paid to carefully weighting the forced convective and filmwise components. Finally, the data from the wavy-annular flow regime are compared with predictions of the wavy and annular flow correlations. These comparisons are used to develop limits of applicability for the two correlations.

6.3.1 Annular flow correlation

Before the annular flow correlation is developed, a brief review of the various correlating forms is warranted. The most theoretical correlation that has been widely used is the Traviss correlation. Under the rather stringent assumptions listed in Section 2.5.3, this method provides an analytical prediction of the Nusselt number. Before a pressure drop model is assumed, the correlation can be written as follows:

$$\mathrm{Nu} = \frac{D^{+}\,\mathrm{Pr}_l}{F_2(\mathrm{Re}_l, \mathrm{Pr}_l)} \tag{6.1}$$

The term D^{+} in Eq. (6.1) is the tube diameter scaled by the turbulent length scale, $\nu_l / \sqrt{\tau_w/\rho_l}$. A simple force balance indicates the proportionality between the wall shear and the pressure drop, establishing the fact that the annular flow Nusselt number is proportional to the square root of the pressure drop per unit length. This dependence becomes important later as design issues are addressed.

The denominator of Eq. (6.1), F_2, can be thought of as a dimensionless heat transfer resistance. Physically, this resistance increases as the dimensionless film thickness increases as would be expected from conduction arguments. It also increases with increasing Prandtl numbers, since high Prandtl numbers reflect more effective transfer of momentum than heat. This function is dependent on the liquid Reynolds number since, under the assumptions of a symmetric annular film and no entrainment, specifying the liquid Reynolds number uniquely specifies the dimensionless film thickness. Equations (2.80a-c) describe the functional form of the dimensionless film thickness. A piecewise function is obtained because of the piecewise nature of the universal velocity profile. The function that is valid for the lowest range of Reynolds number, $\mathrm{Re}_l<50$, corresponds to films so thin that they are entirely contained in the laminar sublayer. The next two levels correspond, respectively, to films that end in the buffer layer and fully turbulent regions. A plot of F_2 versus Re_l for various values of Pr_l is shown in Fig. 6.22. The trends from this plot are very interesting. As Re_l increases from 0 to 1125 (the value where the fully turbulent region begins), F_2 increases very rapidly. As Re_l is increased further, F_2 increases much more slowly. Physically, this occurs because the primary resistance to heat transfer is contained in the laminar sublayer and buffer regions.

Although the Traviss analysis was performed after the advent of the simple shear-based correlations, it provides a useful method for understanding them. For relatively small changes in Re_l when $\mathrm{Re}_l >1125$, one could reasonably assume a constant value of

F_2 at a fixed Prandtl number. If the Prandtl number dependence could be expressed as a power law function[1], the Nusselt number could then be expressed as:

$$\mathrm{Nu} = aD^+ \,\mathrm{Pr}_l^m \tag{6.2}$$

This is exactly the form of the original shear-based correlation of Carpenter and Colburn [1951]. Thus, these correlations are justified for a narrow range of conditions by the more theoretically sound analysis of Traviss.

Only a few more manipulations are required to show the equivalence between the Traviss analysis and the two-phase multiplier approaches. The first important observation is that annular flow is seldom encountered for liquid Reynolds numbers less than 1125. Using the criteria for annular flow that $Fr_{so}=18$, Eq. (2.31a) was solved for the quality above which annular flow could exist with $Re_l = 1125$. For R-134a at 95 °F, a value of over 99.5% was obtained in the .278" i.d tube and a value of over 97.5% was obtained in the .123" i.d. tube. This indicates that the liquid film is seldom so thin that the fully turbulent region is not reached, thus the piecewise definition of F_2 is seldom necessary. With F_2 confined to values of $Re_l > 1125$, a power law function of Re_l and Pr_l was used to curve fit the function F_2. For a range of Re_l from 1125 to 10^5 and Pr_l from 1 to 10, F_2 was well approximated by the following function:

$$F_2 \cong 10.25\,\mathrm{Re}_l^{0.0605}\,\mathrm{Pr}_l^{0.592} \tag{6.3}$$

If this approximation is used in Eq. (6.1), and D^+ is evaluated with a pressure drop correlation using Lockhart and Martinelli's two-phase liquid multiplier approach, the following equation for the Nusselt number is obtained:

$$\mathrm{Nu} = \frac{\sqrt{0.0791/2}\,\mathrm{Re}_l^{0.875}\,\phi_l(X_{tt})\,\mathrm{Pr}_l}{10.25\,\mathrm{Re}_l^{0.0605}\,\mathrm{Pr}_l^{0.592}} = 0.0194\,\mathrm{Re}_l^{0.815}\,\mathrm{Pr}_l^{0.408}\,\phi_l(X_{tt}) \tag{6.4}$$

This is identical in form, and close in value, to the commonly used two-phase multiplier correlations. A two-phase multiplier correlation using the Dittus Boelter correlation for the single-phase heat transfer coefficient, such as the one of Shah [1979], takes the form:

$$\mathrm{Nu} = 0.023\,\mathrm{Re}_l^{0.8}\,\mathrm{Pr}_l^{0.4}\,\underbrace{F\left[P_{rd}^{0.4}\left(\frac{1-x}{x}\right)^{0.8}\right]}_{\text{2-phase multiplier}} \tag{6.5}$$

---

[1] This will be shown subsequently

There is little difference in the form of Eq. (6.4) and Eq. (6.5), except that Shah used a slight modification of the Lockhart-Martinelli parameter for correlating his two-phase multiplier.

If the correlation of Traviss [1973] proved to be the most accurate predictor of experimental data, modifying it would make little sense and the discussion above would be pointless. In fact, even Traviss found that their correlation underpredicted their own data at high qualities. For this reason, they arbitrarily replaced their two-phase multiplier (which they call F rather than ϕ_l) with $F^{1.15}$ at high qualities ($X_{tt}<0.155$). Rather than modifying this function, which was an empirical fit to two-phase pressure drop data to begin with, it appears equally reasonable to determine the function directly from condensing heat transfer data. This is exactly the approach of the two-phase multiplier correlations. Hopefully, the derivation above demonstrates their basic validity in a somewhat more rigorous manner than has been done previously.

One additional benefit of dissecting the Traviss correlation is that it demonstrates the robustness of annular flow heat transfer correlations to the rather serious assumptions used in their derivation. The most serious of these assumptions are: (1) extrapolating the universal velocity profile from single-phase pipe flow, (2) a symmetric annular film, and (3) no entrainment of liquid in the vapor core.

With regard to the first assumption, the presence of waves at the free surface would be expected to cause deviations from the universal velocity profile. However, the impact of these waves is likely to be small in the region closest to the wall where most of the resistance to heat transfer occurs.

With respect to the second assumption, the symmetric annular film, gravity definitely results at a thinner film at the top of the tube than at the bottom. Since the heat transfer is relatively insensitive to variations in film thickness provided that the film remains thicker than the buffer layer, though, these effects would not be expected to significantly alter the heat transfer results.

The impact of violating the third serious assumption, that of no entrainment, can also be assessed from Traviss' analysis. This assumption is necessary when invoking the conservation of liquid statement, which in turn determines the dimensionless film thickness. If the entrained mass fraction E were known, the film Reynolds number used for determining F_2 could be replaced by:

$$Re_l^{corr} = Re_l(1-E) \tag{6.6}$$

Since F_2 only depends on Re_l to the 0.06 power, though, a value of E=0.8 would only increase the Nusselt number by 10%. Provided that the entrainment rate does not become high enough to remove liquid from the laminar sublayer or buffer layer, then, it appears that the role of entrainment on heat transfer should be small.

Based on the work above, the two-phase multiplier approach was selected for correlating the annular flow heat transfer data from this study. To make sure that the correlation was not biased by data outside of the annular flow regime, only data with $Fr_{so}>20$ were used to develop the correlation. This value was previously reported to provide a good indicator of the transition from wavy-annular to annular flow [Dobson, 1993], and agreed well with the data from this study. The following correlating form was selected:

$$Nu = 0.023 Re_l^{0.8} Pr_l^{0.4}\left[1+\frac{a}{X_{tt}^n}\right] \tag{6.7}$$

This form utilizes the single-phase heat transfer correlation of Dittus Boelter [1930] with a Prandtl exponent of 0.4. This value would normally be used for heating rather than cooling, but was selected for this study for three reasons: (1) it was nearly identical to the value obtained by curve-fitting the Traviss correlation, (2) it provided a better fit to the more accurate single-phase correlations (e.g. Gnielinski and Petukov Popov) in the range of Re and Pr from this study, and (3) it has been used with some success by Shah for fluids other than refrigerants. At a quality of zero, the Lockhart-Martinelli parameter approaches infinity and Eq. (6.7) predicts a single-phase liquid Nusselt number.

Values of the constants a and n in Eq. (6.7) were determined by regression analysis of $\ln\left(Nu/\left(0.023Re_l^{0.8}Pr_l^{0.4}\right)-1\right)$ versus $\ln(X_{tt})$ for the entire set of data. The resulting values were adjusted slightly to result in the following final correlation:

$$Nu = 0.023 Re_l^{0.8} Pr_l^{0.4}\left[1+\frac{2.22}{X_{tt}^{0.889}}\right] \tag{6.8}$$

Equation (6.8) is compared to the annular flow data from this study in Fig. 6.23. The overall agreement with the data is excellent, with a mean deviation of 4.5%. Over 67% of the data points were predicted to within ±5%, and 96% of the points were predicted to within ±15%. In the sake of fairness, the other annular flow correlations were also compared to the set of data used to develop this correlation (which included no wavy or wavy-annular flow). The relevant statistics comparing Eq. (6.8) and the other annular flow correlations are summarized in Table 6.3. The data from this table show that Eq. (6.8) was a better predictor of the experimental data than any of the correlations from the literature.

Table 6.3 Comparison of Eq. (6.8) and annular flow correlations from the literature

Correlation	Mean Deviation	% of Points within ±5%	% of Points within ±15%	% of Points within ±25%
Eq. (6.8)	4.5%	68%	96%	100%
Shah	7.7%	40%	87%	99%
Cavallini & Zecchin	6.7%	46%	92%	99%
Traviss et al.	9.8%	25%	81%	97%
Chen et al.	21%	6%	29%	67%

6.3.2 Wavy flow correlation

During wavy flow condensation at sufficiently low mass fluxes, heat is transferred in the upper portion of the tube by filmwise condensation and in the pool at the bottom of the tube by forced convective condensation. At very low vapor velocities, the heat transfer in the bottom of the tube is much smaller than that in the top and can be readily neglected. Under these same conditions, the vapor flow has little effect on the liquid film at the top of the tube and Nusselt's solution for external condensation on a cylinder can be used. This approach was adopted by Chato [1962] and Jaster and Kosky [1976].

As the vapor velocity is increased, several deviations from ideal stratified flow conditions begin to emerge. First, the heat transfer in the bottom of the tube may become significant enough to warrant inclusion. This effect was observed experimentally at mass fluxes above 55 $\mathrm{klb_m/ft^2}$-h, where the $\mathrm{Nu/[GaPr/Ja]^{0.25}}$ curves for different ΔT's no longer converged onto a single line. Previous researchers such as Rosson and Myers [1965] have attempted to include both the filmwise condensation and forced convective condensation with an additive model.

The second deviation from ideal stratified flow has to do with the interfacial shear exerted by the vapor on the condensate film. The effect of this velocity and the related shear is shown for several cases in Fig. 6.24. For conditions approaching stagnant vapor, little shear is exerted on the condensate. Under these conditions, the condensate falls almost straight down the tube and each axial location is independent of those around it. This situation, shown in Fig. 6.24a, is one for which applying solutions from external condensation is certainly justified. The opposite extreme, that of very high vapor velocity and interfacial shear, is shown in Fig. 6.24c. Under this extreme, gravitational forces become negligible and annular flow is observed. In this situation, the film thickness is nearly independent of angle and filmwise condensation solutions are inappropriate. An intermediate region is shown in Fig. 6.24b. In this region, the vapor velocity is high enough to exert a significant shear on the condensate film, but not great enough to overwhelm gravity forces. Here, the condensate flows in a curved path as indicated in the figure.

Based on the data from this study, it appeared that some film condensation was occurring in this intermediate regime. The first question was whether the solutions from external filmwise condensation would remain valid in this region. This question was addressed by solving the conservation equations for the film thickness for two analogous problems. The solutions are presented in detail in Appendix C. Only the conclusions are reviewed in this chapter.

The solutions presented in Appendix C show that two regions of interest occur when a non-negligible vapor shear is imposed. The first region occurs near the inlet of the tube (or plate). In this region, some of the condensate that exists emanates from the tube inlet where the film thickness is zero. There, the film thickness is less than it would be for a zero vapor velocity case and the heat transfer coefficient is higher. The second region of interest occurs in all the tube downstream of the entry region. In this region, at least subject to the assumptions of Nusselt's analysis, the imposition of the interfacial shear stress has no effect on the film thickness or the heat transfer coefficient. Here, the film thickness is independent of the axial coordinate. Thus, any mass flow that enters a differential element in the axial direction is matched by an equal flow out of the element. Under these conditions, perhaps surprisingly, the evolution equation for the film thickness is identical to that for Nusselt's problem. This means that downstream of the entry region, the film thickness and the heat transfer coefficient is identical to the zero shear case. The primary role of the vapor shear is to determine the relative sizes of the entry and fully developed regions. Low shear cases correspond to short entry regions, and the converse is true for high shear cases. Only relatively low shear cases are amenable to film condensation analysis, though, since high interfacial shear cases correspond to turbulent annular flows. The primary result of the analysis in Appendix C, then, is to demonstrate the validity of filmwise condensation solutions which assume no axial velocity component for cases where a relatively small axial velocity does exist.

The development of the correlation was guided by a combination of careful data analysis and physical guidance from analytical solutions. The starting point was to assume that all the heat transfer occurred by film condensation. Under such conditions, the primary matter of interest is the variation of the quantity $\mathrm{Nu} / [\mathrm{Ga\,Pr} / \mathrm{Ja}]^{0.25}$ with quality and mass flux. A plot of this quantity for R-134a in the .278" i.d. tube is shown in Fig. 6.25. The data in the plot cover a range of mass fluxes from 18 to 110 $\mathrm{klb_m/ft^2}$-h, containing data for $Fr_{so}<12$. Several trends can be deduced from the graph. At each of the mass fluxes $Nu/[Ga\,Pr/Ja]^{0.25}$ increases slightly with quality. This was as expected. Also, the quantity $Nu/[Ga\,Pr/Ja]^{0.25}$ increases modestly as the mass flux is increased. If heat transfer occurred due only to filmwise condensation, and this process obeyed the predictions of unmodified theory for external condensation, no such variations should exist. When presented as shown in Fig. 6.25, though, it is impossible to tell whether the heat transfer enhancement is due to increased filmwise condensation or forced convection in the bottom of the tube. However, another trend can be seen that helps to explain this. At the higher mass fluxes, particularly 73 and 110 $\mathrm{klb_m/ft^2}$-h, the points on Fig. 6.25 do not seem to lie on a single curve. A similar trend was observed previously for the R-32/R-125 mixture at a mass flux of 220 $\mathrm{klb_m/ft^2}$-h (Fig. 6.11), and was attributed to forced convective condensation. Since this mode of heat transfer is independent of temperature difference (or Ja), points with higher Ja will appear higher on plots of $Nu/[GaPr/Ja]^{0.25}$ versus quality. As long as filmwise condensation is present, though, they will appear lower on plots of Nu versus quality. This reasoning is consistent with the data from Fig. 6.25.

To isolate increases in filmwise condensation from contributions due to forced convective condensation, it was desired to subtract the contribution of forced convective condensation. This required a model for the heat transfer in the bottom of the liquid pool to be assumed. Several choices were available. Rosson and Myers developed a model of this heat transfer using a heat to momentum transfer analogy, as described in Section 2.4. They assumed that the liquid flow was laminar, however, apparently based on values of $Re_l<2300$. Their correlation for the heat transfer in the bottom of the liquid pool was given in Chapter 2, and is repeated here:

$$Nu_{bot} = \frac{\phi_{l,lt}\sqrt{8\,Re_l}}{5\left[1+\frac{\ln(1+5\ Pr_l)}{Pr_l}\right]} \tag{2.62}$$

Comparison of the denominator of this correlation with the Traviss correlation reveals that it includes the resistances from the laminar sublayer and buffer layers only.

Taitel and Dukler [1976] pointed out that the Reynolds number for determining the laminar to turbulent transition should be based on the actual liquid velocity and the hydraulic diameter of the liquid phase. If the Reynolds number proposed by Taitel and

Dukler for this purpose is denoted as $Re_{l,act}$, it is related to the superficial liquid Reynolds number by:

$$Re_{l,act} = \frac{Re_l}{1-\theta_l/\pi} \tag{6.9}$$

where:

θ_l=angle subtended from top of tube to liquid level

This actual Reynolds number was computed across the full range of quality for a mass flux of 55 klb_m/ft^2-h of R-134a in the .278" i.d. tube. While the superficial Reynolds number would have predicted a laminar liquid flow for all $x>0.2$, the actual liquid Reynolds number predicted laminar flow only for qualities above 0.83. This implies that it might be more correct to assume turbulent-turbulent flow exclusively. Further corroborating evidence is also available. Souza et al. [1992] successfully correlated pressure drop at mass fluxes as low as 18 klb_m/ft^2-h using turbulent-turbulent concepts and a liquid Froude number function to account for gravitational effects. A similar approach for forced convective evaporation by Wattelet [1994] proved more successful than a more complicated approach that accounted for the loss of turbulence at low liquid Reynolds numbers. Based on this evidence, a heat to momentum transfer analogy was selected to predict the Nusselt numbers in the bottom of the liquid pool.

The Traviss [1973] correlation includes thermal resistances in the laminar sublayer, the buffer layer, and the fully turbulent region. Thus, it is more conservative than the two-zone model of Rosson and Myers [1965]. It was shown in section 6.3.1 that this correlation could be curve fit using a power law model. A slightly modified version of Eq. (6.3) was adopted for the present model:

$$Nu_{forced} = 0.0195 Re_l^{0.8} Pr_l^{0.4} \phi_l(X_{tt}) \tag{6.10}$$

$$\phi_l(X_{tt}) = \sqrt{1.376 + \frac{c_1}{X_{tt}^{c_2}}} \tag{6.11}$$

<u>For $0<Fr_l\leq0.7$</u>

$$c_1=4.172+5.48Fr_l-1.564Fr_l^2 \tag{6.12a}$$

$$c_2=1.773-0.169Fr_l \tag{6.12b}$$

<u>For $Fr_l>0.7$</u>

$$c_1=7.242 \tag{6.13a}$$

$$c_2=1.655 \tag{6.13b}$$

Due to the 1.376 inside the radical of Eq. (6.11), the correlation above matches the Dittus Boelter single-phase correlation with x=0.

Before the model given by Eq. (6.10) could be used to subtract the forced convective component of heat transfer from the total Nusselt number, it was necessary to estimate what fraction of the tube perimeter was occupied by filmwise condensation. This was done by neglecting the condensate in the upper part of the tube, and using the stratified flow model of Taitel and Dukler [1976] to calculate the liquid angle, θ_l. The filmwise Nusselt number was then calculated using the following formula:

$$Nu = Nu_{film} + (1-\theta_l/\pi)Nu_{forced} \tag{6.14}$$

Since the liquid level angle becomes large at relatively low qualities, the second term in Eq. (6.14) is small relative to the first except at very high mass fluxes. For the case of R-134a at 55 klb_m/ft^2-h, for instance, the contribution of the second term never exceeded 10% of the total Nusselt number.

The results of this procedure are presented in Fig. 6.26, which shows the variation of $Nu_{film}/[Ga\,Pr/Ja]^{0.25}$ versus quality for the same set of data that were plotted in Fig. 6.25. This correction pulled the curves for the different mass fluxes closer together, although it still appeared that increasing mass flux increased $Nu_{film}/[Ga\,Pr/Ja]^{0.25}$. This increase in filmwise condensation was also noted by Rosson and Myers [1965], who found that it increased with the 0.12 power of the vapor Reynolds number. This modest mass flux dependence could be attributed to interfacial waves generated by the vapor flow and intermittent mixing when waves from the liquid pool wash up and down the region occupied by the condensate film[2]. The trends from the other refrigerants were identical.

Based on the physical insights from these data, an additive model for predicting the local Nusselt numbers was developed. The basic model for predicting the forced convective component was that given by Eq. (6.10). The quantity $Nu_{film}/[Ga\,Pr/Ja]^{0.25}$ clearly varies with the liquid level angle, or the void fraction. The Lockhart-Martinelli parameter, a measure of the local liquid inventory, was used to correlate this dependence since it has been successfully used as a method of correlating the void fraction. The dependence of $Nu_{film}/[Ga\,Pr/Ja]^{0.25}$ on mass flux was accounted for with a power law function of Re_{vo}, reflecting the influence of the vapor flow on the condensate film. The form of the equation is thus:

---

[2] Recall from Section 2.4.1 that based on the falling film Reynolds number, Re_f, no interfacial waves should have been expected for a stagnant vapor case.

$$\mathrm{Nu} = \underbrace{\frac{a\,\mathrm{Re}_{vo}^{b}}{1 + cX_{tt}^{d}}\left[\frac{\mathrm{Ga}\,\mathrm{Pr}}{\mathrm{Ja}}\right]^{0.25}}_{\mathrm{Nu}_{\mathrm{film}}} + (1-\theta_l/\pi)\mathrm{Nu}_{\mathrm{forced}} \tag{6.15}$$

The vapor Reynolds number exponent of 0.12 that was recommended by Rosson and Myers [1965] agreed well with the present data. The dependence on the Lockhart-Martinelli parameter was determined by fitting the data at a mass flux of 55 $\mathrm{klb_m/ft^2}$-h in the .278" i.d. tube for all three refrigerants, since this was the lowest mass flux at which experimental data could be obtained over a wide range of quality. The final form of the correlation is:

$$\mathrm{Nu} = \frac{0.23\,\mathrm{Re}_{vo}^{0.12}}{1 + 1.11X_{tt}^{0.58}}\left[\frac{\mathrm{Ga}\,\mathrm{Pr}}{\mathrm{Ja}}\right]^{0.25} + (1-\theta_l/\pi)\mathrm{Nu}_{\mathrm{forced}} \tag{6.16}$$

The constants were selected such that at a vapor only Reynolds number of 15,000 (the lowest value from the present study, and at the lower limit of the practical range), the filmwise component was equal to $0.728[\mathrm{GaPr/Ja}]^{0.25}$ at a quality of 1. This value is equal to that for external condensation on a cylinder. At higher values of the vapor only Reynolds number, Eq. (6.16) predicts a modest increase in the filmwise heat transfer due to enhancement from the vapor phase.

The only item in Eq. (6.16) that is not straightforward to calculate is the liquid level angle, θ_l. It is geometrically related to the void fraction by the following formula if the area occupied by the thin condensate film is neglected:

$$\alpha = \frac{\theta_l}{\pi} - \frac{\sin(2\theta_l)}{2\pi} \tag{6.17}$$

If a void fraction model is assumed, the transcendental equation posed by Eq. (6.17) must be solved to obtain the desired quantity, θ_l. Jaster and Kosky [1976] deduced an approximate relationship which is much easier to use, albeit for a slightly different purpose. In the context of the present problem, their simplification can be stated as:

$$1 - \frac{\theta_l}{\pi} \cong \frac{\arccos(2\alpha - 1)}{\pi} \tag{6.18}$$

The approximation given by Eq. (6.18) is compared to the exact solution of Eq. (6.17) in Fig. 6.27. The simplicity achieved by this assumption is well worth the modest errors associated with it. These errors are themselves mitigated by the fact that the forced convective Nusselt number that the quantity in Eq. (6.18) is multiplied by is normally considerably smaller than the filmwise Nusselt number. A void fraction correlation must be assumed to solve this equation. The calculations presented hereafter were made using the approximation of Eq. (6.18) and the void fraction correlation of Zivi [1964], Eq. (2.55).

The predictions of Eq. (6.16) are compared to the wavy flow data in Fig. 6.28. Overall, the agreement is very good. The mean deviation between the predicted and experimental values was 6.6%, considerably better than the correlations from the literature. The worst deviations were found for the data at a saturation temperature of 113 °F and some of the data in the .123" i.d. tube. For both of these situations, the uncertainties in both the heat transfer coefficients and the qualities were rather large because the heat losses to the environment became a significant fraction of the overall heat transfer. For the lowest mass flux tests in the .123" i.d. tube, for instance, the test section heat transfer rates were on the order of 170 Btu/h. The uncertainties will be discussed in greater detail in Section 6.5.

6.3.3 Limits of application -- wavy-annular flow regime

The correlations developed in Sections 6.3.1 and 6.3.2 were for the annular and wavy flow regimes, respectively. The annular flow correlation was developed using a set of data restricted to values of $Fr_{so}>20$, which excluded wavy-annular flow. The wavy flow correlation was developed primarily with data for which $Fr_{so}<10$, including primarily wavy flow. A region exists in between these limits where the physics of the condensation process is not so clear cut. In this section, the applicability of the wavy and annular flow correlations will be assessed for data in this transition region. Before beginning this analysis, it is worthwhile to assess how wide the transition region is in the G-x plane. Figure 6.29 plots curves corresponding to $Fr_{so}=10$ and $Fr_{so}=20$ on G-x coordinates for R-134a at 95 °F in a .278" i.d. tube. At mass fluxes above 220 klb_m/ft^2-h, the transition region occupies about 15% of the quality range. This region narrows at higher mass fluxes, occupying about 10% of the quality range at a mass flux of 585 klb_m/ft^2-h. The transition region is widest at mass fluxes below 220 klb_m/ft^2-h.

As a first step, the wavy and annular flow correlations were used to predict the Nusselt numbers for the entire set of data, regardless of the flow regime. The deviation of these correlations from the data were then plotted versus Fr_{so} in Fig. 6.30 and Fig. 6.31. Figure 6.30 shows that at values of $Fr_{so}<10$, the Nusselt numbers were much higher than predicted by the annular flow correlation. In the worst case, this deviation was over a factor of 4, although these points were omitted because of the range of the axis. At values of $Fr_{so}>20$, the data were entirely in the annular flow regime and the predictions were very good. At values of Fr_{so} between 10 and 20, some points were well predicted by the annular flow correlations and others were predicted poorly.

The opposite trend was observed for the wavy flow correlation. At values of $Fr_{so}<10$, all of the data were predicted within a 20% range. At values of $Fr_{so}>20$, the measured Nusselt numbers were substantially larger than the predicted values. For the range of Fr_{so} between 10 and 20, the error in prediction of the wavy flow correlation was much less than the error in prediction of the annular flow correlation.

Based on the observations from several plots such as Fig. 6.30 and Fig. 6.31, the raw data were examined to see if the points in the middle Froude number range that were significantly higher than the wavy flow correlation had anything in common. It was discovered that all of these points had mass fluxes of at least 365 klb_m/ft^2-h. Even though Soliman's Froude number might indicate wavy or wavy-annular flow, and in fact significant stratification was sometimes observed visually, the extremely high velocities in these cases seemed to promote heat transfer more indicative of annular flow than wavy flow in the wavy-annular flow regime. This same observation held, in fact, for the entire quality range at these mass fluxes (even when $Fr_{so}<10$). This point is demonstrated by Fig. 6.32, which shows the ratio of the measured Nusselt number to the annular flow prediction for all the high mass flux data (≥365 klb_m/ft^2-h). Data are included for both the .123" and .278" i.d. tubes. For both tubes, the annular flow correlation remained a good predictor of the experimental data over the entire range of Froude numbers. Since the annular flow correlation is significantly simpler to use than the wavy flow correlation (it does not require knowledge of ΔT) and more accurate at these high mass fluxes, it can be recommended that the annular flow correlation be used across the entire quality range at mass fluxes greater than 365 klb_m/ft^2-h.

Some thought was given to whether this upper limit should be based on a dimensionless parameter rather than a mass flux. The vapor only Reynolds number, Re_{vo}, was originally considered since such a limit would reflect the influence of the vapor flow. If such a criterion was selected, it would be based on the lowest value of Re_{vo} at which the annular flow correlation remained accurate across the entire quality range. This would correspond to a mass flux of 365 klb_m/ft^2-h in the .123" i.d. tube. In the .278" i.d. tube, this limit would correspond to a mass flux of slightly less than 165 klb_m/ft^2-h. Figure 6.21 compared annular flow correlations from the literature to R-22 data at almost exactly these conditions, and revealed that they were inappropriate. Based on this evidence, then, it appears that a mass flux of 365 klb_m/ft^2-h should serve as an appropriate limit for when to stop using the wavy flow correlation.

6.3.4 Mist flow effects

As reviewed in Section 2.6, Soliman [1986] developed a correlation for mist flow based on the premise of an unstable wall film. One goal of this study was to carefully investigate the necessity of such a correlation with a single set of experimental equipment. Based on Soliman's explanation, pure mist flow should be expected for $We_{so}>30$ and his correlation should be applicable for $We_{so}>35$.

Perhaps the most important evidence concerning Soliman's conclusions was visual. According to his flow regime criteria, as shown in Fig. 5.7, mist flow should have been observed for R-134a in the .278" i.d. tube for 65% of the quality range at a mass flux of 365 klb_m/ft^2-h and 75% of the quality range at a mass flux of 475 klb_m/ft^2-h. Pure mist flow with no stable wall film was never observed at qualities below 95%. Moreover, when it was observed at these high qualities, it was always after the adiabatic section and before the test-section inlet. At the outlet sight glass, after condensation had begun in the test-section, a stable wall film was always observed. This was true for test-section outlet qualities as high as 90%. This evidence leads to two important conclusions. First, Soliman's estimates about the extent of the mist flow region appear rather exaggerated. Second, and more importantly, the fact that mist flow was never observed at the outlet sight glass tends to indicate that a stable wall film is formed as soon as condensation begins. This is more intuitive than his idea of a dry wall during condensation, since a continuous supply of liquid is always generated at the wall by the condensation process. Stated another way, the nature of the condensation process itself tends to preclude a dry wall.

Interesting evidence corroborating the findings of the present study can be found in the recent evaporation experiments of Wattelet [1994]. He completed a wide range of evaporation tests, where the heat transfer process at the wall would tend to promote mist formation rather than inhibit it. Also, the constant heat flux boundary condition applied throughout his experiments provided an objective, non-visual method of mist flow detection since breakup of the liquid film resulted in noticeable increases in wall temperature. Still, he reported no mist flow formation for qualities below 95%. The values of We_{so} at which he observed no mist flow were as high as 40.

Based on the visual evidence from the present study, no verification of Soliman's conclusions could be made. The next step, one patterned after his work, was to assess how the predictive ability of the annular flow correlation developed in this study varied with We_{so}. According to Soliman, the annular flow correlation should be accurate for $We_{so}<30$ and become increasingly inaccurate at $We_{so}>35$ due to a transition to mist flow. Figure 6.33 presents the ratio of the measured Nusselt number to the annular flow prediction plotted versus We_{so}. The data in this figure include all the 125 annular flow data points collected from the .278" i.d. tube. Data from the .123" i.d. tube were not included since only a few of these data were predicted to be in the mist flow regime. This figure shows that at modified Weber numbers of up to 80, over twice the limit where pure mist flow should have been observed, the annular flow correlation remained an accurate predictor of the experimental data. Moreover, the deviations from the correlation showed no discernible trend with We_{so}. This agreement supports the concept of a stable wall film and no appreciable effect of entrainment.

The final unique aspect of Soliman's mist flow model was the concept of a dependence on vapor Jakob number (or temperature difference). This effect was assessed for the present data by plotting the ratio of the measured Nusselt number to the annular flow prediction versus liquid Jakob number. These data are presented in Fig. 6.34. This figure indicates that for variations in Jakob number up to a factor of 4.7, experimental deviations from the annular flow correlation showed no discernible trend. The Jakob number dependence from Soliman's correlation ($Ja_v^{-0.33}$) would have predicted a variation of around 67% for such a change in Ja. Thus, this part of his correlation also seems misguided based on the current experimental evidence. It should be pointed out that a liquid Jakob number was used in Fig. 6.34 because the experimental evidence indicated that the heat was in fact being transferred across a distinct liquid layer. The conclusions would have been the same if a vapor Jakob number were used, however.

Besides investigating the various concepts embodied in Soliman's mist flow correlation, the correlation itself was compared to all data with modified Weber numbers larger than 35. The results are shown in Fig. 6.35. The correlation had a mean deviation of 24% with the experimental data, which it consistently overpredicted. The systematic error committed by overstating the effect of Jakob number could result in even larger errors if the temperature difference was varied over a wider range.

As discussed in Chapter 5, a substantial amount of mist was entrained in the core flow at high mass fluxes. The excellent agreement of the annular flow correlation with experimental data containing significant entrainment, though, indicates that the entrainment did <u>not</u> have a significant effect on the heat transfer. Again relying on the insights offered by the Traviss [1973] correlation, the insensitivity of the dimensionless heat transfer resistance (F_2) to the amount of liquid flowing in the wall film (or Re_l) explains this finding. From a practical standpoint, this insensitivity is fortunate since it allows annular flow correlations such as Eq. (6.8) to be successfully used in situations with considerable entrainment.

6.3.5 Design recommendations

For condensation in the annular flow regime, Eq. (6.8) is recommended. This correlation should be used at all qualities for mass fluxes greater than or equal to 365 klb_m/ft^2-h. It should be used at other mass fluxes when $Fr_{so}>20$. For condensation in the wavy and wavy-annular flow regimes, Eq. (6.16) is recommended. This correlation should be used at mass fluxes less than 500 kg/m^2-s when $Fr_{so}<20$.

For $G\geq365$ klb_m/ft^2-h
Use Eq. (6.8) for all qualities
For $G<365$ klb_m/ft^2-h
Use Eq. (6.16) if $Fr_{so}<20$
Use Eq. (6.8) if $Fr_{so}>20$

6.4 Comparisons with Experimental Data

The wavy and annular flow correlations were compared to data known to be in the proper flow regime previously. Based on the design recommendations of Section 6.3.4, the Nusselt number was calculated for each of the experimental runs conducted in the study. The predicted and experimental values are compared in Fig. 6.36, and the mean deviation with each of the fluids is listed in Table 6.4. The inclusion of points in the wavy-annular flow regime detracted little from the predictive ability of the model. When predictive errors were committed in the intermediate range of Froude numbers, they were normally underpredictions. This is fortunate for design purposes, since in the worst case an overly conservative design will be selected.

The predictions of Eq. (6.8) are compared to annular flow data of Altmann et al. [1960] in Fig. 6.37. Their data were collected for R-22 at mass fluxes ranging from 220 klb_m/ft^2-h to 629 klb_m/ft^2-h in a .343" i.d. tube. The mean deviation of the eleven points with $Fr_{so}>7$ was 7%, with a maximum deviation of 11%. Their non-annular flow points were not compared with the wavy flow correlation since insufficient information was given to determine the refrigerant to wall temperature difference.

The correlations from the present study are compared to the R-22 data of Bae et al. [1970] in Fig. 6.38. These data were collected at mass fluxes ranging from 235 klb_m/ft^2-h to 484 klb_m/ft^2-h in a .493" smooth tube. A total of 37 points were examined, with a mean deviation of 13.5%. Most of the errors were overpredictions.

The heat transfer correlations developed above are compared to the R-12 data of Traviss et al. [1971] in Fig. 6.39. These data were collected in a .315" i.d. smooth tube at mass fluxes ranging from 119 to 1129 klb_m/ft^2-h. A total of 93 points were analyzed, with a mean deviation of 13.7%. These data were a rather extreme test of the correlation, since they had mass fluxes up to twice as high as those from the present study. For each run, six local heat transfer coefficients were determined by measuring local water and surface temperatures inside a 16.4 ft long test-section. The experimental data that had the highest deviations with the heat transfer correlations consistently corresponded to the second section of the heat exchanger. These points often appeared inconsistent with values at the adjoining sections, pointing to a potential error. Except for these points, most of the experimental data deviated from the predictions by less than 20%. The mean deviation of the correlation with the six points collected at the highest mass flux, 1129 klb_m/ft^2-h, was only 8%. This relatively good agreement indicates that the annular flow correlation may be used with confidence for mass fluxes considerably higher than those from the present study.

The thermophysical properties used to compute the predicted Nusselt numbers are discussed and summarized in Appendix A. The data for each tube and each refrigerant are presented in tabular form in Appendix D. These tables include the measured and predicted Nusselt numbers, as well as the operating conditions and uncertainties. All relevant quantities that are needed for comparisons with other heat transfer correlations are included unambiguously. It is hoped that future researchers will do the same, since this aids greatly in using external data sources for validation purposes.

Table 6.4 Mean deviations between the heat transfer correlation and the experimental data for each fluid

Fluid	Mean Deviation
R-134a	4.4%
R-22	4.9%
50/50 R-32/R-125	5.9%
60/40 R-32/R-125	6.1%

6.5 Experimental Uncertainty

The experimental uncertainties in quality and heat transfer coefficients were calculated as described in Section 4.2.3. These uncertainties are listed along with the experimental data in Appendix D. The uncertainty in the heat transfer coefficient was normally dominated by the uncertainty of the temperature differences, with typical values of overall uncertainty ranging from 5% to 15%. For a test with a 5.4 °F refrigerant to wall temperature difference, the uncertainty was on the order of 10%. Tests with 3.6 °F temperature differences had uncertainties closer to 15%. The consistency in the measured heat transfer coefficients as the temperature difference was varied might indicate that these uncertainties were overestimated. In both the .123" and .278" i.d. test sections, the circumferential tube wall temperature field showed remarkable consistency. During stratified flow tests, the temperature readings steadily decreased with angle from the top of the tube due to higher heat transfer coefficients at the top of the tube. As the transition towards annular flow was made, the wall temperatures became closer to each other and did not vary monotonically with the angle. This was indicative of nearly uniform heat transfer coefficients around the perimeter during annular flow. The consistent agreement between redundant measurements of the cooling water temperatures also lent a measure of confidence in their accuracy. The redundant measures of temperature difference across the water circuit always agreed to within ±0.09 °F.

Under certain conditions, items other than the temperature differences became significant contributors to the uncertainty. At high saturation temperatures, inaccuracy in estimating the spurious heat exchanges with the environment became problematic. This was most pronounced at low mass fluxes and in the .123" i.d. tube, both being cases where the heat transfer rates were relatively small. In the .123" i.d. tube, in fact, attention to this source of uncertainty dictated much about the experimental procedures. During nearly all of the tests at 95 °F in this tube, the temperature level of the water was adjusted so that it was within 1.8 to 3.6 °F of the ambient temperature. This eliminated the potential for unwanted heat exchange with the environment, canceling this source of uncertainty. A similar procedure was not possible at higher saturation temperatures, since the large temperature differences between the water and refrigerant that would have been necessary to accomplish this would have created undesirably large quality changes. If more reliable data are demanded at high saturation temperatures in the future, implementing guard heating would be helpful.

The uncertainty in quality was on the order of 1% to 2% for most of the tests, posing few serious problems. The primary source of this uncertainty was not the uncertainty of the instruments, but undesired heat exchanges with the environment in both the refrigerant heater and the test-section. This uncertainty only became large ($\geq 5\%$) at low mass fluxes and high saturation temperatures. At low mass fluxes, though, the heat transfer coefficient did not change much with quality so errors in the quality were not as critical.

In addition to careful calibration of instruments, debugging tests were invaluable in removing systematic errors that would not be accounted for properly by uncertainty calculations. The single-phase liquid tests allowed checks with well verified heat transfer correlations, although the value of these tests was mitigated somewhat because the refrigerant temperature profile had to be inferred. Still, errors were found and corrected as a result of these tests. The ability to check energy balances during these tests also provided valuable checks on the instrumentation.

6.6 Summary of Heat Transfer Results

Heat transfer data were reported and analyzed for four refrigerants in two tubes. The heat transfer behavior differed significantly based on the flow regime. At low mass fluxes, wavy flow prevailed and filmwise condensation was the dominant heat transfer mode. In this flow regime, the heat transfer coefficients increased slightly with increasing quality and mass flux. At the highest mass fluxes, annular or annular-mist flow prevailed over nearly the entire quality range. In these regimes, forced convective condensation was the dominant heat transfer mode. This regime was characterized by heat transfer coefficients that increased substantially with increases in quality and mass flux. At intermediate mass fluxes, wavy flow heat transfer behavior was observed at low qualities but became dominated by annular flow at higher mass fluxes. The quality at which this transition to forced convective condensation occurred increased with increases in tube diameter and reduced pressure of the refrigerant. The effect of temperature difference on heat transfer followed the expected -0.25 power dependence at low mass fluxes in the wavy flow regime. As the mass flux was increased, heat transfer contributions from forced convective condensate in the liquid pool reduced the dependence on temperature difference.

The experimental data were compared to several correlations from the literature. The Shah [1979] and Cavallini and Zecchin [1974] correlations for annular flow were relatively good predictors of the experimental data. The main problem with these correlations had to do with their range of applicability. No range was specified for the Cavallini-Zecchin correlation, while the lower mass flux range that was specified by Shah contained significant amounts of wavy flow. Substantial errors in prediction occurred in this region. More significant errors could be observed here depending on the value of the temperature difference. The stratified flow correlations of Chato [1962] and Jaster and Kosky [1976] were adequate predictors of the stratified-wavy flow data. Both of these correlations neglected the forced convective condensation in the liquid pool, which caused problems as the mass flux was increased. The correlation of Rosson and Myers [1965] attempted to account for this heat transfer, but was a worse predictor of the experimental data than the simpler correlations that neglected it.

New correlations were developed for the annular and wavy flow regimes. The annular flow correlation was developed using a two-phase multiplier approach, and agreed with the data from this and other studies very well. Analysis of the more theoretical approaches to annular flow condensation revealed the similarity between these approaches and that of the two-phase multiplier. A wavy flow correlation was developed that accounted both for filmwise condensation at the top of the tube and forced convective condensation in the liquid pool at the bottom of the tube. This correlation approaches the correct limits in extreme cases -- a single-phase liquid correlation at a quality of zero and external condensation for a quality of 1 at low mass fluxes. A systematic analysis was performed to determine the operating condition ranges over which each of these correlations remained valid. A limit for switching from the wavy to the annular correlation was set based on Soliman's Froude number [1982]. Above a certain mass flux limit, it was found that the annular flow correlation could be applied regardless of the Froude number.

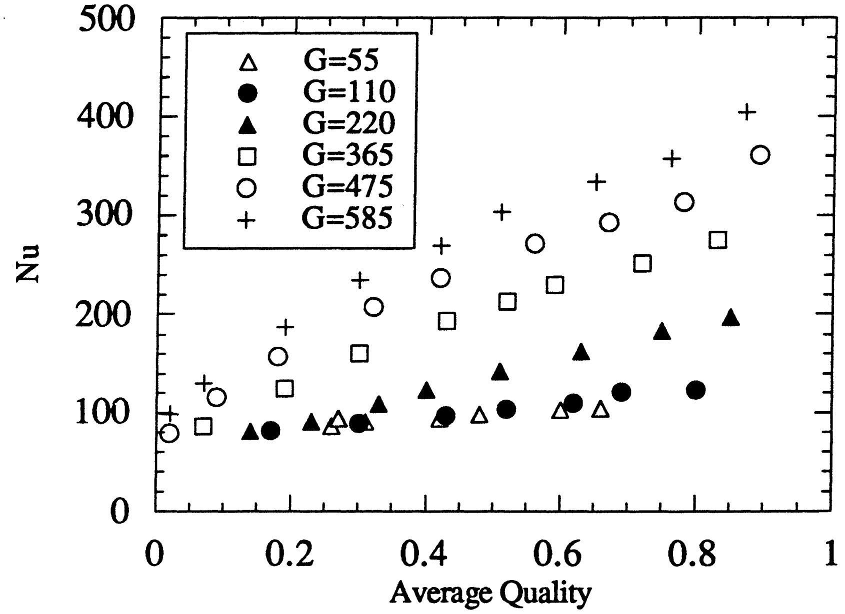

Figure 6.1 Variation of Nu with quality for 60%/40% R-32/R-125 mixture at 95°F in .123" i.d. test-section.

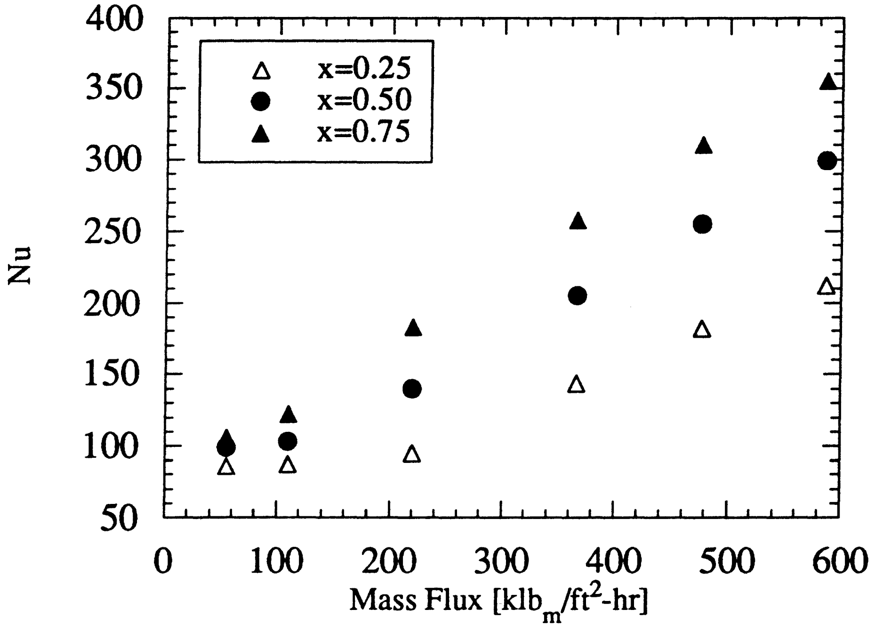

Figure 6.2 Variation of Nu with mass flux for 60%/40% R-32/R-125 mixture at 95 °F in .123" i.d. test-section.

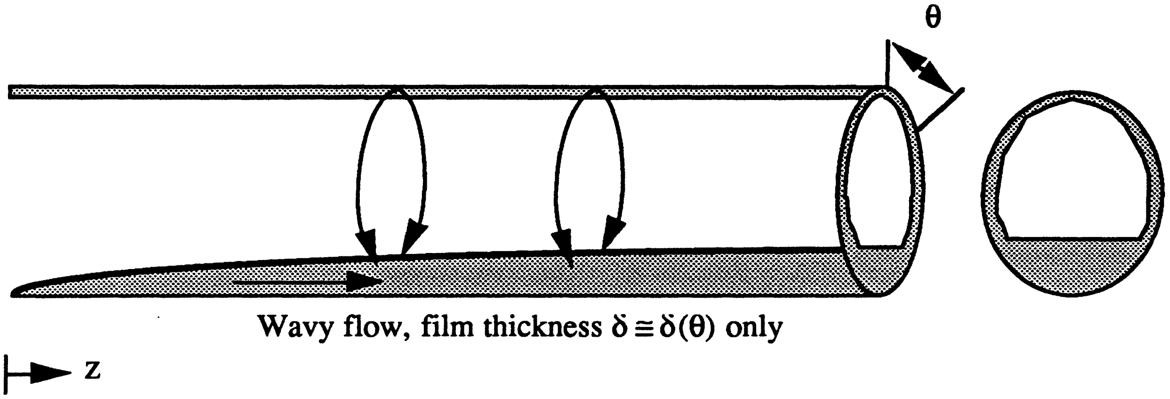

Figure 6.3 Idealized schematic of the wavy flow condensation process.

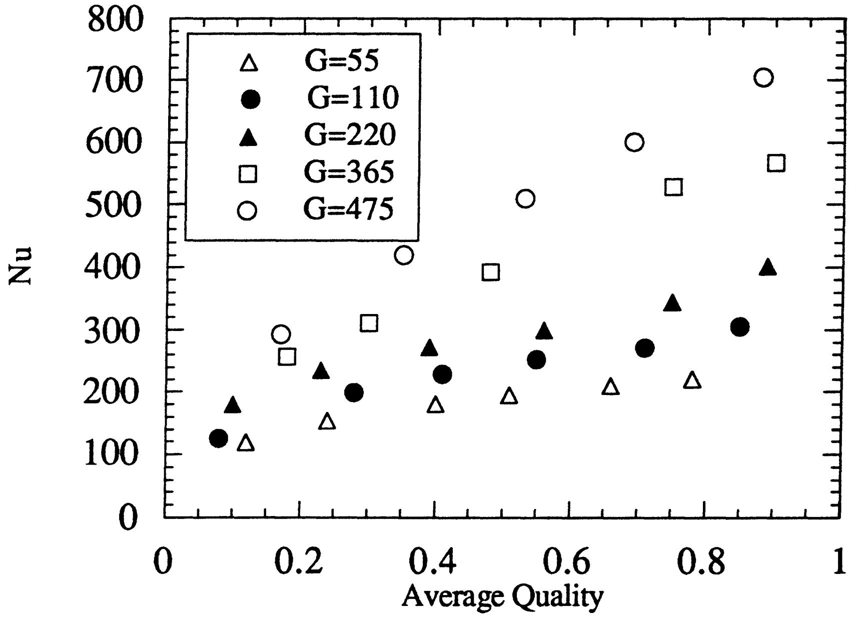

Figure 6.4 Variation of Nu with quality for 50/50 R-32/R-125 at 95 °F in .278" i.d. test-section.

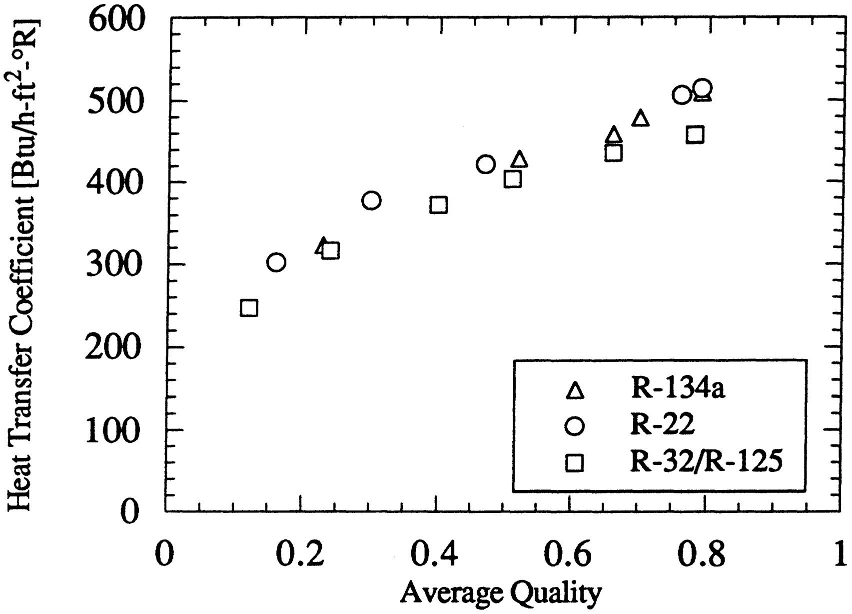

Figure 6.5 Wavy flow heat transfer comparision for R-134a, R-22, and 50/50 R-32/R-125 in the .278" i.d. tube at 95°F. G=55 klb$_m$/ft^2-h, ΔT≈5.4 °F.

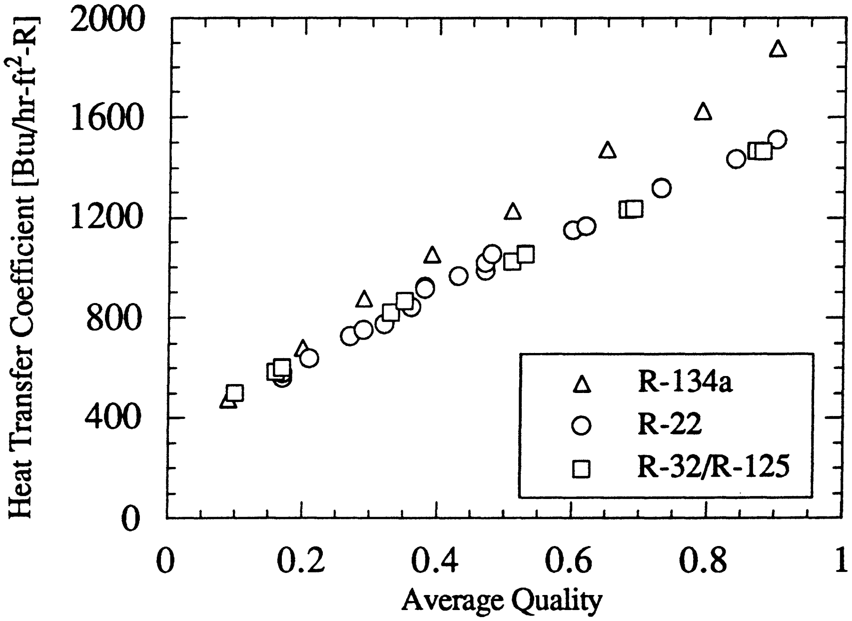

Figure 6.6 Annular flow heat transfer comparision for R-134a, R-22, and 50/50 R-32/R-125 in a .278" i.d. tube at 95 °F, G=475 klb$_m$/ft^2-h.

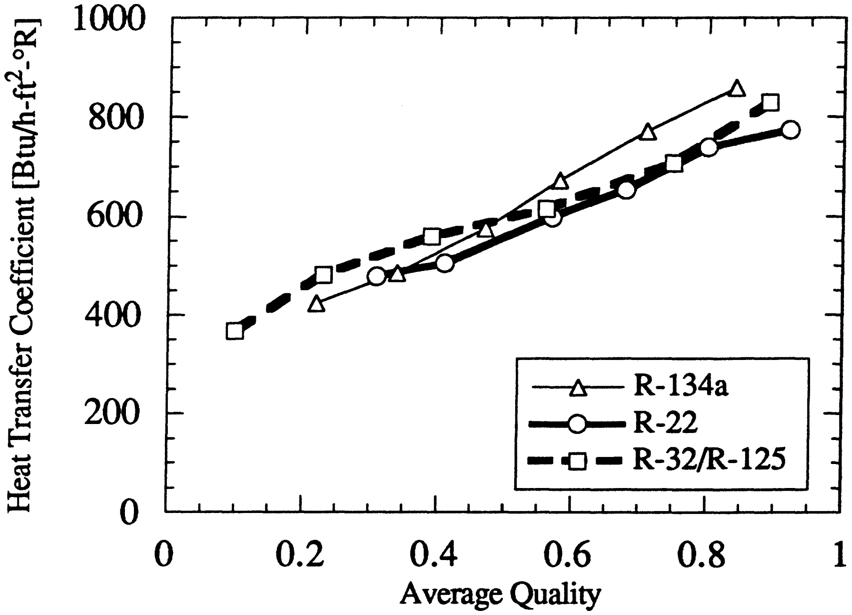

Figure 6.7 Mixed flow regime heat transfer comparision for R-134a, R-22, and 50/50 R-32/R-125 in the .278" i.d. tube at 95 °F, G=220 klb$_m$/ft^2-h.

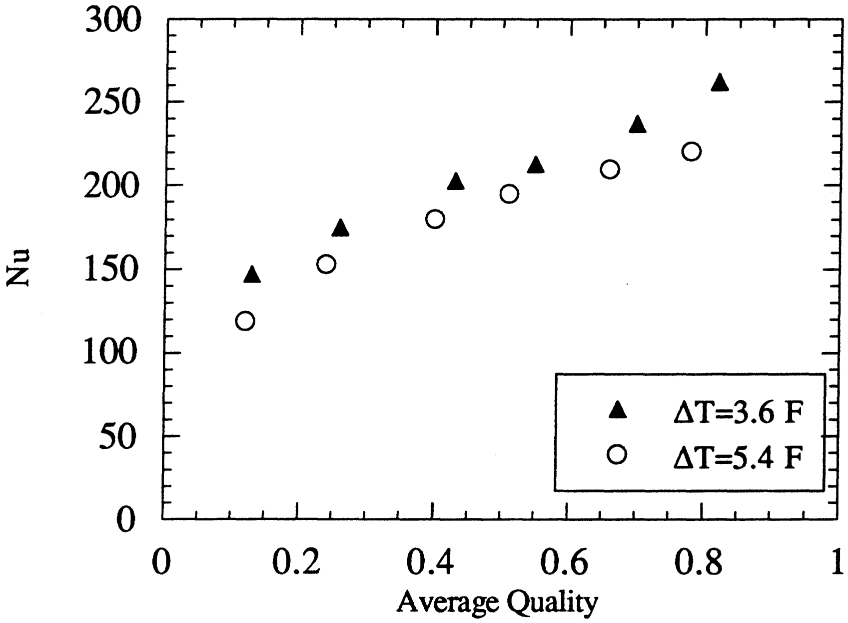

Figure 6.8 Effect of ΔT on Nu for R-32/R-125 in the .278" test-section. G=55 klb$_m$/ft^2-h, T_{sat}= 95 °F.

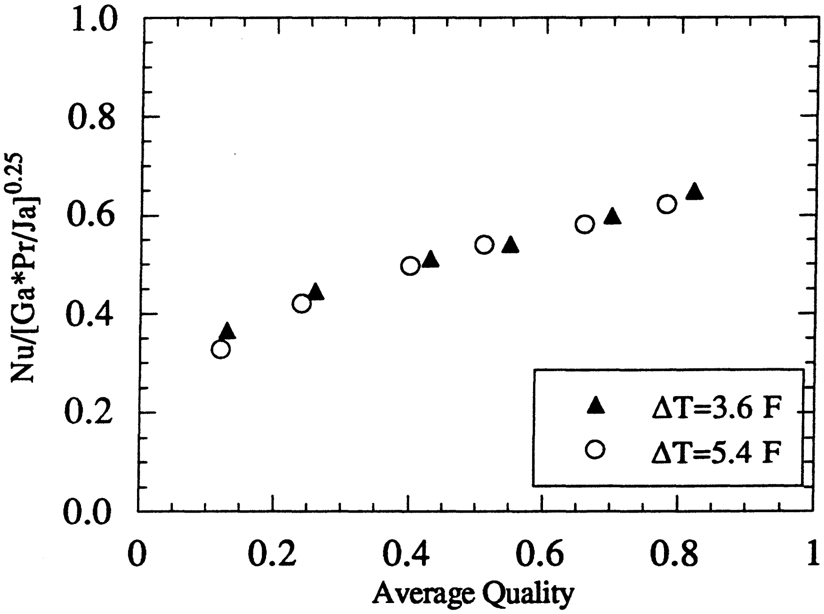

Figure 6.9 Effect of ΔT on $Nu/[Ga*Pr/Ja]^{0.25}$ for R-32/R-125 in the .278" i.d. test-section. $G=55$ klb_m/ft^2-h, $T_{sat}=95$ °F.

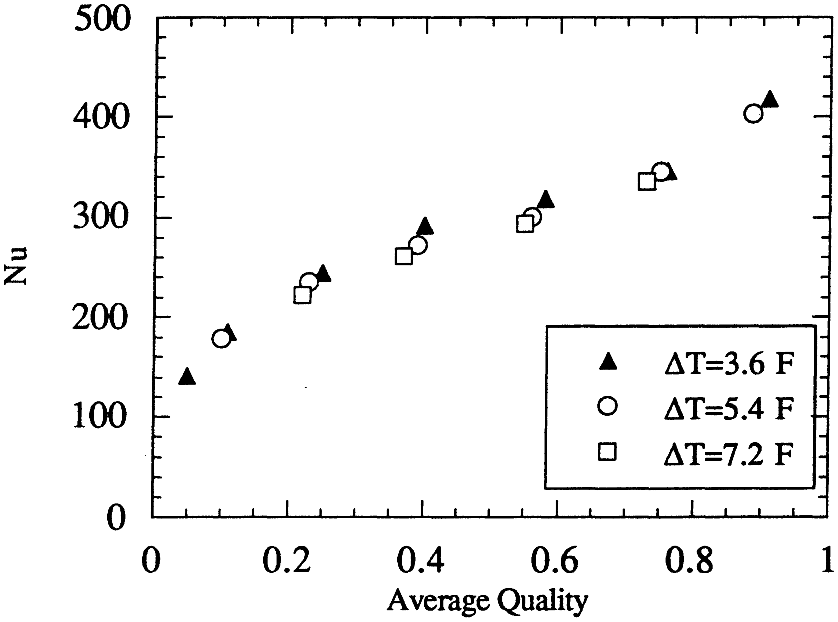

Figure 6.10 Effect of ΔT on Nu for R-32/R-125 in .278" test-section. $G=220$ klb_m/ft^2-h, $T_{sat}=95$ °F.

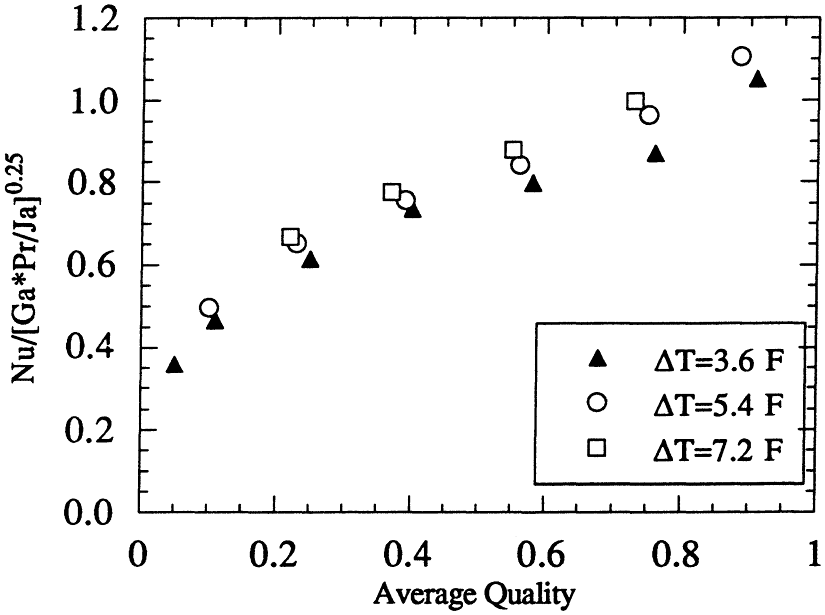

Figure 6.11 Effect of ΔT on $Nu/[Ga*Pr/Ja]^{0.25}$ for R-32/R-125 in the .278" i.d. test-section. G=220 klb_m/ft^2-h, T_{sat}=95 °F.

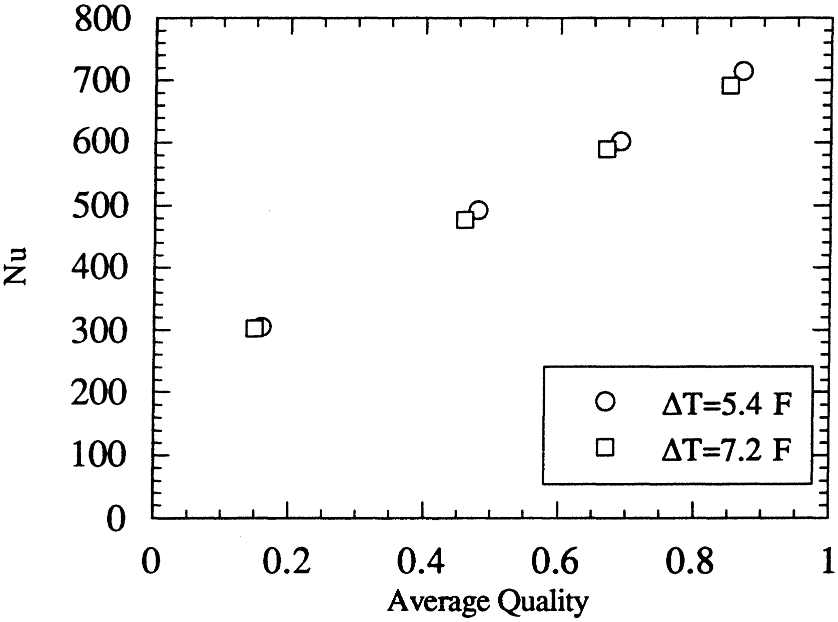

Figure 6.12 Effect of ΔT on Nu for R-32/R-125 in the .278" tube. G=475 klb_m/ft^2-h T_{sat}=95 °F.

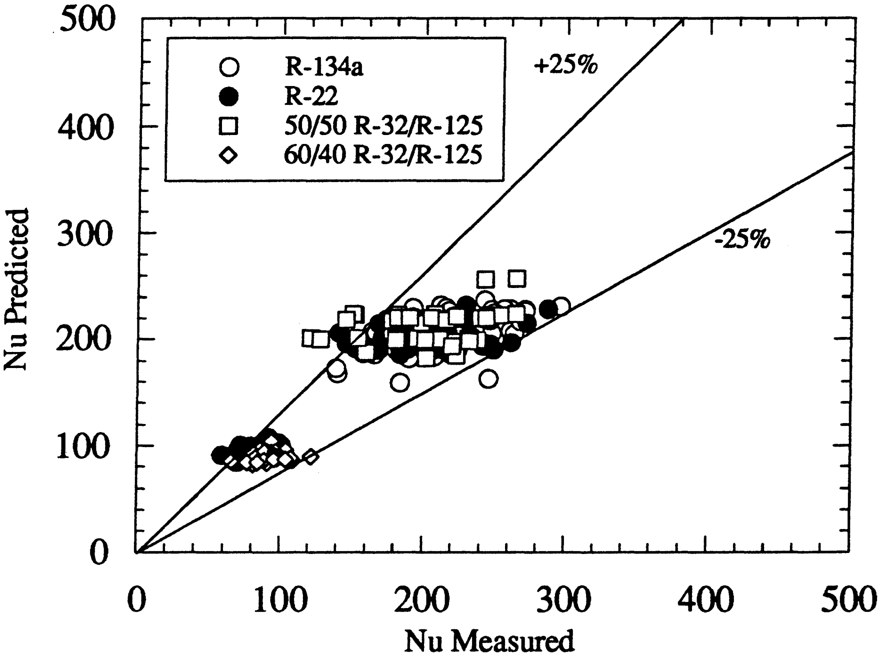

Figure 6.13 Comparison of wavy flow heat transfer data with predictions of the Chato [1962] correlation.

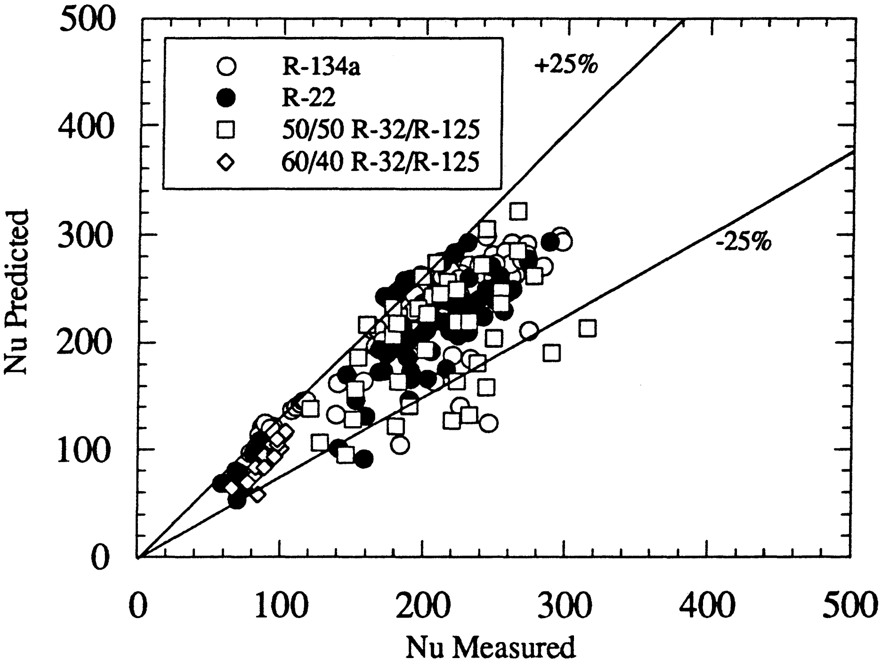

Figure 6.14 Comparison of wavy flow heat transfer data with predictions of the Jaster and Kosky [1976] correlation.

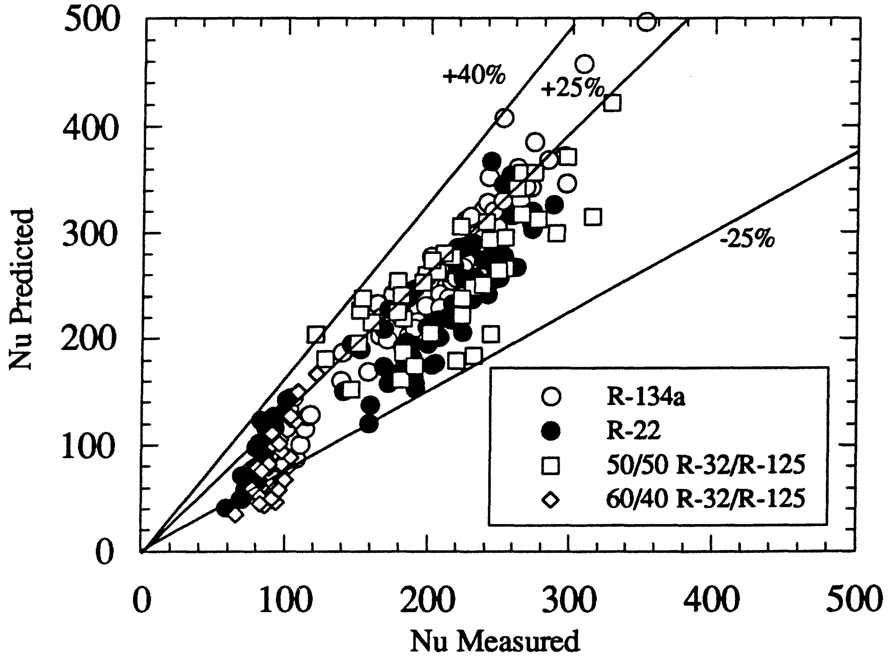

Figure 6.15 Comparison of wavy flow heat transfer data with predictions of the Rosson and Myers [1965] correlation.

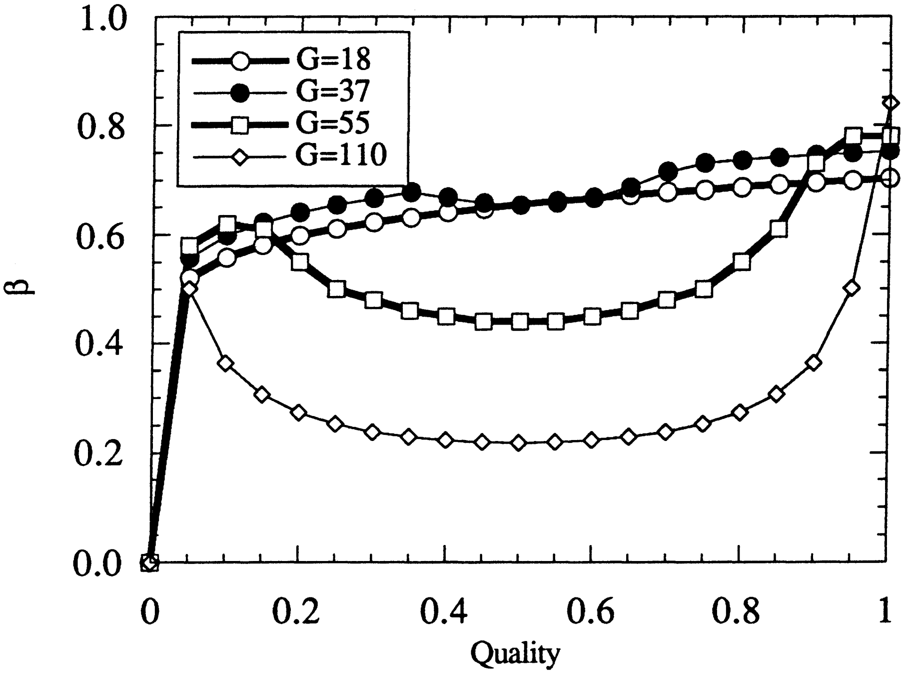

Figure 6.16 Variation of β with quality predicted for R-134a. $G=55\ klb_m/ft^2$-h, $T_{sat}=95$ °F.

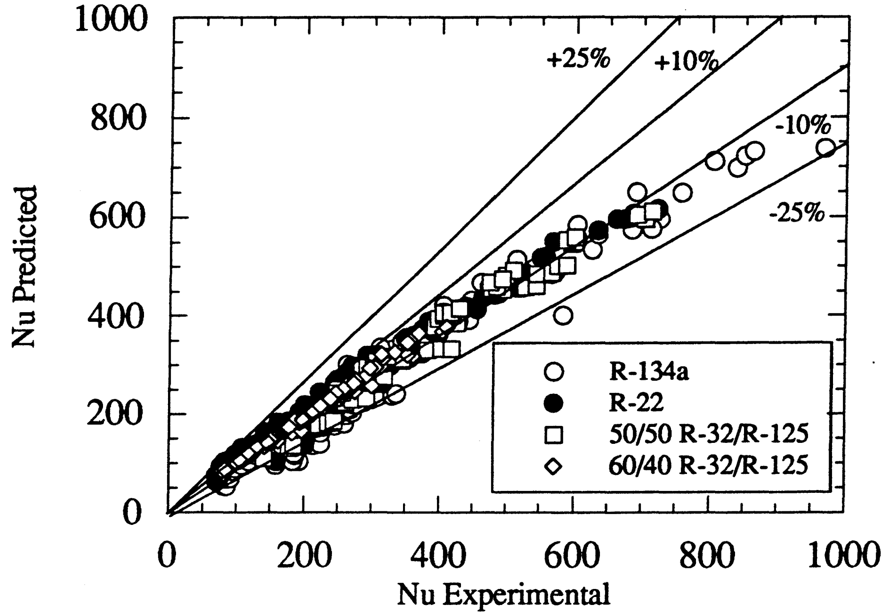

Figure 6.17 Comparison of annular flow heat transfer data with predictions of the Shah [1979] correlation.

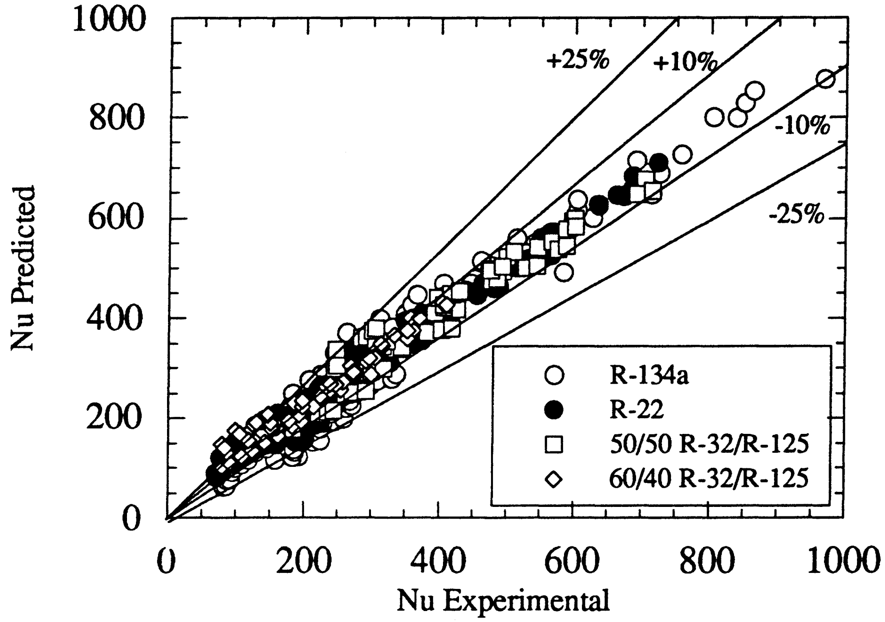

Figure 6.18 Comparison of annular flow heat transfer data with predictions of the Cavallini and Zecchin [1974] correlation.

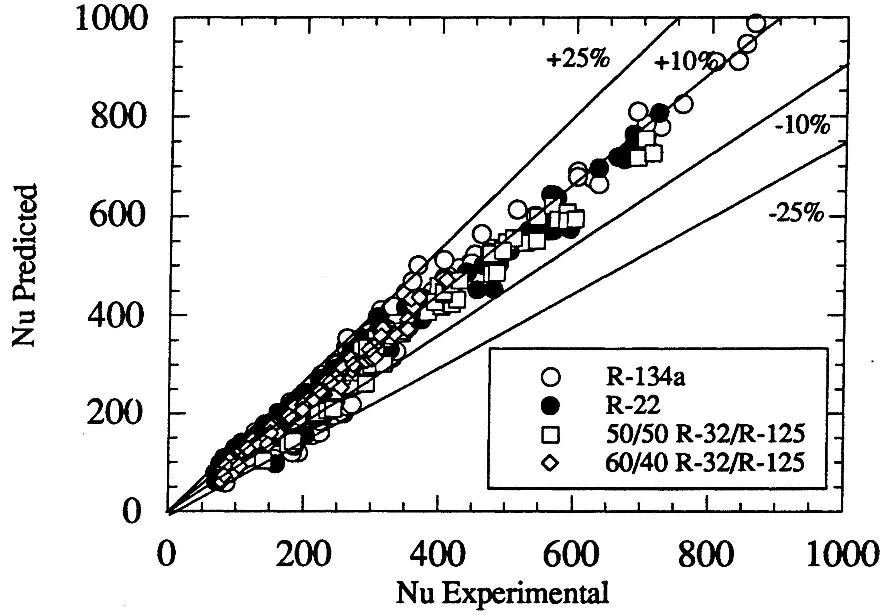

Figure 6.19 Comparison of annular flow heat transfer data with predictions of the Traviss et al. [1973] correlation.

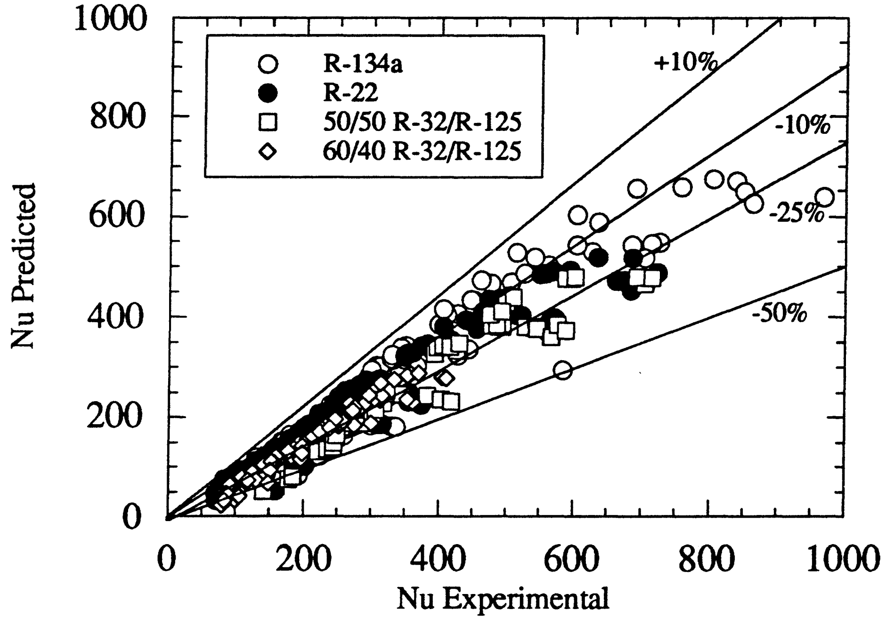

Figure 6.20 Comparison of annular flow heat transfer data with predictions of the Chen et al. [1987] correlation.

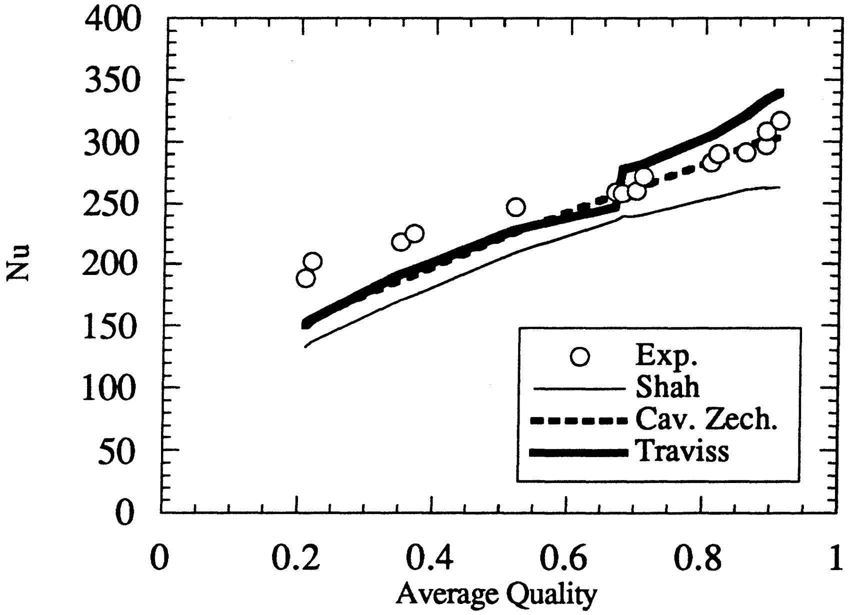

Figure 6.21 Comparison of annular flow correlations with heat transfer data for R-22 in the .278" tube. T_{sat}=95 °F, G=165 klb_m/ft^2-h.

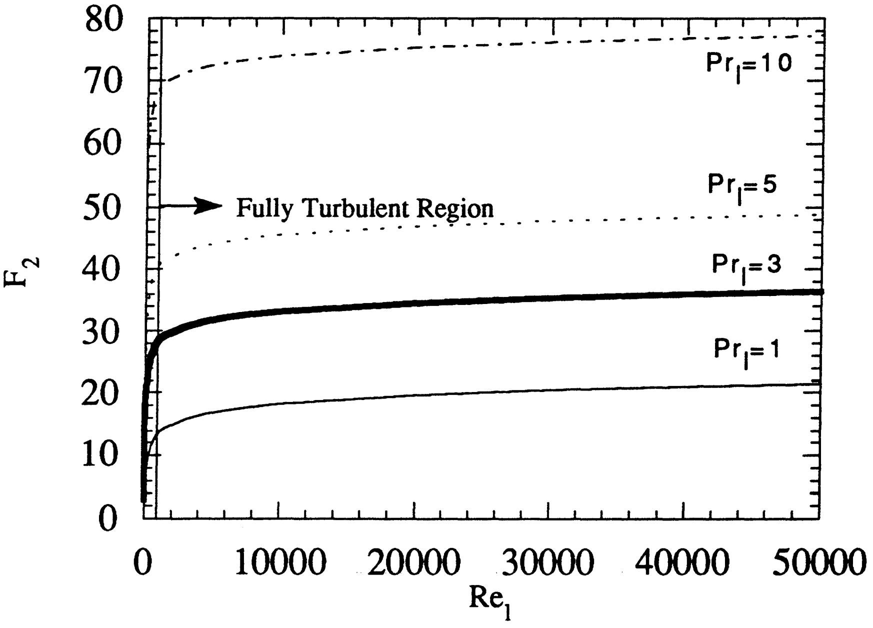

Figure 6.22 Variation of F_2 with Re_l and Pr_l.

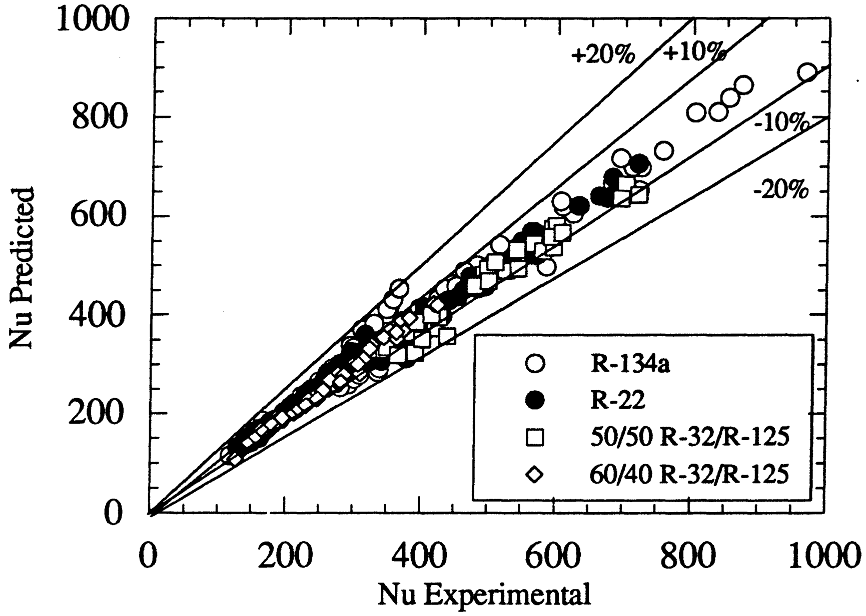

Figure 6.23 Comparison of the annular flow correlation, Eq. (6.8), with the experimental data of the present study.

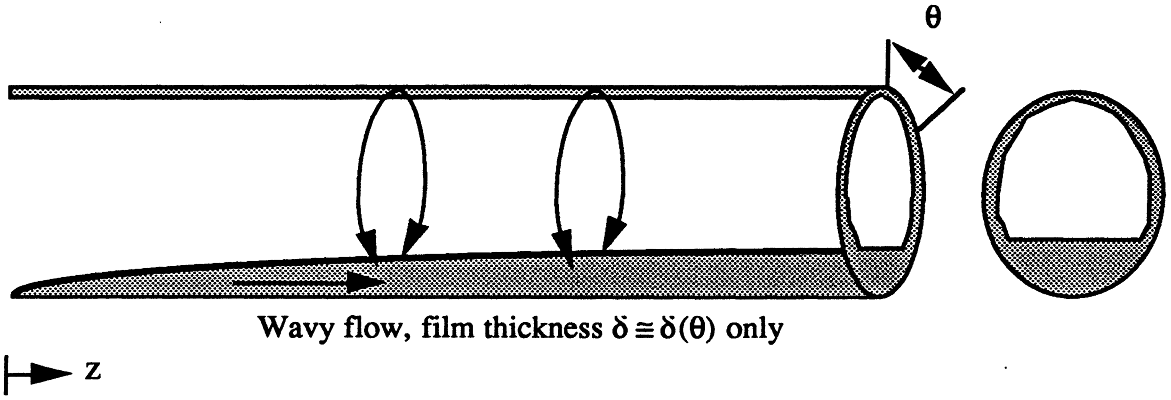

Fig. 6.24a Schematic of stratified flow.

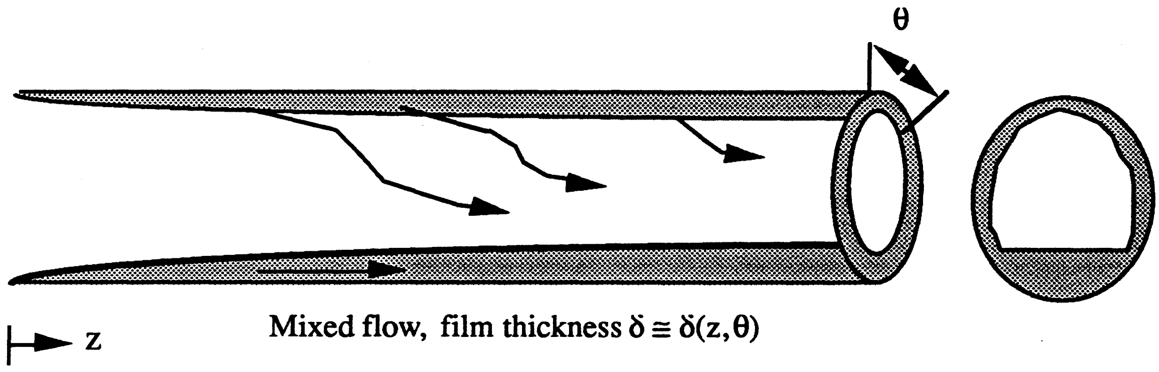

Figure 6.24b Schematic of mixed flow.

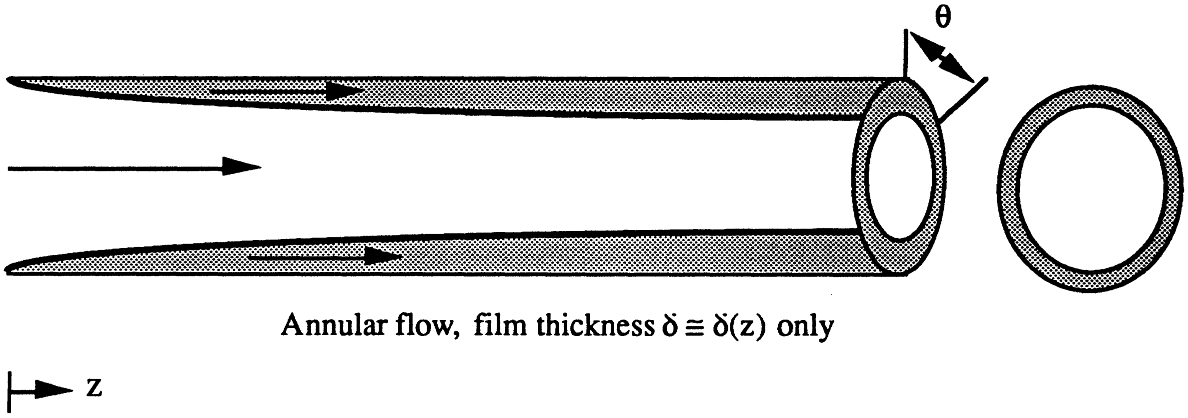

Figure 6.24c Schematic of annular flow.

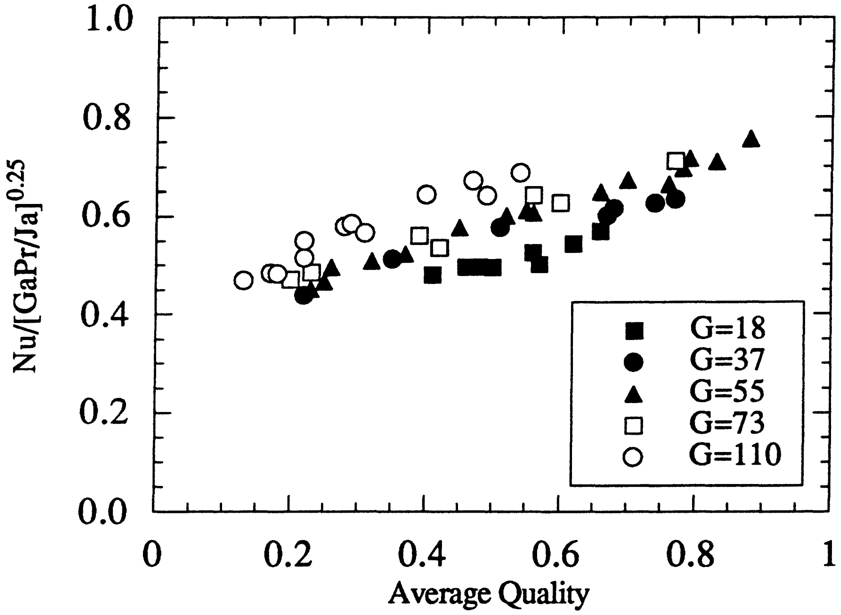

Figure 6.25 Variation of $Nu/[GaPr/Ja]^{0.25}$ with quality assuming all heat transfer occurs by filmwise condensation. R-134a, T_{sat}=95 °F.

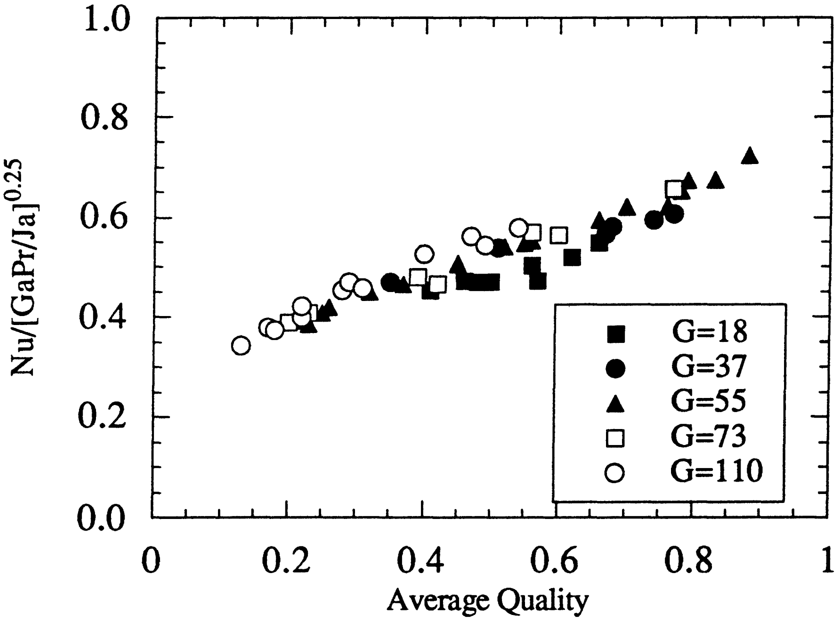

Figure 6.26 Variation of $Nu_{film}/[GaPr/Ja]^{0.25}$ with quality after accounting for forced convective condensation. R-134a, T_{sat}=95 °F.

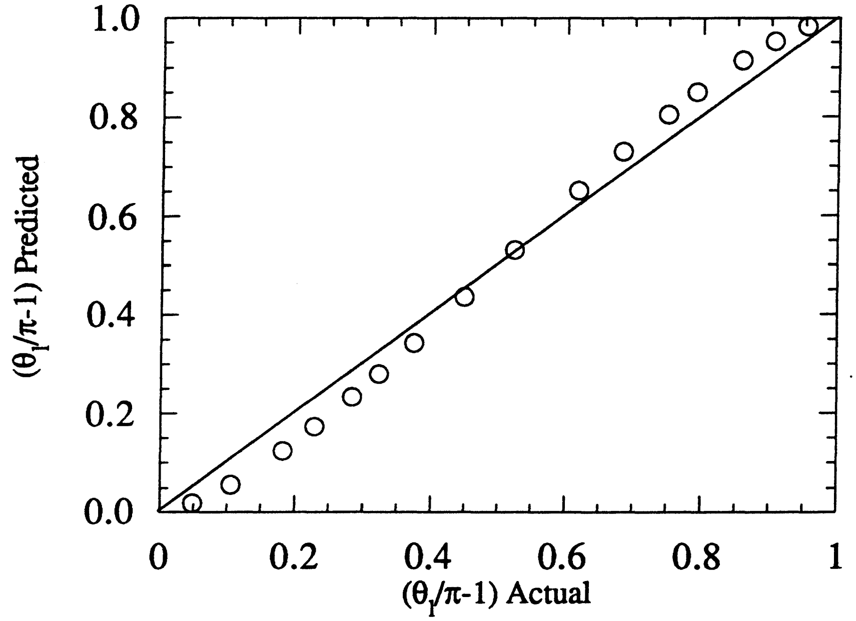

Figure 6.27 Predictions of Eq. (6.18) with the exact solution of Eq. (6.17).

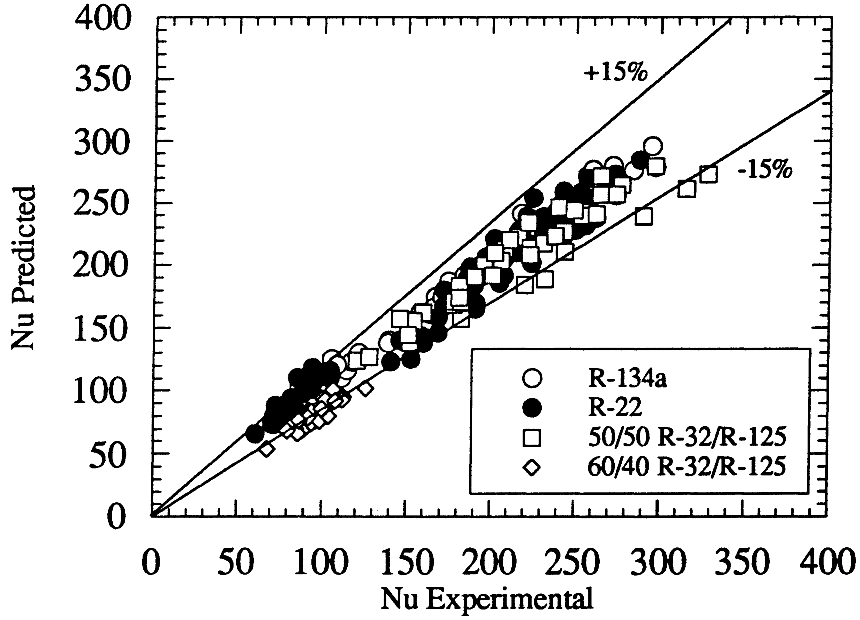

Figure 6.28 Comparison of the wavy flow correlation, Eq. (6.16), with the experimental data of the present study.

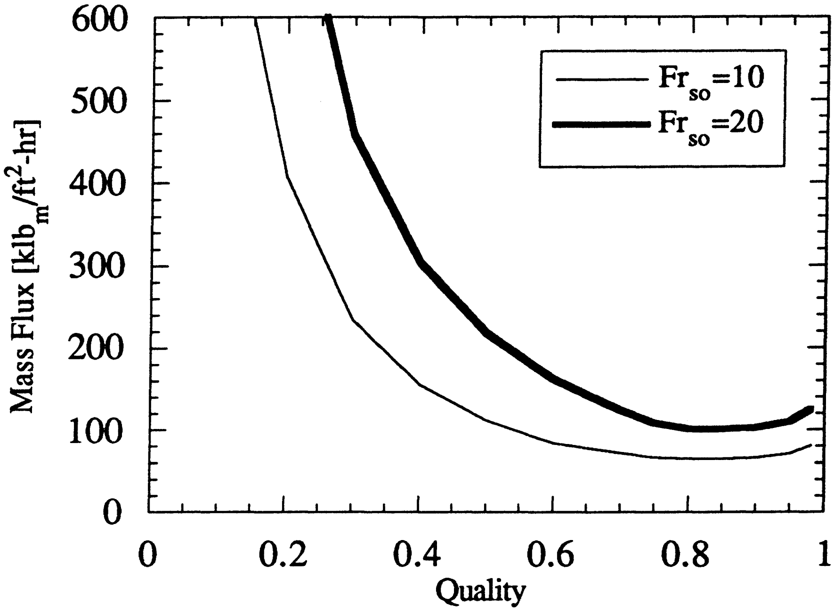

Figure 6.29 Width of the transition region in the G-x plane for R-134a at 95 °F in a .278" i.d. tube.

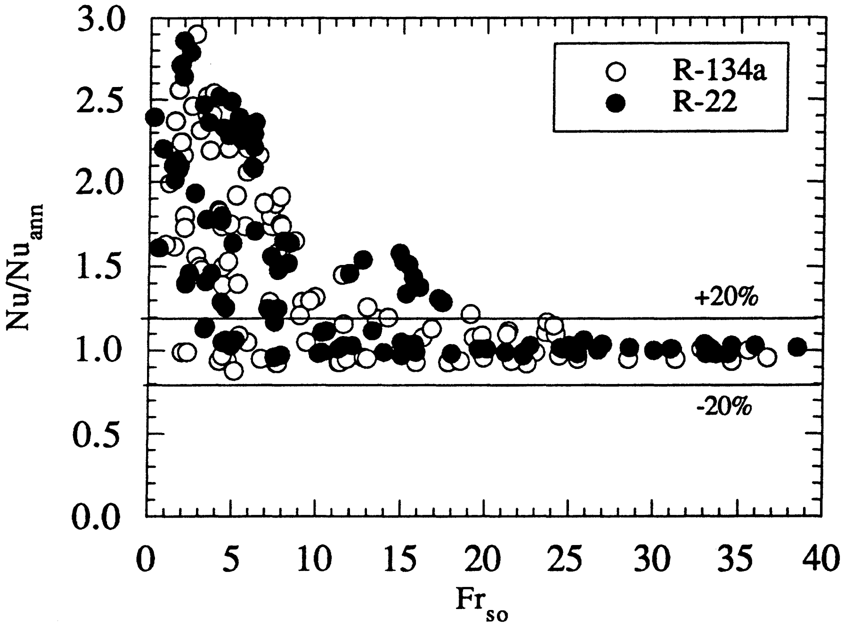

Figure 6.30 Effect of Fr_{so} on the validity of Eq. (6.8).

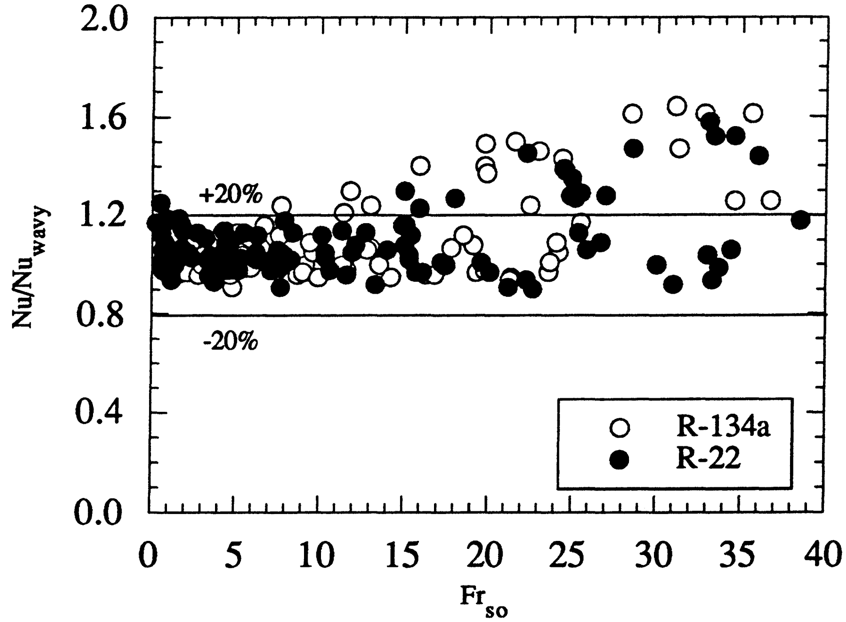

Figure 6.31 Effect of Fr_{so} on the validity of Eq. (6.16).

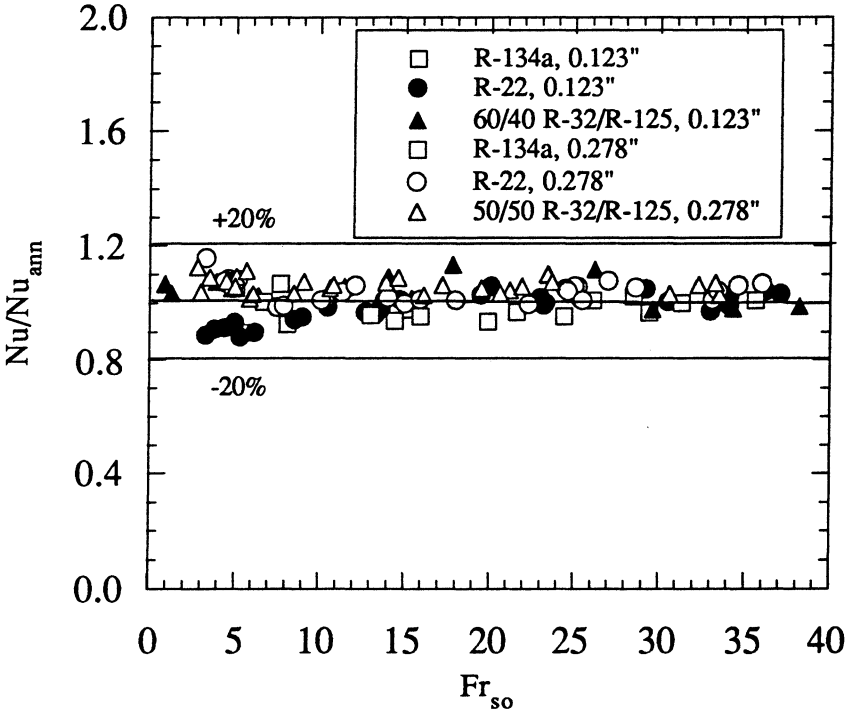

Figure 6.32 Effect of Fr_{so} on the validity of Eq. (6.8) for all data with G>365 klb_m/ft^2-h.

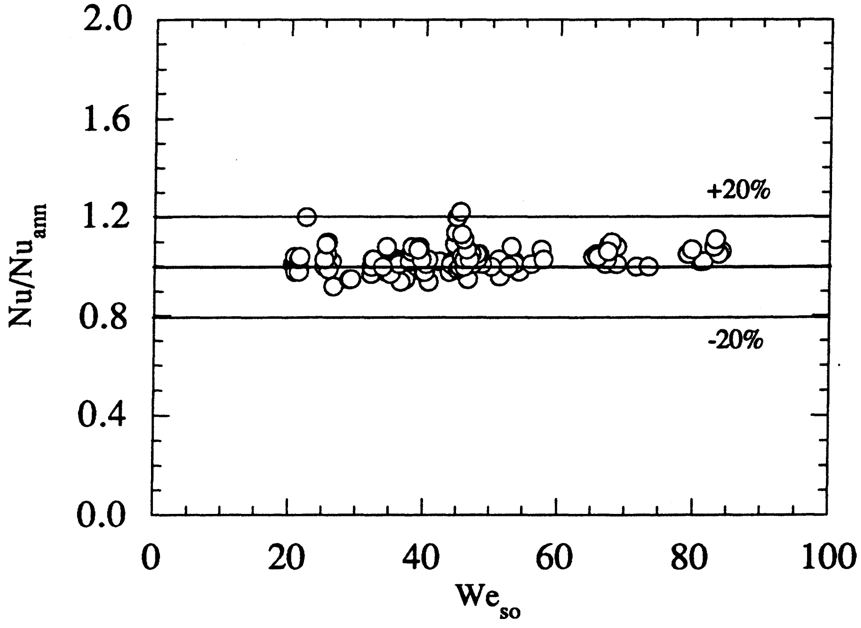

Figure 6.33 Effect of We$_{so}$ on the validity of Eq. (6.8)

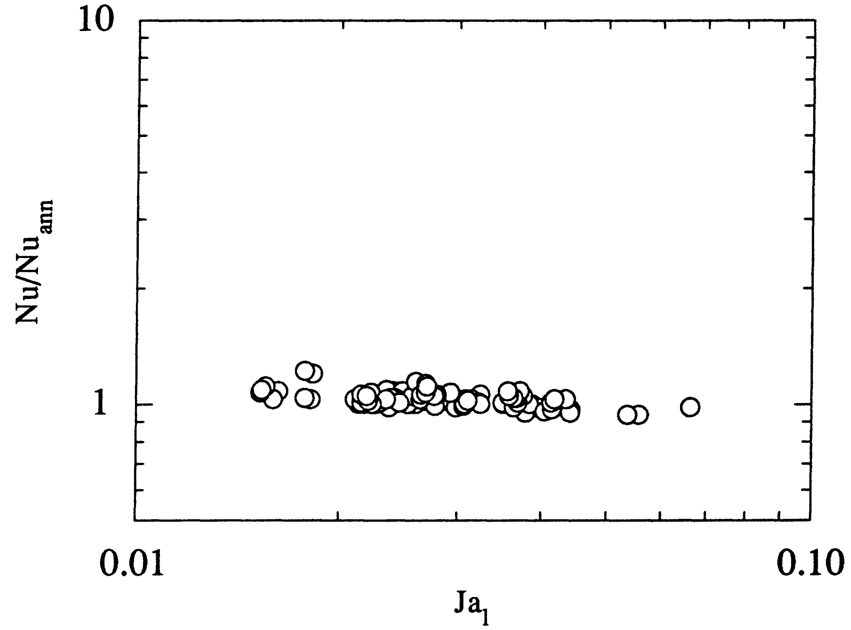

Figure 6.34 Effect of Ja$_l$ on the validity of Eq. (6.8)

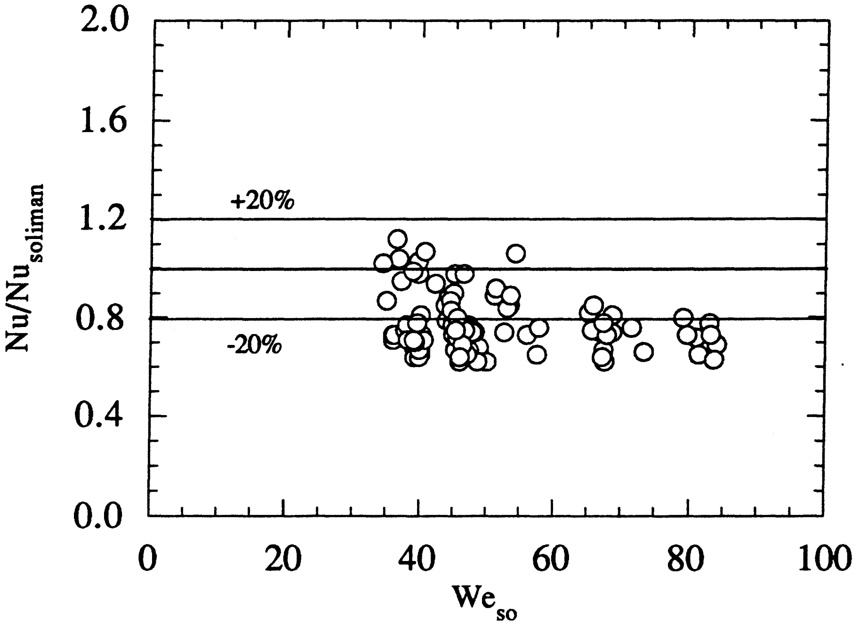

Figure 6.35 Comparison of Soliman's [1986] mist flow correlation with data from the present study with $We_{so}>35$.

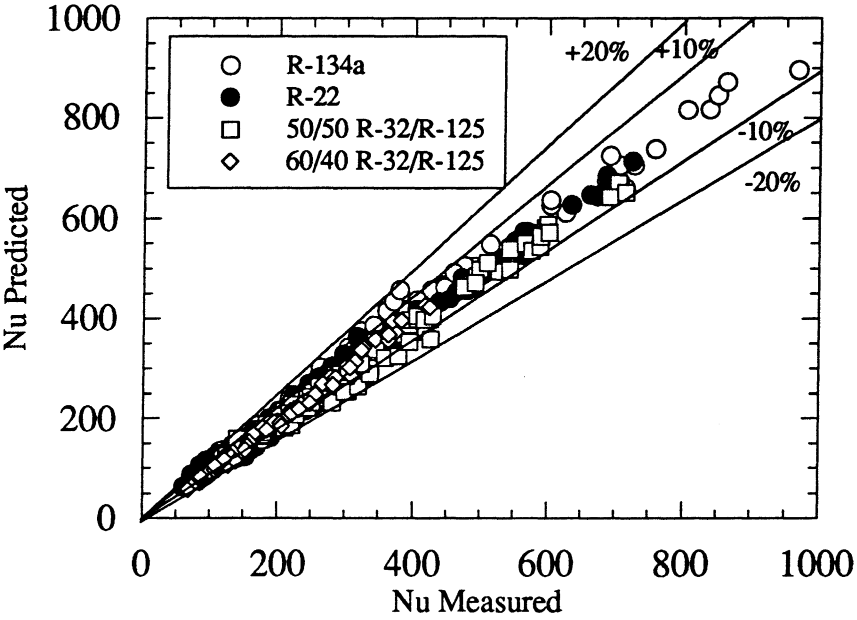

Figure 6.36 Comparison of measured and experimental Nusselt numbers for all data collected in the present study.

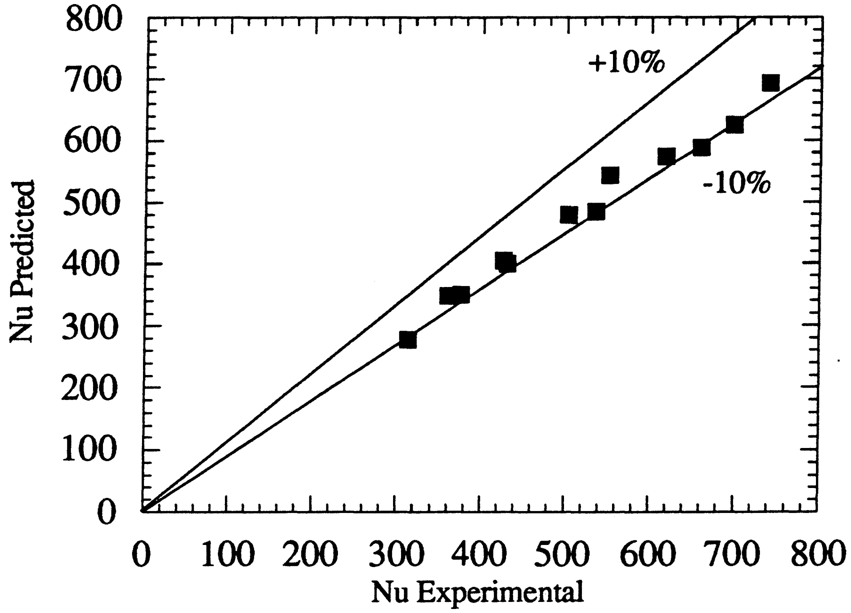

Figure 6.37 Comparison of the annular flow correlation, Eq. (6.8), with the R-22 data of Altmann [1960].

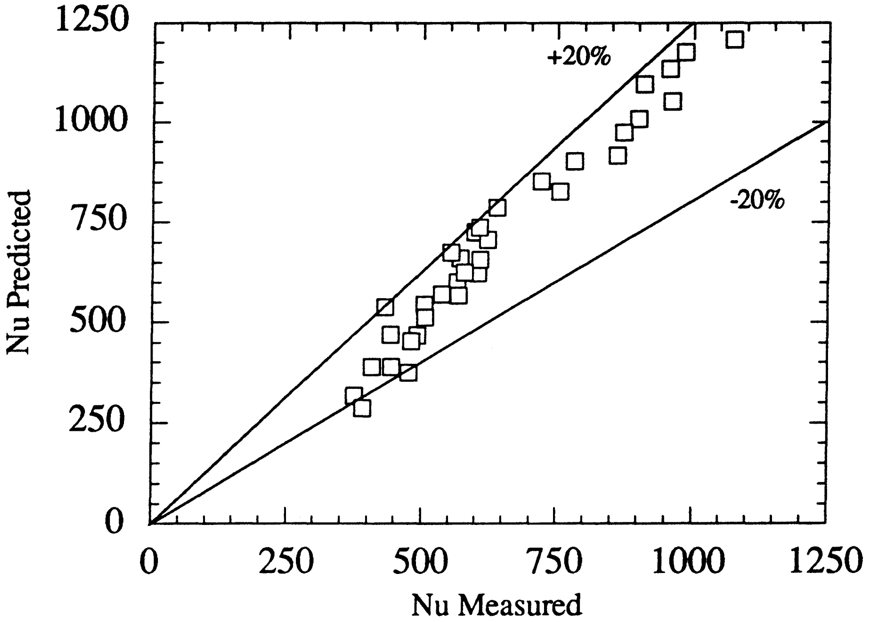

Figure 6.38 Comparison of the heat transfer correlations with the R-22 data of Bae et al. [1970].

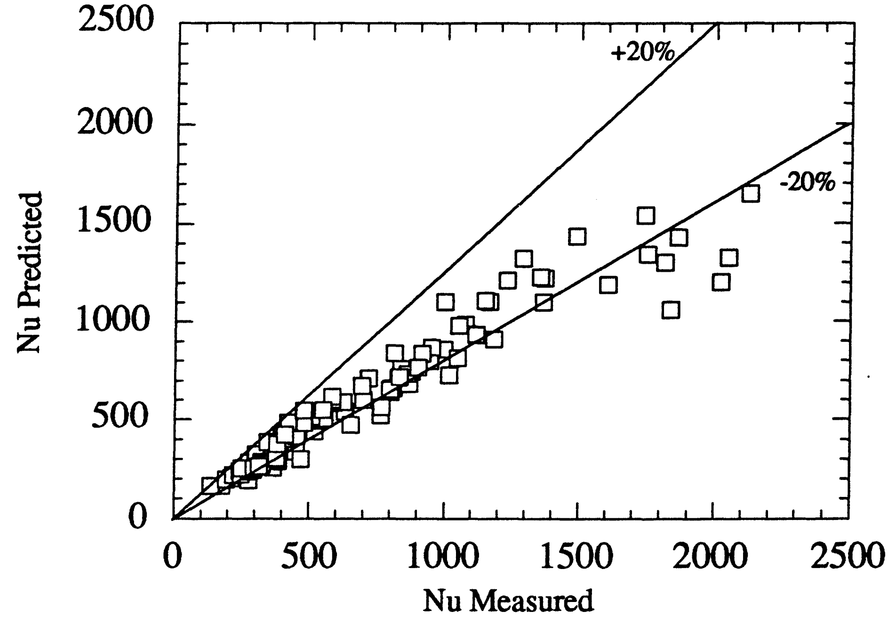

Figure 6.39 Comparison of the heat transfer correlations with the R-12 data of Traviss et al. [1971].

CHAPTER 7

CONDENSER SIMULATION RESULTS

In Chapters 5 and 6, the flow regime and heat transfer results from the study were presented and discussed. While many flow regimes are traversed during the condensation process, the transition of primary importance to condensing heat transfer was shown to be that from a gravity-dominated to a shear-dominated regime. Separate heat transfer correlations were developed for the gravity and shear-dominated regimes, and guidelines for when to use each of these correlations were formulated. The final result was a set of correlations capable of accurately predicting condensing heat transfer coefficients over a wide range of conditions.

While prediction of internal heat transfer coefficients is an important element in simulating a condenser, there are several others. If attention is restricted to the refrigerant side of the heat exchanger, the primary sources of irreversibility are heat transfer across a finite temperature difference and frictional pressure drop. The annular flow correlations of Traviss et al. [1973] and Chen et al. [1987] clearly reflect the interdependence between these two irreversibility sources in the annular flow regime. While this interdependence is not explicitly stated in the annular flow correlation developed for this study, the underlying physics are in fact the same. If the tube geometry and mass flow rate are treated as constants, the magnitudes of these two irreversibility sources can be altered by changing the diameter. As the diameter is decreased, both the heat transfer coefficient and pressure drop will increase due to increases in phase velocities. Thus, one source of irreversibility is minimized at the expense of another. Unlike single-phase situations, the pressure drop has an added role since it destroys the driving temperature difference for heat transfer. This mix of effects suggests, at least qualitatively, that an optimum diameter might exist for each set of conditions.

In this chapter, the two-phase heat transfer correlations developed in this study are combined with the two-phase pressure drop correlation of Souza et al. [1992] and the return bend pressure drop correlation of Christoffersen et al. [1993] to simulate the two-phase portion of a condenser. The governing equations are solved by a simple spreadsheet model initially developed in ACRC Technical Report 42 [Dobson et al., 1992]. This spreadsheet is used to investigate the effect of tube diameter on the length required to completely condense a fixed mass flow rate of refrigerant with the air side resistance per unit length held constant. Simulations are performed for a low flow rate case indicative of a household refrigerator and a high flow rate case typical of a residential air conditioner.

The existence of an optimum diameter at which the condensing surface area is minimized is demonstrated, and the effect of refrigerant properties and operating conditions on this optimum diameter is explored.

7.1 Description of the Physical Model

For steady-state, one-dimensional heat transfer with constant properties, heat transfer can be posed in terms of thermal resistances. Heat exchangers are typically constructed of thin-walled, high conductivity tubes. If fouling effects are small, it is reasonable to neglect the resistance of this tube wall relative to the resistances to heat transfer on the refrigerant and air sides. This results in the following equation for the heat transfer rate:

$$\dot{Q} = \frac{L(T_{sat} - T_a)}{R'_{ref} + R'_a} \tag{7.1}$$

where

$$R'_{ref} = \frac{1}{\pi D h_{ref}} = \frac{1}{\pi Nu_{ref} k_l} \tag{7.2}$$

The quantity R' in Eq. (7.1) and Eq. (7.2) is the thermal resistance per unit length. The air side resistance per unit length, R'_a, is treated as a known constant in the present study so that the effect of changes in refrigerant side conditions can be isolated. It is interesting to note that the refrigerant side resistance includes the product of the heat transfer coefficient times the perimeter. As the diameter is reduced, the heat transfer coefficient is normally increased. This can be misleading, however, since this increase in heat transfer coefficient is mitigated by a corresponding decrease in surface area. Equation (7.2) shows that it is more important to assess how altering the diameter alters the Nusselt number rather than the heat transfer coefficient, since the Nusselt number automatically couples the heat transfer coefficient with the diameter.

Equation (7.1) assumes constant values of the resistances and temperatures with length. In a two-phase heat exchanger, though, the refrigerant side heat transfer coefficients change with length and the saturation temperature decreases due to pressure drop. Thus, it is appropriate to apply Eq. (7.1) only for small quality changes where these assumptions can be reasonably approximated. The total length can be computed for each quality increment, and added as a finite sum. Although the correct mathematical approach is an integration process, algebraic complexities normally preclude this being accomplished analytically.

Figure 7.1 is a schematic for a differential element of the condenser. If the amount of heat transfer over this element is denoted by $\delta\dot{Q}$, its length is denoted by δL, and the temperature of the refrigerant is assumed to change linearly with the axial coordinate, applying Eq. (7.1) to the differential element gives:

$$\delta\dot{Q} = \frac{\delta L((T_{sat,i} + T_{sat,o})/2 - T_a)}{R'_{ref} + R'_a} \tag{7.3}$$

The inlet and outlet saturation temperatures differ due to pressure drop:

$$T_{sat,o} = T_{sat,i} + \frac{\Delta P}{\Delta z}\left(\frac{dT}{dP}\right)_{sat} \delta L \tag{7.4}$$

Since the pressure gradient is negative, the outlet saturation temperature is less than the inlet. If the temperature difference at the inlet of the element is defined as ΔT_i, Eq. (7.3) and Eq. (7.4) can be combined to give:

$$\delta\dot{Q} = \frac{\delta L \Delta T_i + \frac{\Delta P}{\Delta z}\left(\frac{dT}{dP}\right)_{sat} \frac{\delta L^2}{2}}{R'_{ref} + R'_a} \tag{7.5}$$

If the inlet and outlet qualities are assumed known, all quantities except the length in Eq. (7.5) can be calculated at the average quality for the element. In ACRC Technical Report 42 [Dobson et al., 1992], Eq. (7.5) was solved iteratively for the length at each quality increment. As written in Eq. (7.5), it is clearly a simple quadratic equation that can be solved analytically. The solution is given by:

$$\delta L = \frac{-\Delta T_i \pm \sqrt{\Delta T_i^2 + 2\left(\frac{\Delta P}{\Delta z}\right)\left(\frac{dT}{dP}\right)_{sat} \delta\dot{Q}(R'_{ref} + R'_a)}}{\left(\frac{\Delta P}{\Delta z}\right)\left(\frac{dT}{dP}\right)_{sat}} \tag{7.6}$$

Since $\Delta P/\Delta z$ is negative, the possibility of physically unrealistic, complex-valued solutions to Eq. (7.6) must be considered. Just before the solution becomes complex valued, the term inside the radical is zero. At this point, the following equality is satisfied:

$$\underbrace{-\delta L\left(\frac{\Delta P}{\Delta z}\right)\left(\frac{dT}{dP}\right)_{sat}}_{\text{temperature drop}} = \Delta T_i \tag{7.7}$$

This corresponds to the case where the temperature drop due to pressure drop equals the inlet temperature difference, or where the outlet refrigerant temperature is equal to the air temperature. Any greater pressure drop would lead to a second law violation, and is thus prohibited physically and mathematically.

Equation (7.6) can be rewritten in a slightly more intuitive form if nondimensionalized. Scaling the length by the length that would occur if there were no temperature drop, Eq. (7.6) becomes:

$$\delta\tilde{L} = \frac{1-\sqrt{1-2\tilde{T}}}{\tilde{T}} \tag{7.8}$$

$$\delta\tilde{L} = \frac{L\Delta T_i}{\dot{Q}\left(R_a' + R_{ref}'\right)} = \frac{\text{length}}{\text{length w / o temp. drop}} \tag{7.9}$$

$$\tilde{T} = \underbrace{\frac{-\left(\Delta P/\Delta z\right)\left(dT/dP\right)_{sat}}{\Delta T_i}}_{\text{fractional temp. drop/length}} * \underbrace{\frac{\dot{Q}\left(R_a' + R_{ref}'\right)}{\Delta T_i}}_{\text{length w/o temp. drop}} \tag{7.10}$$

This form relates the length of the element to the length that would have existed without any temperature drop. Real solutions to Eq. (7.8) only exist for values of $\tilde{T}$ less than or equal to 0.5. For values of $\tilde{T}$ very close to zero, $\tilde{L}$ is nearly unity and the temperature drop has negligible effect on the length. For $\tilde{T}=0.5$, the limiting value, the effect of temperature drop doubles the length.

7.1.1 Pressure drop model

The pressure gradient in Eq. (7.6) is composed of terms due to friction and phase-change, as shown in Eq. (2.75).

$$\frac{-\Delta P}{\Delta z} = \left(\frac{-\Delta P}{\Delta z}\right)_f - \left(\frac{\Delta P}{\Delta z}\right)_{acc} \tag{7.11}$$

The frictional pressure gradient was calculated using the pressure drop correlation of Souza [1992]. This correlation was used in the wavy flow model, as discussed in Section 6.2.2. The Souza correlation has been compared to a wide range of adiabatic and diabatic pressure drop data from the present study, and consistently predicted the pressure drops with a mean deviation of less than 20%. The correlation is as follows:

$$-\left(\frac{\Delta P}{\Delta z}\right)_f = \underbrace{\frac{2f_l(G(1-x))^2}{\rho_l D}}_{(-\Delta P/\Delta z)\text{ liquid}} \underbrace{\phi_l^2(X_{tt}, Fr_l)}_{\text{2-phase multiplier}} \tag{7.12}$$

$$f_l = \frac{0.0791}{Re_l^{0.25}} \qquad (7.13)$$

The equation for the two-phase multiplier, ϕ_l^2, was given in Section 6.3.2 by Eq. (6.11) through Eq. (6.13). Inclusion of all the terms containing a diameter dependence in Eq. (7.12) reveals that in the annular flow regime, the frictional pressure drop is proportional to $D^{-4.75}$ at constant mass flow rate.

The pressure also changes in a two-phase flow because of phase-change. This is often called acceleration pressure drop, although the phase-change process in a condenser actually decelerates the flow and results in a pressure increase. The equation for the pressure drop due to phase-change is obtained by a simplified one dimensional momentum equation using average velocities for each phase. If quantities at the inlet and outlet of the control volume are subscripted by i and o, respectively, the equation for the so-called acceleration pressure drop is:

$$-\Delta P_{acc} = G^2\left\{\left[\frac{x_o^2}{\rho_V\alpha_o} + \frac{(1-x_o)^2}{\rho_L(1-\alpha_o)}\right] - \left[\frac{x_i^2}{\rho_V\alpha_i} + \frac{(1-x_i)^2}{\rho_L(1-\alpha_i)}\right]\right\} \qquad (7.14)$$

The acceleration pressure drop is proportional to D^{-4} at constant mass flow rate.

In heat exchangers, additional frictional pressure drop also occurs in the return bends. Christoffersen [1993] recently developed a correlation for return bend pressure drop. Using the concept of Pierre [1964], the pressure drop was assumed to consist of additive components due to friction and turning of the flow:

$$\Delta P_{rb} = \Delta P_f + \Delta P_t \qquad (7.15)$$

The frictional component was evaluated using Eq. (7.12) and a length of $\pi D_{rb}/2$. The turning pressure drop was based on a dimensionless resistance factor, ε:

$$\varepsilon = \frac{2\Delta P_t}{G^2}\frac{1}{x\upsilon_v + (1-x)\upsilon_l} \qquad (7.16)$$

This dimensionless resistance factor was found to depend on liquid Reynolds number, Lockhart-Martinelli parameter, and the ratio of the tube diameter to the diameter of the return bend:

$$\varepsilon = \frac{3.465\text{x}10^{-5}}{X_{tt}^{0.712}} Re_l \sqrt{\frac{D}{D_{rb}}} \qquad (7.17)$$

7.1.2 Heat transfer model

The condensing heat transfer coefficients were computed using the annular and wavy flow correlations developed in Chapter 6 according to the guidelines established in Section 6.3.4. In the annular flow regime, Eq. (6.8) shows that at constant mass flow rate the Nusselt number is proportional to $D^{-0.8}$. Thus, decreasing the diameter modestly increases the Nusselt number and decreases the thermal resistance per unit length. In the wavy flow regime, the dominant term in Eq. (6.16) is normally the filmwise component. If all the heat transfer is assumed to occur by filmwise condensation in the wavy flow regime, Eq. (6.16) predicts that the Nusselt number is proportional to $D^{0.63}$ at constant mass flow rate. Thus, decreasing the diameter in the wavy flow regime decreases the Nusselt number and increases the thermal resistance per unit length.

7.2 Computer Model

The equations described above were solved by a simple spreadsheet model. The inputs to the program were: (1) mass flow rate, (2) tube inner diameter, (3) air temperature, (4) inlet refrigerant pressure, (5) return bend diameter, and (6) distance between return bends. The primary output from the program was the length required to completely condense the refrigerant, although other quantities such as heat transfer coefficients and pressure drops were also available. All thermophysical properties of the refrigerants were supplied by calls to spreadsheet macros that were developed for the data reduction procedures described earlier. By implementing the property calls in this way, it was very easy to modify the program for use with different refrigerants.

The solution methodology used in the spreadsheet was to divide the heat exchanger into elements representing a fixed change in quality of 5% and solve for their length. This makes it difficult to place the return bends in a realistic way, since the elements are not of fixed length. Wattelet [1994] recently placed one return bend after each 5% quality change to gauge their general effect. In the present model, the pressure drop that one return bend would create was calculated at the outlet quality for each element. This value was then multiplied by the ratio of the element's length to the desired spacing between return bends. While improvements on this technique could certainly be made, it seems to be the most reasonable method that is compatible with the solution methodology. It also allows the effect of return bends to be neglected by inputting a length between return bends that is much greater than the length of the heat exchanger.

In reality, the effects of changing the condenser diameter would propagate throughout the system. A full system model would be necessary to assess all of these effects. The purpose of the present model was to isolate the changes to the condenser only, yet still accurately assess the competing effects of pressure drop and heat transfer. This was accomplished by holding the inlet saturation pressure constant, which is equivalent to holding the work requirements of the compressor constant. The effect of pressure drop was then to destruct the driving temperature difference, thus increasing the condensing length. It is believed that this was the most realistic method for simultaneously decoupling the condenser from the rest of the system and assessing the tradeoffs between heat transfer and pressure drop.

7.3 Optimum Tube Diameter Simulations

The mixed physical effects that occur when the tube diameter is changed suggest that an optimum diameter might exist for each set of operating conditions. The spreadsheet model was used to address this question for two different situations. The first was a high mass flow rate case that was typical of residential air conditioners, and the second was a low mass flow rate case that was typical of domestic refrigerators. For the residential air conditioner case, the base case simulation was performed for R-22 and compared to two potential replacements, R-134a and the 50/50 R-32/R-125 mixture. For the domestic refrigerator simulation, the base case for R-12 was compared to its replacement refrigerant, R-134a. Inputs to the program for each of these cases are summarized in Table 7.1.

Table 7.1 Required inputs for the condenser simulation

Quantity	High Flow Rate Case	Low Flow Rate Case
$\dot{m}_r$	80.0 lb_m/h	10.0 lb_m/h
$T_{sat,i}$	110 °F	100 °F
T_a	90 °F	75 °F
R'_a	0.073 h-ft-°F/Btu	0.429 h-ft-°F/Btu

7.3.1 High flow rate case

The high flow rate case was designed to simulate the conditions of a condenser from a residential air conditioner. The baseline fluid for this simulation was R-22 at the conditions shown in Table 7.1. The results for this baseline case are presented in Fig. 7.2. Two curves are shown in Fig. 7.2, one representing the condensing length (associated with the left y-axis) and the other representing the heat exchanger surface area (associated with the right y-axis). As the inside diameter is decreased, the required length of heat exchanger slowly increases until eventually the curve takes a sharp upward turn. This can be explained physically as follows. In the part of the curve where the slope is the greatest, the flow regime is primarily annular and the pressure drop is very high. In fact, a substantial portion of the driving temperature difference (on the order of 20% to 80%, changing rapidly with D) is being destroyed due to pressure drop. Since pressure drop is very sensitive to diameter at constant mass flow rate, increasing the diameter even slightly preserves a substantial portion of the temperature difference and reduces the required length. As the slope of the curve decreases, pressure drop becomes less important so that increasing the diameter has only a modest effect on the temperature difference. In this region, annular flow heat transfer correlations would suggest that the length should begin to increase as diameter increases, since the annular flow refrigerant side resistance increases with increasing diameter. What happens to prevent this, though, is that the flow regime becomes wavy over a substantial portion of the heat exchanger. In the wavy flow regime, increasing the diameter decreases the thermal resistance, resulting in a slightly shorter heat exchanger.

Although no clear optimum diameter exists on the length versus diameter curve in Fig. 7.2, there is certainly a point of diminishing return where further increases in diameter allow only small reductions in length. The surface area versus diameter curve, though, does exhibit a distinct optimum diameter of about .177". Comparing the curve of surface area versus diameter (A_s vs. D) with that for length versus diameter (L vs. D), it appears that the optimum diameter is near the point where the slope of the L versus D curve approaches zero. It was noted previously that if annular flow were assumed to exist over the entire condenser, an optimum diameter would also be observed based on the L versus D plots. Although this situation is not physically realistic, interest existed about whether the optimum diameter using this criteria would coincide with that using the A_s versus D criteria. This is addressed in Fig. 7.3, which shows two curves of condenser length versus diameter. The first was calculated with the heat transfer criteria developed in Chapter 6, while the second assumed that annular flow always existed. As expected, the curve labeled "annular only" did have an optimum diameter. This value was about .226", around 28% higher than the .177" optimum diameter from the surface area versus diameter curve. Figure 7.3 also shows that neglecting the transition to wavy flow results in an overprediction of the required length. This is because at conditions where wavy flow exists, the wavy flow heat transfer coefficients are nearly always higher than would be predicted with annular flow correlations. This is opposite to the behavior in evaporation, where heat transfer coefficients in the wavy flow regime are lower than would be predicted using annular flow correlations. Since the area versus diameter curve does exhibit an optimum value, the rest of the results will be presented in this format.

In Fig. 7.2 and 7.3, the effect of return bends was neglected. Their effects are demonstrated in Fig. 7.4, which shows surface area versus diameter plots with and without return bends. Simulations were performed for two different return bend diameters, 1.0" and 3.0", both with a spacing between return bends of 24.0". In both cases, the return bends were assumed adiabatic in recognition of the fact that they are normally unfinned. While the smaller return bend diameter probably corresponds closer with commercially used values, both sets of results were plotted to illustrate the effect of return bend diameter. As expected, the inclusion of return bends increased the required surface area because of the additional pressure drop. This effect was insignificant for large diameter tubes, where the pressure drop itself was negligible. The return bend pressure drop increased as the return bend diameter increased, reflecting dominance of the frictional component (which increases as D_{rb} increases) over the turning component (which decreases as D_{rb} increases). The return bend pressure drop comprised between 9% and 17% of the total pressure drop for the 1.0" and 3.0" diameter return bends, respectively. The inclusion of return bend pressure drop also increased the optimum diameter. The optimum diameter without return bend pressure drop was .177". It increased to .182" and .185" for return bend diameters of 1.0" and 3.0", respectively. Since the spacing and sizing of the return bends are somewhat arbitrary and the trends are the same for all the refrigerants, the comparisons between refrigerants that follow neglect the effects of return bends.

Figure 7.5 compares the required surface areas for R-22, R-134a, and the 50/50 R-32/R-125 mixture for the high flow rate case. In this figure, the mass flow rates of R-134a and R-32/R-125 were adjusted slightly so that the heat rejected in the condensers was identical for each of the three fluids. This resulted in a flow rate of 81.1 lb_m/h for R-134a and a flow rate of 81.5 lb_m/h for R-32/R-125, corresponding to 1.6% and 2.1% increases over the R-22 case. From a refrigeration system standpoint, this corresponds to a constant heating capacity simulation. Figure 7.5 shows that the optimum diameter was lowest for R-32/R-125, followed by R-22 and R-134a. This is primarily because of differences in pressure drop and $(dT/dP)_{sat}$, since the heat transfer data from Chapter 6 showed that the differences in heat transfer between the three fluids were relatively small at equivalent conditions. The R-32/R-125 mixture had the lowest values of both pressure drop and $(dT/dP)_{sat}$, followed by R-22 and R-134a. These two effects, which are both related to the reduced pressure, combined to allow substantially higher mass fluxes for the R-32/R-125 mixture than the other refrigerants, without imposing a substantial penalty due to loss of driving temperature difference. It is interesting to note that achieving better performance with the higher reduced pressure fluids <u>requires</u> decreasing the tube diameter, since the surface area requirements of the three fluids are inverted at large tube diameters.

Figure 7.6 compares the surface area requirements of the three fluids based on a constant cooling capacity comparison. For this comparison, the mass flow rates of R-134a and R-32/R-125 were adjusted so that they achieved the same cooling capacity as the baseline R-22 case. The capacity was calculated assuming a 41 °F evaporating temperature and saturated conditions at the outlet of the evaporator and condenser. This resulted in a mass flow rate of 87.38 lb_m/h for R-134a and 80.79 lb_m/h for R-32/R-125. These adjustments represented an increase over the baseline R-22 case of 9.3% for R-134a and 0.8% for R-32/R-125. The trends are identical to those in Fig. 7.5, with the lowest optimum diameter occurring for R-32/R-125, then R-22 and R-134a. The increased mass flow rate of R-134a necessary to achieve the same cooling capacity resulted in an increased length and increased values of optimum diameter as compared to the results from Fig. 7.5. The optimum diameter for the constant cooling capacity simulations was .153" for R-32/R-125, .177" for R-22, and .207" for R-134a.

7.3.2 Low flow rate case

The low flow rate case was designed to simulate the conditions of a condenser from a domestic refrigerator. The baseline fluid for this simulation was R-12 at the conditions shown in Table 7.1. This case was compared with R-134a on an identical cooling capacity basis. To achieve this, the mass flow rate of R-134a was lowered to 7.90 lb_m/h, about 27% lower than the R-12 case. It is interesting to note that for the comparison of R-12 and R-134a, the constant cooling capacity simulation resulted in the same heat transfer rate in the condenser (within 1%). This result is probably due to the reduced pressures of R-134a and R-12 being very close, which results in a similar shape for their P-i diagrams. This was not the case for the high flow rate comparisons, though, where the constant cooling capacity simulations resulted in significantly different heat transfer rates in the condenser.

The results of the simulations are shown in Fig. 7.7. The shape of the surface area versus diameter curves for the low flow rate case are similar to those from the high flow rate case, although the optimum diameters are considerably smaller (as low as .079"). In fact, no experimental evidence is available to verify that the condensation correlations from Chapter 6 are valid in tube diameters below .118". Thus, any optimum tube diameter predictions below .118" should viewed with some caution. The surface area requirements were lower for R-134a than for R-12. This is because the superior thermal properties of R-134a resulted in nearly identical heat transfer coefficients to those of R-12, even with a 27% reduction in flow rate [Hinde et al., 1992]. This reduction in flow rate resulted in substantially lower pressure drop for R-134a, though, preserving more of its driving temperature difference.

7.4 Analytical Investigation of the Optimum Diameter

The existence of the optimum diameter with respect to surface area was of sufficient interest to warrant further analysis. First, intermediate information in the spreadsheet such as pressure drop, temperature drop, and ratio of refrigerant side to air side resistance were analyzed for all of the simulations. From this analysis, one quantity was found to be nearly constant at the point where the optimum diameter occurred. This quantity was the fraction of the inlet temperature difference that was destroyed by pressure drop. For both the high and low flow rate cases, with and without return bends, this quantity was consistently between 20% and 30% at the optimum diameter. Grannryd [1992] reported a similar finding for evaporation, stating that the optimum loading for a heat exchanger circuit occurred when 25% of the driving temperature difference was destroyed by pressure drop. The consistency of this finding over a fairly wide range of fluids and air side thermal resistances, combined with the relatively simple algebraic nature of the governing equations, led to an analytical search for the optimum tube diameter.

Several simplifications were made before beginning the analysis. At the point where the optimum diameter occurred, the flow regime was annular over nearly the entire condensation path. The fact that no change in heat transfer mechanism had to be accounted for suggested that the finite sum used to compute the length could be approximated by one equation, where all quantities were essentially average values. This equation is:

$$\dot{Q} = \frac{L\left(\Delta T_i + \left(\frac{\Delta P}{\Delta z}\right)\left(\frac{dT}{dP}\right)_{sat}\frac{L}{\gamma}\right)}{R_a' + R_r'} \tag{7.18}$$

The quantity γ that in Eq. (7.18) is a factor introduced to account for the nonlinearity of the temperature drop with axial distance along the heat exchanger. While a linear approximation was assumed in Eq. (7.3), this is unrealistic for high quality changes since the pressure gradient is much higher at the inlet of the condenser than the outlet. A value of γ equal to 2 is equivalent to a linear temperature variation, while a value of 1 would assume that the entire temperature drop occurred immediately at the condenser inlet. This value was calculated for the baseline R-22 case at the minimum diameter, giving a value of 1.57. Although this value varied slightly with conditions, the value of 1.57 was used throughout the present analysis.

Dimensionless quantities similar to those defined by Eq. (7.8) and Eq. (7.9) were introduced. The new variables were defined as follows:

$$L^* = \frac{L}{L_{min}} = \frac{L\Delta T_i}{\dot{Q}R_a'} \tag{7.19}$$

$$R^* = \frac{R_r'}{R_a'} \tag{7.20}$$

$$T^* = \frac{\left(\frac{-\Delta P}{\Delta z}\right)\left(\frac{dT}{dP}\right)_{sat} L_{min}}{\Delta T_i} = \frac{\left(\frac{-\Delta P}{\Delta z}\right)\left(\frac{dT}{dP}\right)_{sat}}{\Delta T_i}\frac{\dot{Q}R_a'}{\Delta T_i} \tag{7.21}$$

The length scale in this analysis was changed from the one defined in Eq. (7.8). The length scale in Eq. (7.19) and Eq. (7.21) is the required condensing length with zero refrigerant side resistance and no pressure drop, thus it was designated as L_{min}. It results in mathematical simplifications later, since it is independent of the tube diameter. Introducing the dimensionless quantities into Eq. (7.18) results in a quadratic equation similar to Eq. (7.5). The physically meaningful solution to this equation is given by:

$$L^* = \frac{\gamma/2 - \sqrt{\left(\gamma/2\right)^2 - \gamma T^*\left(1+R^*\right)}}{T^*} \tag{7.22}$$

The optimum diameter that is sought is the one that minimizes the surface area requirements, or the product of L and D. If the diameter is scaled by L_{min} to form D^*, the desired optimum is achieved when :

$$\frac{d}{dD^*}\left(L^*D^*\right) = 0 \tag{7.23}$$

Applying the product rule to Eq. (7.23) gives:

$$\frac{dL^*}{dD^*} = \frac{-L^*}{D^*} \tag{7.24}$$

Using the chain rule to evaluate the derivative in Eq. (7.24) results in:

$$\frac{\partial L^*}{\partial D^*} = \frac{\partial L^*}{\partial T^*}\frac{\partial T^*}{\partial D^*} + \frac{\partial L^*}{\partial R^*}\frac{\partial R^*}{\partial D^*} \tag{7.25}$$

In the annular flow regime, the thermal resistance per unit length (and hence R^*) is proportional to $D^{0.8}$ at a fixed mass flow rate. If the pressure gradient is assumed to consist entirely of frictional pressure drop, then the pressure gradient and hence T^* is proportional to $D^{-4.75}$ at fixed mass flow rate. These observations lead to:

$$\frac{\partial R^*}{\partial D^*} = \frac{0.8R^*}{D^*} \tag{7.26}$$

$$\frac{\partial T^*}{\partial D^*} = \frac{-4.75T^*}{D^*} \tag{7.27}$$

If these two equations are substituted into Eq. (7.24), the D^* terms in the denominator all cancel. This defines a relationship between T^* and R^* at the optimum point:

$$0.8\frac{R^*T^*}{\gamma/2-\sqrt{\gamma/2-\gamma T^*\left(1+R^*\right)}}\frac{\partial L^*}{\partial R^*}-4.75\frac{T^{*2}}{\gamma/2-\sqrt{\gamma/2-\gamma T^*\left(1+R^*\right)}}\frac{\partial L^*}{\partial T^*}=-1 \tag{7.28}$$

The partial derivatives in Eq. (7.28) were evaluated, and the resulting expression was solved using *Mathematica*. The desired relationship between T^* and R^* at the optimum is given by:

$$T^*_{opt}=\frac{0.182\gamma\left(0.555+R^*_{opt}\right)}{0.80+1.788R^*_{opt}+\left(R^*_{opt}\right)^2} \tag{7.29}$$

If R^*_{opt} is known, it and the resulting value of T^*_{opt} can be substituted into Eq. (7.22) to give L^*_{opt}. The product $L^*_{opt} * T^*_{opt}$ then gives the fraction of the inlet temperature difference destroyed by pressure drop at the optimum diameter. Substitution and simplification results in the following formula for $L^*_{opt} * T^*_{opt}$, which is called ΔT^*_{opt}:

$$\Delta T^*_{opt}=\gamma\left(0.5-\sqrt{0.25-\frac{0.1816\left(R^*_{opt}+1\right)\left(R^*_{opt}+0.555\right)}{\left(R^*_{opt}+0.894\right)^2}}\right) \tag{7.30}$$

During the spreadsheet simulations, this was the quantity that consistently remained between 25% and 30% at the optimum value of diameter.

The relevance of Eq. (7.30) was not immediately apparent, since one does not know R^*_{opt} *a priori*. Since the refrigerant side resistance can not be varied over an infinite range, though, varying R'_a is analogous to varying R^*_{opt}. To check the validity of Eq. (7.30), the spreadsheet model for the high flow rate case was used to find the optimum diameter as the air-side resistance was varied over a range from $1/10$ of its baseline value to 10 times its baseline value. At each value of optimum diameter, the value of ΔT^*_{opt} and R^*_{opt} was recorded.

The results of the simulation are compared with the predicted values of Eq. (7.30) in Fig. 7.8. Several conclusions can be drawn from the plot. First, the predictions of Eq. (7.30) agree very well with the results of the simulation in both trend and magnitude. Second, over a fairly wide range of R^*_{opt} the optimal value of fractional temperature drop is between 25% and 30%. Equation (7.30) can also be used to deduce the optimal temperature drops in the extreme limits of $R^*_{opt}= 0$ and ∞, with resulting values of 0.232 and 0.374. The fact that the optimal value of fractional temperature drop remains so constant over such a wide range of thermal resistance ratios is perhaps surprising. The slope of the curve, though, is rather intuitive. When the air side heat transfer is very poor (low R^*), its thermal resistance is dominant and little improvement is possible by increasing the refrigerant side heat transfer. This results in low values of ΔT^*_{opt}. As the air side heat transfer becomes better, though, the refrigerant side begins to make up an increasing fraction of the overall thermal resistance. In these cases, benefits from increasing the refrigerant side heat transfer persist to higher values of fractional temperature drop.

Although the analysis presented above agrees well with the more involved spreadsheet model, its usefulness must be placed in the proper context. Its primary utility is demonstrating the importance of the fractional temperature drop as a design parameter, and how optimal values of this parameter depend on the air side heat transfer. It does not yield an explicit expression for the optimal diameter. In principle, the relationship between R^*_{opt} and ΔT^*_{opt} could be used in conjunction with heat transfer and pressure drop correlations to solve for this quantity. Attempts to do this analytically were not successful, however. The spreadsheet model, which is itself rather easy to use, should be utilized for this purpose. One other caution should be considered. At very low values of air-side resistance, the optimum operating conditions might result in wavy flow over a substantial portion of the condenser. Since the diameter dependence from an annular flow correlation was used in Eq. (7.26), the equations above should not be used under such conditions. This was probably responsible for some of the deviation between Eq. (7.30) and the results of the spreadsheet at the lowest value of R^*_{opt} in Fig. 7.8. The spreadsheet model properly accounts for the flow regimes under these conditions, though, and should continue to yield accurate results.

7.5 Summary of Condenser Simulation Results

The heat transfer correlations developed in Chapter 6 were combined with existing pressure drop correlations to develop a simple condenser simulation model. The model predicted the length necessary to completely condense a fixed mass flow rate of refrigerant when supplied with the inlet pressure, mass flow rate, air temperature, air side resistance per unit length, and tube diameter. The model properly accounted for the change in heat transfer mechanism with flow regime, and included pressure drop due to friction, acceleration, and return bends.

The model was used to perform simulations for a low flow rate case that was typical of a refrigerator and a high flow rate case that was typical of a residential air conditioner. For all conditions, the condensing length continuously increased as the diameter was decreased. At large diameters, the decrease in length that accompanied an increase in diameter was very small. At a sufficiently small diameter, though, the condensing length became very sensitive to further decreases in diameter. This corresponded with conditions where the pressure drop was destroying a large percentage of the driving temperature difference. When the variation of the required surface area with tube diameter was examined, an optimum diameter existed that corresponded with a minimum surface area. This optimum occurred for all cases. It is to be noted that if the optimum tube size is not available in practice, the next larger available diameter should be selected for safe design.

For the high flow rate simulations, R-32/R-125 had the lowest value of optimum diameter, followed by R-22 and R-134a. Simulations were performed for cases of equivalent heat transfer in the condenser (constant heating capacity), and equivalent heat transfer in the evaporator (constant cooling capacity). For both cases, R-32/R-125 had the lowest optimum diameter, followed by R-22 and R-134a. This trend was more pronounced for the constant cooling capacity simulation, where a 10% increase in the flow rate of R-134a required it to transfer more heat in the condenser. The trends in condensing length were driven primarily by differences in pressure drop and temperature drop per unit pressure drop, with the higher reduced pressure fluids having substantially lower values of both quantities. This allowed them to operate at higher mass fluxes for a given decrease in the driving temperature difference.

For the low flow rate simulation, R-134a had a lower optimum diameter than R-12. This result occurred because the constant cooling capacity simulation required a 27% lower mass flow rate of R-134a than R-12, giving it lower pressure drop. Its superior thermal properties still allowed heat transfer coefficients that were roughly equal to those of R-12.

The simulations for the various refrigerants and flow rates were carefully studied in an effort to discover some parameter that was closely linked with the optimum diameter. It was discovered that at the point where the optimum diameter occurred, the pressure drop always destroyed between 20% and 30% of the driving temperature difference. After simplifying and nondimensionalizing the governing algebraic equation, an equation was derived which related the fractional decrease in temperature difference to the ratio of refrigerant side to air side thermal resistances at the optimum point. The predictions of this equation were compared with simulation results in which the thermal resistance of the air side was varied by a factor of 100. The agreement was excellent. Although the equation does not yield a closed form solution for the optimum diameter, it does demonstrate that this optimum always corresponds with fractional temperature drops between 23% and 37% over the entire range of resistance ratios.

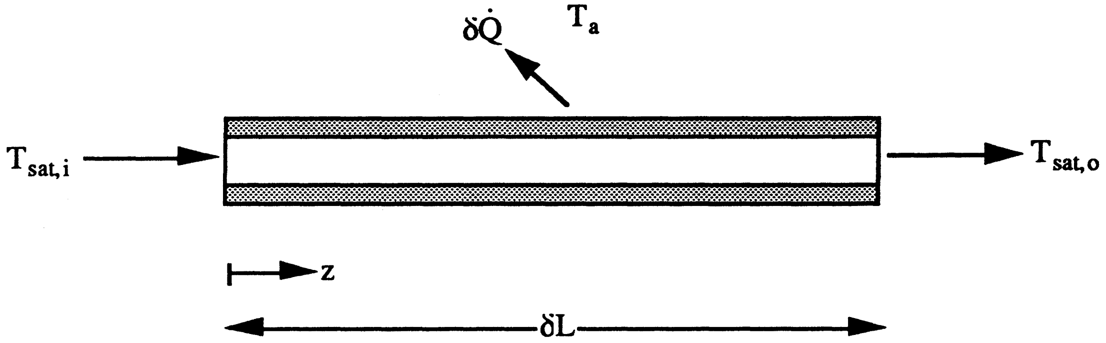

Figure 7.1 Schematic of a differential element of a two-phase heat exchanger

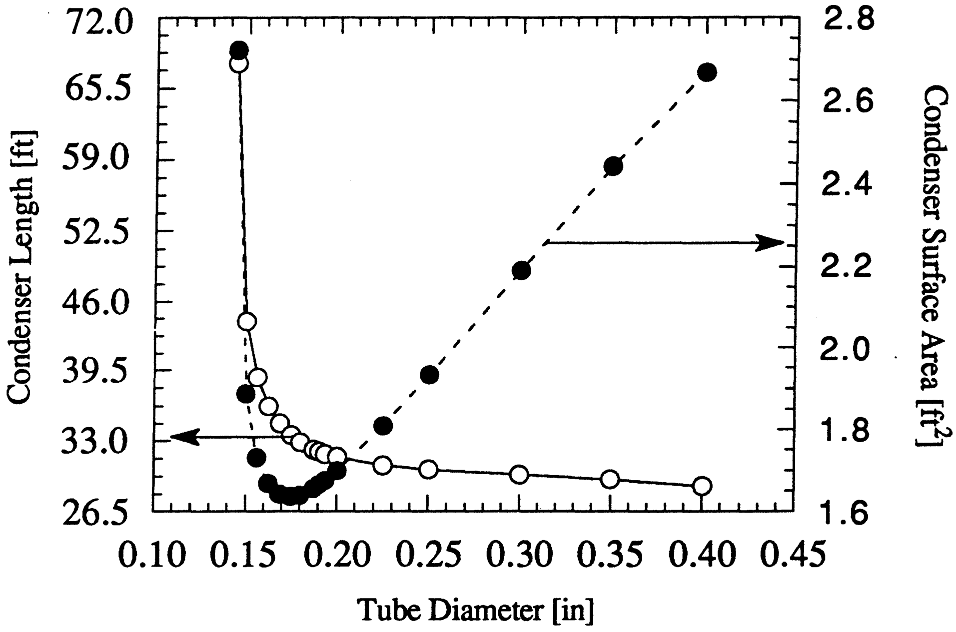

Figure 7.2 Condenser length and surface area for the high mass flow rate with R-22 and no return bends.

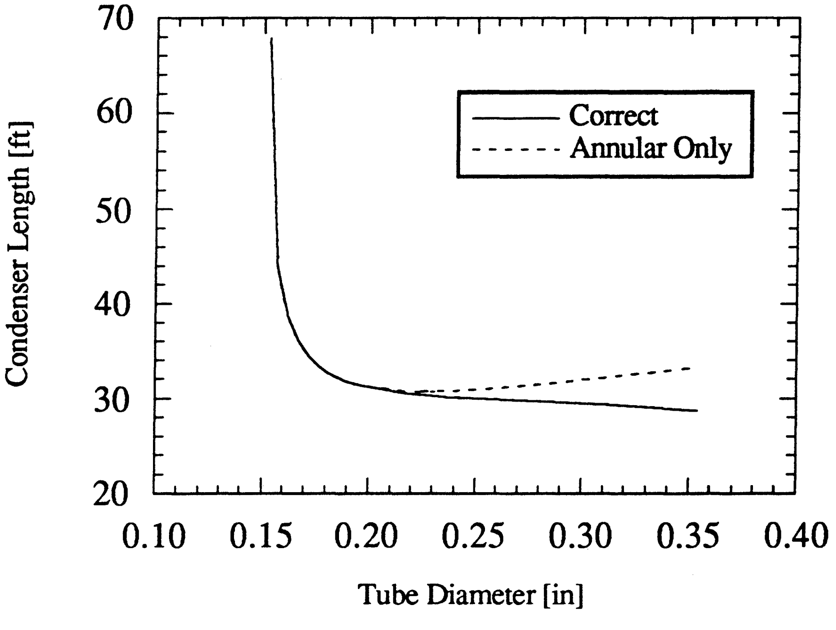

Figure 7.3 Effect of incorrectly using annular flow correlations on the required condensing length for high mass flow rate case of R-22 and no return bends.

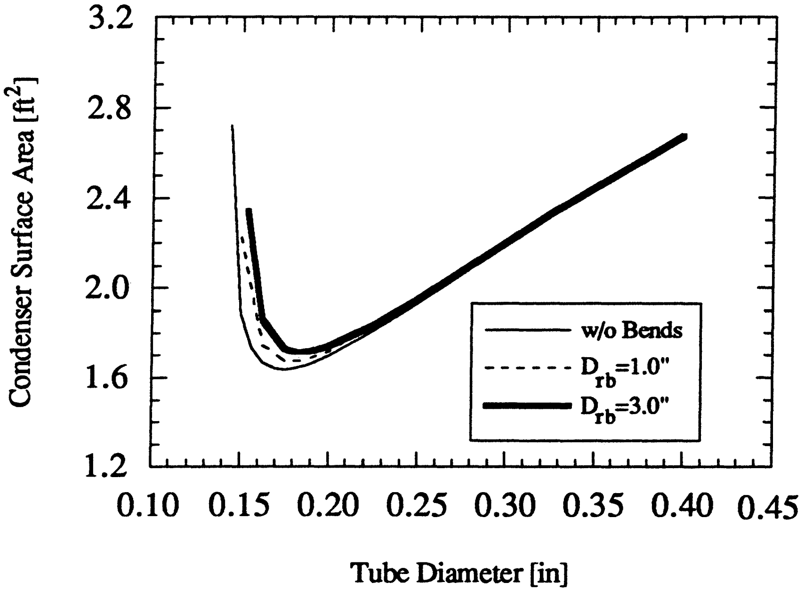

Figure 7.4 Effect of return bends on surface area requirements for the high mass flow rate case of R-22. D_{rb}=1.0" and 3.0", 24" spacing between return bends.

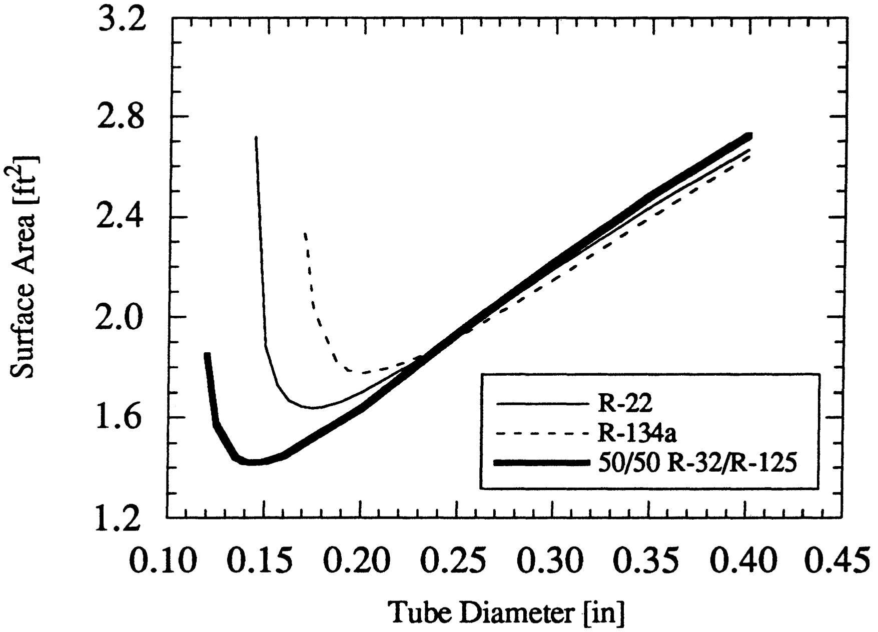

Figure 7.5 Constant heating capacity comparison of R-22, R-134a, and R-32/R-125 for the high flow rate case without return bends.

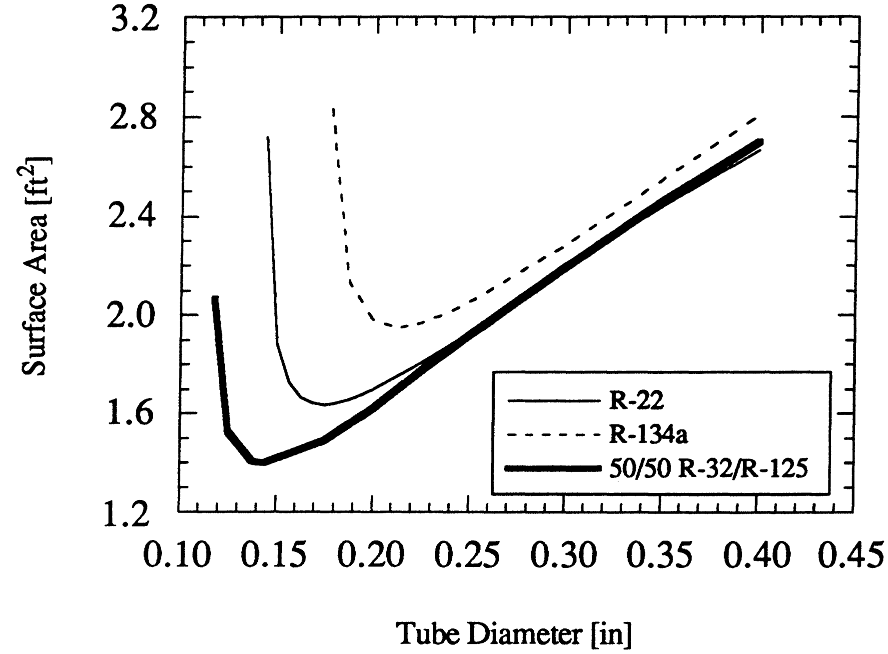

Figure 7.6 Constant cooling capacity comparison of R-22, R-134a, and R-32/R-125 for the high flow rate case without return bends.

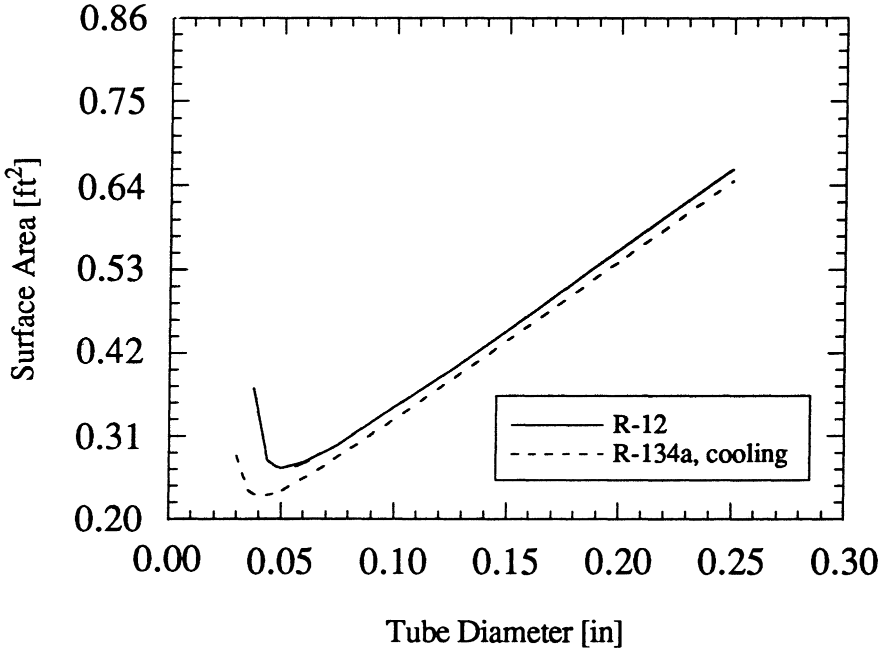

Figure 7.7 Comparison of R-12 and R-134a for the low flow rate case at identical cooling capacity.

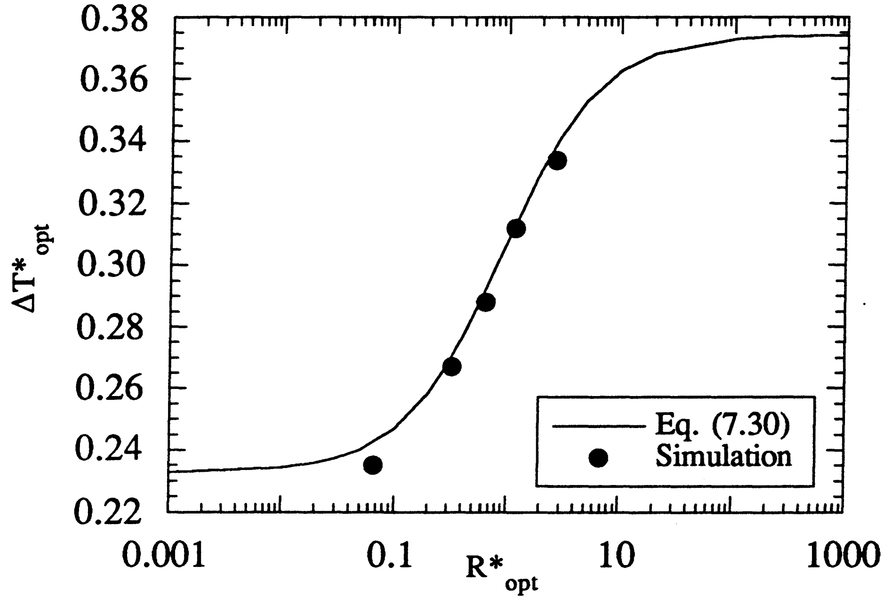

Figure 7.8 Comparison of optimal values of fractional temperature drop predicted by the spreadsheet model and Eq. (7.30)

CHAPTER 8

CONCLUSIONS AND RECOMMENDATIONS

This dissertation described results from an experimental study of condensation inside smooth horizontal tubes. Three primary areas were examined: flow regime observation and prediction, measurement and prediction of heat transfer coefficients, and implementation of heat transfer and pressure drop correlations to address design issues. Experimental data were collected in tubes from .123" to .278" in diameter, over a range of conditions that encompassed most applications from the refrigeration industry. Thus, the conclusions drawn from the study should be generalizable to a wide range of refrigeration applications.

8.1 Conclusions

The present study was divided into three main areas: flow regimes, heat transfer, and design issues. The conclusions from each of these phases of the study are discussed separately.

8.1.1 Flow regimes

A variety of flow regimes were observed during the experiments. These ranged from smooth-stratified flow at low mass fluxes to mist flow at high mass fluxes. Patterns that were identified between these extremes included wavy flow, wavy-annular flow, slug flow, annular flow, and annular-mist flow. From the standpoint of heat transfer performance, the many regimes described above can be broken into two broad categories: (1) gravity-dominated regimes, and (2) shear-dominated regimes. The gravity-dominated regimes include stratified, wavy, and wavy-annular flow. The shear-dominated regimes include annular and annular-mist flow.

Pure mist flow with no stable wall film was observed only in the inlet sight glass, and there only at qualities above 90%. When mist flow was observed at the inlet sight glass, a stable wall film was always observed at the outlet sight glass. This seemed to indicate that what was mist flow in the adiabatic section became annular-mist flow soon after condensation began. Thus, over the range of conditions traversed in the present study, development of a correlation based on the premise of no stable wall film seems misguided.

Three primary techniques for flow regime prediction were evaluated: the Mandhane map using superficial velocity coordinates, the Taitel-Dukler map using dimensionless coordinates related to the physics of the transition processes, and an empirical approach developed by Soliman. The unmodified Mandhane map was a poor predictor of the experimental observations because of vapor densities that were up to 100 times higher than the air water data upon which the map was based. A simple correction to the data suggested by Hanratty [1994] gave each axis the interpretation of a phase kinetic energy, and resulted in much better agreement with the experimental data. The omission of diameter effects in this approach can still prove problematic, however.

The Taitel-Dukler map was a reasonable predictor of the experimentally observed flow regimes. The primary discrepancy occurred at mass fluxes slightly above the annular to intermittent boundary, where the Taitel-Dukler map predicted slug flow at very low qualities and annular flow for the remainder of the quality range. In reality, a gravity-dominated flow including slug, wavy, and wavy-annular flow sometimes persisted to qualities as high as 40% in this regime. While part of this discrepancy was due to differences in classification rather than deficiencies in the map, this regime had heat transfer characteristics much more indicative of wavy flow than annular flow.

Soliman's Froude number served as a good parameter for predicting the wavy to wavy-annular and the wavy-annular to annular flow regime transitions. The value of $Fr_{so}=7$ that was recommended by Soliman delineated the wavy and wavy-annular flow regimes, while a value of $Fr_{so}=18$ predicted the transition from wavy-annular to annular flow. This approach was more accurate than the predictions of the Taitel-Dukler map. Although Soliman's approach lumps the stratified, wavy, and slug flow regions together, which might be heresy from the standpoint of flow regime transitions, this is quite reasonable for delineating regimes where different heat transfer mechanisms prevail. This parameter was successfully utilized to predict when annular or wavy flow prevailed. The modified Weber number that Soliman developed for predicting the annular to mist flow transition has a more questionable theoretical basis. Although it served as a useful tool for predicting when substantial entrainment should be expected, the region that it classified as purely mist flow was occupied almost entirely by annular-mist flow.

8.1.2 Heat transfer

The heat transfer behavior depended strongly on the flow regime. In the gravity-dominated flow regime, filmwise condensation was the dominant heat transfer mode. This regime was characterized by heat transfer coefficients that did depend on temperature difference, but only modestly depended on quality and mass flux. This mode of heat transfer prevailed across the entire range of quality at low mass fluxes, and at low qualities as the mass flux was increased. At very high mass fluxes, the heat transfer mechanism was forced convective condensation across the entire range of quality. This mode of heat transfer was characterized by a strong dependence on both quality and mass flux, and negligible dependence on temperature difference. At intermediate mass fluxes, filmwise condensation prevailed at low quality and forced convective condensation prevailed at high quality. The transition from one regime to another could be detected by a change in slope of the heat transfer coefficient versus quality curve.

Various heat transfer correlations from the literature were compared to the experimental data. The correlations of Shah, Cavallini and Zecchin, and Traviss et al. were reasonable predictors of the annular flow data, although they all had deficiencies. The annular flow correlation of Chen et al. underpredicted nearly all of the experimental data. A major deficiency in the annular flow correlations was the lack of accurate guidelines for when they should be used. Of these correlations, only the Shah correlation had a published lower limit of applicability. At some mass fluxes where Shah's limiting criterion was met, though, heat transfer behavior more indicative of wavy flow than annular flow was observed across much of the quality range.

The wavy flow correlations of Chato and Jaster and Kosky had mean deviations of less than 15% with the data that were within their range of applicability, but had systematic deviations due to neglecting heat transfer in the bottom of the liquid pool. The correlation of Rosson and Myers attempted to account for this heat transfer, but was a substantially worse predictor of the experimental data than the simpler correlations.

The correlation of Traviss et al. was used to show the similarities between the more theoretical annular flow correlations and the simpler two-phase multiplier correlations. Based on this justification, a two-phase multiplier correlation was developed based on the present set of experimental data. The resulting correlation predicted the annular flow data from this study with a mean deviation of less than 5%. It also was an accurate predictor of several sets of data taken from the open literature.

A wavy flow correlation was developed based on the premise of filmwise condensation in the top of the tube and forced convective condensation in the bottom of the tube. The validity of filmwise condensation correlations derived with the assumption of no vapor velocity for conditions with a modest vapor velocity was explored by solving an analogous problem. This solution demonstrated that the gravity forces that govern the film thickness in the region of interest are unaltered by the addition of an interfacial shear stress from the vapor flow. The correlation that was developed predicted the present experimental data quite well, with a mean deviation of less than 7%.

The wavy and annular flow correlations were developed from data that were definitely either wavy or annular flow, omitting data in the wavy-annular flow regime.

Guidelines for how to best predict these data were developed by comparing the wavy and annular flow correlations to data deemed to be in the wavy-annular flow regime based on Soliman's Froude number. These comparisons revealed that for data at mass fluxes of less than 365 kBtu/ft^2-h, the wavy flow correlation remained accurate up to Froude numbers of 20 while annular flow correlations were accurate at higher Froude numbers. For data at mass fluxes of 365 kBtu/ft^2-h, the wavy flow correlation remained accurate up to Froude numbers of 20 while annular fl or greater, the annular flow correlation remained an accurate predictor of the experimental data over the entire quality range. These observations formed the guidelines for when each of the correlations should be used.

8.1.3 Design issues

The heat transfer correlations developed in the present study were combined with existing pressure drop correlations to develop a simple spreadsheet model of the two-phase portion of a condenser. This model was used to predict the required condensing length for a variety of situations. In all cases, the required length increased slowly with decreasing pressure drop over a wide range of diameters. At a sufficiently small diameter, the condensing length began to increase substantially with further decreases in diameter. This corresponded to situations where the pressure drop was destroying a substantial fraction of the driving temperature difference.

When presented in the form of condenser surface area versus diameter, an optimum diameter existed where the required surface area was a minimum. This optimal diameter was found to coincide with a fractional temperature drop of between 20% and 30% for a wide range of cases, leading to an analytical search for the criteria governing the optimum diameter. This analysis resulted in a closed form expression relating the fractional temperature drop at the optimal conditions to the thermal resistance ratio (refrigerant side to air side). For high air side resistances, the optimum value of fractional temperature drop was near 0.23. For very low air side resistances, the optimal value of fractional temperature drop increased to around 0.37. The predictions of this equation agreed very well with the results of the computer model for a factor of 100 variation in the air side resistance. This clearly demonstrated the importance of the fractional temperature drop as a design parameter for condensers, and how optimal values of this parameter depend on the air side heat transfer coefficients.

8.2 Recommendations

This study should provide a sound basis for future work regarding in-tube condensation, much of which will continue in the ACRC. Recommendations are provided here for some areas that should be investigated in the future.

Three areas of immediate interest that were not covered in the present study are surface enhancements, zeotropic mixtures, and the effects of lubricant on heat transfer. Surface enhancements such as micro-finned tubes are used in a variety of applications to increase the refrigerant side heat transfer coefficients. The heat transfer enhancement achieved by these tubes is partly due to an increase in the surface area, and partly due to induced mixing and turbulence. Work in this area should carefully delineate how much of the increased heat transfer is due to each of these effects, since in the annular flow regime the enhancement is likely due to area increases only. For conditions that should correspond to wavy flow in a smooth tube, the effect of temperature difference should be carefully studied to assess whether the heat transfer mechanism is primarily filmwise, forced convective, or a mixture of the two. Since this is the region where other investigators have found the most heat transfer enhancement, it warrants close study. If effects such as helix angle are to be studied, the rest of the geometric parameters should be held constant while the helix angle is varied. Correlations that are developed based on these data should be utilized in the condenser simulation model from the present study to assess the performance benefits of surface enhancements.

The complexity of the zeotropic heat transfer processes might make a complete solution to this problem very difficult. Fortunately, however, early studies in the ACRC seem to suggest that pure refrigerant correlations might remain valid in the annular flow regime. This finding should be verified with different refrigerants and under a wider range of conditions, though. In the wavy flow regime, where substantial heat transfer degradation is likely, the present study would suggest that significant parallels exist with external condensation. The external condensation literature should therefore be thoroughly reviewed before a significant modeling effort is begun. As a practical matter, though, designing heat exchangers for zeotropes such that they operate primarily in the annular flow regime might largely avoid the issue of heat transfer degradation.

Recent work in the ACRC that will be reported in the thesis of Gaibel [1994] has shed interesting light on the problem of heat transfer of refrigerant lubricant mixtures. Using a gas chromatograph technique developed by the Electric Power Research Institute Condensation Project, Gaibel was able to measure the oil concentration across the full range of quality and mass flux in his study. Significant variations in oil concentration were found with mass flux, casting doubt on many studies that have assumed that the flowing oil concentration remained constant with operating conditions. This study suggests that either on-line measurement of oil concentration, or at least frequent sampling, is necessary if the processes are to be fully understood. A second significant problem concerning heat transfer characteristics of refrigerant lubricant mixtures is the lack of thermal conductivity data for the lubricants. Such data are essential if correlations are to be developed that account for the effect of the oil in a physically meaningful way. A third problem with accurately determining heat transfer coefficients of refrigerant lubricant mixtures concerns the effect of the oil on the pressure temperature relationship. At very high qualities, the "apparent superheat" increases rapidly and in a highly nonlinear fashion. Short of measuring the local vapor temperature throughout the heat exchanger, which would be very difficult, getting meaningful data at high qualities seems doubtful. This problem should be carefully considered if high quality data are of interest.

The condenser simulation model developed in this study produced interesting findings. If sufficient interest exists within the ACRC, this model should be refined to include desuperheating and subcooled regions which are present in real condensers. Optimization results from the model would then be of increased interest to equipment manufacturers, since it would more closely parallel condensers in commercial systems.

One area of importance that was indirectly highlighted by the present work is enhancement of air side heat transfer. In many cases, the primary resistance to heat transfer remains on the air side. It seems natural to concentrate on the dominant thermal resistance in the network, since this offers more potential for improvement. Significant research in this area is currently under way in the ACRC, and should be pursued vigorously. The optimization results from Chapter 7 clearly indicated the importance of the air side heat transfer, since the optimal fractional temperature drop of the refrigerant was directly related to the air side heat transfer resistance.

REFERENCES

Abis, L.V., "Forced convection condensation inside horizontal tubes", Ph.D. Dissertation, Kansas State University, 1969.

Akers, W.W., H.A. Deans, and O.K. Crosser, "Condensing heat transfer within horizontal tubes", *Chemical Engineering Progress Symposium Series,* 29, 171-176, 1958.

Allied Signal, *Genetron AZ-20 Bulletin for 60/40 R-32/R-125,* Allied Signal Corporation, Buffalo, NY, 1993.

Allied Signal, *Genetron AZ-20 Bulletin for 50/50 R-32/R-125,* Allied Signal Corporation, Buffalo, NY, 1994.

Altman, M., F.W. Staub, and R.H. Norris, "Local heat transfer and pressure drop for refrigerant 22 condensing in horizontal tubes", *Chemical Engineering Progress Symposium Series*, 56(30), 151-159, 1960.

ASHRAE Fundamentals, American Society of Heating, Refrigerating, and Air Conditioning Engineers, 1989.

"ASHRAE guidelines: guide for engineering analysis of experimental data", *ANSI/ASHRAE Standard 41.5-75R*, 1986.

Azer, N.Z., L.V. Abis, and H.M. Soliman, "Local heat transfer coefficients during annular flow condensation", *ASHRAE Transactions,* 1(78), 135-143, 1972.

Azer, N.Z., and S.A. Said, "Heat transfer analysis of annular flow condensation inside circular and semi-circular horizontal tubes", *ASHRAE Transactions,* 92(1), 41-54, 1976.

Bae, S., J.S. Maulbetsch, and W.M. Rohsenow, "Refrigerant forced-convection condensation inside horizontal tubes", Report No. DSR 72591-71, Massachusetts Institute of Technology, Cambridge, 1970.

Baker, O., "Simultaneous flow of oil and gas", *Oil and Gas Journal,* 53, 185-195, 1954.

Barnea, D., O. Shoham, Y. Taitel, and A.E. Dukler, "Flow pattern transition for gas-liquid flow in horizontal and inclined pipes: Comparisons of experimental data with theory", *International Journal of Multiphase Flow*, 6, 217-225, 1980.

Barnea, D., Y. Luninski, and Y. Taitel, "Flow pattern in horizontal and vertical two phase flow in small diameter pipes", *The Canadian Journal of Chemical Engineering*, 61, 617-620, 1983.

Barnhart, J., "An experimental investigation of flow patterns and liquid entrainment in a horizontal-tube evaporator", Ph.D. Dissertation, University of Illinois, 1992.

Bivens, D., Personal Communication, April 1994.

Blasius, "Das Ahnlichkeitsgesetz bei Reibungsvorgangen in Flussikeiten", *Forsch. Arb. Ing.-Wes.*, 134, 1913.

Bonhomme, D.M., "Condensation of ozone-safe refrigerants in horizontal tubes: experimental test facility and preliminary results", M.S. Thesis, University of Illinois, 1991.

Brauer, H., "Stromung and warmeubergang bei reiselfilmen", *VDI Forschung*, 22, 1-40, 1956.

Bromley, L.A., "Effect of heat capacity on condensation", *Industrial and Engineering Chemistry*, 44, 2966-2969, 1952.

Butterworth, D., "A visual study of mechanisms in horizontal, air-water flow", AERE Report M2556, Harwell, England, 1972.

Carey, V.P., *Liquid-vapor phase change phenomena: An introduction to the thermophysics of vaporization and condensation processes in heat transfer equipment,* Hemisphere, New York, 1992.

Carpenter, E.F. and A.P. Colburn, "The effect of vapor velocity on condensation inside tubes", *Proceedings of General Discussion on Heat Transfer*, 20-26, 1951.

Cavallini, A., and R. Zecchin, "A dimensionless correlation for heat transfer in forced convective condensation", *Proceedings of the Fifth International Heat Transfer Conference,* Japan Society of Mechanical Engineers, 3, 309-313, 1974.

Chato, J.C., "Laminar condensation inside horizontal and inclined tubes", *ASHRAE Journal*, 4, 52-60, 1962.

Chen, M.M., "An analytical study of laminar film condensation. Part II: Single and multiple horizontal tubes", *Journal of Heat Transfer,* 83, 55-60, 1961.

Chen, S.L., F.M. Gerner, and C.L. Tien, "General film condensation correlations", *Experimental Heat Transfer,* 1, 93-107, 1987.

Chisholm, D., "The influence of mass velocity on friction pressure gradients during steam-water flow", *Proceedings of the Institute of Mechanical Engineers*, 182(3), 336-341, 1968.

Christoffersen, "Heat transfer and flow characteristics of R-22, R-32/R-125, and R-134a in smooth and micro-fin tubes", M.S. Thesis, University of Illinois, 1993.

Damianides, C.A., and J.W. Westwater, "Two-phase flow patterns in a compact heat exchanger and in small tubes", *Second UK Conference on Heat Transfer,* Institute of Mechanical Engineers, 2, 1257-1268, 1988.

Denglor, C.E., and J.N. Addoms, "Heat transfer mechanism for vaporization of water in a vertical tube", *Chemical Engineering Progress Symposium Series*, 52(18), 95-103, 1956.

Denny , V.E., and A.F. Mills, "Laminar film condensation of a flowing vapor on a horizontal cylinder at normal gravity", *Journal of Heat Transfer*, 91, 495-510, 1969.

Denny, V.E., and A.F. Mills, "Nonsimilar solutions for laminar film condensation on a vertical surface", *International Journal of Heat and Mass Transfer*, 12, 965-979, 1969.

Dhir, V., and J. Lienhard, "Laminar film condensation on plane and axisymmetric bodies in nonuniform gravity", *Journal of Heat Transfer*, 93, 97-100, 1971.

Dittus, F.W., and L.M.K. Boelter, University of California Publications on Engineering, 2, 443, 1930.

Dobson, M.K., J.C. Chato, D.K. Hinde, and S.P. Wang, "Experimental determination of internal condensation of refrigerants 134a and R-12 in horizontal tubes", *ASHRAE Transactions*, 1994.

Dobson, M.K., J.P. Wattelet, and J.C. Chato, "Optimal sizing of two-phase heat exchangers", ACRC Technical Report 42, 1993.

Dukler, A.E., "Fluid mechanics and heat transfer in vertical falling-film systems", *Chemical Engineering Progress Symposium Series,* 56(30), 1-10, 1960.

Dukler, A.E., and M.G. Hubbard, "A model for gas-liquid slug flow in horizontal and hear horizontal tubes", *Ind. Eng. Chem. Fundamentals*, 1975.

DuPont, *Thermodynamic Properties of HFC-134a (1,1,1,2-tetrafluoroethane)*, T-134a-ENG, Document H-47751-1, E.I. du Pont de Nemours and Co., Wilmington, DE, 1993.

DuPont, *Transport Properties of SUVA Refrigerants: SUVA COLD-MP (HFC-134a), SUVA TRANS A/C (HFC-134a), SUVA CENTRI-LP (HCFC-123),* ART-1, Document 43855-1, E.I. du Pont de Nemours and Co., Wilmington, DE, 1992.

Eckels, S.J., and M.B. Pate, "An experimental comparison of evaporation and condensation heat transfer coefficients for HFC-134a and CFC-12", *International Journal of Refrigeration,* 14(2), 70-77, 1990.

Gaddis, E.S., "Solution of the two-phase boundary-layer equations for laminar film condensation of vapour flowing perpendicular to a horizontal cylinder", *International Journal of Heat and Mass Transfer*, 22, 371-382, 1979.

Gaibel, J.."Condensation of a 50/50 blend of R-32/R-125 in horizontal tubes with and without oil", M.S. Thesis, University of Illinois, 1994.

Galbiati, L., and P. Andreini, "The transition between stratified and annular regimes for horizontal two-phase flow in small diameter tubes", *International Communications in Heat and Mass Transfer*, 19(2), 185-190, 1992.

Gnielinski, V., "New equations for heat and mass transfer in turbulent pipe and channel flow", *International Chemical Engineering*, 16, 359-368, 1976.

Grannryd, E., "Optimum circuit length and pressure drop on the refrigerant side of evaporators", *Proceedings of the ASHRAE-Purdue CFC Conference*, 73-82, 1992.

Hanratty, T.J., private communication, April 1994.

Hinde, D.K., M.K. Dobson, J.C. Chato, M.E. Mainland, and N. Rhines, "Condensation of R-134a with and without oils", ACRC Technical Report 26, 1992.

Hubbard, M.G., and A.E. Dukler, "The characterization of flow regimes for horizontal two-phase flow: statistical analysis of wall pressure fluctuations", *Proceedings of the 1966 Heat Transfer and Fluid Mechanics Institute*, 100-121, 1966.

Hu, X., and A.M. Jacobi, "Vapor shear and pressure gradient effects during filmwise condensation from a flowing vapor onto a sphere", *Experimental Thermal and Fluid Science,* 5, 548-555, 1992.

Incropera, F. P., and D.P. DeWitt, *Fundamentals of Heat and Mass Transfer,* 3rd edition, Wiley, New York, 1990.

Jacobi, A.M., "Filmwise condensation from a flowing vapor onto isothermal, axisymmetric bodies", *Journal of Thermophysics and Heat Transfer*, 6(2), 321-325, 1992.

Jacobi, A.M., "High efficiency boilers: condensation and transient behavior", Ph.D. Dissertation, Purdue University, 1989.

Jeffreys, H., "On the formation of water waves by wind", *Proceedings of the Royal Society*, A107, 189, 1925.

Jeffreys, H., "On the formation of water waves by wind", *Proceedings of the Royal Society*, A110, 241, 1926.

Jaster, H., and P.G. Kosky, "Condensation in a mixed flow regime", *International Journal of Heat and Mass Transfer*, 19, 95-99, 1976.

Kakac, S., R.K. Shah, and W. Aung, *Handbook of single-phase convective heat transfer*, Wiley-Interscience, New York, 1987.

Kapitsa, P.L., "Wave flow of thin layers of a viscous fluid", *Zh. Eksp. Teoret. Fiz.*, 18(1), 1948.

Kenney, J.P., " ", M.S. Thesis, University of Illinois, 1994.

Koh, J.C.Y., E.M. Sparrow, and J.P. Hartnett, "The two-phase boundary layer in laminar film condensation", *International Journal of Heat and Mass Transfer*, 2, 69-82, 1961.

Kosty, P.G., and F.W. Staub, "Local heat transfer coefficients in the annular flow regime", *A.I.Ch.E. Journal*, 17, 1037, 1971.

Lin, P.Y. and T.J. Hanratty, "Detection of slug flow from pressure measurements", *International Journal of Multiphase Flow*, 15(2), 209-226, 1989.

Lockhart, R.W. and R.C. Martinelli, "Proposed correlation of data for isothermal, two-phase, two-component flow in pipes", *Chemical Engineering Progress*, 45(1), 39-48, 1947.

Mandhane, J.M., G.A. Gregory, and K. Aziz, "A flow pattern map for gas-liquid flow in horizontal and inclined pipes", *International Journal of Multiphase Flow*, 1, 537-553, 1974.

Martinelli, R.C., and B. Nelson, "Prediction of pressure drop during forced-circulation boiling of water", *ASME Transactions*, 70, 695-702, 1948.

Moffat, R.J., "Describing the uncertainties in experimental results", *Experimental Thermal and Fluid Science*, 1, 3-17, 1988.

Morrison, G., M. McLinden, and J. Ely, "NIST thermodynamic properties of refrigerants and refrigerant mixtures database, (REFPROP)", National Institute of Standards and Technology, 1991.

Nicholson, M.K., K. Aziz, and G.A. Gregory, "Intermittent two phase flow: predictive models", *27th Canadian Chemical Engineering Conference*, Calgary, Alberta, 1978.

Nusselt, W., "Die oberflachenkondensation des wasserdampfes", *Z. Vereins deutscher Ininuere,* 60, 541-575, 1916.

Rahman, M.M., A.M. Fathi, and H.M. Soliman, "Flow pattern boundaries during condensation: new experimental data, *Canadian Journal of Chemical Engineering,* 63, 547-552, 1985.

Rohsenow, W.M., "Heat transfer and temperature distribution in laminar film condensation", *Transactions ASME*, 78, 1645-1648, 1956.

Rosson, H.F., and J.A. Meyers, "Point values of condensing film coefficients inside a horizontal tube", *Chemical Engineering Progress Symposium Series,* 61(59), 190-199, 1965.

Rowland, F.S., and M.R. Molina, "Stratospheric sink for chloroflouromethanes: Chlorine atom catalyzed destruction of ozone", *Nature*, 249, 810-812, 1974.

Rufer, C.E., and S.P. Kezios, "Analysis of stratified flow with condensation", *Journal of Heat Transfer*, 88, 265-275, 1966.

Said, S.A., "Augmentation of condensation heat transfer of R-113 by internally finned tubes and twisted tape inserts", Ph.D. Dissertation, Kansas State University, 1982.

Sadasivan, P., and J.H. Lienhard, "Sensible heat correction in laminar film boiling and condensation", *Journal of Heat Transfer*, 109, 545-546, 1987.

Shah, M.M., "A general correlation for heat transfer during film condensation inside pipes", *International Journal of Heat and Mass Transfer*, 22, 547-556, 1979.

Shah, M.M., "Heat transfer during film condensation in tubes and annuli: A review of the literature", *ASHRAE Transactions,* 87(3) , 1086-1100, 1981.

Shawki, T.G., *Lectures on Mathematical Methods for Engineers and Physicists II,* Department of Theoretical and Applied Mechanics, Urbana, 1988.

Shekriladze, and Gomelauri, "Theoretical study of laminar film condensation of flowing vapour", *International Journal of Heat and Mass Transfer,* 9, 581-591, 1966.

Soliman, M., J.R. Schuster, and P.J. Berenson, "A general heat transfer correlation for annular flow condensation", *Journal of Heat Transfer*, 90, 267-276, 1968.

Soliman, H.M., "On the annular-to-wavy flow pattern transition during condensation inside horizontal tubes", *The Canadian Journal of Chemical Engineering*, 60, 475-481, 1982.

Soliman, H.M., "Correlation of mist-to-annular transition during condensation", *The Canadian Journal of Chemical Engineering*, 61, 178-182, 1983.

Soliman, H.M., "The mist-annular transition during condensation and its influence on the heat transfer mechanism", *International Journal of Multiphase Flow,* 12(2), 277-288, 1986.

Souza, A.M., J.C. Chato, and J.P. Wattelet, "Pressure drop during two-phase flow of refrigerants in horizontal smooth tubes", ACRC Technical Report 25, 1992.

Sparrow, E.M., and J.L. Gregg, "A boundary-layer treatment of laminar film condensation", *Journal of Heat Transfer*, 81, 13-23, 1959.

Taitel, Y., and A.E. Dukler, "A model for predicting flow regime transitions in horizontal and hear horizontal gas-liquid flow", *American Institute of Chemical Engineering Journal,* 22(1), 47-55, 1976.

Tien, C.L., S.L. Chen, and P.F. Peterson, 1988, "Condensation inside tubes", *EPRI Project 1160-3 Final Report.*

Traviss, D.P., A.B. Baron, and W.M. Rohsenow, "Forced-convection condensation inside tubes", Report No. DSR 72591-74, Massachussetts Institure of Technology, Cambridge, 1971.

Traviss, D.P., W.M. Rohsenow, and A.B. Baron,"Forced convective condensation in tubes: A heat transfer correlation for condenser design", *ASHRAE Transactions*, 79(1), 157-165, 1973.

Wattelet, J.P., "Heat transfer flow regimes of refrigerants in a horizontal-tube evaporator", Ph.D. Dissertation, University of Illinois, 1994.

Zivi, S.M., "Estimation of steady-state steam void-fraction by means of the principle of minimum entropy production, *Journal of Heat Transfer*, 86, 247-252, 1964.

APPENDIX A

THERMOPHYSICAL PROPERTIES

The preferred source of thermophysical properties, when possible, was the refrigerant manufacturer. For R-134a, both the thermodynamic and transport properties were obtained from technical bulletins published by DuPont. Dr. Don Bivens [1994] at DuPont suggested that these bulletins contained the most accurate properties available for R-134a. For R-22, the properties published in the ASHRAE Fundamentals [1989] were used per Dr. Bivens' suggestion. For both of the R-32/R-125 mixtures, thermodynamic properties were taken from bulletins published by Allied Signal [1993, 1994]. No measured transport property data were available for either of these mixtures, so transport properties were taken from the REFPROPS program [Morrison et al., 1991].

For each of the refrigerants, curve fits of the thermophysical property data were used to develop spreadsheet macros.. These spreadsheet macros were used to generate property tables that are included in Table A.1 through Table A.4. The units in each of the tables are as follows:

Temperature	°C
Pressure	kPa
Enthalpy	kJ/kg
Density	kg/m^3
Thermal Conductivity	W/m-K
Viscosity	μPa-s
Surface Tension	mN/m.

Table A.1 Thermophysical properties for R-134a

T	P	Pred	rhol	rhov	hl	hlv	hv	kl	cpl	mul	σ
10	416.2	0.083	1259.0	21.11	65.15	191.06	256.21	0.0902	1.382	234.9	10.05
12	444.3	0.089	1251.9	22.62	67.82	189.42	257.24	0.0892	1.393	229.2	9.79
14	473.8	0.095	1244.8	24.12	70.52	187.73	258.26	0.0881	1.404	223.7	9.52
16	504.8	0.101	1237.7	25.64	73.25	186.02	259.27	0.0871	1.415	218.4	9.26
18	537.4	0.108	1230.6	27.17	76.00	184.28	260.28	0.0861	1.426	213.4	9.00
20	571.6	0.115	1223.5	28.74	78.78	182.50	261.29	0.0850	1.437	208.7	8.73
22	607.5	0.122	1216.3	30.35	81.59	180.70	262.29	0.0840	1.448	204.1	8.48
24	645.1	0.129	1209.0	32.02	84.42	178.87	263.29	0.0830	1.459	199.7	8.22
26	684.5	0.137	1201.7	33.77	87.28	177.01	264.29	0.0819	1.470	195.5	7.96
28	725.7	0.146	1194.3	35.60	90.17	175.12	265.29	0.0809	1.481	191.5	7.71
30	768.8	0.154	1186.8	37.53	93.08	173.20	266.28	0.0799	1.492	187.6	7.45
32	813.8	0.163	1179.1	39.57	96.02	171.25	267.27	0.0788	1.503	184.0	7.20
34	860.9	0.173	1171.3	41.74	98.98	169.27	268.25	0.0778	1.514	180.4	6.95
36	910.0	0.183	1163.4	44.04	101.97	167.26	269.23	0.0768	1.525	177.0	6.70
38	961.2	0.193	1155.4	46.50	104.99	165.21	270.20	0.0757	1.536	173.7	6.45
40	1014.6	0.203	1147.1	49.12	108.03	163.12	271.15	0.0747	1.547	170.6	6.21
42	1070.2	0.215	1138.7	51.91	111.10	160.99	272.09	0.0737	1.558	167.5	5.96
44	1128.1	0.226	1130.1	54.90	114.20	158.81	273.01	0.0726	1.569	164.5	5.72
46	1188.4	0.238	1121.3	58.09	117.32	156.59	273.91	0.0716	1.580	161.6	5.48
48	1251.0	0.251	1112.2	61.49	120.47	154.32	274.78	0.0706	1.591	158.8	5.24
50	1316.2	0.264	1102.9	65.13	123.64	151.98	275.63	0.0695	1.602	156.1	5.00
52	1383.8	0.278	1093.4	69.00	126.84	149.59	276.43	0.0685	1.613	153.4	4.77
54	1454.1	0.292	1083.6	73.13	130.07	147.13	277.20	0.0675	1.624	150.7	4.53
56	1527.0	0.306	1073.6	77.53	133.32	144.60	277.92	0.0664	1.636	148.1	4.30
58	1602.5	0.321	1063.2	82.21	136.60	141.99	278.60	0.0654	1.647	145.5	4.07
60	1680.9	0.337	1052.6	87.18	139.91	139.30	279.21	0.0644	1.658	142.9	3.85

Table A.2 Thermophysical properties for R-22

T	P	Pred	rhol	rhov	hl	hlv	hv	kl	cpl	mul	σ
10	680.4	0.136	1258.8	29.58	211.59	196.50	408.09	0.0954	1.199	219.3	10.22
12	722.1	0.145	1251.6	31.00	213.80	194.74	408.54	0.0945	1.205	216.4	9.93
14	765.9	0.154	1244.3	32.46	216.04	192.94	408.98	0.0936	1.212	213.7	9.64
16	811.6	0.163	1236.9	34.00	218.32	191.10	409.42	0.0927	1.218	211.1	9.35
18	859.3	0.172	1229.3	35.67	220.64	189.22	409.87	0.0918	1.225	208.6	9.07
20	909.2	0.182	1221.4	37.49	223.00	187.31	410.31	0.0909	1.232	206.2	8.78
22	961.2	0.193	1213.3	39.51	225.39	185.36	410.75	0.0899	1.240	203.8	8.50
24	1015.4	0.204	1204.8	41.73	227.83	183.37	411.20	0.0889	1.247	201.6	8.22
26	1071.9	0.215	1195.8	44.16	230.30	181.35	411.65	0.0880	1.255	199.4	7.94
28	1130.7	0.227	1186.4	46.81	232.81	179.30	412.11	0.0870	1.264	197.2	7.66
30	1192.0	0.239	1176.3	49.67	235.36	177.21	412.57	0.0860	1.273	195.1	7.38
32	1255.6	0.252	1165.6	52.73	237.95	175.08	413.03	0.0850	1.283	193.0	7.11
34	1321.8	0.265	1154.1	56.00	240.57	172.92	413.49	0.0839	1.293	190.9	6.84
36	1390.5	0.279	1141.8	59.45	243.24	170.71	413.95	0.0829	1.303	188.9	6.57
38	1461.9	0.293	1128.5	63.08	245.94	168.46	414.40	0.0819	1.315	186.8	6.30
40	1535.9	0.308	1114.2	66.87	248.68	166.16	414.84	0.0808	1.327	184.7	6.04
42	1612.7	0.323	1098.7	70.82	251.46	163.82	415.27	0.0797	1.339	182.6	5.77
44	1692.2	0.339	1081.8	74.91	254.27	161.41	415.69	0.0786	1.353	180.5	5.51
46	1774.6	0.356	1063.6	79.15	257.13	158.95	416.08	0.0775	1.367	178.3	5.25
48	1860.0	0.373	1043.9	83.52	260.02	156.42	416.44	0.0764	1.382	176.1	5.00
50	1948.2	0.391	1022.5	88.05	262.96	153.82	416.78	0.0753	1.398	173.8	4.74
52	2039.6	0.409	999.3	92.73	265.93	151.14	417.07	0.0742	1.414	171.5	4.49
54	2134.0	0.428	974.2	97.59	268.94	148.38	417.31	0.0730	1.432	169.0	4.24
56	2231.5	0.448	947.0	102.66	271.98	145.52	417.50	0.0719	1.451	166.5	4.00
58	2332.3	0.468	917.6	107.98	275.07	142.56	417.63	0.0707	1.470	163.9	3.75
60	2436.3	0.489	885.8	113.59	278.19	139.50	417.69	0.0695	1.491	161.1	3.51

Table A.3 Thermophysical properties for 50/50 R-32/R-125

T	P	Pred	rhol	rhov	hl	hlv	hv	kl	cpl	mul	σ
10	1081.2	0.217	1129.1	40.98	83.49	211.16	294.65	0.1035	1.294	188.3	10.22
12	1146.6	0.230	1120.6	43.73	86.84	208.36	295.21	0.1019	1.298	183.4	9.93
14	1214.9	0.244	1112.1	46.65	90.21	205.52	295.73	0.1003	1.302	178.6	9.64
16	1286.4	0.258	1103.6	49.71	93.59	202.64	296.23	0.0987	1.306	173.8	9.35
18	1360.9	0.273	1095.0	52.90	96.97	199.73	296.70	0.0971	1.310	169.2	9.07
20	1438.7	0.289	1086.3	56.22	100.35	196.80	297.15	0.0955	1.314	164.6	8.78
22	1519.9	0.305	1077.4	59.67	103.73	193.84	297.57	0.0938	1.319	160.2	8.50
24	1604.4	0.322	1068.4	63.24	107.11	190.86	297.97	0.0921	1.324	155.9	8.22
26	1692.5	0.339	1059.1	66.95	110.50	187.84	298.34	0.0904	1.329	151.8	7.94
28	1784.2	0.358	1049.5	70.81	113.89	184.79	298.68	0.0887	1.335	147.8	7.66
30	1879.6	0.377	1039.6	74.83	117.29	181.70	298.99	0.0870	1.341	144.0	7.38
32	1978.7	0.397	1029.3	79.05	120.71	178.55	299.26	0.0853	1.347	140.3	7.11
34	2081.7	0.418	1018.5	83.49	124.17	175.33	299.50	0.0836	1.354	136.8	6.84
36	2188.7	0.439	1007.3	88.19	127.66	172.02	299.69	0.0818	1.361	133.4	6.57
38	2299.8	0.461	995.6	93.19	131.22	168.61	299.83	0.0800	1.368	130.2	6.30
40	2414.9	0.484	983.4	98.53	134.84	165.08	299.92	0.0783	1.377	127.2	6.04
42	2534.4	0.508	970.5	104.26	138.55	161.40	299.95	0.0765	1.385	124.3	5.77
44	2658.1	0.533	957.0	110.44	142.37	157.54	299.91	0.0746	1.395	121.5	5.51
46	2786.3	0.559	942.8	117.13	146.32	153.48	299.80	0.0728	1.405	118.8	5.25
48	2919.1	0.585	927.9	124.39	150.41	149.19	299.60	0.0710	1.417	116.3	5.00
50	3056.4	0.613	912.2	132.31	154.68	144.63	299.31	0.0691	1.429	113.8	4.74
52	3198.4	0.641	895.7	140.94	159.14	139.77	298.92	0.0672	1.442	111.4	4.49
54	3345.2	0.671	878.3	150.39	163.84	134.58	298.41	0.0653	1.456	109.1	4.24
56	3497.0	0.701	860.0	160.72	168.78	129.00	297.79	0.0634	1.471	106.8	4.00
58	3653.7	0.733	840.8	172.04	174.02	123.01	297.03	0.0615	1.488	104.4	3.75
60	3815.4	0.765	820.5	184.44	179.57	116.55	296.12	0.0596	1.506	102.1	3.51

Table A.4 Thermophysical properties for 60/40 R-32/R-125

T	P	Pred	rhol	rhov	hl	hlv	hv	kl	cpl	mul	σ
10	1117.4	0.224	1126.5	39.18	70.45	225.06	295.51	0.1113	1.316	188.4	10.22
12	1183.9	0.237	1118.9	40.99	73.58	222.49	296.07	0.1095	1.318	183.4	9.93
14	1253.3	0.251	1110.9	43.01	76.77	219.88	296.65	0.1076	1.320	178.6	9.64
16	1325.7	0.266	1102.6	45.27	80.01	217.23	297.24	0.1058	1.322	173.8	9.35
18	1401.2	0.281	1094.1	47.74	83.32	214.52	297.83	0.1039	1.325	169.1	9.07
20	1479.9	0.297	1085.2	50.44	86.68	211.74	298.42	0.1021	1.328	164.5	8.78
22	1561.8	0.313	1076.1	53.37	90.09	208.89	298.98	0.1002	1.332	160.1	8.50
24	1647.1	0.330	1066.6	56.52	93.57	205.95	299.52	0.0984	1.337	155.7	8.22
26	1735.8	0.348	1056.8	59.89	97.10	202.92	300.02	0.0966	1.342	151.4	7.94
28	1828.1	0.367	1046.8	63.49	100.69	199.78	300.47	0.0947	1.347	147.3	7.66
30	1923.9	0.386	1036.4	67.31	104.34	196.52	300.86	0.0929	1.353	143.2	7.38
32	2023.4	0.406	1025.8	71.35	108.05	193.14	301.19	0.0910	1.359	139.3	7.11
34	2126.6	0.427	1014.8	75.62	111.81	189.62	301.43	0.0892	1.366	135.4	6.84
36	2233.6	0.448	1003.6	80.11	115.63	185.96	301.59	0.0873	1.374	131.7	6.57
38	2344.6	0.470	992.0	84.83	119.50	182.14	301.65	0.0855	1.381	128.1	6.30
40	2459.5	0.493	980.2	89.77	123.44	178.16	301.59	0.0836	1.390	124.5	6.04
42	2578.6	0.517	968.0	94.93	127.43	174.00	301.43	0.0818	1.398	121.1	5.77
44	2701.7	0.542	955.6	100.32	131.48	169.65	301.13	0.0799	1.408	117.8	5.51
46	2829.1	0.567	942.8	105.93	135.58	165.11	300.69	0.0781	1.418	114.6	5.25
48	2960.8	0.594	929.8	111.77	139.75	160.36	300.11	0.0762	1.428	111.5	5.00
50	3096.9	0.621	916.5	117.83	143.97	155.40	299.37	0.0744	1.439	108.4	4.74
52	3237.4	0.649	902.8	124.11	148.25	150.21	298.45	0.0726	1.450	105.5	4.49
54	3382.5	0.678	888.9	130.62	152.58	144.78	297.36	0.0707	1.462	102.7	4.24
56	3532.3	0.708	874.6	137.35	156.97	139.11	296.09	0.0689	1.474	100.0	4.00
58	3686.7	0.739	860.1	144.31	161.42	133.18	294.61	0.0670	1.486	97.5	3.75
60	3845.9	0.771	845.3	151.49	165.93	126.99	292.92	0.0652	1.500	95.0	3.51

APPENDIX B

AXIAL CONDUCTION ANALYSIS

The equations governing the wall temperature profile before and within a condensing heat exchanger are derived and solved in this appendix. The analysis was originally performed to decide an appropriate distance inside the test-section for installing the first set of wall thermocouples. The analysis has since been used for three primary purposes: (1) quantifying the length of the transition region in the wall temperature at the ends of the test-section, (2) predicting the error in the average wall temperature committed by ignoring measurements in the transition region, and (3) quantifying the magnitude of axial conduction through the ends of the test-section in relation to the convection from the inner fluid.

B.1 Physical Model

A schematic of the physical situation modeled, as well as a diagram of the expected temperature profile, is shown in Fig. B.1. Far away from the inlet and outlet of the test-section, adiabatic conditions prevail and the wall temperature is equal to that of the inner fluid. Inside the test-section, the wall temperature assumes a value between the inner and outer fluid temperatures as dictated by the ratio of the inner and outer thermal resistances. Near the test-section inlet and outlet, the temperature begins a transition from the inner fluid temperature towards its value inside the test-section.

For the most general case, the temperature of both the inner and outer fluids change inside the test-section due to heat transfer. For a condensing inner fluid, the temperature changes are only due to pressure drop and are normally negligible. To end up with a problem that was analytically tractable, it was assumed that the temperature of the outer fluid also remained constant. This would be true for phase-change processes on both sides, or for a very high outer fluid flow rate. Although it would not accurately model the true wall temperature profile for the present system where some temperature increase of the outer fluid was necessary, it would likely give accurate estimates of the three primary effects of interest herein. The assumptions used in the present analysis are enumerated below:

1. Constant heat transfer coefficients for the inner and outer fluid
2. No temperature change of the inner or outer fluid
3. Negligible temperature gradients across the copper in the radial direction

4. Negligible heat loss through the insulation

5. Negligible axial conduction inside the refrigerant

Subject to these assumptions, first law statements for the tube wall before and within the test-section are given by Eq. (B.1) and Eq. (B.2), respectively:

$$\frac{d^2T_1}{dz^2} - \frac{h_i S_i}{k_t A_t}(T_1 - T_i) = 0 \tag{B.1}$$

$$\frac{d^2T_2}{dz^2} - \frac{h_i S_i + h_o S_o}{k_t A_t}(T_2 - T_o) = -\frac{h_i S_i}{k_t A_t}(T_i - T_o) \tag{B.2}$$

In the equations above, different variables (T_1 and T_2) are used for the the regions outside and inside the test-section, respectively. This is necessary since different conservation equations describe the behavior in these regions. The four boundary conditions that are necessary for the solution of these ordinary differential equations are:

$$\begin{aligned} &T_1(z=-\infty) = T_i \\ &T_1(z=0) = T_2(z=0) \\ &\frac{dT_1}{dz}(z=0) = \frac{dT_2}{dz}(z=0) \\ &\frac{dT_2}{dz}(z=L) = 0 \end{aligned} \tag{B.3 a-d}$$

These boundary conditions represent, respectively: (a) adiabatic conditions far before the test-section, (b) matching temperatures at the inlet of the test-section, (c) matching heat flux at the inlet of the test-section, and (d) a symmetric temperature profile at the center of the test-section that is a result of isothermal inner and outer fluids.

B.2 Solution of Governing Equations

The solution is both more useful and somewhat simpler if the set of equations listed above is nondimensionalized. The dimensionless variables chosen for this purpose are:

$$\begin{aligned} z^* &= \frac{z}{L} \\ \theta_1 &= \frac{T_1 - T_i}{T_o - T_i} \\ \theta_2 &= \frac{T_2 - T_i}{T_o - T_i} \end{aligned} \tag{B.4 a-c}$$

In nondimensional form, the governing differential equations are given by Eq. (B.5a) and Eq. (B.5b), while the boundary conditions are given by Eq. (B.6a) through Eq. (B.6d):

$$\theta_1'' - \xi_i^2\theta_1 = 0$$
$$\theta_2'' - \frac{\xi_i^2}{\Gamma^2}\theta_2 = -\frac{\xi_i^2}{\Gamma^2}\left(1-\Gamma^2\right) \qquad \text{(B.5 a-b)}$$

$$\theta_1(z^* = -\infty) = 0$$
$$\theta_1(z^* = 0) = \theta_2(z^* = 0)$$
$$\theta_1'(z^* = 0) = \theta_2'(z^* = 0) \qquad \text{(B.6 a-d)}$$
$$\theta_2'(z^* = 1) = 0$$

The two nondimensional parameters introduced in Eq. (B.5) are defined below:

$$\xi_i^2 = Bi_i\frac{A_s}{A_t} = \frac{h_iL}{k_t}\frac{L/t}{\left(1+t/D_i\right)} \qquad \text{(B.7)}$$

$$\Gamma^2 = \frac{R_o'}{R_t'} = \frac{1}{\frac{h_o}{h_i}\left(1+\frac{2t}{D_i}\right)+1} \qquad \text{(B.8)}$$

Significant physical insight can be inferred from these dimensionless variables before the mathematical problem is solved. The first parameter is the product of a Biot number, Bi_i, and an area ratio. The Biot number represents the effectiveness of convection from the inner fluid relative to axial conduction, with high values corresponding to a dominance of convection over conduction. This quantity is multiplied by the ratio of the convective area to the conductive area. This implies that high values of the parameter ξ_i^2 correspond to situations where axial conduction is dominated by convection from the inner fluid. The other dimensionless parameter is the square of the ratio of the outer thermal resistance to the total thermal resistance. This parameter governs the value of dimensionless temperature inside the test-section at values of z^* beyond the transition region. Low values of Γ^2 correspond to high values of θ_2 (near unity) and high values of Γ^2 corresponding to low values of θ_2 (near 0).

The solution to Eq. (B.5) was accomplished first by hand, then verified using *Mathematica*. The equations for the dimensionless temperature profile before and within the test-section are:

$$\theta_1 = \frac{\left(1-\Gamma^2\right)\left(1-e^{(2\xi_i/\Gamma)}\right)}{1-\Gamma-e^{(2\xi_i/\Gamma)}(\Gamma+1)}e^{\xi_i z^*} \qquad \text{(B.9)}$$

$$\theta_2 = \left(1-\Gamma^2\right)\left[1+\frac{\Gamma\left(e^{\xi_i/\Gamma(2-z^*)}+e^{\xi_i z^*/\Gamma}\right)}{1-\Gamma-e^{(2\xi_i/\Gamma)}(\Gamma+1)}\right] \tag{B.10}$$

A plot of the dimensionless temperature profile for cases with ζ_i=1,10, and 100 is shown in Fig. B.2. The value of Γ^2 was maintained at 0.5 for all three cases, so that in the absence of a transition region they would all approach θ_2=0.5 inside the test-section. In this plot, negative values of z^* correspond to the region before the test-section, while positive values of z^* correspond to the region inside the test-section. Since the length-scale was selected as the half-length of the test-section, a value of z^*=1 corresponds to the middle of the test-section. For the case where ζ_i=1, the transition region was so extensive that the dimensionless temperature never reached the fully developed value of 0.5. The other two cases did properly reach θ_2=0.5 inside the test-section, with faster developing temperature profiles for higher values of ζ_i.

B.2.1 Length of transition region

The first question addressed with the solution was how far into the test-section the first set of thermocouples should be installed. The concern was that if thermocouples were placed inside the transition region, the abnormally high readings therein would cause an upwards bias in the average wall temperature. This problem was addressed by solving for the dimensionless length at which the temperature profile inside the test-section reached 99% of its fully-developed value of 1-Γ^2. This value is referred to hereafter as z^*_{crit}, since at values greater than this the temperature field is essentially unaffected by the transition region. The value of z^*_{crit} was solved for using the FindRoot procedure in *Mathematica* for a wide range of ζ_i and Γ. The results are plotted in Figure B.3. At a fixed value of Γ, increasing ζ_i decreases the length of the transition range and results in a lower value of z^*_{crit}. At a fixed value of ζ_i, decreasing the value of Γ decreases the length of the transition region and therefore decreases z^*_{crit}. Physically, decreasing Γ at a fixed value of ζ_i corresponds to increasing the outer heat transfer coefficient. This decreases the total resistance to convective transport and shortens the transition region. Included on Fig. B.3 is a line at z^*=0.33. This corresponds to the minimum value of dimensionless length at which a thermocouple station was located on any of the test-sections. For the range of Γ plotted, Fig. B.3 indicates that less than 1% error in that thermocouple reading would be realized for any value of ζ_i greater than or equal to 10. This corresponds to an inner heat transfer coefficient of about 285 W/m^2-K, a reasonable value for single-phase testing at moderate mass fluxes. Thus, the surface thermocouples from the study should have been unaffected for any two-phase testing, where the heat transfer coefficients were a factor of 7 or 8 higher than this.

B.2.2 Error in measured temperature profile

The calculations presented above indicate that all locations where the wall temperature was measured were effectively beyond the transition region. For condensing heat transfer, this implies that no over-prediction of the wall temperature resulted due to one measurement station being inside the transition region. The true average wall temperature, however, includes both the short transition region and the longer region beyond this. By intentionally ignoring the transition region in the measured temperature field, a systematic (though small) error was committed which resulted in measured temperature differences (inner fluid - wall) that were too high. This error can be readily quantified with the solution presented above.

The way that the wall temperatures were measured and used to compute the average temperature difference was equivalent to ignoring the transition region, or assuming that $\theta=1-\Gamma^2$ throughout the test-section. The true average value can be determined by integrating θ from $z^*=0$ to 1. Forming the ratio of these two quantities results in:

$$\frac{\Delta T_{meas}}{\Delta T_{true}}=\frac{\int_0^1\left(1-\Gamma^2\right)dz^*}{\int_0^1 \theta_2 dz^*} \qquad \text{(B.11)}$$

This quantity was also solved for symbolically using *Mathematica*. The solution is given by:

$$\frac{\Delta T_{meas}}{\Delta T_{true}}=\frac{\xi_i\left[-1+\Gamma+e^{\left(2\xi_i/\Gamma\right)}(\Gamma+1)\right]}{\Gamma^2\left(1-e^{\left(2\xi_i/\Gamma\right)}\right)+\xi_i(\Gamma+1)\left(1+e^{\left(2\xi_i/\Gamma\right)}\right)} \qquad \text{(B.12)}$$

This quantity is plotted in Fig. B.4a for the same range of ζ_i and Γ included in the previous plots. This figure shows that at very low values of ζ_i and high values of Γ, this error can approach 40%. Figure B.4b presents the same data for the restricted range of ζ_i greater than 10, the range of operating parameters used in the present study. For this restricted range of conditions, the overprediction is always less than 5%. The error decreases as ζ_i increases and Γ decreases, since both of these changes shorten the transition region.

B.2.3 Effect of axial conduction

The final issue addressed with this analysis regards the role of axial conduction. For the condensation case, axial conduction acts as an additional source of energy entering the test-section. Thus, the outer fluid which is used to measure the heat transfer rate receives energy not only by convection from the inner fluid, but also by the unwanted axial conduction. This results in a measured heat transfer rate that is higher than that due to convection from the inner fluid, which falsely inflates the measured heat transfer coefficients. Again, this effect can be quantified using the analysis presented above. The ratio of the axial heat conduction to the convection from the inner fluid can be formed in primitive variables as follows:

$$\frac{\dot{Q}_{cond}}{\dot{Q}_{conv,i}} = \frac{-k_t A_t \, {}^{dT}\!/_{dz}(z=0)}{-h_i S_i \int_{z=0}^{z=1} (T - T_i) dz} \tag{B.13}$$

In dimensionless variables, Eq. (B.13) becomes:

$$\frac{\dot{Q}_{cond}}{\dot{Q}_{conv,i}} = \frac{\theta_2'(z^* = 0)}{\xi_i^2 \int_{z^*=0}^{z^*=1} \theta_2 dz^*} \tag{B.14}$$

This expression was also solved symbolically using *Mathematica*, leading to:

$$\frac{\dot{Q}_{cond}}{\dot{Q}_{conv,i}} = \frac{e^{2\xi_i/\Gamma} - 1}{\Gamma^2\left(1 - e^{\left(2\xi_i/\Gamma\right)}\right) + \xi_i(\Gamma + 1)\left(1 + e^{\left(2\xi_i/\Gamma\right)}\right)} \tag{B.15}$$

The ratio from Eq. (B.15) is plotted versus ζ_i and Γ in Fig. B.5a and Fig. B.5b. Figure B.5a presents data for ζ_i from 1 to 100, and shows that at very low ζ_i the conduction and convection are of comparable magnitudes. Figure B.5b restricts the range of ζ_i from 10 to 100, the working range from the study. The axial conduction poses much less of a problem in this range, with its magnitude reaching a maximum of 9% of that due to convection from the inner fluid. The trends of this error are different than those of the temperature measurement errors. Increasing ζ_i at constant Γ decreases the error, as for the other cases, since this results in both more effective convection and more area over which it occurs. The magnitude of the axial conduction error increases with decreasing Γ, though, unlike the temperature measurement error which decreases as Γ decreases. This is because decreasing Γ moves the wall temperature closer to the temperature of the outer fluid, resulting in steeper gradients at the ends of the test-section.

The two errors quantified above can be combined to solve for the ratio of the measured heat transfer coefficient to the true heat transfer coefficient. This ratio is plotted in Fig. B.6a for ζ_i=1 to 100 and in Fig. B.6b for ζ_i=10 to 100. The trends indicate the axial conduction error is more significant than the temperature measurement error, resulting in a net overprediction. This can be significant at low ζ_i. For the range of ζ_i used in the present study, though, it was always less than 7% for single-phase testing and always less than 3.5% for two-phase testing.

B.3 Summary

In summary, the conduction problem describing the variation of the wall temperature before and within the test-section was solved in dimensionless form. Two dimensionless parameters were found to govern the temperature profile. The most important parameter, ζ_i, was the product of a Biot number based on the inner fluid heat transfer coefficient and the ratio of the inner surface area to the tube cross-sectional area. High values of this parameter resulted in a short transition region and low values of axial conduction relative to inner fluid convection. Quantitatively, values of this parameter greater than 10 resulted in the first thermocouple station being outside the transition region. The combined effects of neglecting the temperature variation in the transition region and undesired axial conduction resulted in a calculated heat transfer coefficient that was greater than the true value, but this error was confined to magnitudes of less than 7% for ζ_i greater than 10. The second dimensionless parameter, Γ, was equal to the square root of the ratio of outside to total thermal resistance. Its range was thus constrained to values between 0 and unity. Low values of Γ resulted in wall temperatures near those of the outer fluid, thereby increasing the axial conduction error. The effect of Γ on the length of the transition region and associated errors was opposite in trend, with low values of Γ decreasing the length of the transition region and the accompanying overprediction of the temperature difference. In addition to providing interesting physical insights, this solution showed that the present test-sections would not give reliable estimates of <u>single-phase</u> heat transfer coefficients at very low mass fluxes, where the value of ζ_i would fall below 10. For two-phase tests, where the values of ζ_i were always greater than 20, the effects modeled above never caused errors in excess of 3.5%.

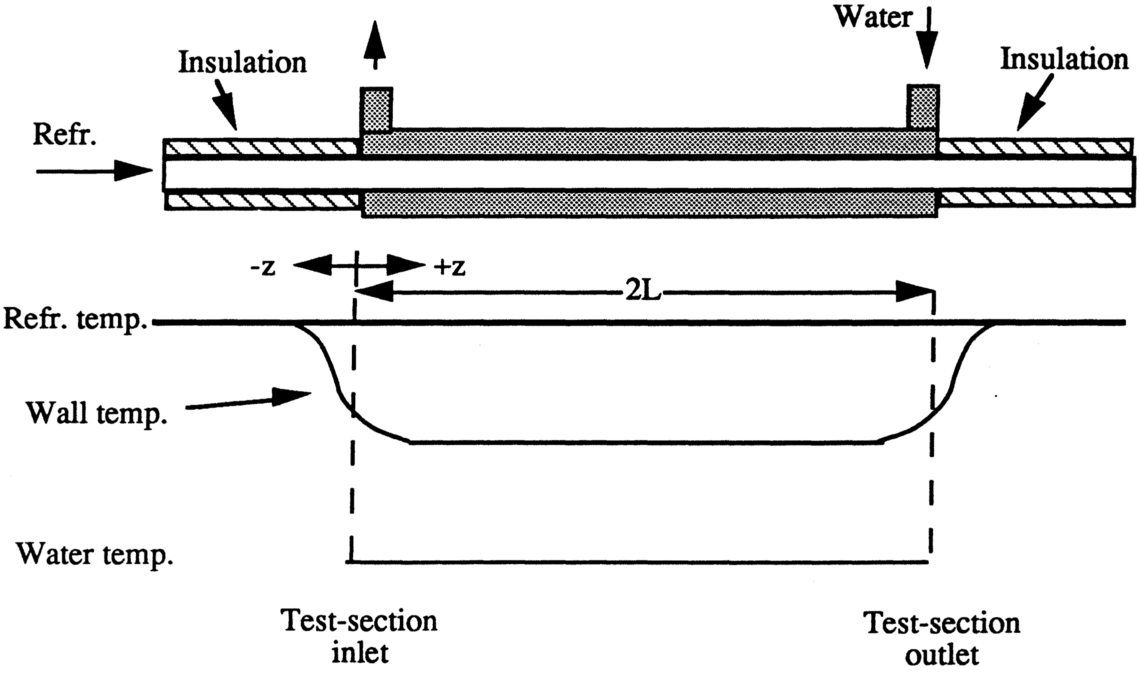

Figure B.1 Schematic of the physical situation and temperature.

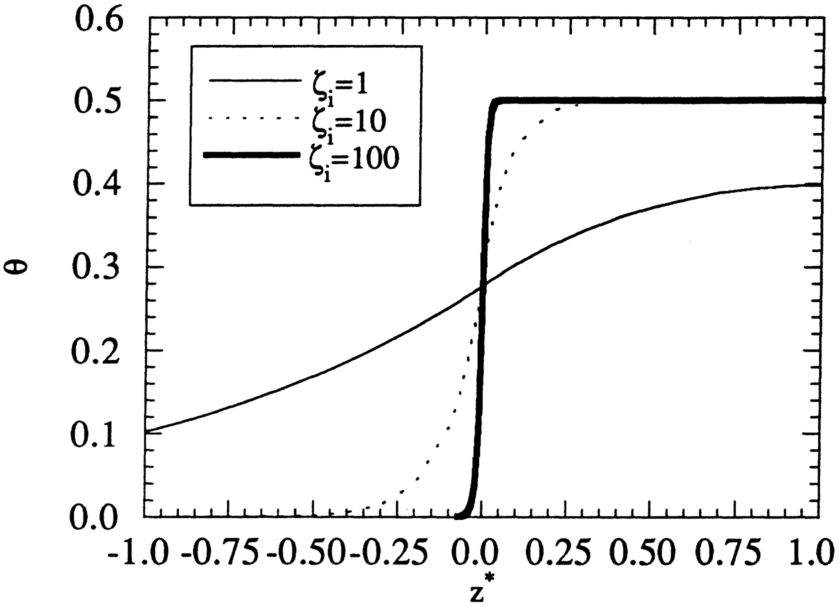

Figure B.2 Effect of ζ_i on the dimensionless profile for Γ=0.5.

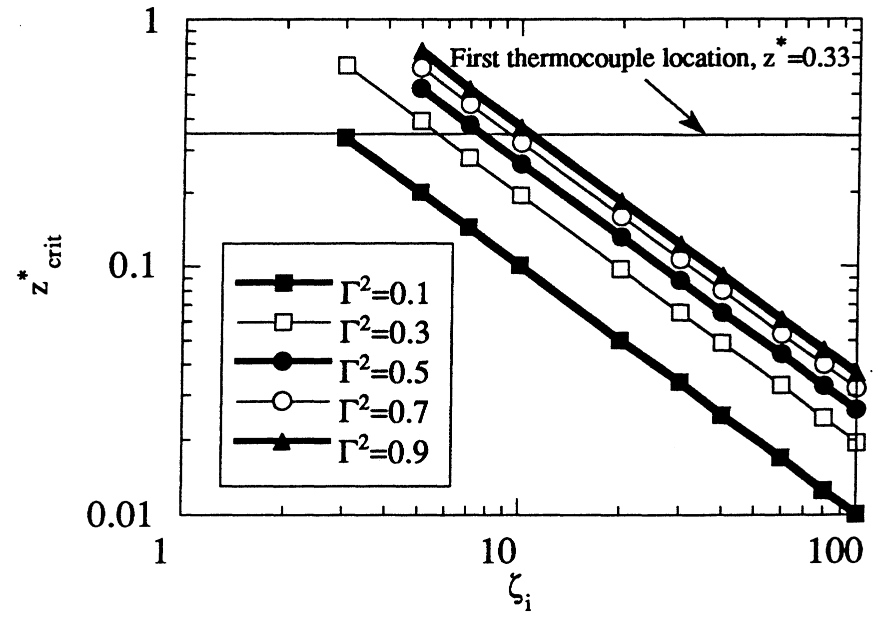

Figure B.3 Effect of ζ_i and Γ on the value of z* where $\theta=0.99\theta_{ss}$.

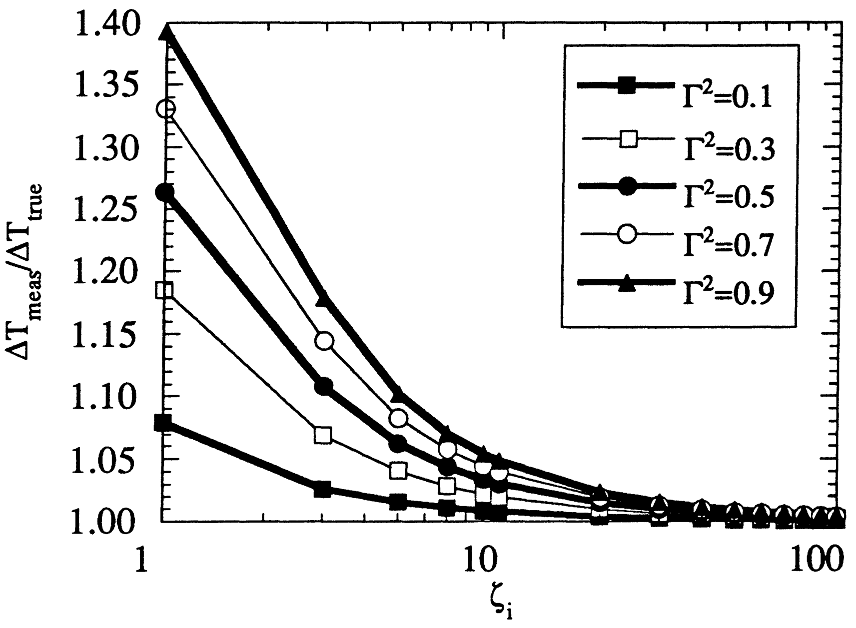

Figure B.4a Effect of ζ_i and Γ on $\Delta T_{meas}/\Delta T_{true}$ for ζ_i=1 to 100.

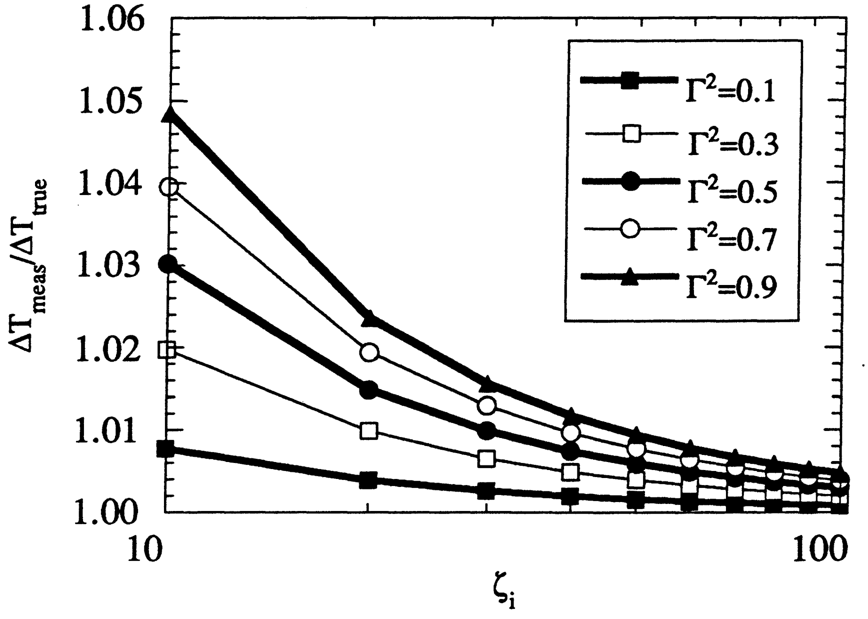

Figure B.4b Effect of ζ_i and Γ on $\Delta T_{meas}/\Delta T_{true}$ for ζ_i=10 to 100.

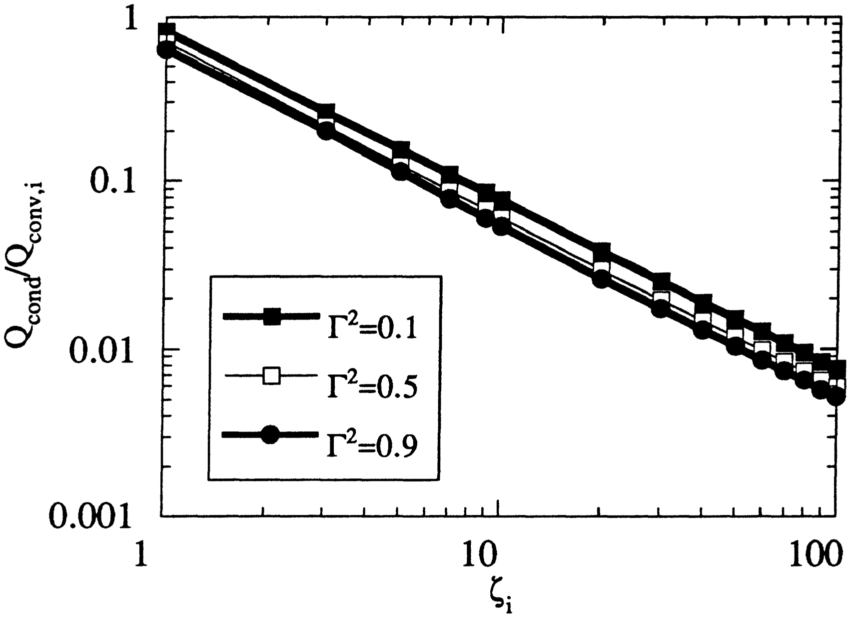

Figure B.5a Effect of ζ_i and Γ on $\dot{Q}_{cond}/\dot{Q}_{conv,i}$ for ζ_i between 1 and 100.

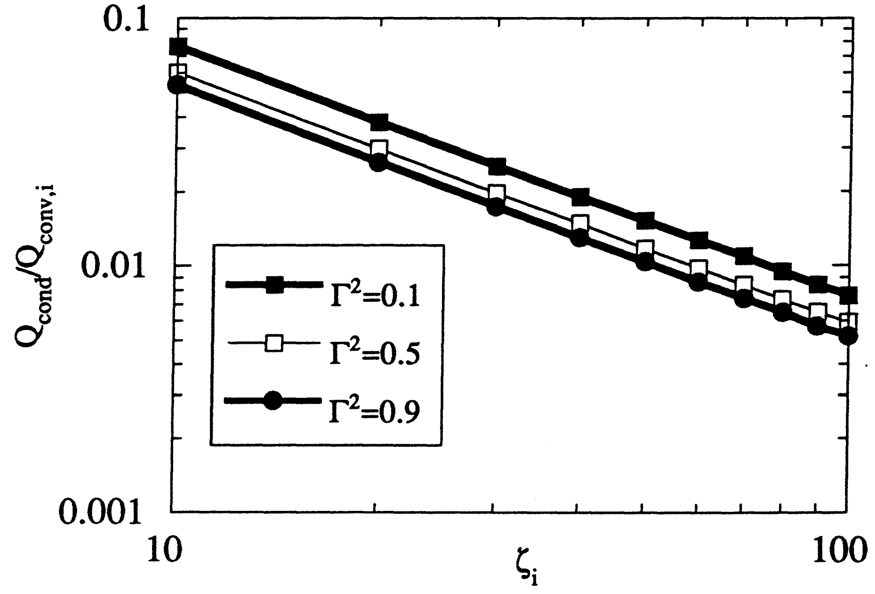

Figure B.5b Effect of ζ_i and Γ on $\dot{Q}_{cond}/\dot{Q}_{conv,i}$ for ζ_i between 10 and 100.

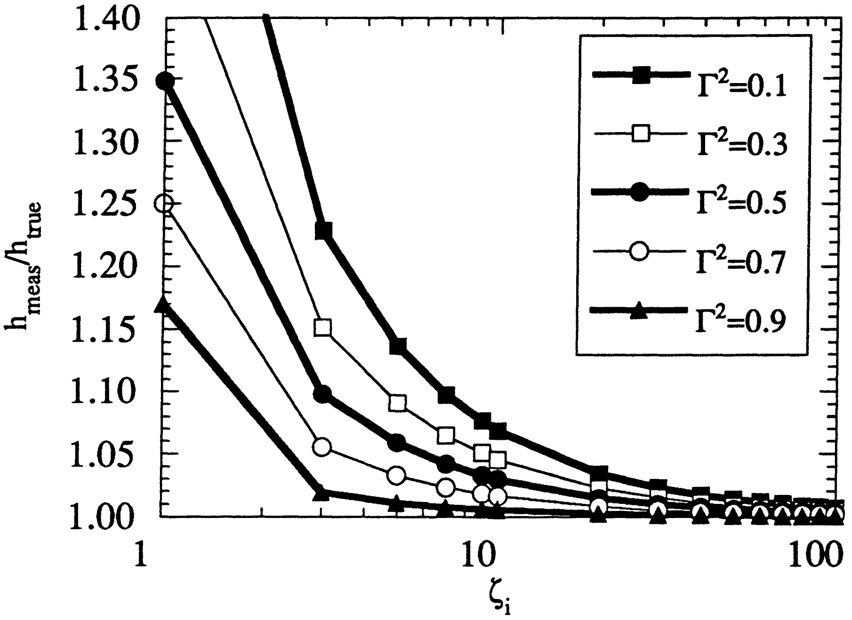

Figure B.6a Effect of ζ_i and Γ on h_{meas}/h_{true} for ζ_i between 1 and 100.

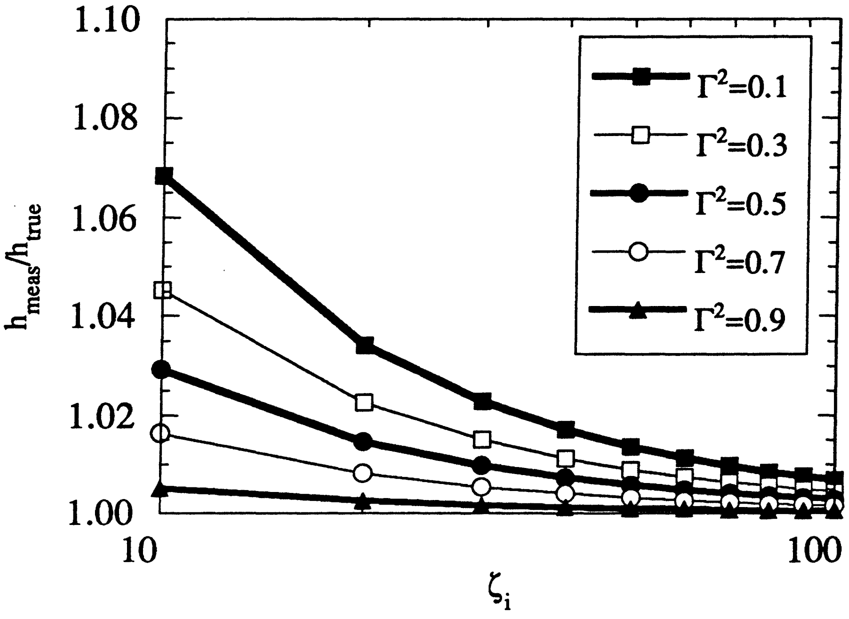

Figure B.6b Effect of ζ_i and Γ on h_{meas}/h_{true} for ζ_i between 10 and 100.

APPENDIX C

EFFECT OF VAPOR VELOCITY ON FILM CONDENSATION

The problem of gravity-driven internal condensation has historically been solved by applying Nusselt type solutions which were valid for external condensation. This approach was pioneered by Chato [1962], and has been refined by other investigators as described in Chapter 2. One immediate difficulty with applying this type of solution methodology to internal condensation is predicting how much of the tube area will be available for gravity driven condensation and how much of the tube area will be occupied by the liquid pool at the bottom of the tube. Chato argued that the liquid depth was fairly independent of quality, and hence his prefactor was a constant, 0.555. However, his flow was of the open channel type and other investigators have argued that pressure-driven flow would behave differently [Rufer and Kezios, 1966]. Jaster and Kosky [1976] used geometric arguments to argue that the prefactor should be proportional to the void fraction, α, raised to the 0.75 power. Tien et al. [1988] used Nusselt's solution in the upper part of the tube, and determined the liquid depth using conservation laws as a part of their solution methodology. Thus, their solution did not assume anything about the liquid pool depth except the validity of their conservation equations.

There is, however, one additional problem with applying Nusselt's solution to internal condensation that has not been formally addressed. Nusselt's solution assumes that the condensate flow is all driven by gravity in the downward direction. In an internal flow, however, a finite shear stress always exists in the mean flow direction. This is indicated schematically in Figure C.1. This shear stress will curve the streamlines of the condensate, so that they are not straight down as assumed. Thus, Nusselt type solutions appear to be strictly applicable only for zero shear cases, or cases of stagnant vapor. The finite vapor velocity is in fact what ultimately creates the transition from stratified flow towards annular flow.

C.1 The Vertical Plate

To simplify the mathematics somewhat, the first problem that was modeled was the effect of a vapor flow (or a finite shear stress) on external condensation on a vertical surface. The physical situation modeled is shown in Fig. C.2. It is assumed throughout this analysis that inertial forces are negligible in comparison with viscous, gravity, and pressure forces in the momentum equations, and that convective heat transfer is negligible in comparison to conduction across the film. These are the classical Nusselt assumptions, hence much of the analysis follows his original integral analysis [1916]. Based on the literature review, these assmptions should be applicable to the present study where the Prandtl numbers were greater than unity and the Jakob numbers were much less than unity.

C.1.1 Derivation of governing equations

The addition of the vapor flow in the z-direction has no effect on the x-momentum equation. This means that the u-velocity profile is that from Eq. (2.35).

$$u = \frac{g(\rho_l - \rho_v)\delta^2}{\mu_l}\left[\frac{y}{\delta} - \frac{1}{2}\left(\frac{y}{\delta}\right)^2\right] \qquad (C.1)$$

The mass flow rate per unit width in the z-direction due to this gravitational component of the flow is designated as $\dot{m}'_g$. It and its derivative with respect to δ are identical to those given from Chapter 2. These are repeated for convenience:

$$\dot{m}'_g = \rho_l \int_0^\delta u \, dy = \frac{g(\rho_l - \rho_v)\delta^3}{3\nu_l} \qquad (C.2)$$

The derivative of the gravity driven mass flow rate with respect to δ is then given by:

$$\frac{d\dot{m}'_g}{d\delta} = \frac{g(\rho_l - \rho_v)\delta^2}{\nu_l} \qquad (C.3)$$

Neglecting inertial terms in the z-momentum equation and the pressure gradient (which is appropriate for the external case) results in:

$$0 = \mu_l \frac{\partial^2 w}{\partial y^2} \qquad (C.4a)$$

subject to:

$$w(y=0)=0 \qquad (C.4b)$$

$$\frac{\partial w}{\partial y}(y = \delta) = \frac{\tau_i}{\mu_l} \qquad (C.4c)$$

The freestream velocity, U, is specified rather than the interfacial shear stress. It will be treated as a known quantity herein, though, and could be evaluated using the asymptotic shear method discussed in Section 2.4 once the film thickness is known. Integrating Eq. (6.12a) twice gives a linear relationship for the w-velocity component:

$$w = \frac{\tau_i}{\mu_l} y \qquad (C.5)$$

The w-velocity profile can also be integrated across the film to determine the shear driven mass flow rate per unit width in the x-direction. The result is:

$$\dot{m}_s' = \rho_l \int_0^{\delta} w \, dy = \frac{\tau_i \delta^2}{2\nu_l} \tag{C.6}$$

The derivative of the shear driven mass flow rate is then given by:

$$\frac{d\dot{m}_s'}{d\delta} = \frac{\tau_i \delta}{\nu_l} \tag{C.7}$$

Conservation of mass over an element from x_1 to x_2 and z_1 to z_2 requires that the net flow into the element due to gravity, shear, and condensate formation be zero:

$$\dot{m}_g(x_1) - \dot{m}_g(x_2) + \dot{m}_s(z_1) - \dot{m}_s(z_2) + \dot{m}_c = 0 \tag{C.8}$$

Solving Eq. (C.8) for the condensed mass flow rate, expressing the other terms in integral form, and grouping the integrals in the x and z directions,, gives:

$$\dot{m}_c = \int_{z_1}^{z_2} \left[\dot{m}_g'(\delta(x_2,z)) - \dot{m}_g'(\delta(x_1,z))\right] dz + \int_{x_1}^{x_2} \left[\dot{m}_s'(\delta(x,z_2)) - \dot{m}_s'(\delta(x,z_1))\right] dx \tag{C.9}$$

If the derivatives of the gravity and shear driven mass flow rates given by Eq. (C.3) and Eq. (C.7) exist and are integrable over the element, the fundamental theorem of calculus can be used to express each of the bracketed terms in Eq. (C.9) as integrals. This, combined with the chain rule, results in the following equation:

$$\dot{m}_c = \int_{x_1}^{x_2} \int_{z_1}^{z_2} \left[\frac{d\dot{m}_g'}{d\delta}\frac{\partial \delta}{\partial x} + \frac{d\dot{m}_s'}{d\delta}\frac{\partial \delta}{\partial z}\right] dz \, dx \tag{C.10}$$

Neglecting energy advection, a first law statement on an arbitrary element of the liquid film gives:

$$\dot{Q} = \dot{m}_c \, i_{lv} \tag{C.11}$$

The classical Nusselt assumptions lead to a linear temperature profile, which results in the heat transfer coefficient being given by:

$$h = \frac{k_l}{\delta} \tag{C.12}$$

The heat transfer rate can be expressed in terms of the heat transfer coefficient as:

$$\dot{Q} = \int_{x_1}^{x_2} \int_{z_1}^{z_2} h(x,z) \Delta T \, dz \, dx \tag{C.13}$$

Equating Eq. (C.11) and Eq. (C.13), substituting Eq. (C.10) and Eq, (C.12), realizing that the area of integration is arbitrary, and rearranging, the following partial differential equation for δ arises:

$$\frac{d\dot{m}_g'}{d\delta}\frac{\partial\delta}{\partial x}+\frac{d\dot{m}_s'}{d\delta}\frac{\partial\delta}{\partial z}=\frac{k_l\Delta T}{i_{lv}\delta} \tag{C.14}$$

Substituting Eq. (C.3) and Eq. (C.7) into Eq. (C.14) gives:

$$\frac{g(\rho_l-\rho_v)\delta^2}{\nu_l}\frac{\partial\delta}{\partial x}+\left(\frac{\tau_i\delta}{\nu_l}\right)\frac{\partial\delta}{\partial z}=\frac{k_l\,\Delta T}{i_{lv}\delta} \tag{C.15}$$

Once the solution to Eq. (C.15) is found, the heat transfer coefficient is immediately known as a function of both x and z based on Eq. (C.12). This equation can be cast in dimensionless form by scaling all lengths by the following length scale:

$$L_f=\left[\frac{\mu_l^2}{\rho_l(\rho_l-\rho_v)g}\right]^{1/3} \tag{C.16}$$

The dimensionless variables that emerge are defined as:

$$\tilde{\delta}={}^{\delta}\!/_{L_f} \tag{C.17a}$$

$$\tilde{x}={}^{x}\!/_{L_f} \tag{C.17b}$$

$$\tilde{z}={}^{z}\!/_{L_f} \tag{C.17c}$$

The resulting dimensionless equation is:

$$\frac{Pr}{Ja}\tilde{\delta}^2\frac{\partial\tilde{\delta}}{\partial\tilde{x}}+\frac{Pr\,\tau_i^*}{Ja}\frac{\partial\tilde{\delta}}{\partial\tilde{z}}=1 \tag{C.18}$$

The Prandtl and Jakob numbers have been defined previously. The dimensionless interfacial shear stress, τ_i^*, was defined by Rohsenow [1956] for a similar problem as:

$$\tau_i^*=\frac{\tau_i}{L_f(\rho_l-\rho_v)g} \tag{C.19}$$

C.1.2 Solution methodology

Eq. (C.15) is a quasilinear, first order partial differential equation which can be written in the following form:

$$a(x,z,u)\frac{\partial u}{\partial x} + b(x,z,u)\frac{\partial u}{\partial z} = h(x,z,u) \qquad \text{(C.20)}$$

This type of equation can be solved by the method of characteristics as outlined by Shawki [1992]. This method essentially finds certain curves in the x-z plane, called characteristic curves, along which the partial differential equation in x and z reduces to an ordinary differential equation in the variable r(x,z). The boundary data which are generally in the form u=f(x,z) are expressed parametrically in terms of a variable s which represents the distance along the curve Γ upon which boundary data are provided. Thus, the boundary data which supplement Eq. (C.20) are given by:

$$u(x,z) = u[X(s),Z(s)] = f(s) \ \text{ along } \Gamma \qquad \text{(C.21)}$$

The solution to Eq. (C.20) and Eq. (C.21) is then given by solving the following set of ordinary differential equations:

$$\frac{dx}{dr} = a(x,z,u) \quad : \ x(r=0,s) = X(s) \qquad \text{(C.22a)}$$

$$\frac{dz}{dr} = b(x,z,u) \quad : \ z(r=0,s) = Z(s) \qquad \text{(C.22b)}$$

$$\frac{du}{dr} = h(x,z,u) \quad : \ u(r=0,s) = f(s) \qquad \text{(C.22c)}$$

The solution to Eq. (C.22a-c) gives x(r,s), z(r,s), and u(r,s), and can often be accomplished analytically. The solution can then, in principle, be inverted to solve for r(x,z) and s(x,z). When possible, this gives u(x,y) in closed form.

The problem will first be solved for those characteristics emanating from z=0, where the film thickness is everywhere zero. For this problem, the differential equations to be solved in terms of characteristic variables are:

$$\frac{d\tilde{x}}{dr} = \frac{\Pr\tilde{\delta}^3}{Ja} \quad : \ \tilde{x}(r=0,s) = s \qquad \text{(C.23a)}$$

$$\frac{d\tilde{z}}{dr} = \frac{\tau_i^* \Pr\tilde{\delta}^2}{Ja} \quad : \ \tilde{z}(r=0,s) = 0 \qquad \text{(C.23b)}$$

$$\frac{d\tilde{\delta}}{dr} = 1 \quad : \ \tilde{\delta}(r=0,s) = 0 \qquad \text{(C.23c)}$$

Equations (C.23b) and (C.23c) can be solved to give:

$$\tilde{\delta} = \left[\frac{3 \mathrm{Ja}\, \tilde{z}}{\tau_i^* \, \mathrm{Pr}} \right]^{1/3} \qquad \text{(C.24)}$$

This solution is valid only in the portion of the x-z plane covered by characteristics. The characteristic equation is given by:

$$\tilde{z} = \frac{0.943 \tau_i^* \, \mathrm{Pr}^{1/4}}{\mathrm{Ja}^{1/4}} (\tilde{x} - \tilde{x}_o)^{3/4} \qquad \text{(C.25)}$$

A plot of the characteristic field predicted by Eq. (C.25) is shown in Fig. C.3. The solution for the film thickness can also be given in terms of x and x_o, where x_o is the x-intercept of the characteristic line. This equation is given by:

$$\tilde{\delta} = \left[\frac{4(\tilde{x} - \tilde{x}_o)\mathrm{Ja}}{\mathrm{Pr}} \right]^{1/4} \qquad \text{(C.26)}$$

Of particular interest is the characteristic emanating from the origin, $(\tilde{x}, \tilde{z})=(0,0)$. Along this characteristic, the film thickness can be calculated by setting $\tilde{x}_0=0$ in Eq. (C.26). This solution is exactly that given by Nusselt's analysis with no interfacial shear. Furthermore, this characteristic is a so-called limiting characteristic [Sparrow and Seigel, 1956]. For all values of $\tilde{z}$ greater than this, the dimensionless film thickness is identical (and independent of $\tilde{z}$). This is because the film thickness at the origin is zero, just as it is at all points along the $\tilde{z}$-axis. This point can be verified by solving the same partial differential equation and specifying zero film thickness along the $\tilde{z}$-axis.

The existence of the limiting characteristic means that at any value of $\tilde{x}$, there is some value of $\tilde{z}$ beyond which the film thickness no longer changes (given by Eq. (C.25) with $\tilde{x}_o=0$). If the dimensionless film thickness at this value of $\tilde{z}$ is denoted as $\tilde{\delta}_{fd}$, then Eq. (C.24) can be used to show that $\tilde{\delta}$ approaches $\tilde{\delta}_{fd}$ as follows:

$$\frac{\tilde{\delta}}{\tilde{\delta}_{fd}} = \left(\frac{\tilde{z}}{\tilde{z}_{fd}} \right)^{1/3} \qquad \text{(C.27)}$$

C.1.3 Implications

The solution to the governing partial differential equations predicted that at z values lower than those of the limiting characteristic, the film thickness would be less than its fully developed value. This would increase the Nusselt number there. In the region ahead of the leading characteristic, though, the film thickness and Nusselt number would be unaffected by the interfacial shear. In theory, this solution holds for any value of interfacial shear. The effect of the shear is then relegated to determining the shape of the limiting characteristic. In the limit of zero interfacial shear, the solution converges to Nusselt's solution for all z and x. For infinite shear, the limiting characteristic covers nearly the entire plate. Cases with very high interfacial shear will significantly lengthen the flow length, probably causing a transition to turbulence. For the analagous problem of flow inside a cylinder, cases with high interfacial shear correspond to annular flow rather than stratified flow. For the modest interfacial shear values where wavy flows are expected to exist, the region behind the limiting characteristic should be much shorter than the length of the heat exchanger. Thus, neglecting the increased heat transfer there should have little consequence.

Careful physical reasoning might have deduced that the interfacial shear would have no effect in front of the leading characteristic without any mathematical derivation. Once it is decided that there is a region where $\delta=\delta(x)$ only, the continuity relationship used to deduce the condensation rate is dependent only on flow in the x-direction. This flow is independent of any shear in the z-direction.

C.2 The Horizontal Cylinder

The problem solved above is clearly an analog rather than a replica of the problem of direct interest. Still, the insights offered by it are worthwhile. The similar problem of condensation on a horizontal cylinder is set up mathematically. The assumptions under which a finite vapor velocity will have no effect on this problem are briefly discussed.

C.2.1 Derivation of governing equations

As is customary for the case of the cylinder or the more general axisymmetric case, it is assumed that $\delta/R<<1$. The coordinate system is shown in Fig. C.4. The x-momentum equation is identical to that from the vertical plate, except that the gravitational acceleration is dependent on the angle θ. The velocity field and gravity driven mass flow rate are therefore given by:

$$u(y)=\frac{g(\rho_l-\rho_v)\delta^2}{\mu_l}\left[\frac{y}{\delta}-\frac{1}{2}\left(\frac{y}{\delta}\right)^2\right] \qquad \text{(C.28)}$$

$$\dot{m}_g'=\rho_l\int_0^\delta u\,dy=\frac{g(\rho_l-\rho_v)\delta^3\sin\theta}{3\nu_l} \qquad \text{(C.29)}$$

$$\frac{\partial m_g'}{\partial x}=\frac{2}{D}\frac{\partial m_g'}{\partial \theta}=\frac{2}{D}\frac{\partial}{\partial \theta}\left(\frac{\rho_l(\rho_l-\rho_v)g\delta^3\sin\theta}{3\mu_l}\right) \qquad \text{(C.30)}$$

Both the w-velocity field and the shear driven mass flow rate, are identical to those defined for the vertical plate. Carrying out the same steps for conserving mass and energy results in the following partial differential equation:

$$\frac{2g(\rho_l-\rho_v)}{3D\nu_l}\frac{\partial}{\partial\theta}\left(\delta^3\sin\theta\right)+\frac{\tau_i\delta}{\nu_l}\frac{\partial\delta}{\partial z}=\frac{k_l\Delta T}{\delta\, i_{lv}} \qquad \text{(C.31)}$$

This equation can be nondimensionalized by scaling all lengths by the tube diameter, D. The dimensionless variables are defined as:

$$\tilde{z}=z/D \qquad \text{(C.32)}$$

$$\tilde{\delta}=\delta/D \qquad \text{(C.33)}$$

In dimensionless form, the governing partial differential equation becomes:

$$\frac{2\,\mathrm{Ga\,Pr}}{3\mathrm{Ja}}\tilde{\delta}\frac{\partial}{\partial\theta}\left(\tilde{\delta}^3\sin\theta\right)+\frac{\Sigma\,\mathrm{Pr}}{\mathrm{Ja}}\tilde{\delta}^2\frac{\partial\tilde{\delta}}{\partial\tilde{z}}=1 \qquad \text{(C.34)}$$

$$\Sigma=\frac{\rho_l\tau_i D^2}{\mu_l^2} \qquad \text{(C.35)}$$

C.2.2 Solution methodology

In this form, the equation is not amenable to solution by the method of characteristics. Carrying out the chain rule on the partial derivative with respect to ϕ results in the proper form, but the result is too complex to solve analytically. A significant simplification can be made using the transformation suggested by Jacobi [1989]:

$$\begin{aligned}\zeta&=\tilde{\delta}^3\sin\theta\\ \tilde{\delta}&=\zeta^{1/3}\sin^{-1/3}\theta\end{aligned} \qquad \text{(C.36a-b)}$$

and

$$\frac{\partial\tilde{\delta}}{\partial\tilde{z}}=\frac{\partial\tilde{\delta}}{\partial\zeta}\frac{\partial\zeta}{\partial\tilde{z}}=\frac{1}{3}\zeta^{-2/3}\sin^{-1/3}\theta\frac{\partial\zeta}{\partial\tilde{z}} \qquad \text{(C.37)}$$

This transformation results in the following partial differential equation:

$$\Pi_1\left(\frac{\zeta}{\sin\theta}\right)^{1/3}\frac{\partial\zeta}{\partial\phi}+\frac{\Pi_2}{\sin\theta}\frac{\partial\zeta}{\partial\tilde{z}}=1 \qquad \text{(C.38)}$$

where:

$$\Pi_1 = \frac{2\mathrm{Ga\,Pr}}{3\mathrm{Ja}} \tag{C.39}$$

$$\Pi_2 = \frac{\Sigma \mathrm{Pr}}{3\mathrm{Ja}} \tag{C.40}$$

The appropriate characteristic equations and boundary conditions for the set of characteristics propagating off of the θ axis are:

$$\frac{d\theta}{dr} = \Pi_1\left(\frac{\zeta}{\sin\theta}\right)^{1/3} \qquad \theta(r=0,s)=s \tag{C.41a}$$

$$\frac{d\tilde{z}}{dr} = \frac{\Pi_2}{\sin\theta} \qquad \tilde{z}(r=0,s)=0 \tag{C.41b}$$

$$\frac{d\zeta}{dr} = 1 \qquad \zeta(r=0,s)=0 \tag{C.41c}$$

The solution for the transformed film thickness can only be obtained in quadrature form since $\sin^{1/3}\theta$ is not integrable. This is given by:

$$\zeta = \left(\frac{4}{3\Pi_1}\right)^{3/4}\left[\int_{\phi_o}^{\phi}\sin^{1/3}\lambda\,d\lambda\right]^{3/4} \tag{C.42}$$

If one knew the characteristic equation, supplying θ and $\tilde{z}$ would give the angle of intersection of the characteristic with the θ axis (e.g. θ_o). Then, the quadrature could be solved numerically for ζ. The complete procedure can be accomplished numerically, but only for specific cases.

Perhaps more importantly, though, the physics of the problem are very similar to the vertical plate. The characteristic field that emanates from the ϕ axis will cover only part of the $\theta-\tilde{z}$ plane. The solutions for the remainder of the cylinder can be derived by solving the problem for the characteristics emanating from the $\tilde{z}$ axis. Everywhere along this axis, ζ is identically zero since sin(0)=0. The resulting set of characteristic equations are:

$$\frac{d\theta}{dr} = \Pi_1\left(\frac{\zeta}{\sin\theta}\right)^{1/3} \qquad \theta(r=0,s)=0 \tag{C.43a}$$

$$\frac{d\tilde{z}}{dr} = \frac{\Pi_2}{\sin\theta} \qquad \tilde{z}(r=0,s)=s \tag{C.43b}$$

$$\frac{d\zeta}{dr} = 1 \qquad \zeta(r=0,s)=0 \tag{C.43c}$$

The solution for ζ in the region of the $\theta-\tilde{z}$ plane covered by characteristics from this solution is:

$$\zeta = \left(\frac{4}{3\Pi_1}\right)^{3/4} \left[\int_{\phi=0}^{\phi} \sin^{1/3}\lambda d\lambda \right]^{3/4} \tag{C.44}$$

This solution will be less than any of those emanating from the $\tilde{z}$ axis, since it is integrated over a narrower range and the integrand is always positive. This result is also similar to that of the vertical plate.

The reason that a limiting characteristic existed for the vertical plate was that the condensate thickness at (x,z)=(0,0) was identical to that all along the z-axis. Whether this is the case for the horizontal cylinder is not so clear. The transformed variable, ζ, is zero all along the z-axis since sin(0)=0. This implies that, at least in the transformed variable, a limiting characteristic might in fact exist. If the problem were solved in terms of δ instead, though, the most physically realistic boundary condition would be a zero thickness on the θ axis and a zero gradient on the z-axis ($\partial\delta/\partial\theta = 0$). This would not be expected to yield a limiting characteristic.

Although the mathematical complexities of this boundary condition choice are interesting, the practical implications may be less important. The widely used solution of Dhir and Lienhard [1971] utilizes a zero film thickness at θ=0 and obtains values of overall Nusselt numbers within 1% of other solutions [Chen, 1961] that do not make this assumption. Thus, even if a zero film thickness along the z-axis had to be assumed for a limiting characteristic to exist, this should impact the heat transfer results in a very minor way.

C.3 Conclusion

Several problems were investigated to assess the impact of the axial velocity component inside a tube on the validity of solutions from external, filmwise condensation. On the vertical plate, the solution for the film thickness was accomplished analytically. This solution showed that a limiting characteristic existed in the x-z plane, and that at z values in front of this characteristic the film thickness and hence the Nusselt number was no different than that with no axial velocity component (or shear stress). The mathematical complexities associated with the horizontal cylinder precluded an analytical solution, however it appears that similar results should be expected. If filmwise condensation prevailed at high vapor velocities during internal flow, the numerical results offered by the solutions would be of direct interest. In reality, though, the high vapor velocities that would create a substantial region where the film thickness was affected correspond to annular rather than stratified flow. A different physical model is necessary for this situation. Thus, the analyses presented in this appendix are useful for verifying the validity of applying filmwise condensation from the external cylinder to internal flows with modest vapor velocities.

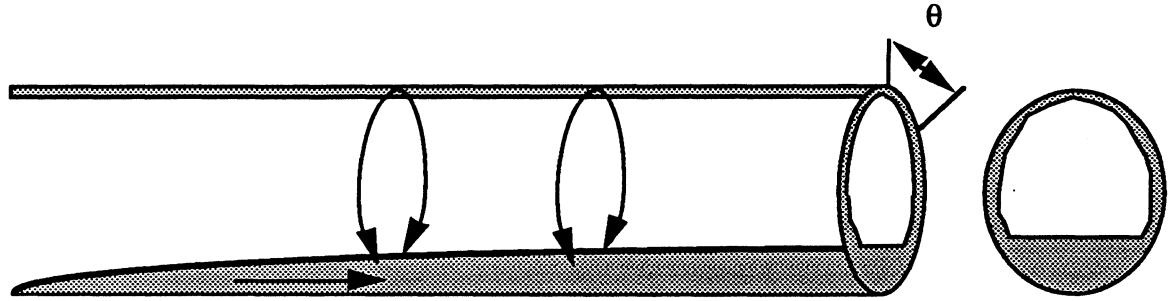

Wavy flow, film thickness $\delta \cong \delta(\theta)$ only

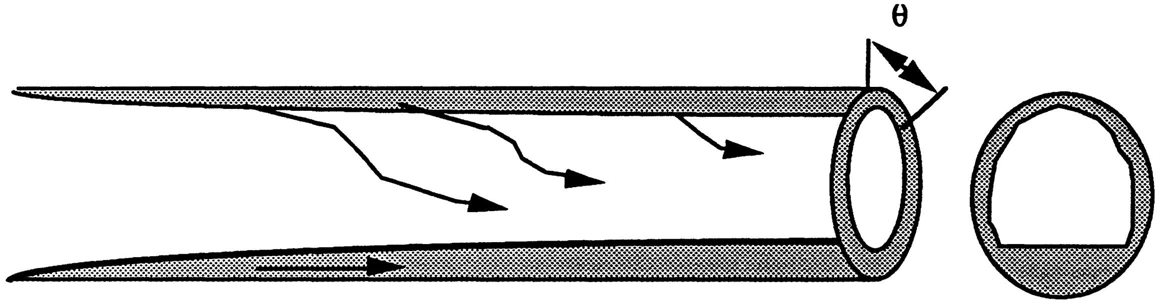

Mixed flow, film thickness $\delta \cong \delta(z,\theta)$

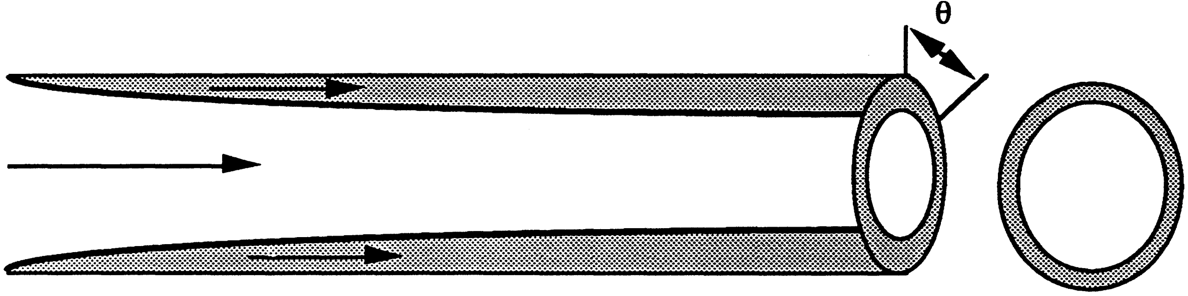

Annular flow, film thickness $\delta \cong \delta(z)$ only

Figure C.1 Effect of vapor velocity on filmwise condensation

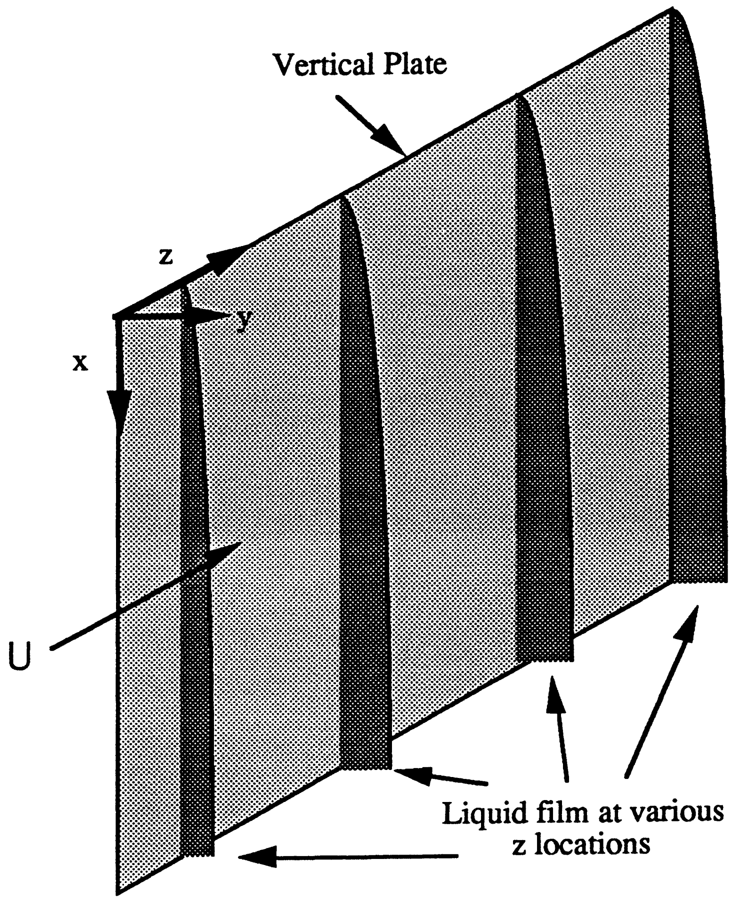

Figure C.2 Schematic and coordinate system for condensation of a flowing vapor on a vertical plate

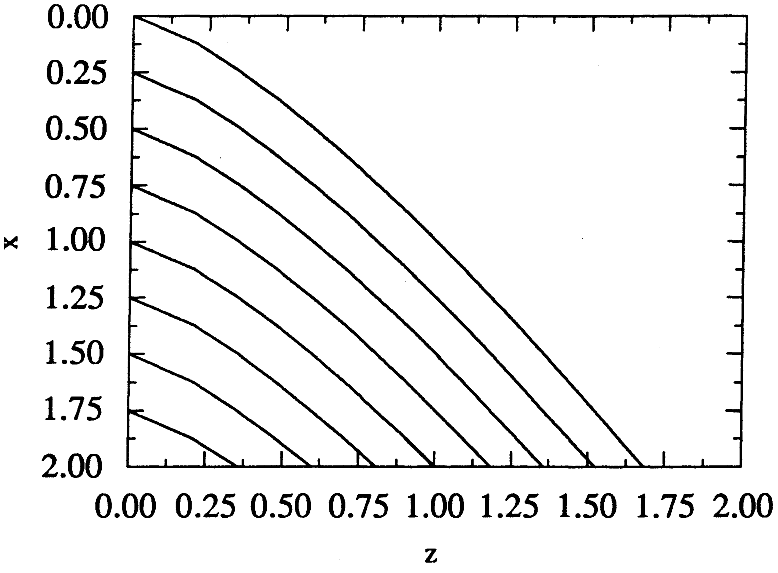

Figure C.3 Characteristic field for condensation on the vertical plate

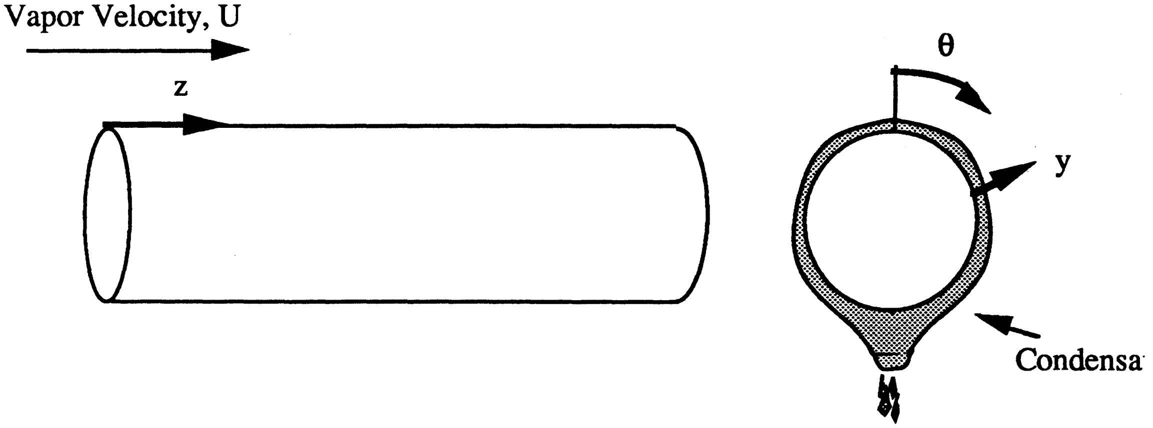

Figure C.4 Coordinate system for filmwise condensation on the horizontal cylinder

APPENDIX D

HEAT TRANSFER DATA

All heat transfer data collected in the 3.14 and 7.04 mm i.d. tubes are included in Table D.1 through Table D.6. The column headings and the respective units (if any) are as follows: G, mass flux (kg/m^2-s); x, average quality in the test-secton; xi-xo, inlet quality minus outlet quality; dx, uncertainty in the average quality; Tsat, average saturation temperature (°C); DT, circumferentially averaged refrigerant to wall temperature difference (°C); h, heat transfer coefficient (W/m2-K); dh/h, fractional uncertainty in the heat transfer coefficient; Frso, Soliman's Froude number at the average quality; File, the filename which is the date and time when the data were collected; Nu, measured Nusselt number; NuPred, predicted Nusselt number; %Diff, percentage error in the predicted Nusselt number.

Table D.1 Heat transfer data for R-134a in the 3.14 mm i.d. tube

G	x	xi-xo	dx	Tsat	DT	h	dh/h	Frso	File	Nu	NuPred	%Diff
74	0.33	0.61	0.06	36.1	3.36	2475	0.10	2.9	19930802-1542	101	93	-9.1%
53	0.42	0.96	0.08	35.9	4.15	2279	0.08	2.3	19930802-1359	93	90	-3.7%
70	0.46	0.95	0.08	37.7	4.97	2430	0.07	3.8	19930804-1211	101	93	-8.6%
75	0.48	0.57	0.05	35.3	2.78	2849	0.12	4.6	19930802-1557	116	109	-6.3%
76	0.57	0.59	0.05	35.5	2.83	2925	0.11	5.6	19930802-1637	119	115	-3.6%
79	0.66	0.57	0.05	35.6	2.78	2981	0.12	6.8	19930802-1648	122	122	0.3%
81	0.73	0.55	0.05	35.7	2.71	3051	0.12	7.7	19930802-1706	125	127	2.1%
79	0.75	0.57	0.05	35.8	2.68	3093	0.12	7.4	19930802-1711	126	129	1.7%
151	0.15	0.29	0.03	34.8	3.90	2078	0.09	2.6	19930730-1220	84	86	1.9%
151	0.16	0.25	0.03	35.2	3.18	2177	0.11	2.7	19930803-0930	89	90	1.9%
155	0.26	0.28	0.03	35.0	3.63	2226	0.10	5.5	19930730-1241	90	102	11.1%
146	0.30	0.25	0.03	35.3	2.83	2348	0.12	6.2	19930803-0944	96	109	12.7%
153	0.40	0.29	0.03	35.2	3.43	2425	0.10	10.1	19930730-1255	99	115	14.4%
146	0.49	0.82	0.04	35.9	8.81	2504	0.05	13.2	19930804-1459	102	98	-4.0%
151	0.53	0.28	0.03	35.3	2.84	2741	0.12	15.5	19930730-1316	112	129	13.5%
150	0.62	0.29	0.03	35.4	2.64	3016	0.12	18.1	19930730-1400	123	137	10.2%
157	0.71	0.26	0.02	35.6	2.33	3275	0.13	21.6	19930730-1505	134	132	-1.0%
148	0.85	0.29	0.03	35.8	2.20	3661	0.14	20.8	19930730-1518	150	141	-6.0%
301	0.11	0.21	0.02	35.6	5.88	2013	0.07	3.2	19930729-1447	82	88	6.8%
296	0.24	0.20	0.02	35.0	4.12	2731	0.09	9.5	19930729-1510	111	116	4.2%
292	0.39	0.20	0.02	35.0	2.96	3640	0.11	19.7	19930729-1531	148	139	-6.1%
308	0.53	0.64	0.03	34.9	8.63	4255	0.06	32.8	19930804-1531	173	188	8.2%
290	0.55	0.24	0.02	34.8	2.91	4552	0.11	33.6	19930729-1550	185	185	0.3%
299	0.63	0.27	0.02	34.7	2.99	5061	0.10	43.4	19930729-1600	205	206	0.3%
304	0.71	0.31	0.02	34.8	3.24	5511	0.09	54.7	19930729-1610	224	224	0.2%
301	0.84	0.32	0.02	35.1	2.98	6027	0.10	64.9	19930729-1648	245	248	1.1%
492	0.11	0.16	0.01	34.0	5.55	2671	0.07	5.5	19930729-1049	108	117	7.9%
486	0.24	0.19	0.01	34.1	4.21	4112	0.08	16.1	19930729-1108	166	170	2.3%
486	0.36	0.20	0.01	33.8	3.40	5329	0.09	29.7	19930729-1128	215	216	0.4%
492	0.51	0.21	0.01	33.6	3.06	6431	0.10	51.1	19930729-1147	259	268	3.5%
489	0.60	0.23	0.01	33.6	3.05	6950	0.10	66.6	19930729-1202	280	295	5.3%
506	0.73	0.24	0.01	36.0	3.02	7457	0.10	96.9	19930730-1615	305	342	10.8%
484	0.89	0.25	0.01	36.7	2.86	7856	0.10	132.3	19930730-1703	323	375	13.8%
151	0.18	0.22	0.06	45.6	2.61	2248	0.13	2.8	19930803-1102	98	96	-2.9%
147	0.30	0.27	0.06	45.8	2.98	2263	0.11	5.4	19930803-1118	99	107	7.0%
146	0.47	0.28	0.06	44.9	2.78	2526	0.12	10.6	19930803-1148	110	123	10.4%
151	0.59	0.26	0.05	45.0	2.56	2647	0.12	15.6	19930803-1224	115	134	14.1%
149	0.69	0.35	0.05	45.1	3.15	2903	0.10	17.3	19930803-1237	127	133	5.0%
145	0.81	0.35	0.05	45.4	2.80	3125	0.11	18.0	19930803-1257	136	143	4.8%
152	0.86	0.35	0.05	45.5	2.80	3243	0.11	19.2	19930803-1311	142	148	4.0%
312	0.14	0.14	0.03	45.7	3.54	2189	0.10	3.9	19930803-1341	96	103	6.8%
294	0.26	0.19	0.03	46.0	3.75	2573	0.09	8.8	19930803-1355	113	118	4.5%
299	0.37	0.20	0.03	46.1	3.40	3071	0.10	15.1	19930803-1432	135	132	-1.8%
302	0.46	0.20	0.03	46.2	2.82	3650	0.11	21.5	19930803-1501	160	165	2.9%
301	0.58	0.22	0.02	45.1	2.71	4329	0.11	31.1	19930803-1521	189	188	-0.3%
305	0.63	0.22	0.02	45.1	2.49	4673	0.12	37.4	19930803-1532	204	202	-0.9%
294	0.80	0.27	0.02	45.3	2.74	5078	0.11	55.1	19930803-1618	222	225	1.4%

Table D.1 Heat transfer data for R-134a in the 3.14 mm i.d. tube

G	x	xi-xo	dx	Tsat	DT	h	dh/h	Frso	File	Nu	NuPred	%Diff
295	0.88	0.28	0.03	45.6	2.69	5312	0.11	54.8	19930803-1629	232	239	2.9%
513	0.16	0.11	0.01	44.2	3.33	3113	0.10	8.1	19930803-1642	135	144	6.2%
506	0.25	0.13	0.02	44.4	2.87	4084	0.11	15.3	19930803-1657	177	179	0.8%
497	0.37	0.14	0.02	44.5	2.44	5061	0.13	26.1	19930803-1711	220	216	-1.6%
511	0.48	0.18	0.02	44.3	2.68	6027	0.11	40.7	19930803-1741	261	259	-0.9%
503	0.56	0.20	0.02	44.3	2.77	6422	0.11	51.1	19930803-1748	278	279	0.3%
497	0.68	0.20	0.02	44.4	2.58	6958	0.11	72.0	19930803-1803	302	312	3.3%
492	0.85	0.22	0.02	44.5	2.59	7499	0.11	117.2	19930803-1901	325	354	8.2%
487	0.85	0.23	0.02	44.6	2.60	7669	0.11	116.4	19930803-1850	333	352	5.3%
657	0.10	0.14	0.01	45.0	5.25	3050	0.07	5.8	19930803-2239	133	146	9.0%
661	0.20	0.16	0.01	45.1	4.29	4268	0.07	14.4	19930803-2229	186	196	5.2%
659	0.33	0.16	0.01	44.4	3.30	5734	0.09	29.4	19930803-2208	249	254	2.0%
654	0.41	0.18	0.02	45.2	3.34	6362	0.09	40.5	19930803-2137	278	286	3.1%
653	0.54	0.18	0.01	44.5	2.89	7176	0.10	63.3	19930803-2122	311	337	7.7%
650	0.65	0.19	0.01	44.1	2.87	7871	0.10	87.1	19930803-1952	341	376	9.4%
660	0.66	0.17	0.01	43.9	2.63	7909	0.11	93.0	19930803-2108	342	387	11.6%
650	0.77	0.20	0.01	44.0	2.70	8438	0.11	122.6	19930803-2016	365	417	12.5%
641	0.78	0.20	0.02	44.2	2.78	8339	0.11	124.5	19930803-2009	361	416	13.1%
648	0.83	0.20	0.02	44.2	2.66	8570	0.11	146.6	19930803-2027	371	435	14.8%
641	0.91	0.20	0.02	44.4	2.66	8763	0.11	184.7	19930803-2041	380	457	16.9%

Table D.2 Heat transfer data for R-134a in the 7.04 mm i.d tube

G	x	xi-xo	dx	Tsat	DT	h	dh/h	Frso	File	Nu	NuPred	%Diff
26	0.41	0.72	0.07	35.52	2.93	1937	0.10	0.8	19940220-1819	177	175	-1.2%
26	0.46	0.63	0.07	35.48	2.36	2119	0.13	0.9	19940220-1803	194	190	-1.8%
26	0.48	0.77	0.06	35.60	3.13	1969	0.10	0.9	19940220-1847	180	181	0.6%
26	0.50	0.73	0.06	35.60	2.92	2001	0.10	1.0	19940220-1831	183	186	1.8%
26	0.56	0.62	0.07	35.67	2.11	2301	0.14	1.1	19940220-1904	211	209	-0.6%
28	0.57	0.82	0.06	35.84	3.63	1912	0.08	1.2	19940220-2001	175	186	5.8%
27	0.62	0.61	0.06	35.74	2.15	2365	0.14	1.3	19940220-1921	217	217	0.1%
28	0.66	0.51	0.06	35.76	1.65	2655	0.18	1.4	19940220-1934	243	238	-2.3%
50	0.22	0.33	0.03	35.33	2.83	1795	0.11	0.9	19940220-2144	164	160	-2.4%
50	0.35	0.33	0.03	35.04	2.27	2215	0.13	1.8	19940220-2133	202	195	-3.3%
48	0.51	0.36	0.04	34.85	2.11	2541	0.14	2.7	19940220-2122	231	223	-3.8%
48	0.67	0.46	0.04	34.91	2.73	2480	0.11	3.4	19940220-2030	226	229	1.2%
48	0.68	0.43	0.04	34.92	2.44	2615	0.12	3.4	19940220-2043	238	236	-0.7%
48	0.74	0.44	0.04	34.99	2.49	2642	0.12	3.7	19940220-2053	241	242	0.7%
48	0.77	0.37	0.04	35.03	1.91	2863	0.15	3.8	19940220-2110	261	263	0.9%
75	0.23	0.23	0.02	34.94	2.87	1835	0.11	1.5	19940221-1153	167	174	3.7%
75	0.25	0.17	0.02	34.92	1.87	2119	0.16	1.7	19940221-1141	193	199	2.9%
79	0.26	0.33	0.02	36.77	4.40	1796	0.07	1.8	19940209-1728	166	165	-0.6%
75	0.32	0.18	0.02	34.97	1.79	2330	0.17	2.5	19940221-1127	212	216	1.8%
76	0.37	0.19	0.02	35.23	1.86	2371	0.16	3.0	19940221-1233	216	223	2.9%
79	0.45	0.35	0.02	37.00	3.90	2146	0.08	4.1	19940209-1755	198	200	1.0%
79	0.45	0.35	0.02	37.00	3.94	2144	0.08	4.2	19940209-1816	198	200	1.0%
76	0.52	0.30	0.02	35.47	2.89	2434	0.10	5.2	19940221-1307	222	224	0.6%
80	0.55	0.35	0.02	37.10	3.67	2315	0.08	5.7	19940209-1849	214	216	1.0%
76	0.56	0.23	0.02	35.45	1.94	2717	0.15	5.8	19940221-1250	248	251	1.2%
78	0.66	0.33	0.02	35.52	3.01	2603	0.10	7.3	19940209-1910	238	240	0.8%
76	0.70	0.34	0.02	35.62	2.92	2715	0.10	7.2	19940221-1324	248	245	-1.5%
75	0.76	0.25	0.02	35.06	1.94	2983	0.15	7.5	19940221-1345	272	278	2.3%
76	0.78	0.34	0.02	35.13	2.77	2860	0.11	7.8	19940221-1413	261	259	-0.8%
77	0.79	0.36	0.02	35.72	2.96	2887	0.10	7.8	19940209-1935	264	256	-3.2%
76	0.83	0.25	0.02	35.13	1.82	3239	0.16	7.8	19940221-1356	295	294	-0.6%
77	0.88	0.36	0.02	35.69	2.76	3099	0.11	7.9	19940209-2014	284	274	-3.6%
99	0.20	0.19	0.01	34.62	3.14	1883	0.10	1.7	19940221-1752	171	173	1.3%
99	0.23	0.15	0.01	34.59	2.22	2112	0.14	2.0	19940221-1818	192	196	1.9%
100	0.39	0.21	0.01	34.99	2.84	2284	0.11	4.3	19940221-1731	208	216	3.6%
99	0.42	0.16	0.01	35.04	1.98	2398	0.15	4.8	19940221-1659	218	239	8.7%
98	0.56	0.26	0.01	35.38	3.10	2561	0.10	7.6	19940221-1546	234	235	0.6%
99	0.60	0.18	0.01	35.30	1.92	2818	0.15	8.7	19940221-1640	257	269	4.5%
98	0.77	0.29	0.01	35.59	3.02	2853	0.10	11.5	19940221-1523	261	262	0.5%
156	0.13	0.15	0.01	34.92	4.26	1736	0.08	1.5	19940209-1600	158	160	1.3%
149	0.17	0.10	0.01	35.52	2.18	2109	0.14	2.1	19940222-0858	193	197	2.0%
147	0.18	0.12	0.01	35.29	2.58	2016	0.12	2.1	19940222-0821	184	190	3.3%
149	0.22	0.14	0.01	34.96	3.13	2052	0.10	2.8	19940221-1915	187	195	4.0%
155	0.22	0.18	0.01	35.24	4.15	2043	0.08	3.0	19940209-1542	186	186	-0.2%
155	0.28	0.18	0.01	34.82	4.01	2177	0.08	4.4	19940209-1529	198	202	1.9%
152	0.29	0.15	0.01	35.33	3.02	2348	0.10	4.4	19940222-0920	214	215	0.1%
153	0.31	0.12	0.01	35.56	2.19	2458	0.14	4.7	19940222-0940	225	233	3.7%

Table D.2 Heat transfer data for R-134a in the 7.04 mm i.d tube

G	x	xi-xo	dx	Tsat	DT	h	dh/h	Frso	File	Nu	NuPred	%Diff
154	0.40	0.19	0.01	34.96	3.64	2473	0.08	7.2	19940209-1454	225	227	0.6%
155	0.47	0.17	0.01	35.01	3.07	2694	0.10	9.1	19940222-1031	245	245	-0.1%
153	0.47	0.19	0.01	35.03	3.61	2518	0.08	9.0	19940209-1445	229	236	2.8%
154	0.49	0.12	0.01	35.33	2.01	2848	0.15	9.9	19940222-1015	260	273	4.9%
154	0.54	0.20	0.01	35.06	3.56	2654	0.08	11.6	19940209-1435	242	247	2.2%
154	0.59	0.18	0.01	34.79	2.96	2890	0.10	13.5	19940222-1048	263	264	0.4%
157	0.61	0.13	0.01	34.91	2.17	2979	0.14	14.2	19940222-1108	271	286	5.0%
152	0.67	0.20	0.01	34.82	3.29	2790	0.09	16.3	19940209-1424	254	266	4.4%
153	0.67	0.16	0.01	34.81	2.60	2956	0.11	16.8	19940209-1413	269	281	4.4%
156	0.72	0.19	0.01	35.98	3.07	2946	0.10	19.3	19940222-1138	270	277	2.5%
156	0.73	0.19	0.01	35.81	3.00	3005	0.10	19.8	19940222-1153	275	280	1.6%
156	0.76	0.15	0.01	35.80	2.21	3148	0.13	21.4	19940222-1226	288	261	-10.6%
150	0.76	0.16	0.01	34.86	2.44	3059	0.12	21.3	19940209-1357	278	255	-9.0%
151	0.84	0.16	0.01	34.88	2.33	3290	0.13	23.6	19940209-1343	300	273	-9.6%
155	0.86	0.22	0.01	35.05	3.03	3380	0.10	24.2	19940222-1314	308	282	-9.4%
155	0.89	0.16	0.01	35.39	2.06	3621	0.14	23.7	19940222-1254	331	286	-15.5%
157	0.90	0.21	0.01	34.64	2.72	3698	0.11	24.1	19940222-1357	336	295	-14.0%
297	0.22	0.12	0.01	35.06	4.58	2409	0.07	5.9	19920208-2121	220	222	1.0%
299	0.34	0.13	0.01	35.08	4.31	2763	0.07	11.3	19940208-2145	252	252	-0.1%
297	0.47	0.13	0.01	35.14	3.71	3267	0.08	17.8	19940208-2201	298	277	-7.4%
296	0.58	0.14	0.01	35.14	3.35	3819	0.09	25.5	19940208-2220	348	370	5.9%
296	0.71	0.15	0.01	35.02	3.03	4380	0.10	36.7	19940208-2242	399	419	4.7%
296	0.84	0.14	0.01	35.08	2.60	4873	0.11	54.6	19940208-2254	444	466	4.8%
297	0.95	0.16	0.01	35.09	2.30	5383	0.13	59.7	19940208-2309	491	504	2.6%
493	0.07	0.11	0.01	35.10	8.18	2019	0.04	2.0	19940210-1415	184	186	1.3%
491	0.13	0.12	0.01	35.35	7.31	2473	0.04	4.7	19940210-1432	226	241	6.4%
502	0.18	0.13	0.01	35.69	6.87	2861	0.04	7.6	19940210-1457	262	288	8.9%
495	0.24	0.14	0.01	34.83	6.21	3379	0.05	11.4	19940210-1521	308	331	7.2%
498	0.35	0.15	0.01	34.76	5.13	4390	0.06	19.8	19940210-1540	399	412	3.0%
496	0.39	0.15	0.01	34.66	4.91	4696	0.06	23.0	19940210-1558	427	436	2.1%
510	0.48	0.15	0.01	34.58	4.30	5577	0.07	32.8	19940210-1742	507	507	0.0%
502	0.57	0.15	0.01	34.31	3.91	6195	0.07	43.3	19940210-1801	562	558	-0.6%
496	0.67	0.16	0.01	33.91	3.55	6932	0.08	56.8	19940210-1838	627	611	-2.6%
495	0.77	0.16	0.01	33.51	3.24	7594	0.09	78.0	19940210-1933	685	673	-1.8%
505	0.82	0.17	0.01	34.97	3.41	7978	0.08	89.3	19940210-2004	727	705	-3.1%
646	0.09	0.10	0.01	34.70	7.45	2703	0.04	4.2	19940210-2121	246	263	6.6%
640	0.20	0.11	0.01	34.65	5.90	3866	0.05	11.8	19940210-2143	351	372	5.7%
643	0.29	0.12	0.01	34.14	4.79	4982	0.06	19.8	19940210-2210	451	454	0.7%
640	0.39	0.12	0.01	34.27	4.18	5974	0.07	31.1	19940210-2226	542	542	0.1%
631	0.51	0.14	0.01	35.11	3.87	6971	0.08	45.4	19940210-2249	635	626	-1.5%
637	0.65	0.13	0.01	34.17	3.17	8363	0.09	71.0	19940210-2308	758	738	-2.7%
627	0.79	0.14	0.01	34.44	2.99	9237	0.10	101.7	19940210-2318	838	818	-2.5%
633	0.90	0.14	0.01	34.45	2.69	10668	0.11	152.4	19940210-2327	968	897	-7.9%
80	0.21	0.41	0.03	44.97	6.60	1437	0.05	1.2	19940217-1514	140	138	-1.5%
73	0.31	0.36	0.03	45.11	4.05	1853	0.08	1.9	19940217-1614	181	171	-5.8%
74	0.47	0.24	0.03	45.26	2.25	2291	0.14	3.6	19940217-1638	224	223	-0.6%
74	0.56	0.25	0.03	45.42	2.07	2552	0.15	4.7	19940217-1722	250	240	-4.0%

Table D.2 Heat transfer data for R-134a in the 7.04 mm i.d tube

G	x	xi-xo	dx	Tsat	DT	h	dh/h	Frso	File	Nu	NuPred	%Diff
74	0.64	0.26	0.03	45.52	1.99	2775	0.15	5.8	19940217-1743	272	254	-6.9%
75	0.76	0.26	0.03	45.69	1.85	3023	0.16	6.5	19940217-1821	297	276	-7.5%
75	0.80	0.30	0.03	45.39	2.39	2737	0.12	6.8	19940217-1917	268	266	-0.8%
142	0.12	0.21	0.02	45.60	5.92	1421	0.06	1.0	19940209-2238	139	136	-2.1%
144	0.27	0.23	0.02	45.47	4.80	1944	0.07	3.1	19940209-2250	190	183	-3.9%
144	0.39	0.23	0.02	45.57	4.34	2233	0.07	5.3	19940209-2305	219	208	-5.4%
144	0.56	0.22	0.02	44.75	3.61	2591	0.08	9.6	19940209-2321	252	241	-4.9%
145	0.66	0.24	0.02	44.86	3.55	2803	0.08	13.0	19940209-2329	273	254	-7.5%
143	0.82	0.25	0.02	44.97	3.34	3042	0.09	19.1	19940209-2339	297	276	-7.5%
300	0.17	0.11	0.01	45.67	4.59	2123	0.07	3.4	19940212-1708	208	203	-2.5%
300	0.23	0.12	0.01	45.64	4.29	2379	0.07	5.4	19940212-1736	233	224	-3.9%
299	0.34	0.13	0.01	45.72	3.89	2791	0.08	9.4	19940212-1805	274	252	-8.5%
300	0.42	0.13	0.01	45.68	3.91	2879	0.08	12.8	19940212-1827	282	265	-6.5%
299	0.53	0.14	0.01	45.75	3.64	3224	0.08	18.5	19940212-1841	316	284	-11.6%
299	0.60	0.22	0.01	45.77	5.54	3374	0.05	22.5	19940212-1857	331	364	9.1%
298	0.75	0.16	0.01	45.85	3.44	3964	0.09	34.6	19940212-1910	389	417	6.6%
298	0.88	0.17	0.01	46.06	3.30	4344	0.09	51.5	19940212-1920	427	457	6.6%
502	0.08	0.11	0.01	46.13	7.71	2111	0.04	2.3	19940218-0830	208	210	1.0%
525	0.13	0.12	0.01	46.23	7.13	2526	0.04	4.4	19940218-0940	249	259	3.8%
518	0.18	0.12	0.01	46.36	6.08	2821	0.05	6.7	19940218-1025	278	296	6.0%
493	0.29	0.11	0.01	44.27	4.46	3547	0.07	13.0	19940218-1205	345	363	5.2%
500	0.39	0.13	0.01	45.30	4.33	4202	0.07	19.9	19940218-1232	411	431	4.6%
495	0.45	0.13	0.01	45.14	3.95	4573	0.07	24.4	19940218-1248	447	463	3.5%
491	0.53	0.13	0.01	44.99	3.79	4883	0.08	31.3	19940218-1309	477	506	5.8%
495	0.58	0.14	0.01	45.90	3.81	5358	0.08	35.6	19940218-1349	527	533	1.2%
515	0.71	0.12	0.01	44.70	2.99	6202	0.10	54.9	19940218-1410	604	625	3.4%
509	0.78	0.12	0.01	43.40	2.39	7400	0.12	67.9	19940218-1437	714	660	-8.2%
503	0.88	0.12	0.01	43.92	2.49	7272	0.12	94.9	19940218-1453	705	706	0.3%
658	0.12	0.12	0.01	46.06	8.11	2679	0.04	5.1	19940219-1400	264	302	12.7%
652	0.17	0.12	0.01	45.11	7.20	3195	0.04	7.7	19940219-1421	312	342	8.6%
642	0.28	0.14	0.01	44.86	6.08	4161	0.05	15.9	19940219-1516	406	438	7.3%
644	0.35	0.14	0.01	45.21	5.57	4719	0.05	21.6	19940219-1544	461	492	6.3%
643	0.42	0.15	0.01	45.57	5.33	5245	0.06	28.5	19940219-1557	514	548	6.1%
646	0.54	0.15	0.01	44.55	4.43	6208	0.07	42.8	19940219-1612	604	636	5.0%
645	0.67	0.15	0.01	44.71	4.06	7093	0.07	62.4	19940219-1627	691	724	4.5%
648	0.81	0.29	0.01	44.75	6.65	8263	0.04	94.4	19940219-1715	805	817	1.5%
641	0.87	0.17	0.01	45.42	3.68	8683	0.08	114.7	19940219-1654	850	846	-0.5%
643	0.91	0.11	0.01	44.84	2.26	8852	0.13	135.6	19940219-1706	863	872	1.1%

Table D.3 Heat transfer data for R-22 in the 3.14 mm i.d. tube

G	x	xi-xo	dx	Tsat	DT	h	dh/h	Frso	File	Nu	NuPred	%Diff
153	0.11	0.33	0.03	35.80	5.72	1608	0.07	1.3	19930909-1238	61	64	5.3%
150	0.15	0.36	0.03	36.19	5.18	1880	0.07	2.1	19930909-1328	71	72	1.1%
150	0.24	0.36	0.03	35.70	4.48	2209	0.08	3.9	19930909-1432	84	85	1.6%
145	0.37	0.39	0.03	36.11	4.38	2360	0.08	6.8	19930909-1520	89	95	6.3%
147	0.44	0.57	0.04	35.88	6.87	2232	0.05	9.0	19930910-1128	84	91	7.4%
149	0.50	0.36	0.03	36.05	3.79	2548	0.09	11.2	19930909-1641	97	108	10.6%
149	0.53	0.58	0.03	35.58	6.36	2480	0.05	12.0	19930910-1214	94	98	4.7%
151	0.56	0.25	0.03	36.18	2.47	2823	0.13	12.8	19930909-1726	107	123	12.9%
307	0.09	0.14	0.01	35.46	3.85	1978	0.09	2.2	19930824-0130	75	82	8.9%
300	0.13	0.16	0.02	35.01	4.41	1947	0.08	3.4	19930928-1008	73	87	15.7%
300	0.24	0.18	0.02	35.60	4.15	2381	0.08	8.0	19930928-1032	90	104	13.7%
304	0.26	0.13	0.01	35.07	2.89	2518	0.11	9.2	19930824-0149	95	115	17.6%
299	0.31	0.20	0.02	34.89	3.87	2785	0.09	11.6	19930901-1112	105	113	7.5%
296	0.32	0.18	0.02	34.94	3.58	2761	0.09	12.1	19930928-1043	104	116	10.2%
305	0.37	0.21	0.01	35.43	4.13	2884	0.08	14.9	19930825-0027	109	117	6.9%
302	0.37	0.21	0.02	35.16	3.77	3137	0.09	15.2	19930901-1142	118	119	1.1%
295	0.39	0.14	0.01	35.35	2.57	2979	0.12	15.6	19930824-0218	112	129	12.9%
296	0.41	0.19	0.02	35.28	3.27	3144	0.09	17.1	19930928-1105	119	125	5.1%
288	0.48	0.20	0.01	35.53	3.08	3463	0.10	21.0	19930824-0240	131	132	1.2%
303	0.49	0.22	0.02	35.32	3.46	3605	0.09	22.8	19930901-1206	136	139	2.5%
296	0.49	0.18	0.02	35.13	2.65	3629	0.11	22.4	19930928-1129	137	137	0.4%
311	0.54	0.22	0.01	35.30	3.33	3847	0.09	27.5	19930825-0053	145	151	3.9%
298	0.56	0.19	0.02	35.08	2.59	3950	0.12	28.2	19930928-1209	149	150	0.6%
310	0.57	0.22	0.02	35.92	2.97	4146	0.10	29.7	19930901-1529	157	155	-1.2%
293	0.62	0.16	0.01	35.54	2.18	4019	0.14	33.3	19930824-0301	152	157	3.5%
292	0.66	0.18	0.01	35.69	2.33	4094	0.13	36.5	19930824-0317	155	162	4.4%
311	0.66	0.23	0.01	35.71	3.00	4328	0.10	39.8	19930825-0128	164	172	4.6%
308	0.71	0.24	0.01	35.25	2.80	4779	0.11	45.6	19930824-0412	180	178	-1.1%
506	0.09	0.10	0.01	35.54	4.61	2113	0.08	3.3	19930826-0125	80	91	12.3%
503	0.17	0.12	0.01	35.38	3.75	2952	0.09	8.5	19930826-0152	111	120	7.5%
506	0.24	0.12	0.01	34.95	3.17	3630	0.10	13.6	19930826-0212	137	142	3.9%
499	0.35	0.14	0.01	35.10	2.78	4529	0.11	23.0	19930826-0223	171	172	0.6%
503	0.45	0.14	0.01	35.24	2.48	5289	0.12	34.1	19930826-0249	199	200	0.2%
507	0.56	0.14	0.01	34.90	2.16	5993	0.14	48.8	19930826-0309	225	229	1.4%
503	0.64	0.19	0.01	35.10	2.78	6487	0.11	62.4	19930826-0337	244	248	1.5%
503	0.67	0.14	0.01	35.03	2.03	6627	0.15	66.9	19930826-0322	249	254	1.6%
507	0.73	0.21	0.01	35.30	2.74	7090	0.11	80.9	19930826-0353	267	270	0.9%
514	0.82	0.20	0.01	34.98	2.59	7295	0.12	106.2	19930826-0420	275	292	6.1%
651	0.10	0.10	0.01	34.53	4.68	2709	0.08	5.3	19930826-0835	102	117	13.2%
653	0.19	0.09	0.01	34.53	2.78	3904	0.12	12.7	19930826-0854	147	154	5.1%
637	0.29	0.10	0.01	34.60	2.34	4958	0.13	23.3	19930826-0906	186	191	2.3%
655	0.37	0.10	0.01	34.84	2.21	5716	0.14	34.1	19930826-0926	215	222	3.3%
650	0.46	0.11	0.01	34.79	2.22	6321	0.14	47.4	19930826-0953	238	251	5.3%
645	0.58	0.12	0.01	34.67	2.04	6996	0.15	67.0	19930826-1007	263	284	7.4%
651	0.65	0.14	0.01	35.23	2.22	7453	0.13	81.9	19930826-1029	281	305	7.9%
655	0.71	0.18	0.01	35.28	2.80	8019	0.11	98.2	19930826-1108	302	324	6.7%
647	0.74	0.14	0.01	35.26	2.20	7898	0.14	105.8	19930826-1050	298	329	9.5%

Table D.3 Heat transfer data for R-22 in the 3.14 mm i.d. tube

G	x	xi-xo	dx	Tsat	DT	h	dh/h	Frso	File	Nu	NuPred	%Diff
656	0.81	0.20	0.01	35.99	2.85	8495	0.11	133.2	19930826-1148	322	352	8.5%
655	0.87	0.20	0.01	36.19	2.91	8377	0.11	157.3	19930826-1209	318	364	12.7%
306	0.08	0.17	0.03	45.54	4.95	1802	0.07	1.5	19930922-1512	73	72	-0.4%
302	0.10	0.14	0.03	45.36	3.76	1903	0.09	2.0	19930923-1127	77	80	3.6%
297	0.15	0.25	0.03	44.89	7.06	1801	0.05	3.3	19930916-1036	72	79	8.4%
299	0.17	0.14	0.03	45.10	3.59	2046	0.10	4.0	19930916-1308	82	92	10.6%
298	0.22	0.26	0.03	45.04	6.47	2056	0.05	6.0	19930916-1101	83	90	8.0%
302	0.29	0.15	0.03	45.69	3.68	2124	0.09	8.8	19930923-1151	86	107	19.7%
298	0.31	0.16	0.03	44.97	3.21	2558	0.10	9.6	19930916-1248	103	112	7.9%
301	0.35	0.24	0.03	45.12	4.68	2597	0.07	11.3	19930916-1132	105	107	2.5%
309	0.37	0.17	0.03	44.97	3.21	2795	0.10	13.0	19930916-1220	112	118	4.9%
299	0.38	0.23	0.03	45.62	4.27	2739	0.08	12.8	19930916-1347	111	111	0.5%
303	0.44	0.22	0.03	45.79	3.58	3108	0.09	16.3	19930923-1225	126	120	-5.0%
305	0.54	0.22	0.03	45.84	3.29	3519	0.09	22.4	19930923-1236	142	139	-2.4%
299	0.55	0.19	0.03	45.00	2.84	3496	0.11	23.4	19930921-2255	141	140	-0.3%
294	0.55	0.25	0.03	45.78	3.61	3465	0.09	22.7	19930916-1456	140	138	-1.9%
301	0.56	0.19	0.03	45.22	2.68	3704	0.11	24.3	19930923-1305	149	142	-4.8%
309	0.60	0.18	0.03	45.20	2.35	4030	0.13	28.1	19930923-1344	162	151	-7.4%
305	0.61	0.19	0.03	45.28	2.56	3922	0.12	28.3	19930923-1317	158	151	-4.8%
296	0.64	0.21	0.03	45.11	2.75	3774	0.11	29.8	19930921-2313	152	151	-0.6%
307	0.70	0.20	0.03	45.16	2.52	4091	0.12	36.9	19930921-2336	165	164	-0.3%
299	0.72	0.20	0.03	45.12	2.45	4176	0.12	38.2	19930921-2345	168	164	-2.8%
505	0.11	0.15	0.02	44.96	5.79	2177	0.07	3.8	19930917-1239	87	98	10.3%
497	0.12	0.13	0.02	44.50	5.05	2260	0.07	4.4	19930917-1201	91	101	9.9%
496	0.13	0.11	0.02	44.94	4.07	2380	0.09	5.0	19930917-1257	96	104	8.2%
504	0.22	0.12	0.02	45.14	3.30	3184	0.10	10.5	19930917-1312	128	133	3.4%
500	0.29	0.13	0.02	45.25	2.98	3651	0.11	14.7	19930917-1324	147	149	1.0%
513	0.35	0.13	0.02	45.25	2.63	4307	0.12	20.1	19930917-1339	173	168	-3.4%
497	0.46	0.19	0.02	45.24	3.37	4807	0.09	29.2	19930917-1409	194	189	-2.4%
506	0.52	0.19	0.02	45.23	3.20	5180	0.09	36.2	19930917-1422	209	205	-1.5%
502	0.71	0.20	0.02	45.30	2.76	6122	0.11	63.7	19930917-1517	247	246	-0.4%
654	0.12	0.09	0.01	44.15	3.75	2806	0.09	6.2	19930920-1317	112	127	11.6%
649	0.22	0.10	0.01	44.38	2.90	4015	0.11	13.8	19930920-1345	161	163	1.2%
644	0.29	0.11	0.01	44.47	2.61	4584	0.12	19.5	19930920-1400	184	183	-0.5%
650	0.35	0.15	0.01	45.16	3.46	4958	0.09	25.4	19930920-1422	200	202	1.1%
646	0.45	0.16	0.01	45.10	3.02	5770	0.10	37.1	19930920-1438	232	230	-0.8%
652	0.50	0.15	0.01	44.96	2.74	6263	0.11	44.4	19930920-1455	252	247	-2.1%
653	0.58	0.17	0.01	44.77	2.85	6660	0.10	56.9	19930920-1522	267	269	0.5%
655	0.66	0.17	0.01	44.75	2.70	7239	0.11	73.5	19930920-1541	291	292	0.5%
649	0.76	0.18	0.01	44.78	2.60	7562	0.11	95.3	19930920-1555	304	313	3.1%
642	0.84	0.18	0.01	44.83	2.55	7812	0.11	120.1	19930920-1610	314	329	4.7%
806	0.14	0.07	0.01	45.07	2.73	3670	0.11	9.0	19930923-1451	148	158	6.4%
798	0.19	0.10	0.01	45.20	3.28	4161	0.09	13.3	19930923-1502	168	177	5.6%
803	0.28	0.10	0.01	45.19	2.74	5171	0.11	23.2	19930923-1513	208	214	2.8%
807	0.34	0.13	0.01	45.15	3.06	5770	0.10	30.5	19930923-1528	232	236	1.8%
803	0.36	0.13	0.01	44.61	3.07	5744	0.09	33.0	19930924-0836	230	243	5.0%
795	0.42	0.13	0.01	45.13	2.79	6301	0.10	41.0	19930923-1537	254	261	2.9%

Table D.3 Heat transfer data for R-22 in the 3.14 mm i.d. tube

G	x	xi-xo	dx	Tsat	DT	h	dh/h	Frso	File	Nu	NuPred	%Diff
791	0.45	0.15	0.01	45.44	3.18	6406	0.09	45.9	19930924-0850	258	271	4.7%
797	0.48	0.13	0.01	45.18	2.65	6723	0.11	51.6	19930923-1549	271	284	4.5%
794	0.54	0.14	0.01	45.30	2.86	6957	0.10	61.2	19930924-0908	280	300	6.7%
795	0.62	0.17	0.01	45.26	3.10	7515	0.09	78.6	19930924-0930	303	327	7.4%

Table D.4 Heat transfer data for R-22 in the 7.04 mm i.d. tube

G	x	xi-xo	dx	Tsat	DT	h	dh/h	Frso	File	Nu	NuPred	%Diff
25	0.48	0.65	0.05	34.65	2.37	2132	0.13	0.7	19940227-1511	180	177	-1.7%
25	0.53	0.68	0.05	36.44	2.62	2024	0.12	0.7	19940227-1559	172	176	2.0%
24	0.53	0.61	0.05	35.38	2.11	2197	0.14	0.7	19940227-1536	186	186	0.2%
26	0.60	0.62	0.05	35.81	2.22	2239	0.14	0.9	19940227-1618	190	193	1.8%
27	0.66	0.61	0.05	35.93	2.22	2326	0.13	1.1	19940227-1633	197	203	2.6%
27	0.68	0.56	0.05	36.00	1.91	2497	0.16	1.1	19940227-1651	212	213	0.5%
27	0.73	0.49	0.05	36.03	1.52	2713	0.19	1.1	19940227-1704	230	232	0.6%
28	0.81	0.55	0.05	36.17	1.82	2600	0.16	1.2	19940227-1722	221	234	5.4%
74	0.16	0.22	0.02	35.59	2.98	1719	0.11	0.7	19940225-1044	146	138	-5.8%
74	0.18	0.18	0.02	35.69	2.07	1990	0.15	0.8	19940225-1109	169	155	-9.1%
76	0.30	0.27	0.02	35.74	2.96	2145	0.10	1.8	19940225-1145	182	170	-6.8%
75	0.33	0.27	0.02	35.65	2.86	2184	0.11	2.0	19940226-1134	185	176	-5.0%
75	0.33	0.20	0.02	35.92	2.00	2346	0.15	2.0	19940225-1123	199	191	-4.2%
75	0.37	0.20	0.02	35.57	1.90	2448	0.16	2.4	19940226-1117	207	201	-3.1%
76	0.47	0.31	0.02	35.96	3.01	2392	0.10	3.5	19940225-1207	203	195	-4.0%
77	0.52	0.22	0.02	36.03	1.96	2714	0.15	4.1	19940225-1231	231	222	-3.6%
76	0.54	0.30	0.02	35.48	2.80	2571	0.11	4.4	19940226-1156	218	208	-4.8%
76	0.58	0.22	0.02	35.61	1.81	2878	0.16	4.8	19940226-1214	244	236	-3.1%
76	0.64	0.24	0.02	35.74	1.95	2912	0.15	5.3	19940226-1436	247	240	-2.7%
77	0.76	0.35	0.02	35.67	2.96	2872	0.10	6.1	19940226-1351	243	233	-4.3%
77	0.79	0.36	0.02	35.76	2.99	2916	0.10	6.2	19940226-1403	247	236	-4.9%
77	0.79	0.27	0.02	35.57	2.03	3225	0.14	6.2	19940226-1329	273	260	-5.1%
77	0.82	0.23	0.02	35.42	1.62	3409	0.18	6.3	19940226-1254	288	279	-3.3%
77	0.84	0.27	0.02	35.83	2.03	3222	0.14	6.2	19940226-1422	273	267	-2.5%
156	0.15	0.12	0.01	34.84	2.78	2043	0.11	1.5	19940224-1818	172	164	-5.1%
148	0.16	0.09	0.01	35.65	1.93	2055	0.16	1.4	19940228-0857	174	175	0.5%
152	0.28	0.14	0.01	35.25	2.73	2369	0.11	3.4	19940224-1838	200	196	-2.3%
147	0.34	0.11	0.01	35.81	1.98	2543	0.15	4.3	19940228-0918	216	221	2.2%
152	0.37	0.16	0.01	35.42	2.99	2525	0.10	5.0	19940224-1856	214	208	-2.9%
147	0.49	0.18	0.01	36.00	2.96	2729	0.10	7.3	19940228-0952	232	224	-3.3%
146	0.50	0.23	0.01	36.08	3.94	2632	0.07	7.7	19940228-1016	224	212	-5.4%
147	0.51	0.12	0.01	36.00	1.90	2982	0.15	8.0	19940228-0939	253	252	-0.6%
149	0.52	0.16	0.01	35.61	2.72	2804	0.11	8.3	19940224-1916	238	234	-1.5%
149	0.64	0.19	0.01	35.35	2.82	3068	0.10	11.9	19940224-1926	259	248	-4.7%
149	0.73	0.21	0.01	35.20	3.14	3042	0.09	15.3	19940228-1109	257	253	-1.8%
145	0.74	0.14	0.01	35.09	1.93	3270	0.15	15.7	19940228-1033	276	284	2.7%
146	0.85	0.21	0.01	35.74	2.97	3208	0.10	17.2	19940224-1939	272	270	-0.6%
148	0.88	0.21	0.01	35.45	2.93	3267	0.10	17.4	19940228-1138	276	276	0.0%
149	0.88	0.20	0.01	35.81	2.78	3291	0.11	17.5	19940224-1947	279	280	0.4%
147	0.93	0.15	0.01	35.45	1.93	3584	0.15	16.1	19940228-1159	303	314	3.3%
226	0.21	0.10	0.01	35.21	3.10	2223	0.10	3.4	19940228-1938	188	195	3.5%
227	0.22	0.07	0.01	35.23	2.05	2386	0.15	3.7	19940228-1919	202	216	6.6%
227	0.35	0.12	0.01	34.80	3.35	2589	0.09	7.1	19940228-1745	218	222	1.7%
226	0.37	0.08	0.01	34.87	2.11	2673	0.14	7.7	19940228-1826	225	248	9.1%
227	0.52	0.09	0.01	34.58	2.23	2940	0.13	13.3	19940228-1704	247	270	8.5%
227	0.52	0.09	0.01	34.58	2.23	2940	0.13	13.3	19940228-1704	247	270	8.5%
226	0.67	0.14	0.01	34.64	3.26	3071	0.09	20.1	19940228-1558	259	256	-1.1%

Table D.4 Heat transfer data for R-22 in the 7.04 mm i.d. tube

G	x	xi-xo	dx	Tsat	DT	h	dh/h	Frso	File	Nu	NuPred	%Diff
226	0.68	0.11	0.01	34.68	2.51	3059	0.12	21.2	19940228-1630	258	260	0.8%
224	0.70	0.13	0.01	34.69	2.95	3082	0.10	22.3	19940228-1254	260	263	1.2%
223	0.71	0.09	0.01	34.77	1.97	3223	0.15	22.7	19940228-1228	272	263	-3.1%
223	0.81	0.15	0.01	34.79	3.07	3361	0.09	30.0	19940228-1322	283	284	0.4%
223	0.82	0.10	0.01	34.79	2.00	3439	0.15	31.0	19940228-1346	290	287	-1.1%
224	0.86	0.19	0.01	34.86	3.86	3456	0.08	34.4	19940228-1517	291	297	1.8%
224	0.89	0.14	0.01	34.85	2.89	3519	0.10	33.7	19940228-1503	297	303	2.0%
223	0.89	0.10	0.01	34.91	1.93	3651	0.15	33.3	19940228-1359	308	302	-2.0%
223	0.91	0.15	0.01	34.86	2.77	3759	0.10	33.0	19940228-1415	317	305	-4.1%
291	0.31	0.09	0.01	35.65	2.98	2721	0.10	7.5	19940223-2236	231	234	1.4%
296	0.41	0.09	0.01	35.45	3.02	2869	0.10	11.6	19940223-2246	243	253	3.9%
294	0.57	0.09	0.01	35.56	2.56	3393	0.12	19.6	19940223-2257	287	284	-1.3%
292	0.68	0.12	0.01	35.50	2.93	3713	0.10	26.7	19940223-2309	314	315	0.1%
291	0.80	0.13	0.01	35.40	2.91	4193	0.10	38.5	19940223-2318	355	349	-1.8%
291	0.92	0.14	0.01	35.59	2.98	4391	0.10	48.8	19940223-2329	372	378	1.5%
502	0.14	0.06	0.01	35.81	3.53	2605	0.09	4.5	19940307-1258	221	211	-4.6%
504	0.14	0.05	0.01	36.13	3.06	2649	0.10	4.6	19940307-1318	225	212	-6.1%
504	0.26	0.06	0.01	35.71	3.00	3255	0.10	10.3	19940307-1222	276	280	1.4%
508	0.31	0.05	0.01	35.09	2.09	3696	0.14	14.0	19940307-1347	312	315	0.9%
498	0.46	0.08	0.01	34.75	2.84	4622	0.10	24.9	19940307-1440	389	387	-0.5%
498	0.47	0.07	0.01	34.69	2.42	4727	0.12	25.2	19940307-1425	398	389	-2.3%
500	0.47	0.10	0.01	35.39	3.31	4724	0.09	25.0	19940307-1456	400	389	-2.7%
491	0.59	0.10	0.01	35.51	2.94	5378	0.10	36.0	19940307-1527	455	440	-3.4%
495	0.72	0.12	0.01	34.94	2.97	6112	0.10	52.7	19940307-1628	516	500	-3.0%
495	0.72	0.09	0.01	34.89	2.35	6199	0.12	53.2	19940307-1605	523	502	-4.1%
494	0.85	0.12	0.01	35.12	2.79	6763	0.10	78.6	19940307-1641	571	553	-3.2%
499	0.88	0.15	0.01	34.72	3.45	6817	0.08	89.3	19940307-1710	574	571	-0.6%
499	0.89	0.13	0.01	34.84	3.14	6696	0.09	92.3	19940307-1659	564	574	1.7%
501	0.89	0.16	0.01	35.56	3.66	6717	0.08	92.8	19940307-1721	569	574	0.9%
651	0.17	0.05	0.01	35.19	3.12	3192	0.10	7.5	19940307-2308	270	280	3.7%
665	0.17	0.09	0.01	35.77	5.62	3293	0.05	7.9	19940309-2328	279	288	3.1%
658	0.21	0.05	0.01	35.11	2.89	3630	0.10	10.1	19940309-2347	307	312	1.6%
658	0.27	0.10	0.01	35.06	5.00	4136	0.06	15.0	19940309-2310	349	359	2.8%
656	0.29	0.06	0.01	35.47	3.03	4272	0.10	15.9	19940309-2253	362	367	1.4%
642	0.32	0.07	0.01	35.60	3.25	4413	0.09	18.0	19940307-2240	374	381	1.8%
668	0.36	0.12	0.01	35.56	5.47	4792	0.05	22.3	19940309-2132	406	419	3.2%
662	0.38	0.07	0.01	34.86	2.82	5232	0.10	24.5	19940309-2210	441	433	-1.9%
664	0.38	0.07	0.01	35.15	2.88	5198	0.10	24.6	19940309-2210	439	434	-1.1%
643	0.43	0.09	0.01	35.50	3.23	5480	0.09	28.6	19940307-2134	464	453	-2.3%
653	0.47	0.13	0.01	35.21	4.81	5602	0.06	33.1	19940309-2059	473	482	1.8%
656	0.47	0.09	0.01	35.54	3.29	5779	0.09	33.4	19940307-2101	489	484	-1.0%
652	0.48	0.08	0.01	34.95	2.79	5976	0.10	34.6	19940309-2037	504	490	-3.0%
644	0.60	0.13	0.01	35.13	4.04	6519	0.07	49.8	19940309-2010	551	555	0.8%
642	0.62	0.10	0.01	35.05	2.96	6613	0.10	51.3	19940309-1945	558	560	0.3%
656	0.73	0.11	0.01	35.68	3.02	7503	0.10	71.0	19940307-1841	636	627	-1.4%
656	0.73	0.12	0.01	35.88	3.33	7486	0.09	71.1	19940307-1831	635	627	-1.3%
652	0.84	0.11	0.01	34.71	2.88	8149	0.10	100.1	19940307-1755	686	685	-0.2%

Table D.4 Heat transfer data for R-22 in the 7.04 mm i.d. tube

G	x	xi-xo	dx	Tsat	DT	h	dh/h	Frso	File	Nu	NuPred	%Diff
647	0.90	0.12	0.01	34.83	2.87	8586	0.10	127.2	19940307-1736	724	713	-1.5%
70	0.14	0.24	0.04	45.84	2.93	1685	0.11	0.5	19940305-1308	153	122	-25.1%
76	0.22	0.26	0.04	45.82	3.01	1861	0.10	0.9	19940305-1241	169	142	-18.8%
77	0.33	0.30	0.03	45.91	3.28	2028	0.09	1.8	19940305-1220	184	160	-14.9%
77	0.35	0.28	0.03	45.96	2.98	2088	0.10	1.9	19940305-1230	189	167	-13.8%
77	0.49	0.30	0.03	46.00	2.97	2290	0.10	3.2	19940305-1203	208	187	-11.4%
78	0.64	0.34	0.03	46.10	3.13	2459	0.10	4.7	19940305-1151	223	203	-10.2%
79	0.77	0.36	0.03	46.12	3.01	2752	0.10	5.5	19940305-1128	250	222	-12.7%
78	0.79	0.33	0.03	46.17	2.60	2880	0.11	5.5	19940305-1139	262	232	-13.0%
151	0.06	0.08	0.02	45.77	2.17	1556	0.15	0.3	19940305-0830	141	120	-17.3%
149	0.12	0.13	0.02	46.03	3.17	1758	0.10	0.8	19940305-0846	160	135	-17.9%
151	0.19	0.14	0.02	45.96	2.87	2100	0.11	1.6	19940305-0902	191	161	-18.5%
148	0.21	0.14	0.02	45.99	2.76	2108	0.11	1.8	19940305-0902	191	166	-15.5%
149	0.28	0.15	0.02	45.72	2.81	2261	0.11	2.7	19940305-0922	205	181	-12.9%
149	0.38	0.17	0.02	45.91	3.03	2470	0.10	4.3	19940305-0935	224	197	-14.0%
148	0.49	0.17	0.02	46.07	2.79	2668	0.11	6.3	19940305-0950	242	216	-12.4%
148	0.58	0.19	0.02	45.77	2.94	2819	0.10	8.4	19940305-1012	256	226	-13.2%
149	0.72	0.20	0.02	45.91	2.89	3026	0.10	12.7	19940305-1028	275	244	-12.5%
149	0.84	0.21	0.02	46.10	2.76	3214	0.11	15.4	19940305-1056	292	261	-11.8%
149	0.89	0.23	0.02	46.12	2.98	3369	0.10	15.1	19940305-1042	306	264	-16.2%
149	0.90	0.21	0.02	46.06	2.57	3497	0.11	14.9	19940305-1050	318	275	-15.6%
298	0.05	0.06	0.01	45.25	2.76	1765	0.11	0.6	19940305-1345	159	141	-12.7%
297	0.14	0.07	0.01	45.58	2.92	2093	0.10	2.2	19940305-1412	190	180	-5.0%
296	0.15	0.05	0.01	45.62	1.98	2239	0.15	2.4	19940305-1422	203	197	-2.7%
296	0.23	0.08	0.01	46.00	3.06	2384	0.10	4.3	19940305-1451	216	205	-5.5%
296	0.25	0.06	0.01	45.97	2.19	2395	0.14	4.6	19940305-1439	217	222	2.1%
296	0.42	0.09	0.01	44.49	2.90	2802	0.10	10.3	19940305-1524	252	245	-2.6%
295	0.43	0.07	0.01	44.88	2.14	2850	0.14	10.6	19940305-1515	257	262	2.0%
295	0.53	0.12	0.01	45.37	3.37	3019	0.09	15.0	19940305-1550	273	253	-8.0%
295	0.54	0.10	0.01	45.60	2.97	2981	0.10	15.3	19940305-1539	270	260	-4.0%
295	0.55	0.07	0.01	45.72	2.02	3028	0.15	15.8	19940305-1605	274	282	2.9%
297	0.72	0.12	0.01	45.72	2.87	3491	0.10	25.4	19940305-1646	316	308	-2.9%
297	0.72	0.08	0.01	45.75	1.84	3616	0.16	25.9	19940305-1626	328	309	-6.1%
297	0.90	0.14	0.01	45.53	2.98	3914	0.10	44.5	19940305-1704	354	352	-0.7%
297	0.92	0.09	0.01	45.72	1.96	4126	0.15	43.3	19940305-1712	374	355	-5.4%
500	0.13	0.04	0.01	45.43	2.11	2489	0.15	3.3	19940309-1144	225	198	-13.5%
493	0.16	0.07	0.01	45.26	4.15	2500	0.08	4.4	19940309-1021	226	214	-5.4%
494	0.17	0.05	0.01	44.86	2.95	2520	0.10	4.9	19940309-1040	227	221	-2.8%
494	0.18	0.04	0.01	44.85	2.00	2649	0.15	5.2	19940309-1053	239	226	-5.8%
499	0.31	0.07	0.01	45.95	3.04	3282	0.10	11.3	19940309-1310	298	295	-1.1%
497	0.32	0.05	0.01	44.84	1.99	3443	0.15	12.1	19940309-1247	310	300	-3.2%
496	0.53	0.09	0.01	45.39	2.96	4233	0.10	25.5	19940309-1340	383	391	2.2%
499	0.55	0.06	0.01	44.84	1.93	4642	0.15	27.0	19940309-1415	418	400	-4.4%
493	0.71	0.14	0.01	45.75	3.79	5308	0.08	41.8	19940309-1521	481	457	-5.2%
491	0.72	0.11	0.01	45.91	2.89	5387	0.10	43.5	19940309-1501	489	461	-5.9%
499	0.87	0.21	0.01	45.74	5.08	5875	0.06	69.7	19940309-1622	532	521	-2.3%
497	0.88	0.13	0.01	44.80	3.10	6285	0.09	74.5	19940309-1552	566	527	-7.4%

Table D.4 Heat transfer data for R-22 in the 7.04 mm i.d. tube

G	x	xi-xo	dx	Tsat	DT	h	dh/h	Frso	File	Nu	NuPred	%Diff
498	0.89	0.15	0.01	45.97	3.41	6181	0.08	76.9	19940309-1605	561	528	-6.4%
653	0.69	0.16	0.01	45.53	4.85	6287	0.06	54.3	19940309-1838	569	568	-0.2%
650	0.70	0.10	0.01	44.32	2.87	6613	0.10	56.7	19940309-1819	593	575	-3.2%
646	0.88	0.17	0.01	46.29	4.36	7401	0.07	95.1	19940309-1716	673	643	-4.8%
643	0.89	0.19	0.01	45.32	4.92	7334	0.06	98.0	19940309-1744	663	647	-2.5%
644	0.89	0.18	0.01	45.49	4.40	7515	0.07	100.1	19940309-1732	680	649	-4.7%
643	0.92	0.12	0.01	45.82	3.00	7550	0.10	110.9	19940309-1802	685	657	-4.2%

Table D.5 Heat transfer data for 60/40 R-32/R-125 in the 3.14 mm i.d. tube

G	x	xi-xo	dx	Tsat	DT	h	dh/h	Frso	File	Nu	NuPred	%Diff
72	0.26	0.47	0.05	34.98	2.70	2493	0.11	1.8	19930809-1143	89	74	-19.5%
78	0.27	0.34	0.04	35.06	1.97	2719	0.15	2.0	19930809-1127	97	82	-18.2%
77	0.31	0.49	0.04	34.99	2.85	2646	0.11	2.5	19930809-1152	94	79	-19.3%
73	0.42	0.56	0.05	35.01	3.02	2726	0.10	3.3	19930809-1207	97	86	-13.0%
76	0.48	0.56	0.04	35.08	2.95	2851	0.10	4.0	19930809-1213	102	91	-12.0%
76	0.60	0.56	0.04	35.14	2.86	2987	0.11	5.1	19930809-1226	106	99	-7.7%
77	0.66	0.56	0.04	35.18	2.86	3028	0.11	5.6	19930809-1234	108	103	-4.7%
154	0.17	0.24	0.02	35.30	3.11	2375	0.11	2.2	19930806-1534	85	74	-14.7%
152	0.30	0.25	0.03	35.48	2.94	2585	0.12	4.7	19930806-1543	92	89	-4.2%
150	0.43	0.27	0.03	35.61	2.86	2812	0.12	8.0	19930806-1553	101	100	-0.9%
151	0.52	0.27	0.03	35.65	2.74	2996	0.12	10.8	19930806-1601	107	107	-0.2%
147	0.62	0.33	0.03	35.74	2.99	3172	0.11	14.3	19930806-1612	114	111	-2.5%
155	0.69	0.32	0.03	35.81	2.80	3481	0.11	17.5	19930806-1620	125	118	-5.9%
155	0.80	0.32	0.03	36.00	2.79	3543	0.11	18.9	19930806-1630	127	126	-1.5%
307	0.14	0.20	0.02	34.71	5.12	2370	0.09	3.6	19930806-1246	84	76	-10.2%
299	0.23	0.21	0.02	34.81	4.80	2651	0.09	6.5	19930806-1300	94	87	-8.2%
297	0.33	0.23	0.02	34.85	4.26	3178	0.09	10.9	19930806-1322	113	98	-14.7%
302	0.40	0.24	0.02	34.85	4.01	3600	0.09	15.1	19930806-1337	128	106	-20.8%
303	0.51	0.24	0.02	34.84	3.59	4122	0.10	22.1	19930806-1402	146	144	-1.4%
298	0.63	0.27	0.02	34.90	3.38	4707	0.10	31.2	19930806-1419	167	161	-4.1%
308	0.75	0.27	0.02	34.92	3.12	5317	0.10	45.1	19930806-1438	189	182	-3.7%
299	0.85	0.29	0.02	35.15	3.26	5712	0.10	54.4	19930806-1508	204	192	-5.9%
495	0.07	0.11	0.01	35.56	4.48	2493	0.09	2.3	19930806-1040	89	91	1.4%
496	0.19	0.12	0.01	35.86	3.34	3589	0.10	8.5	19930806-1056	129	130	0.7%
495	0.30	0.14	0.01	34.98	3.00	4650	0.11	16.7	19930806-1114	165	161	-2.5%
493	0.43	0.15	0.01	35.01	2.70	5619	0.11	28.3	19930806-1133	200	195	-2.7%
494	0.52	0.16	0.01	34.98	2.62	6193	0.12	37.4	19930806-1141	220	215	-2.5%
496	0.59	0.19	0.01	35.02	2.86	6687	0.11	47.4	19930806-1150	238	233	-2.0%
490	0.72	0.20	0.01	35.11	2.69	7332	0.11	66.9	19930806-1202	261	258	-1.3%
493	0.83	0.23	0.01	35.28	2.88	7976	0.11	93.3	19930806-1213	285	282	-1.0%
651	0.02	0.08	0.01	35.10	4.83	2301	0.08	0.5	19930809-1316	82	83	1.6%
647	0.09	0.09	0.01	35.55	3.51	3346	0.10	4.1	19930809-1333	120	120	0.3%
646	0.18	0.10	0.01	35.54	2.83	4527	0.11	10.3	19930809-1356	162	156	-4.1%
639	0.32	0.11	0.01	35.76	2.38	5960	0.13	22.8	19930809-1409	214	203	-5.5%
640	0.42	0.12	0.01	35.87	2.34	6829	0.13	34.9	19930809-1419	245	236	-4.0%
635	0.56	0.14	0.01	35.92	2.26	7814	0.13	55.4	19930809-1429	281	276	-1.7%
644	0.67	0.16	0.01	35.96	2.46	8420	0.12	75.6	19930809-1441	303	307	1.4%
638	0.78	0.17	0.01	36.09	2.46	8983	0.12	104.4	19930809-1448	323	334	3.3%
663	0.89	0.18	0.01	35.95	2.31	10381	0.13	159.5	19930809-1458	373	372	-0.2%
796	0.02	0.09	0.01	35.18	5.14	2877	0.08	0.9	19930810-0936	103	102	-0.5%
792	0.07	0.10	0.01	35.58	4.33	3758	0.08	3.9	19930810-0949	135	133	-1.4%
792	0.19	0.12	0.01	35.93	3.51	5378	0.09	14.0	19930810-1003	193	189	-2.0%
794	0.30	0.13	0.01	36.09	3.02	6714	0.10	26.2	19930810-1014	242	234	-3.2%
812	0.42	0.13	0.01	36.06	2.65	7735	0.11	43.8	19930810-1023	278	283	1.8%
803	0.51	0.15	0.01	36.12	2.69	8713	0.11	60.1	19930810-1032	314	315	0.5%
793	0.65	0.16	0.01	36.18	2.69	9577	0.11	89.6	19930810-1041	345	358	3.5%
800	0.76	0.18	0.01	36.31	2.79	10241	0.11	124.4	19930810-1050	369	395	6.4%

Table D.5 Heat transfer data for 60/40 R-32/R-125 in the 3.14 mm i.d. tube

G	x	xi-xo	dx	Tsat	DT	h	dh/h	Frso	File	Nu	NuPred	%Diff
804	0.87	0.20	0.01	36.29	2.77	11595	0.11	175.5	19930810-1059	418	427	2.1%
77	0.17	0.48	0.08	44.50	3.84	1730	0.08	0.9	19930810-1903	68	58	-17.7%
75	0.29	0.53	0.09	44.78	3.28	2166	0.09	1.8	19930810-1934	86	71	-20.5%
77	0.40	0.53	0.09	44.81	2.95	2509	0.10	3.1	19930810-1945	99	83	-20.6%
76	0.50	0.60	0.09	44.83	3.13	2619	0.10	3.9	19930810-1957	104	88	-18.6%
79	0.62	0.61	0.09	44.90	3.36	2556	0.09	5.1	19930810-2013	101	94	-7.8%
76	0.76	0.65	0.09	44.88	3.41	2565	0.09	5.5	19930810-2032	102	102	0.4%
152	0.21	0.30	0.05	45.35	4.06	1998	0.08	2.5	19930810-1718	80	72	-10.5%
156	0.31	0.31	0.05	45.46	3.70	2314	0.09	4.5	19930810-1727	92	84	-10.2%
152	0.41	0.32	0.05	45.55	3.48	2489	0.09	6.6	19930810-1735	100	92	-7.9%
155	0.51	0.33	0.05	45.65	3.27	2791	0.10	9.3	19930810-1742	112	100	-11.4%
152	0.61	0.35	0.05	45.75	3.13	2967	0.10	12.4	19930810-1750	119	107	-10.7%
153	0.70	0.35	0.05	45.89	3.02	3138	0.10	15.8	19930810-1757	126	113	-11.0%
156	0.83	0.35	0.05	45.95	2.96	3281	0.10	17.8	19930810-1805	132	123	-6.9%
299	0.14	0.16	0.03	45.40	3.99	2187	0.09	2.9	19930810-1534	87	78	-12.3%
299	0.27	0.17	0.03	45.65	3.43	2686	0.10	7.2	19930810-1547	108	96	-12.1%
295	0.38	0.19	0.03	45.83	3.13	3141	0.10	11.6	19930810-1555	126	107	-17.5%
297	0.48	0.21	0.03	45.96	3.26	3449	0.10	16.8	19930810-1606	139	114	-21.7%
296	0.60	0.23	0.03	46.16	3.05	3904	0.10	24.0	19930810-1615	157	155	-1.6%
298	0.70	0.25	0.03	46.34	3.24	4087	0.10	32.1	19930810-1626	165	169	2.6%
307	0.77	0.25	0.03	46.33	3.06	4447	0.10	39.7	19930810-1632	179	182	1.4%
306	0.85	0.26	0.03	46.31	2.87	4865	0.11	51.8	19930810-1642	196	193	-2.0%
514	0.04	0.10	0.02	45.44	4.19	2152	0.08	0.9	19930810-1321	86	85	-0.9%
488	0.14	0.12	0.02	45.98	3.41	3028	0.09	4.8	19930810-1335	122	118	-3.4%
485	0.27	0.12	0.02	45.76	2.70	3955	0.11	11.5	19930810-1357	159	152	-4.1%
486	0.36	0.13	0.02	45.83	2.36	4606	0.12	17.8	19930810-1415	185	176	-5.2%
495	0.50	0.17	0.02	45.93	2.63	5510	0.11	29.6	19930810-1434	221	210	-5.2%
501	0.57	0.20	0.02	46.09	3.06	5831	0.10	38.2	19930810-1443	235	230	-2.0%
499	0.68	0.22	0.02	46.15	2.95	6557	0.10	51.9	19930810-1454	264	252	-4.9%
503	0.77	0.24	0.02	46.36	3.21	6607	0.09	66.7	19930810-1502	267	270	1.3%
501	0.85	0.30	0.02	46.37	3.40	7676	0.09	85.8	19930810-1512	310	285	-8.8%
658	0.04	0.08	0.01	44.11	3.41	2759	0.09	1.3	19930810-1130	109	104	-3.9%
641	0.14	0.11	0.01	44.71	3.36	3927	0.09	6.4	19930810-1141	156	145	-7.1%
653	0.26	0.13	0.01	44.98	2.85	5170	0.10	15.4	19930810-1150	205	191	-7.6%
647	0.35	0.16	0.01	45.09	3.12	5825	0.10	23.5	19930810-1159	232	219	-6.0%
651	0.45	0.18	0.01	45.15	3.27	6433	0.09	34.3	19930810-1209	256	249	-2.8%
647	0.58	0.19	0.01	45.29	3.05	7174	0.10	50.5	19930810-1219	286	282	-1.4%
649	0.70	0.19	0.02	45.41	2.78	7899	0.11	71.4	19930810-1229	315	314	-0.5%
658	0.80	0.23	0.02	45.58	3.28	8176	0.09	96.7	19930810-1238	327	342	4.3%
656	0.86	0.25	0.02	45.47	3.16	9121	0.10	120.4	19930810-1248	364	357	-2.2%
811	0.07	0.09	0.01	44.13	3.42	3883	0.10	2.9	19930809-1523	153	137	-11.5%
802	0.16	0.11	0.01	44.57	2.95	5203	0.11	10.1	19930809-1532	206	184	-11.6%
802	0.28	0.11	0.01	44.74	2.66	6254	0.12	20.8	19930809-1539	248	231	-7.2%
796	0.38	0.13	0.01	44.86	2.62	7112	0.12	32.3	19930809-1546	282	267	-5.8%
793	0.48	0.14	0.01	44.99	2.52	7732	0.12	47.0	19930809-1552	307	302	-1.7%
810	0.57	0.14	0.01	44.99	2.57	8160	0.12	62.9	19930809-1559	324	336	3.4%
794	0.69	0.18	0.01	45.15	2.85	9156	0.10	88.2	19930809-1607	364	369	1.1%

Table D.5 Heat transfer data for 60/40 R-32/R-125 in the 3.14 mm i.d. tube

G	x	xi-xo	dx	Tsat	DT	h	dh/h	Frso	File	Nu	NuPred	%Diff
793	0.80	0.20	0.01	45.17	2.95	9600	0.10	118.4	19930809-1617	382	397	3.7%
800	0.89	0.22	0.01	45.28	2.97	10641	0.10	163.7	19930809-1624	424	424	0.1%

Table D.6 Heat transfer data for 50/50 R-32/R-125 in the 7.04 mm i.d. tube

G	x	xi-xo	dx	Tsat	DT	h	dh/h	Frso	file	Nu	NuPred	%Diff
25	0.32	0.50	0.10	35.7	1.92	2061	0.16	0.4	19940311-2002	177	156	-13.7%
25	0.45	0.64	0.10	35.3	2.52	2046	0.12	0.7	19940311-1934	175	165	-5.9%
28	0.51	0.81	0.09	35.4	3.83	1857	0.08	0.9	19940311-1822	159	158	-0.3%
26	0.59	0.37	0.10	35.4	1.10	2705	0.27	0.9	19940311-1922	231	224	-3.4%
28	0.64	0.57	0.09	35.6	2.19	2262	0.14	1.0	19940311-1845	194	197	1.9%
27	0.68	0.53	0.09	35.6	1.90	2369	0.16	1.1	19940311-1855	203	209	2.9%
27	0.75	0.37	0.09	35.7	1.08	2952	0.27	1.1	19940311-1905	253	252	-0.3%
68	0.12	0.19	0.04	34.9	2.87	1404	0.11	0.4	19940311-1437	119	122	2.3%
68	0.13	0.15	0.04	35.4	1.92	1723	0.16	0.4	19940311-1420	147	136	-8.4%
68	0.24	0.24	0.04	34.8	2.87	1801	0.11	1.0	19940311-1458	153	152	-0.4%
68	0.26	0.20	0.04	34.9	2.12	2062	0.14	1.1	19940311-1513	175	168	-4.4%
68	0.40	0.28	0.04	34.9	2.91	2113	0.10	2.0	19940311-1554	180	179	-0.3%
68	0.43	0.22	0.04	35.0	2.02	2382	0.15	2.3	19940311-1543	203	200	-1.5%
69	0.51	0.31	0.04	35.0	2.93	2293	0.10	3.0	19940311-1609	195	195	0.1%
69	0.55	0.24	0.04	35.1	2.09	2506	0.14	3.4	19940311-1630	213	217	1.6%
69	0.66	0.33	0.04	35.0	2.95	2472	0.10	4.7	19940311-1707	210	215	2.2%
69	0.70	0.26	0.04	35.0	2.02	2781	0.14	4.9	19940311-1645	237	241	1.6%
71	0.72	0.46	0.04	35.0	4.29	2383	0.07	5.2	19940311-1752	203	205	1.1%
71	0.78	0.36	0.04	35.1	3.11	2597	0.09	5.4	19940311-1727	221	228	3.1%
71	0.82	0.26	0.04	35.2	1.88	3067	0.15	5.5	19940311-1739	262	265	1.3%
145	0.08	0.10	0.02	34.7	2.97	1476	0.11	0.4	19940310-2349	125	126	0.3%
145	0.09	0.07	0.02	34.8	1.88	1713	0.16	0.5	19940310-2329	146	143	-1.9%
151	0.15	0.09	0.02	34.9	2.04	2085	0.15	1.1	19940311-0028	177	167	-6.0%
151	0.28	0.15	0.02	35.0	2.98	2334	0.10	2.7	19940311-0057	199	188	-5.7%
150	0.30	0.11	0.02	35.0	1.97	2565	0.15	3.0	19940311-0042	218	210	-4.1%
151	0.41	0.17	0.02	35.0	2.93	2693	0.10	4.9	19940311-0113	229	214	-7.3%
150	0.44	0.12	0.02	35.0	1.93	2932	0.15	5.3	19940311-0134	250	238	-4.9%
151	0.55	0.18	0.02	35.0	2.92	2959	0.10	7.8	19940311-0201	252	235	-7.4%
151	0.58	0.14	0.02	35.1	2.02	3196	0.14	8.4	19940311-0149	272	258	-5.7%
150	0.71	0.21	0.02	35.1	3.06	3185	0.10	12.2	19940311-0214	272	252	-7.9%
152	0.73	0.15	0.02	35.2	2.07	3425	0.14	13.0	19940311-0226	292	278	-5.0%
154	0.85	0.21	0.02	35.0	2.90	3593	0.10	18.9	19940311-0251	306	276	-10.8%
151	0.88	0.16	0.02	35.1	2.02	3793	0.14	18.1	19940311-0235	323	303	-6.7%
151	0.91	0.16	0.02	35.2	1.98	3950	0.15	17.5	19940311-0242	337	310	-8.6%
299	0.05	0.04	0.01	35.1	2.10	1658	0.15	0.6	19940311-2052	141	156	9.3%
299	0.10	0.07	0.01	35.6	2.99	2084	0.10	1.3	19940311-2112	179	171	-4.2%
299	0.11	0.05	0.01	35.8	2.01	2152	0.15	1.5	19940311-2127	185	188	1.9%
300	0.22	0.11	0.01	35.8	4.08	2584	0.07	4.1	19940311-2200	222	204	-8.8%
301	0.23	0.09	0.01	35.8	2.98	2741	0.10	4.4	19940311-2210	235	219	-7.5%
299	0.25	0.06	0.01	35.7	2.01	2847	0.15	4.7	19940311-2144	244	239	-2.3%
301	0.37	0.13	0.01	35.8	3.91	3043	0.08	8.4	19940311-2253	261	236	-10.9%
300	0.39	0.10	0.01	35.8	2.99	3171	0.10	9.0	19940311-2242	272	251	-8.5%
300	0.40	0.07	0.01	35.8	2.00	3398	0.15	9.5	19940311-2232	292	274	-6.6%
300	0.55	0.14	0.01	35.9	4.00	3417	0.07	15.5	19940311-2308	294	259	-13.3%
301	0.56	0.11	0.01	35.9	3.10	3495	0.09	16.2	19940311-2319	300	275	-9.4%
301	0.58	0.08	0.01	35.9	1.98	3700	0.15	17.2	19940311-2332	318	303	-4.8%
306	0.73	0.16	0.01	35.1	3.93	3926	0.07	26.9	19940312-1340	335	333	-0.5%

Table D.6 Heat transfer data for 50/50 R-32/R-125 in the 7.04 mm i.d. tube

G	x	xi-xo	dx	Tsat	DT	h	dh/h	Frso	file	Nu	NuPred	%Diff
300	0.75	0.13	0.01	35.7	3.03	4019	0.10	27.7	19940311-2357	345	333	-3.6%
302	0.76	0.09	0.01	35.7	2.02	4019	0.14	29.1	19940311-2348	345	338	-2.0%
306	0.87	0.19	0.01	35.5	4.01	4470	0.07	41.7	19940312-1402	382	368	-3.8%
306	0.89	0.14	0.01	35.4	2.83	4706	0.10	46.0	19940312-1418	403	374	-7.5%
306	0.91	0.10	0.01	35.4	1.99	4895	0.14	48.8	19940312-1431	418	378	-10.8%
494	0.18	0.06	0.01	35.5	2.93	2995	0.10	5.1	19940312-1533	256	240	-6.8%
492	0.20	0.04	0.01	35.1	1.94	3149	0.15	5.7	19940312-1544	268	247	-8.7%
493	0.30	0.07	0.01	35.2	2.98	3633	0.10	10.6	19940312-1613	310	303	-2.3%
494	0.31	0.05	0.01	35.4	2.03	3706	0.14	10.8	19940312-1601	317	306	-3.5%
498	0.48	0.09	0.01	35.9	3.11	4575	0.09	21.2	19940312-1646	393	389	-1.2%
494	0.51	0.06	0.01	34.6	1.96	5013	0.15	23.4	19940312-1630	425	398	-6.7%
493	0.72	0.15	0.01	34.9	4.14	5812	0.07	43.8	19940312-1818	494	486	-1.6%
491	0.75	0.11	0.01	34.8	2.78	6216	0.10	46.9	19940312-1802	528	494	-6.8%
490	0.76	0.08	0.01	35.0	1.98	6388	0.14	48.4	19940312-1743	544	498	-9.1%
496	0.86	0.19	0.01	36.2	4.65	6311	0.06	66.0	19940312-1846	544	538	-1.2%
493	0.90	0.13	0.01	35.6	2.99	6615	0.10	77.9	19940312-1906	567	550	-3.1%
661	0.10	0.06	0.01	37.5	4.12	2844	0.08	3.0	19940312-2253	249	244	-2.1%
659	0.16	0.06	0.01	35.2	3.97	3345	0.08	5.9	19940312-2226	285	287	0.5%
659	0.17	0.05	0.01	35.2	3.10	3429	0.10	6.1	19940312-2239	293	290	-0.9%
654	0.33	0.09	0.01	35.4	3.99	4649	0.07	16.1	19940312-2153	397	397	0.0%
653	0.35	0.07	0.01	35.2	2.96	4916	0.10	17.2	19940312-2211	420	406	-3.5%
654	0.51	0.12	0.01	35.8	4.11	5809	0.07	30.6	19940312-2051	499	498	-0.2%
653	0.53	0.08	0.01	35.2	2.86	5973	0.10	33.5	19940312-2119	510	511	0.3%
645	0.68	0.14	0.01	35.0	3.98	7000	0.07	50.9	19940312-1933	596	581	-2.6%
644	0.69	0.10	0.01	35.3	2.82	7020	0.10	52.4	19940312-1921	600	586	-2.3%
640	0.87	0.15	0.01	34.5	3.60	8337	0.08	91.1	19940312-2003	706	666	-6.0%
639	0.88	0.12	0.01	34.5	2.83	8318	0.10	95.1	19940312-2019	704	670	-5.1%
146	0.78	0.23	0.04	45.7	2.93	3161	0.10	12.3	19940313-1135	304	254	-20.0%
293	0.14	0.09	0.02	46.1	3.21	2175	0.09	1.8	19940313-0735	211	181	-16.3%
293	0.15	0.08	0.02	45.9	2.89	2284	0.10	1.9	19940313-0744	221	186	-18.7%
294	0.17	0.06	0.02	45.1	1.94	2375	0.15	2.3	19940313-0757	227	207	-9.5%
299	0.32	0.10	0.02	44.8	2.95	2954	0.10	5.9	19940313-0839	281	233	-20.6%
297	0.34	0.07	0.02	44.9	1.98	3138	0.15	6.3	19940313-0813	299	254	-17.8%
299	0.50	0.11	0.02	44.8	2.87	3348	0.10	11.7	19940313-0854	319	265	-20.5%
301	0.52	0.08	0.02	44.6	1.91	3549	0.15	12.4	19940313-0916	337	290	-16.4%
301	0.72	0.13	0.02	44.5	2.92	3781	0.10	22.6	19940313-1004	359	322	-11.4%
300	0.75	0.09	0.02	44.6	2.04	3975	0.14	24.0	19940313-0939	378	326	-15.7%
301	0.86	0.15	0.02	44.5	3.01	4152	0.10	35.0	19940313-1027	394	354	-11.3%
302	0.89	0.10	0.02	44.4	1.99	4499	0.14	38.2	19940313-1041	426	360	-18.6%
509	0.13	0.07	0.02	46.0	3.89	2539	0.08	2.8	19940313-0549	245	222	-10.5%
507	0.15	0.05	0.02	44.9	2.97	2616	0.10	3.5	19940313-0615	250	233	-7.1%
505	0.29	0.09	0.02	45.4	4.06	3184	0.07	8.5	19940313-0507	306	303	-0.9%
503	0.30	0.07	0.02	45.5	2.90	3366	0.10	9.1	19940313-0521	323	309	-4.7%
509	0.49	0.11	0.02	45.3	3.89	4238	0.08	19.5	19940313-0451	406	398	-2.0%
507	0.51	0.09	0.02	45.3	2.92	4236	0.10	20.6	19940313-0442	406	404	-0.4%
505	0.67	0.14	0.02	45.3	4.06	4974	0.07	32.3	19940313-0409	477	464	-2.9%
506	0.68	0.11	0.02	45.4	3.05	5051	0.10	33.3	19940313-0427	485	468	-3.5%

Table D.6 Heat transfer data for 50/50 R-32/R-125 in the 7.04 mm i.d. tube

G	x	xi-xo	dx	Tsat	DT	h	dh/h	Frso	file	Nu	NuPred	%Diff
506	0.86	0.17	0.02	45.4	4.10	5994	0.07	59.0	19940313-0330	576	535	-7.7%
504	0.89	0.13	0.02	45.4	2.97	6128	0.10	65.9	19940313-0346	588	543	-8.4%
658	0.15	0.07	0.02	45.4	4.17	3144	0.07	4.5	19940313-0019	302	286	-5.5%
658	0.16	0.05	0.02	45.4	2.94	3183	0.10	5.0	19940313-0027	305	294	-3.8%
652	0.33	0.07	0.02	45.0	3.16	4359	0.09	13.9	19940313-0059	416	398	-4.5%
651	0.34	0.05	0.02	45.0	2.24	4495	0.13	14.6	19940313-0047	429	405	-6.0%
647	0.46	0.11	0.02	45.6	4.00	4940	0.07	21.9	19940313-0131	476	463	-2.8%
645	0.48	0.08	0.02	44.9	2.94	5159	0.10	23.7	19940313-0116	492	472	-4.2%
644	0.67	0.13	0.02	45.1	3.97	6156	0.07	41.9	19940313-0219	589	564	-4.3%
642	0.69	0.10	0.02	45.2	2.98	6284	0.10	44.0	19940313-0203	602	571	-5.3%
641	0.85	0.16	0.02	45.1	3.96	7242	0.07	73.1	19940313-0241	692	643	-7.7%
645	0.87	0.12	0.02	45.5	2.98	7440	0.10	76.5	19940313-0301	715	650	-9.9%

VITA

Monte Keith Dobson was born May 7, 1965 in Texarkana, Arkansas. After graduating with honors from Arkansas Senior High School in 1983, he began his undergraduate education in a combined physics and engineering program at the Centenary College of Louisiana. He completed the final years of this program at Texas A & M University. In May 1989, Monte concurrently received a Bachelor of Science degree in Mechanical Engineering from Texas A & M and a Bachelor of Arts degree in Physics from Centenary, graduating *summa cum laude* from both programs. During his undergraduate studies, Monte received the Centenary College Alumni Scholarship, Shell Foundation and Leverett Brothers Scholarships from Texas A & M, and the Houston Trane Award for Outstanding Achievement in Heating, Ventilation, and Air Conditioning. He received his Master of Science degree in Mechanical Engineering from Texas A & M University in 1991 after completing an analytical and experimental study of the transient response of ground-coupled heat pumps. Monte began his Ph.D. program at the University of Illinois in May 1991, focusing on condensing heat transfer characteristics of alternative refrigerants. While at the University of Illinois, he has been the recipient of the DuPont Graduate Fellowship in Mechanical Engineering, the University Fellowship, and the DuPont Departmental Fellowship. He has held a research assistantship in the Air Conditioning and Refrigeration Center throughout his studies at the University of Illinois. Monte's professional experience includes three cooperative education work terms at the Trane Dealer Products Group and an internship for E.I. duPont de Nemours and Company. Upon completing the requirements for the Ph.D., Monte will work as a research engineer in the Reservoir Properties Section of the Exxon Production Research Company in Houston, Texas. Monte married Christine René Ludy on May 27, 1989.